CASCADED VOLTAGE STEP-UP CANONICAL ELEMENTS FOR POWER PROCESSING IN PV APPLICATIONS.

Reham Haroun Mohamed Abdelkarim

Dipòsit Legal: T 1668-2014

ADVERTIMENT. L'accés als continguts d'aquesta tesi doctoral i la seva utilització ha de respectar els drets de la persona autora. Pot ser utilitzada per a consulta o estudi personal, així com en activitats o materials d'investigació i docència en els termes establerts a l'art. 32 del Text Refós de la Llei de Propietat Intel·lectual (RDL 1/1996). Per altres utilitzacions es requereix l'autorització prèvia i expressa de la persona autora. En qualsevol cas, en la utilització dels seus continguts caldrà indicar de forma clara el nom i cognoms de la persona autora i el títol de la tesi doctoral. No s'autoritza la seva reproducció o altres formes d'explotació efectuades amb finalitats de lucre ni la seva comunicació pública des d'un lloc aliè al servei TDX. Tampoc s'autoritza la presentació del seu contingut en una finestra o marc aliè a TDX (framing). Aquesta reserva de drets afecta tant als continguts de la tesi com als seus resums i índexs.

ADVERTENCIA. El acceso a los contenidos de esta tesis doctoral y su utilización debe respetar los derechos de la persona autora. Puede ser utilizada para consulta o estudio personal, así como en actividades o materiales de investigación y docencia en los términos establecidos en el art. 32 del Texto Refundido de la Ley de Propiedad Intelectual (RDL 1/1996). Para otros usos se requiere la autorización previa y expresa de la persona autora. En cualquier caso, en la utilización de sus contenidos se deberá indicar de forma clara el nombre y apellidos de la persona autora y el título de la tesis doctoral. No se autoriza su reproducción u otras formas de explotación efectuadas con fines lucrativos ni su comunicación pública desde un sitio ajeno al servicio TDR. Tampoco se autoriza la presentación de su contenido en una ventana o marco ajeno a TDR (framing). Esta reserva de derechos afecta tanto al contenido de la tesis como a sus resúmenes e índices.

WARNING. Access to the contents of this doctoral thesis and its use must respect the rights of the author. It can be used for reference or private study, as well as research and learning activities or materials in the terms established by the 32nd article of the Spanish Consolidated Copyright Act (RDL 1/1996). Express and previous authorization of the author is required for any other uses. In any case, when using its content, full name of the author and title of the thesis must be clearly indicated. Reproduction or other forms of for profit use or public communication from outside TDX service is not allowed. Presentation of its content in a window or frame external to TDX (framing) is not authorized either. These rights affect both the content of the thesis and its abstracts and indexes.

Cascaded Voltage Step-up Canonical Elements for Power Processing in PV Applications

by

Reham Haroun Mohamed Abdelkarim

Departament d'Enginyeria Electrònica, Elèctrica i Automàtica

Universitat Rovira i Virgili

2014

Cascaded Voltage Step-up Canonical Elements for Power Processing in PV Applications

by

Reham Haroun Mohamed Abdelkarim

Advisors:
Dr. Angel Cid-Pastor
Dr. Abdelali El Aroudi

Departament d'Enginyeria Electrònica, Elèctrica i Automàtica

Universitat Rovira i Virgili

2014

UNIVERSITAT ROVIRA I VIRGILI
DEPARTAMENT D'ENGINYERIA ELECTRÓNICA, ELÈCTRICA I AUTOMÀTICA

I STATE that the present study, entitled "Cascaded Voltage Step-up Canonical Elements for Power Processing in PV Applications", presented by Reham Haroun Mohamed Abdelkarim for the award of the degree of Doctor, has been carried out under my supervision at the Departament d'Enginyeria Electrónica, Elèctrica i Automàtica of this university, and that it fulfils all the requirements to be eligible for doctorate award.

Tarragona, 23 October 2014

Dr. Angel Cid-Pastor

Dr. Abdelali El Aroudi

To my husband Hatem and my son Ahmed

To my mother and the soul of my father

Abstract

Renewable energy sources (RES) such as photovoltaic (PV), wind, hydro, fuel cells cannot be used directly since they are unregulated. In order to convert energy from these RES to a regulated and usable form, a power electronic converter is always necessary. The maximum power can be extracted from these RES and supplied to local loads with a lower or a higher voltage to form a power supply in remote areas. For instance, in PV applications, the voltage available from the PV panel source has to be boosted from a low DC value to either a higher DC level or to an AC voltage with a particular amplitude and frequency. This approach finds application in many areas like rural, isolated microgrids using Distributed Energy Sources (DES). For rural electrification, several RESs are combined to form a high voltage DC bus followed by an inverter to supply either isolated DC or AC loads or to feed power to the main grid.

DC microgrid can be considered as an alternative approach for integrating small scale distributed generation system (around 1MW) into low-voltage electricity distribution systems. Microgrids can be designed to operate semi-independently to reduce the cost, increase the reliability, efficiency etc and to meet other specific objectives. One of the problems is to step-up the low voltage of the RESs to the relatively high voltage of the DC bus in the microgrid system. Challenges include high conversion efficiency, high conversion ratio, small number of components, reliability and high dynamic performance, resulting in appropriate Maximum Power Point Tracking (MPPT) accuracy and tracking speed.

In this thesis, cascaded boost converters based on canonical elements under Sliding Mode Control (SMC) will be used as a solution for the high gain conversion ratio in PV applications. The three basic canonical elements for power processing are the DC-transformer, the DC-gyrator and the Loss Free resistor (LFR). Two cascaded boost converters will be synthesized based on one or two canonical elements using single or double sliding surfaces respectively. Different connections will be compared in terms of dynamic performance, stability, and settling time. It will be shown that the two cascaded LFRs is the best candidate for these kinds of applications in terms of dynamic performance and stability.

The two cascaded LFRs will be applied to make an impedance matching between a PV generator and a DC voltage bus of 380 V. Maximum Power Point Tracker (MPPT) that employs an extremum-seeking control algorithm will be used. The ideal reduced-order sliding-mode dynamics model will be derived from the full-order switched model taking into account the sliding constraints, the nonlinear characteristic of the PV module and the dynamics of the MPPT controller. Moreover, the two cascaded LFRs will be used to connect a PV panel and AC distribution system. A comparison with other alternative converters for high gain conversion ratio will be carried out. The Z-source converter and the high step-up converter based on coupled-inductor are selected in order to make this comparison. These converters will be analyzed in order to address the advantages and disadvantages of each topology to be compared with the two cascaded LFRs in terms of volume, number of components, dynamic performance, stability and efficiency.

Then, the two cascaded LFRs system will be used to synthesize a nanogrid consisting of n output paralleled two-stage boost converters which are used to connect n PV panels to a DC voltage bus of 380 V. Each PV panel is connected to the DC bus using two-stage cascaded LFRs and the n systems are connected in parallel at the output side which is then used as an interface between the panels and the DC grid. Moreover, a storage battery will be connected to the grid as a backup for the DC bus through a bidirectional converter and also for regulating the voltage of the DC bus.

The thesis includes experimental implementations for validating the theoretical analysis and the numerical simulations.

Resum

Les fonts d'energia renovables (FER) com la fotovoltaica, eólica, hidroelèctrica, les piles de combustible no es poden utilitzar directament, ja que no estan regulades. Per tal de convertir l'energia elèctrica proporcionada per aquestes fonts a una forma regulada i utilitzable, es necessiten sistemes processadors de potència basats en convertidors commutats. D'aquesta manera, la màxima potència disponible provinent d'aquestes fonts es pot extreure i utilitzar per alimentar càrregues locals a baixa tensió, o bé, a més alta tensió per constituir un sistema d'alimentació autónom en àrees remotes. Per exemple, en aplicacions fotovoltaiques, la tensió continua proporcionada pel generador fotovoltaic s'ha d'elevar des d'un valor relativament baix fins a un valor més alt o fins i tot convertir-lo en una tensió alterna d'amplitud i freqüència determinades. Aquest enfoc es pot aplicar en zones rurals o en microxarxes a"ıllades que utilitzin Fonts d'Energia Distribu"ıts (FED). En aquest tipus de xarxes elèctriques, diferents FER es combinarien per implementar un bus de tensió en corrent continu (CC) que posteriorment es podria utilitzar per alimentar càrregues de corrent continu o bé, a través d'un inversor, per alimentar càrregues d'alterna o inclús per injectar energia a la xarxa elèctrica d'alterna.

Una microxarxa de CC es pot considerar una alternativa per integrar FED a petita escala (al voltant d'1 MW) en sistemes de distribució d'energia elèctrica de baixa tensió. Les microxarxes es poden dissenyar per operar de forma quasi-autónoma per reduir el cost, augmentar la fiabilitat, etc. Un dels problemes és el d'elevar el baix nivell de la tensió de sortida de les FER al nivell de tensió del bus de CC d'una microxarxa que habitualment és molt més elevat. Els reptes a assolir són l'alt rendiment de conversió, elevats cicles de treball, nombre redu"ıt de components, fiabilitat i elevades prestacions dinàmiques que permetin una bona precisió i velocitat de recerca del sistema per la recerca del punt de màxima potència, en anglés *Maximum Power Point Tracking* (MPPT).

En aquesta tesis, es proposarà, com a solució per al disseny d'etapes d'elevat guany en aplicacions fotovoltaiques, la connexió en cascada d'elements canónics per al processat de potència basats en el convertidor elevador boost treballant sota un control en mode lliscant. Els tres elements canónics per al processat de potència són el transformador de corrent continu (CC), el girador de CC i el *Loss-Free Resistor* (LFR) o resistor lliure de pèrdues. La connexió en cascada de dos convertidors elevadors s'ha realitzat mitjançant diferents enfocs: dos elements canónics idèntics, dos elements canónics diferents i també mitjançant una única superfcie de lliscament per controlar els dos convertidors. Les diferents connexions s'han comparat en termes de prestacions dinàmiques, estabilitat y temps d'establiment. Es podrà veure que la connexió en cascada de dos LFR és la millor opció per les aplicacions citades en termes de prestacions dinàmiques i estabilitat.

La connexió en cascada de dos LFR s'aplicarà per la implementació d'una etapa d'adaptació d'impedàncies entre un generador fotovoltaic i un bus de tensió continua de 380 V. Per fer-ho s'utilitzarà un sistema MPPT basat en un algoritme de control extremal. Es modelarà la dinàmica ideal en mode lliscant d'ordre redu"ıt a partir del model complet commutat tenint en compte les restriccions del mode lliscant, la caracterstica no lineal del generador fotovoltaic i la dinàmica del control MPPT. A més a més, la connexió en cascada de dos LFR s'utilitzarà per inyectar la potència provinent d'un generador PV a una xarxa de corrent altern.

A continuació, es durà a terme una comparació entre la connexió en cascada de dos LFR i dos convertidors amb guany elevat: el convertidor Z-source i un convertidor basat amb inductors acoblats. Aquests convertidors s'analitzaran per tal d'identificar els avantatges i els desavantatges de cada topologia en front a la connexió en cascada de dos LFR. La comparació es farà en termes de volum, nombre de components, prestacions dinàmiques, estabilitat i rendiment.

Finalment, els dos LFR connectats en cascada s'utilitzaran per dissenyar una nanoxarxa formada per n LFR connectats en parallel que actuaran com etapa adaptadora entre n generadors fotovoltaics i un bus de CC de 380 V. Cada generador fotovoltaic es connectarà al bus de CC utilitzant dos LFR en cascada de forma que els n sistemes tindran els seus ports de sortida connectats en parallel. A més a més, es connectarà una bateria al sistema a través d'un convertidor bidireccional que serà l'encarregat de regular la tensió del bus de CC de la nanoxarxa.

En el marc d'aquesta tesis s'han implementat diferents prototipus experimentals per tal de validar els anàlisis teórics i les simulacions numèriques efectuades.

Acknowledgements

Firstly, I would like to thank my advisors for their supervision, Dr. Angel Cid-Pastor and Dr. Abdelali El Aroudi, not only for their great guidance and fruitful discussions but also for their confidence in giving me the opportunity to carry on this thesis.

I would also like to thank Professor Luis Martinez-Salamero for his guidance and his discussion during the years of the work in this thesis. Also, I would like to express my special gratitude to all former and current members of GAEI research group in the Departament d'Enginyeria Electrònica, Elèctrica i Automàtica (DEEEiA) at Rovira i Virgili University, Tarragona, Spain: Carlos Olalla, Carlos Restrepo, Laura Albiol, Javier Arturo, Harrynson Ramirez, Freddy Flores, Mirko Bodetto, Adria Marcos, Toni Leon, Ruben Marcos and Ricardo Bonache. Special thanks for Josep Maria Bosque for his help in the laboratory and useful advices.

I should express the deepest and warmers gratitude to my wonderful lovely husband Hatem, my son Ahmed, my brother and my sisters. Also, special thanks to my mother for supporting and praying for me. I am very grateful for the invaluable support received from innumerable friends at Rovira i Virgili University and elsewhere, Fatima, Rahma, Hany, Hamdy and Gorg.

In addition, this thesis would not have reached completion without the financial support from the Agència de Gestió d'Ajuts Universitaris i de Recerca (AGAUR) through the scholarships FI/DGR-2011.

Last but not least, I want to thank all those anonymous reviewers who have made worthy suggestions on my conference and journal publications.

Contents

List of Figures

List of Tables

List of Abbreviations

BIF	Buck with Input Filter
BOF	Boost with Output Filter
CCM	Continuous Conduction Mode
CMC	Current Mode Control
DE	Distributed Energy
DGS	Distributed Generation Systems
EMI	Electromagnetic Interference
ESC	Extremum Seeking Control
HC	Hysteresis Comparator
ISOP	Input-Series Output-Parallel
ISOS	Input-Series Output-Series
IPOP	Input-Parallel Output-Parallel
IPOS	Input-Parallel Output-Series
LFR	Loss-Free Resistor
LPF	Low Pass Filter
MIMO	Multi-Input Multi-Output
MPPT	Maximum Power Point Tracking
PI	Proportional Integral
POPI	Power Output is equal to Power Input
PV	Photovoltaic
PWM	Pulse-Width Modulated

RES	Renewable Energy Sources
SMC	Sliding Mode Control
VSS	Variable Structure Systems
VMC	Voltage Mode Control
VSC	Variable Structure Control

List of Symbols

A	The diode quality factor
C_t	The temperature coefficient
g_1	The conductance of the first g-gyrator
g_2	The conductance of the second g-gyrator
g_{r1}	The conductance of the first LFR
g_{r2}	The conductance of the second LFR
g_b	The conductance of the buck converter
h_1	The width for the hysteresis comparator for 1st stage
h_2	The width for the hysteresis comparator for 2st stage
i_1	The input current of the first converter
i_2	The input current of the second converter
i_3	The output current of the second converter
i_{L1}	The current of the inductor L_1
i_{L2}	The current of the inductor L_2
i_{L3}	The current of the inductor L_3
i_p	The current of the PV panel
I_{L1}	The steady-state current of the inductor L_1
I_{L2}	The steady-state current of the inductor L_2
I_{L3}	The steady-state current of the inductor L_3
k	The gain of the PI controller
K	Boltzmann constant
n	The number of the PV panels
n_{t1}	The conversion ratio of the first DC-transformer
n_{t2}	The conversion ratio of the second DC-transformer
n_t	The conversion ratio of the two cascaded converters
N_s	The number of cells connected in series in PV panel
q	The charge of the electron
s_1	The switching function for the 1st stage
s_2	The switching function for the 2st stage

S	The ambient irradiance
S_n	The nominal irradiance
T	The ambient tempreture
T_n	The nominal tempreture
u_{eq1}	The equivalent control for the 1st stage
u_{eq2}	The equivalent control for the 2st stage
v_1	The input voltage
v_2	The output voltage of the first converter
v_3	The output voltage of the second converter
v_{c1}	The capacitor voltage of C_1
v_{c2}	The capacitor voltage of C_2
v_{c3}	The capacitor voltage of C_3
v_p	The voltage of the PV panel
V_g	The DC input voltage
V_b	The voltage of the storage battery
V_{grid}	The voltage of the grid
$\mathcal{W}$	The Lambert-W function
$\mathbf{x}$	The state variable vector
τ	The time constant of the PI controller
$\top$	The transpose of a vector

Chapter 1

Introduction

In recent years, many countries, policy makers and research centers have recognized the need to develop high efficient electrical systems that would change the current electrical distribution and generation systems to be more reliable, economic, safe and environmentally friendly Boroyevich et al. (2010), Cellatoglu and Balasubramanian (2010), Rtten and Harting (2010), Yinger and Kamiab (2011), Heydt et al. (2009), Cecati et al. (2011), Dong et al. (2013a,b), Chen et al. (2013). In this new scenario, Distributed Generation Systems (DGS) will be one of the key points to obtain higher sustainability using Renewable Energy Sources (RES) and home energy storage to supply the local demand of energy Cellatoglu and Balasubramanian (2010).

The presence of DGS with associated electronic converters, which are not controlled by the electric power utility operator, required fresh thinking about the future operation of the electric grid and structure. The so-called microgrid is a widely known concept that comprises energy storage and a larger number of generating units in order to optimize the operation of the naturally available RESs. The microgrid can be applied to residential electrical system at the low power level (10-100 kW), to be called a nanogrid Bryan et al. (2004), Schonberger et al. (2006), Fahimi et al. (2011). Combining net-metering, communications, and remote control such nanogrids could become building blocks of the so called *smart-grid*. According to the future trends of the *smart-grid*, the upcoming customers will not have only a role of energy consumers, but also they will have a role of active stakeholders of the energy generation, distribution and management Marwali et al. (2004), Luo and Batarseh (2005), Mozina (2012).

The domain of electricity generation can be divided into centralized generation in large scale power plants and individual distributed generation in customer sites like homes, stores and small business. The future *smart-grid* will allow the coupling of the decentralized distributed generators such as small wind genera-

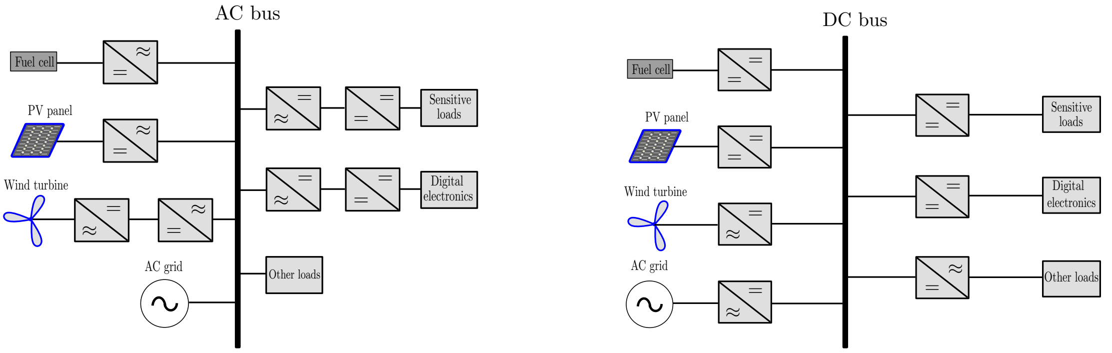

(a) (b)

Figure 1.1: Simplified block diagram of (a) AC distribution system (b) DC distribution system.

tor, photovoltaic (PV) panels, fuel cells, with the aim of local optimization and load management facilitating also a further integration of plug-in hybrid/electrical vehicles and distributed generators in the local grid.

The nanogrid can either work in the stand-alone mode or be connected to the utility grid performing peak shaving and smooth transitions between the different modes of operation. Nanogrids can be classified into two main subcategories depending on the nature of the main distribution bus: AC or DC (Fig. 1.1). While the realization of the future nanogrids remains an open question, it seems that DC distribution systems presents several advantages with respect to AC systems, despite of the cheaper protection circuit breakers and lower maintenance costs of the latter. Firstly, DC systems are more efficient and can provide higher power quality with lower harmonics Sannino et al. (2003), Nilsson (2005). Secondly, a significant advantage of the DC-based approach is the fact that power handling can be completely uninterrupted by having switched-mode power converters featuring current limitation Xu and Cheng (2011), allowing the eventual aggregation of DGS to the main DC grid Fahimi et al. (2011), Chang et al. (2013). Indeed, most of the typical consumer loads are supplied in DC and most of RES such as PV generators, fuel cells as well as storage batteries and super-capacitors use also DC current. In the DC-based nanogrid context, the future home electric system is expected to have two DC voltage levels: a high-voltage DC (380 V) powering major home appliances and electric vehicle charging and a low-voltage (48 V) for supplying computer loads, low power consumer electronics, lighting etc. Boroyevich et al. (2010), Salomonsson and Sannino (2007), Karlsson and Svensson (2003), Brenna et al. (2006).

One of the key technology issues in the DC distribution system is the implementation of power converters to connect the low output voltage of the RESs, such as PV panels or fuel cells, to the main distribution bus of 380 V. For example, the interconnection of residential scale PV systems to such a DC bus can typically be carried out by many approaches Kjaer et al. (2005). However, the best approach is to employ a power converter per module, in order to perform high granularity Maximum Power Point Tracking (MPPT) as will be explained in detail later. This approach provides higher flexibility in system layout, lower sensitivity to shading, better protection of PV sources, redundancy in case of failures, and easier and safer installation and maintenance, besides of data gathering Walker and Sernia (2004). On the other hand, the main problem for the converter per module approach, is converting a low DC voltage to a high DC one which requires a power converter operating with a high conversion ratio. For this purpose, it is necessary to have an adaptation stage with a high voltage conversion ratio in addition to a good static and dynamic performances and high efficiency. As an example, these adaptation stages could allow the implementation of a high performance MPPT of a PV generator or even the control of the operating conditions of a fuel cell to increase its lifetime Ramos-Paja et al. (2009), Cid-Pastor et al. (2011, 2013), Petrone et al. (2012).

In this work, both DC and AC grid will be considered. For DC distribution system, the required DC voltage of the grid is around 380 V, as mentioned before. In turn, the AC distribution system requires a minimum high DC voltage around 340 V before the inverter stage carrying out the DC-AC conversion from DC voltage to AC (230 V rms). In both distribution systems, the required DC voltage is higher than the output voltage of the RES. For this purpose, a power converter with a high conversion ratio and high efficiency is necessary. The system which will be studied in this thesis consists mainly of three parts: the RESs which are the used supply in the distributed generation system, the power stage which is the responsible for achieving a high conversion ratio with an efficiently way and finally, the control of the power stage. A summarized state-of-the art of each of these parts will be discussed in the following sections.

1.1 Renewable Energy Sources (RES)

Renewable Energy Sources (RES) include, but are not limited to, photovoltaic (PV), wind, microturbine, fuel cells (FC), and internal combustion engines as shown in Fig. 1.2. RES are expected to have a significant impact in the nearest future because of the increase in energy demand and the related harmful greenhouse gases. In addition, several energy storage systems, such as batteries and flywheels are under a consideration for distributed generation systems to harness excess electricity produced by the most efficient generators during low loading. In order to eliminate the need for high-cost generators, this harvested energy can be released onto the grid, when needed. Popular sources of power for DGS are solar heat collection panels and photovoltaic panels which can be installed on the roofs of buildings or free-standing making the installation of PV power plants easy. The production cost for electricity produced from PV panels is close to the cost of using the coal power plants. The wind turbine is also one type of clean RES. However, the installation of the wind turbine power plants is more complex than the PV ones and needs a very large free space outside the cities. Moreover, the cost of electricity produced by wind turbines is higher than the one corresponding to PV panels. FC also have the same problem of volume and the cost production. Furthermore, the maintenance of the PV power plants is easier than the wind turbine and FC power plants.

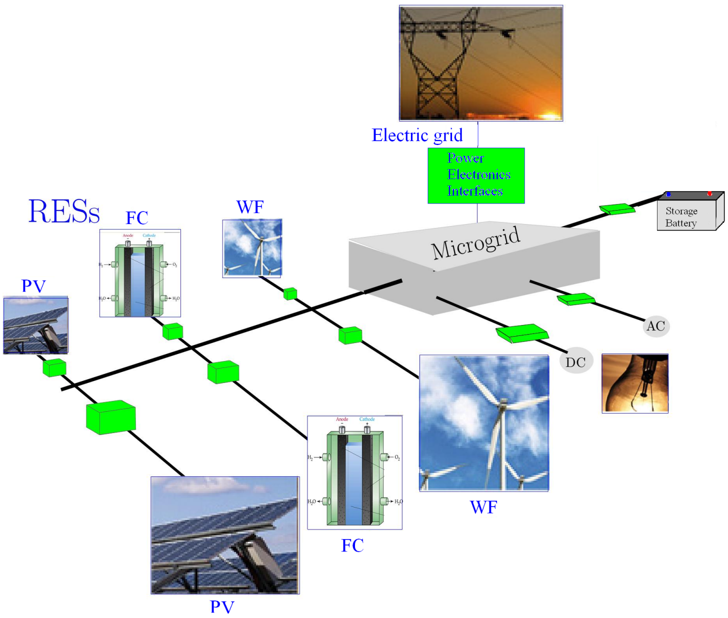

Figure 1.2: Example of electrical architecture of a microgrid supplied from RES.

Generally, RESs such as PV and FC do not have self dispatchability Kramer et al. (2008). Therefore, inclusion of storage in the distributed generation system actually provides the user dispatchability of its distributed resources. Nowadays, RESs are receiving increased attention because of their ability to provide combined heat and power, peak power, demand reduction, backup power and improved power quality. In this thesis, the PV generators will be used in distribution systems using a power stage with a high conversion ratio as it will be shown in the next chapters. Therefore, the PV generators will be discussed in details in the following section.

1.2 Photovoltaic Generator

PV technology involves converting solar energy directly into electrical energy by means of a solar cell and it can be considered one of the most common RES. A solar cell is typically made of semiconductor materials, such as crystalline silicon and absorbs sunlight in order to produce electricity through a process called the photovoltaic effect. The efficiency of a solar cell is determined by its ability to convert available sunlight into usable electrical energy and is typically around 10%-15% Madan et al. (2013). Typically, the solar plants must have large surface areas to produce a significant amount of electrical energy (Fig. 1.3).

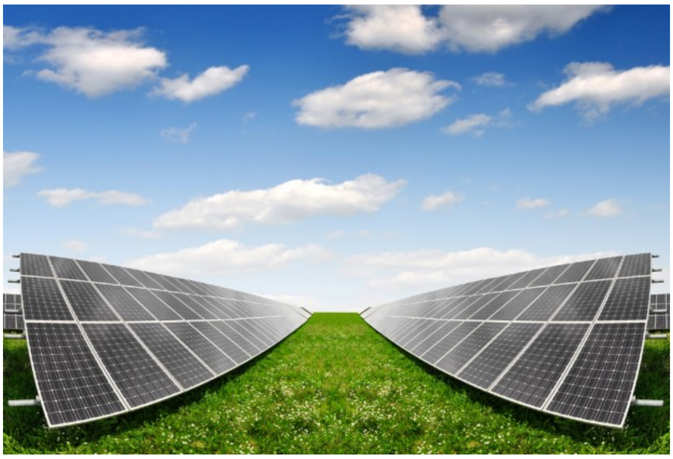

Figure 1.3: PV panels for large surface areas.

The PV generators have a nonlinear characteristic with a Maximum Power Point (MPP) that depends on the temperature (T) and irradiation (S) as depicted in Fig. 1.4. The short circuit current of the PV panel depends mainly on the irradiance level. When the irradiance increases, the output current of the PV panel increases, consequently, the maximum power increases as shown in Fig. 1.4(a). Furthermore, the open circuit voltage of the PV panel depends mainly on the temperature. When the temperature decreases, the power of the PV panel increases as shown in Fig. 1.4(b).

It should be mentioned that if the PV panel is connected directly to a DC load as shown in Fig. 1.5, the maximum power transfer from the PV panel to the load is not guaranteed. Fig. 1.6 shows the $i - v$ and $p - v$ characteristic curves of a PV panel and characteristic curves of three different cases of DC load (constant voltage load, constant current load and resistive load). It can be noted that for the three different loads, the PV panel cannot work at the MPP. The operating points resulting from the intersection of the characteristic of the PV panel and different

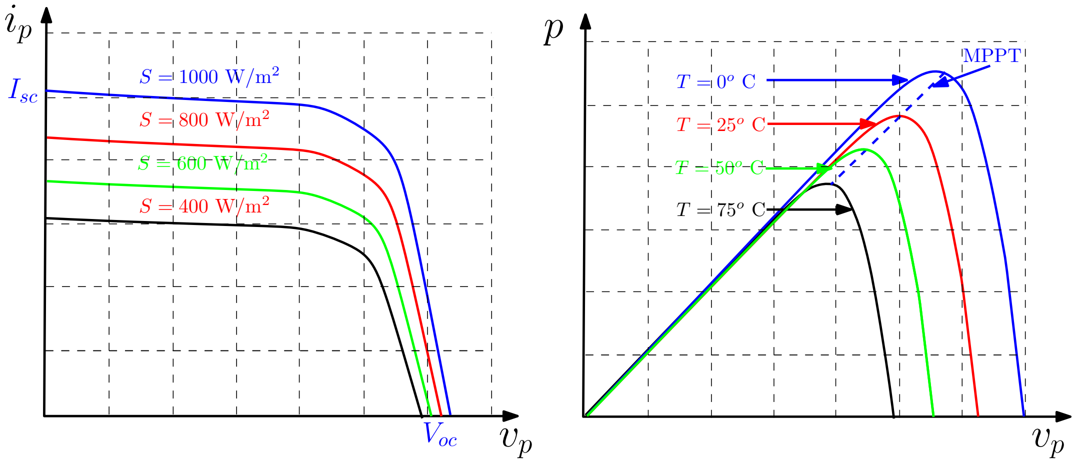

(a) (b)

Figure 1.4: PV module characteristic (a) $i - v$ characteristic (b) $p - v$ characteristic.

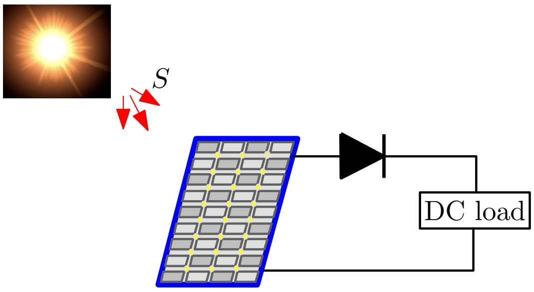

Figure 1.5: Direct connection of a PV panel to a DC load.

DC load characteristics are also depicted in the same figure. These points are A, B and C corresponding to the resistive load, the constant voltage load and the constant current load, respectively. It can be observed that the generating power in all the cases are less than the maximum power of the PV panel.

Therefore, to extract the maximum power from a PV panel, an adaptation stage with a Maximum Power Point Tracking (MPPT) system should be inserted between the PV panel and the load to control the operating point of the PV panel as depicted in Fig. 1.7. The main requirement of power electronic interfaces for the PV systems is to convert the generated DC voltage into a suitable AC for consumer use and utility connection in the AC distribution system or connected directly to the main DC bus of 380 V for the DC distribution system as was shown in Fig. 1.1. Generally, the DC voltage magnitude of a PV array is required to be stepped up to a sufficient level before connected to the AC or DC distribution system. In the past, for AC distribution system, one centralized inverter was responsible for

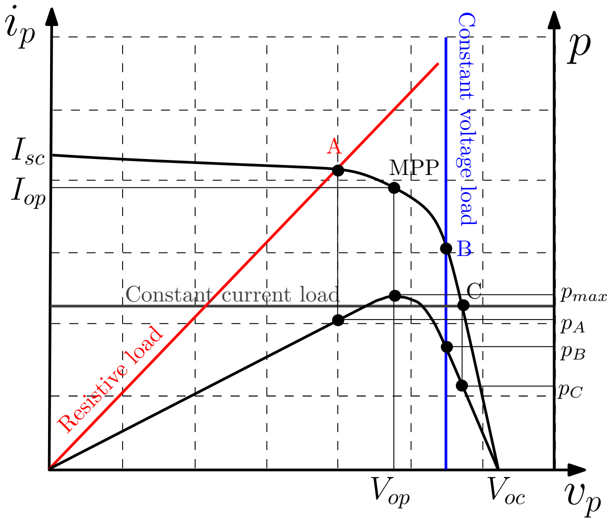

Figure 1.6: Operating points for a PV panel for the direct connection with different loads.

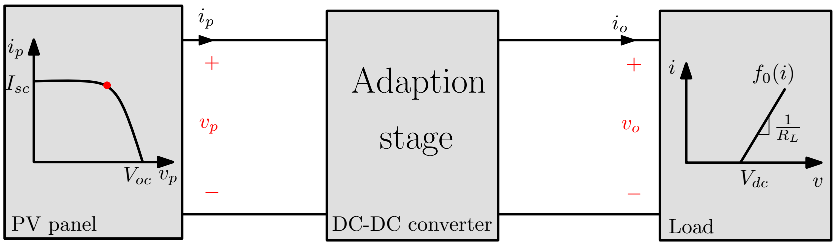

Figure 1.7: Adaption stage as an interface between a PV panel and a DC load.

connecting several modules or other RES into the AC grid. The PV modules are divided into series connections (called a string), each generating a sufficiently voltage to avoid further amplification as depicted in Fig. 1.8(a). The limitations of the centralized inverter, such as high-voltage DC cables between the PV modules and the inverter, power losses due to a centralized MPPT, mismatch losses between the PV modules, losses in the string diodes, and a nonflexible design, yield that the benefits of mass production could not be reached. The string inverter, shown in Fig. 1.8(b), is a reduced version of the centralized inverter, where a single string of PV modules is connected to the inverter. The input voltage may be high enough to avoid voltage amplification. This requires roughly 16 PV modules in series for European systems Kjaer et al. (2005). However, this connection of Fig. 1.8(b) have the same disadvantages of the first connection of Fig. 1.8(a).

The possibility of using fewer PV modules in series also exists if a DC-DC converter or line-frequency transformer is used for voltage amplification (Fig. 1.8(c)) Kjaer et al. (2005). Since every string can be controlled individually, the solar panels can be utilized more efficiently. This provides greater flexibility and facilitates

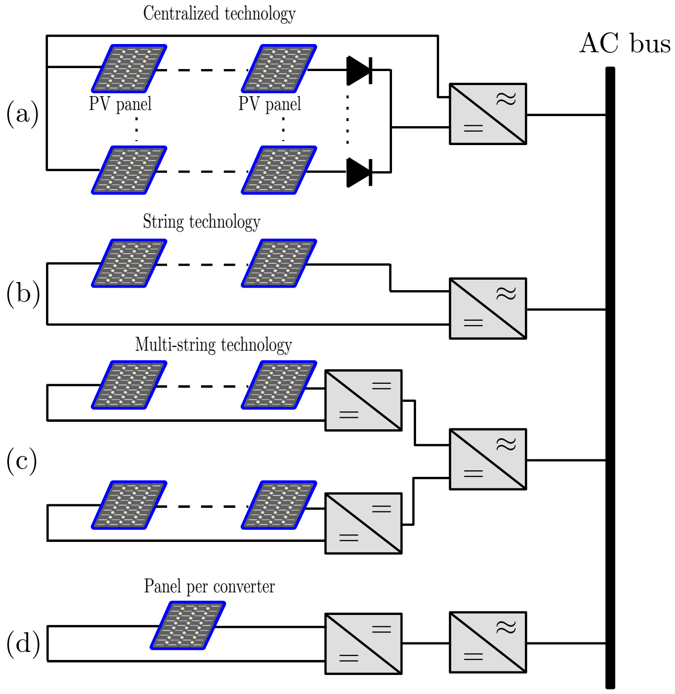

Figure 1.8: Different connecions of the PV panels and the AC grid Kjaer et al. (2005).

the control and occasional replacement of individual panels. However, the same problem of power losses due to a centralized MPPT still exist for the structure of Fig. 1.8(c). Finally, in Fig. 1.8(d), the block diagram of the converter per module approach is shown. The main advantage of this structure is that it removes the mismatch losses between PV modules, since there is only one PV module, as well as supports optimal adjustment between the PV module and the inverter and, hence, the individual MPPT Esram and Chapman (2007). Each panel in this structure has its own MPPT controller, which provides higher flexibility in system layout, lower sensitivity to shading, better protection of PV sources, redundancy in case of failures, and easier and safer installation and maintenance, besides of data gathering Walker and Sernia (2004). The structure of Fig. 1.8(d) has one major disadvantage, which is low efficiency due to high voltage amplification, thus the price per watt is the largest of the four topologies discussed. Moreover, the converter per module approach can present difficulties for achieving the desired output voltage under mismatched conditions of some PV modules when converters are connected in series at the output in case of failure of any PV panels Bratcu et al. (2011). Therefore, one of the key technology issues is the implementation of a power converter that interfaces the possibly low voltage and power of the PV module, to the main voltage DC distribution bus of 380 V. For this reason, it is necessary to have an adaptation stage with a high voltage conversion ratio (above 10) in addition to good static and dynamic performances, which should guarantee a good impedance matching of the PV generator regardless of the load variations and/or the weather conditions like fast moving clouds, temperature changes or shadowing effects.

1.3 Power Processing System

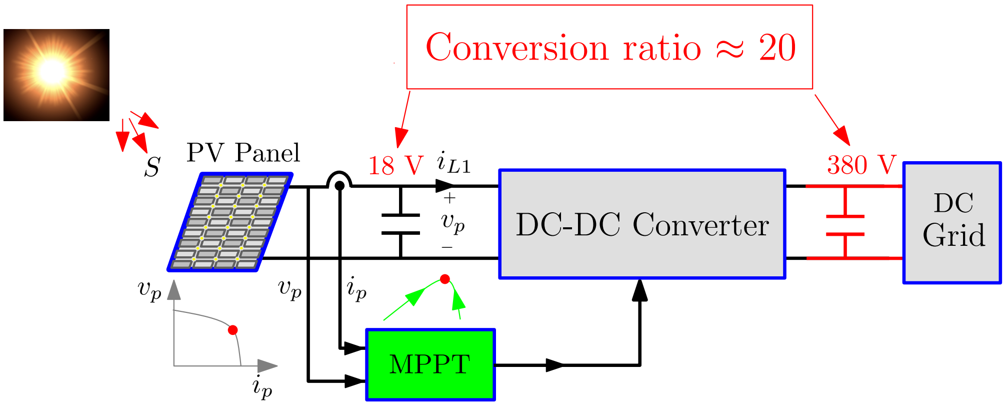

Figure 1.9: DC-DC converter suplied from PV panel and loaded by a DC bus.

All DGS technologies require specific power electronics stage to convert the generated power into a regulated one that can be directly interconnected with the utility grid and/or can be used to supply the consumer loads. The development of scalable, modular, low cost, highly reliable power electronic interfaces improves the overall cost and durability of RESs. The high gain conversion ratio in the DGS can be achieved using a single stage converter to decrease the number of elements (diode, MOSFET, inductor,...etc) or interconnected converters to reduce the duty cycle for each converter. Each approach has some advantages and disadvantages which will be addressed in the following subsections.

1.3.1 Single-stage converters

The design of a single high step-up converter supplied from RES, maintaining a good tradeoff between converter efficiency, MPPT accuracy and tracking speed is not a simple task Sullivan et al. (2013), Latham et al. (2013), Petrone et al. (2008), Poshtkouhi et al. (2012), Serna et al. (2013). The use of an individual power converter to obtain a high voltage conversion ratio as shown in Fig. 1.9

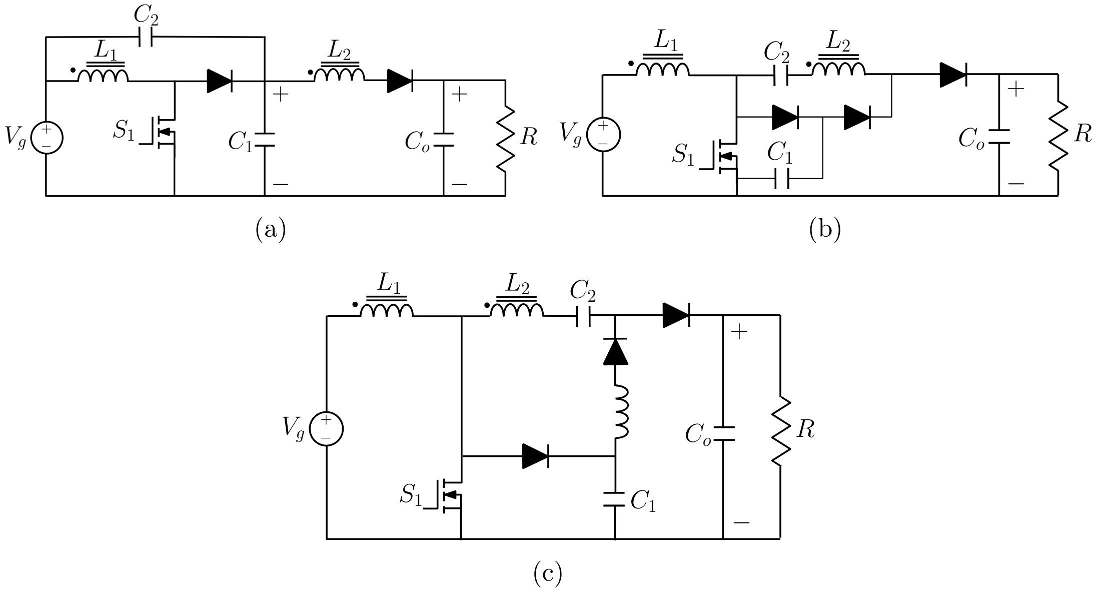

(a)

(b)

(c)

Figure 1.10: (a) Boost converter using DC-input front-end converter Zhao and Lee (2003). (b) High step-up converter with coupled inductor Wai et al. (2008). (c) High step-up DC-DC converter with hybrid transformer Gu et al. (2013).

implies working with a high duty cycle, which results in some design limitations due to the finite commutation times of the power devices, that could lead to their saturation, and also requires relatively a high size of the passive elements. Moreover, high duty cycle in the step-up converters can present difficulties in the controller design and stability problems. Therefore, some researchers investigated how to obtain a high voltage conversion ratio with a lower duty cycle.

In Zhao and Lee (2003), a coupled inductor and a diode have been used to modify the boost converter to increase the conversion ratio (Fig. 1.10(a)). The modified boost used in Zhao and Lee (2003) increases the gain of the boost converter up to 8 with 90 % efficiency. A possible solution is to use a step-up transformer but this would limit the operating frequencies and would increase the problems of switching surges Wolfs and Li (2002). To remedy these problems, an approach based on a modified boost topology with coupled inductors allowing high converter efficiencies for high step-up ratios was proposed in Wai and Duan (2005) (Fig. 1.10(b)). This structure can adapt a low voltage PV generator to a DC output voltage of 200 V with a good conversion efficiency Wai et al. (2008). However, its large input current ripple imposes the use of an electrolytic capacitor with large capacitance value in parallel with the PV generator in order to reduce the voltage ripple Sullivan et al. (2013), Latham et al. (2013). This capacitance could compromise the reliability of the whole PV system Petrone et al. (2008), Castillo et al. (2010), Koutroulis and

Blaabjerg (2013). Most of the converters that achieve a high step-up conversion ratio with a high efficiency have the same limitation Wai et al. (2008).

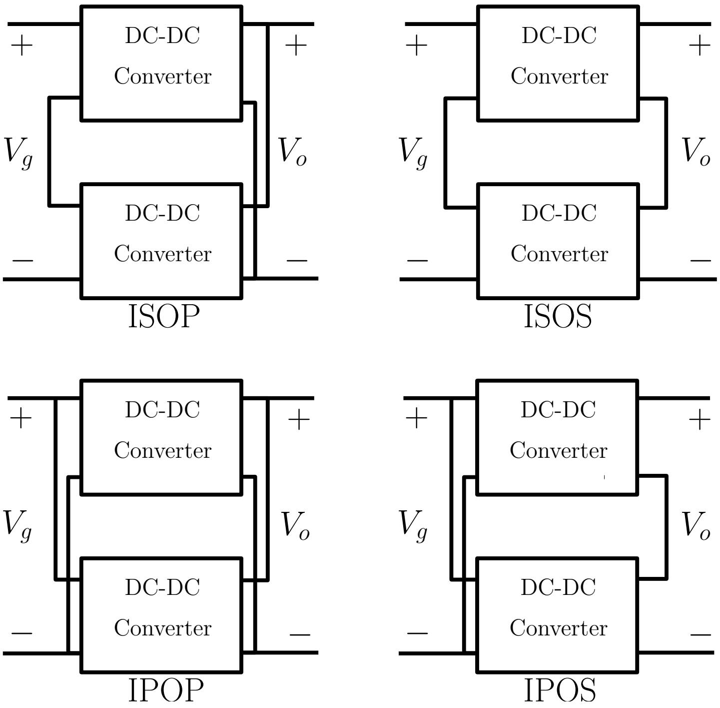

Figure 1.11: Different connections for the DC-DC converters Ayyanar et al. (2004).

1.3.2 Interconnected converters

Interconnected converters constitute one of the most important subjects in modern power electronic research and have been widely studied by many researchers Kim et al. (2001), Giri et al. (2004), Shi et al. (2012). The converters can be connected in different manners, such as Input-Series Output-Parallel (ISOP), Input-Parallel Output-Parallel (IPOP), Input-Series Output-Series (ISOS), Input-Parallel Output-Series (IPOS) as shown in Fig. 1.11 Ayyanar et al. (2004). Some of these connections can be used for high conversion ratio applications such as ISOS and IPOS. However, the design of these kind of connections is not easy, because it should be assured that the input currents for the converters are equal if they are Input-Parallel connected. Similarly, the input voltages should be assured to be equal for the converters if they are Input-Series connected and the same implies for the output side. Normally, some feedback loops design (input and output voltage loops and input and output current loops) are required for these kind of connections which make the control more complex. In addition, instability problems can appear if there is a mismatch between the parameters of the converters Ayyanar et al. (2004).

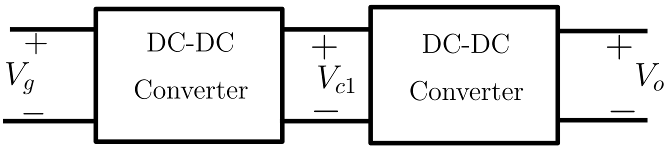

Figure 1.12: Two cascaded boost converters.

One of the most widely studied combination of switched-mode power converters is the cascade connection of converters Middlebrook (1976), Walker and Sernia (2004), Wang et al. (2003), Veerachary and Sudhakar (2009), Yang et al. (2009), Akagi (2011), Vighetti et al. (2012), Zhang et al. (2013). Moreover, there exist many works dealing with the stability analysis of cascaded DC-DC converters Middlebrook (1976), Walker and Sernia (2004), Wang et al. (2003). The control of the cascaded converters is not as complex as the other connections. Furthermore, there are no extra loops for the cascaded connections and there is no problem of mismatching parameters between the converters compared to the previous mentioned connections.

The elementary DC-DC boost converter presents several advantages like high efficiency, reliability and low price and is a good candidate to connect in cascade in order to achieve a high conversion ratio. It has been used as an impedance matching stage between a PV generator and a DC load Cid-Pastor et al. (2007b, 2010, 2013). The cascaded connection of boost converters which is depicted in Fig. 1.12 has been tackled in terms of the efficiency Vighetti et al. (2012). In this thesis, the main purpose is achieving a high conversion ratio using the cascaded connection of boost converters while ensuring stability and good dynamic performances of the system.

1.4 Control Techniques

As DC-DC converters are nonlinear and time variant systems, the application of linear control techniques to control these converters cannot be done directly. In order to design a linear controller system using classical linear control techniques, the small signal model is first derived by linearization around a certain operating point from the state space average model. The controllers based on these techniques are simple to implement. However, it is difficult to account for variations of system parameters and large signal transient such as those produced in the start up or against changes in the load. Different control algorithms can be applied to switching converters for achieving a regulated output voltage and a high conversion ratio. Some of these control techniques will be discussed in the following subsections.

1.4.1 Pulse width modulation control

Pulse-Width Modulated (PWM) DC-DC converters have been very popular for the last three decades, and are widely used at all power levels. Voltage mode control (VMC) and current mode control (CMC) are two traditional PWM control techniques Erickson and Maksimovic (2001). Multi-loop control techniques, such as CMC greatly improves the dynamic behavior, however the control design remains difficult especially for higher order converter topologies because of existence of two loops (voltage and current). Some other disadvantages for PWM are the high cost and complexity of the circuit design. Therefore, the design of a PWM controller for a high order system, such as an interconnected power converter, is challenging.

1.4.2 Sliding-mode control

Sliding Mode Control (SMC) was firstly proposed and elaborated by several researchers Emelyanov (1970), Itkis (1976), Utkin (1978), Utkin et al. (1999). Since then, SMC has been developed into a general control method applicable to a wide range of system types including nonlinear systems, Multi-Input Multi-Output (MIMO) systems, discrete time models, large scale and infinite-dimensional systems Saglam et al. (2011). Essentially, SMC utilizes discontinuous feedback control laws to force the system state to reach, and subsequently to remain on, a specialized surface within the state space (the so called switching surface). When the dynamic system reaches the sliding surface, it can be described by an ideal sliding model that represents the controlled system behavior Hung et al. (1993). Obtaining such a sliding motion has two advantages, firstly the system order is reduced with respect to the original plant. Secondly the movement on the sliding surface of the system is insensitive to a particular kind of perturbation and model uncertainties.

SMC can be applied to a kind of systems called variable structure systems (VSS) that can be described in general with the following equation

$$\dot{\mathbf{x}}(t) = \mathbf{f}(\mathbf{x}, t) + \mathbf{g}(\mathbf{x}, t)\mathbf{u}(t) \tag{1.1}$$

where $\mathbf{x}(t) \in \mathbb{R}^N$ and $\mathbf{f}(\mathbf{x}, t) \in \mathbb{R}^N$ are continuous function vectors, $\mathbf{g}(\mathbf{x}, t) \in \mathbb{R}^{N\times m}$ is a continuous function matrix and $\mathbf{u} \in \mathbb{R}^m$ is the vector of discontinuous control inputs. The vector $\mathbf{u}$ represents the discontinuous control inputs of the system

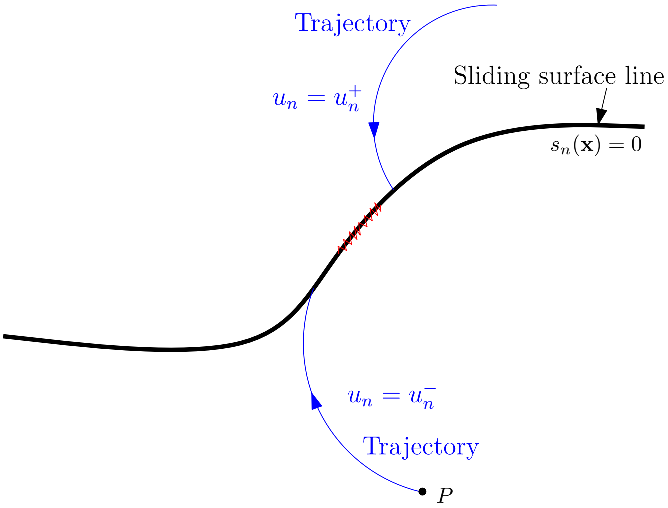

Figure 1.13: Ideal sliding motion for a variable structure system.

and can be expressed as follows:

$$\mathbf{u} = \begin{pmatrix} u_1 \\ u_2 \\ \vdots \\ u_m \end{pmatrix} \tag{1.2}$$

where u_n, for $n = 1, 2, ...m$, are the discontinuous inputs which given by

$$u_n = \begin{cases} u_n^+(\mathbf{x}, t) & \text{if} \quad s_n(\mathbf{x}) > 0 \\ u_n^-(\mathbf{x}, t) & \text{if} \quad s_n(\mathbf{x}) < 0, \end{cases} \tag{1.3}$$

where s_n, for $n = 1, 2, ...m$, are the switching functions describing the sliding surfaces, and m is the number of the control inputs. To introduce SMC, the full-order switched model (1.1) must be first derived. The switching functions s_n are a linear combination of the state variables and suitable references r_n and they can be defined by the following equation

$$s_n(\mathbf{x}) = r_n + \sum_{i=1}^{N} C_i x_i \tag{1.4}$$

All these switching functions can be grouped in a matrix form as follows

$$\mathbf{s}(\mathbf{x}) = \mathbf{r} + \mathbf{C}\mathbf{x} \tag{1.5}$$

where $\mathbf{r}$ is a suitable reference vector with dimension m and $\mathbf{C}$ is a matrix of sliding coefficients with dimension $m \times N$. $\mathbf{s}(\mathbf{x}) = 0$ represents the intersection of all the switching surfaces. In this way, the phase space is divided in regions separated by the sliding surfaces, each associated to one of the sub-topologies defined by $\mathbf{u}$. Let us suppose that the system state is in a point P, as shown in Fig. 1.13. Since we are in the region $s_n < 0$, the switch is closed and the motion occurs along a phase trajectory corresponding to $u_n = u_n^+$. When the system state reaches the region $s_n(\mathbf{x}) > 0$, $u_n = u_n^-$, and the system follows the corresponding phase trajectory. Observing that the phase trajectories, in proximity of the sliding surface, are directed toward the surface itself, the resulting motion is made by continuous commutations around the sliding surface, so that the system remains in this surface if certain conditions are fulfilled as it will be discussed later.

When the system is in the sliding mode, its evolution is independent of the circuit parameters. It depends only on the selected sliding surface. Moreover, if N is the order of the original system, the order of the controlled system in sliding mode is $N - m$, since the state variables are constrained by the equation $\mathbf{s}(\mathbf{x}) = \mathbf{0}$.

Under SMC, the system trajectories stay on the sliding surface, hence:

$$\mathbf{s}(\mathbf{x}) = \mathbf{0} \Rightarrow \frac{\mathrm{d}\mathbf{s}(\mathbf{x})}{\mathrm{d}t} = \mathbf{0} \tag{1.6}$$

$$\frac{\mathrm{d}\mathbf{s}(\mathbf{x})}{\mathrm{d}t} = \frac{\mathrm{d}\mathbf{s}(\mathbf{x})}{\mathrm{d}\mathbf{x}}\frac{\mathrm{d}\mathbf{x}}{\mathrm{d}t} = \mathbf{C}\dot{\mathbf{x}} = \mathbf{0} \tag{1.7}$$

In sliding mode, the discontinuous variable u_n can be substituted by a continuous variable u_{eq_n} which can take all the values between u_n^- and u_n^+. This variable represents the control law that describes the behavior of the system restricted to the switching surface where the motion takes place on the average. By using Eqs. (1.1) and (1.7), we can obtain

$$\mathbf{C}\dot{\mathbf{x}} = \mathbf{C}(\mathbf{f}(\mathbf{x}, t) + \mathbf{g}(\mathbf{x}, t)\mathbf{u}_{\mathbf{eq}}(t)) = \mathbf{0} \tag{1.8}$$

Using (1.8), the expression for the vector of the equivalent control variables can be obtained as follows:

$$\mathbf{u}_{eq} = -(\mathbf{C}\mathbf{g}(\mathbf{x}, t))^{-1}\mathbf{C}\mathbf{f}(\mathbf{x}, t) \tag{1.9}$$

Finally, by substituting this expression into Eq. (1.1) and taking in to account (1.6), we obtain the following equations

$$\dot{\mathbf{x}} = [\mathbf{I} - \mathbf{g}(\mathbf{x}, t)(\mathbf{C}\mathbf{g}(\mathbf{x}, t))^{-1}\mathbf{C}]\mathbf{f}(\mathbf{x}, t) \tag{1.10}$$

$$\mathbf{s}(\mathbf{x}) = \mathbf{0} \tag{1.11}$$

Equations (1.14), (1.15) describe the system motion under SMC and represent the reduced-order model. As mentioned before, the order of this model is less than the full switched model. This is because, under sliding regime, the system motion is constrained to be on the sliding surface. As a consequence, the equivalent system described by Eqs. (1.14), (1.15) is of order $N - m$. This order reduction is of high interest in the case of interconnection of multiple converters. SMC will be used in this work to design cascaded converter systems with a high conversion ratio. More details about SMC can be found in Emelyanov (1970), Itkis (1976), Utkin (1978), Utkin et al. (1999), Spiazzi and Mattavelli (2001).

Conditions for the sliding motion

In the system considered previously, SMC design requires only selection of sliding surface. This surface must be selected in such a way to ensure the following three constraints Spiazzi et al. (1995)

1. The hitting condition, which requires that the system trajectories cross the sliding surface irrespective of their starting point in the phase plane.
2. The existence condition, which requires that the system trajectories near the sliding surface (in both regions) are directed toward the surface itself. This condition can be expressed as follows:
$$s_n(\mathbf{x})\frac{\mathrm{d}s_n(\mathbf{x})}{\mathrm{d}t} < 0 \tag{1.12}$$
3. The stability condition of the system motion on the sliding surface (i.e. the motion must be directed toward the equilibrium point). Stability can be studied by using the reduced order model.

The nature of the SM controller is to ideally operate at an infinite switching frequency such that the controlled variables can track a certain reference path to achieve the desired dynamic response and steady-state operation Mattavelli et al. (1993), Utkin et al. (1999). This requirement for operation at infinite switching frequency, challenges the feasibility of applying ideal SMC in power converters. This is because extreme high speed switching in power converters results in excessive switching losses, inductor and transformer core losses, and electromagnetic interference (EMI) noise issues. This can be solved using a hysteretic comparator in the feedback loop of the switching regulator to limit the switching frequency by adjusting the hysteresis width h_n as shown in Fig. 1.14. The frequency f_n of the subsystem controlled by the surface s_n can be expressed as follows Barrado et al. (2012)

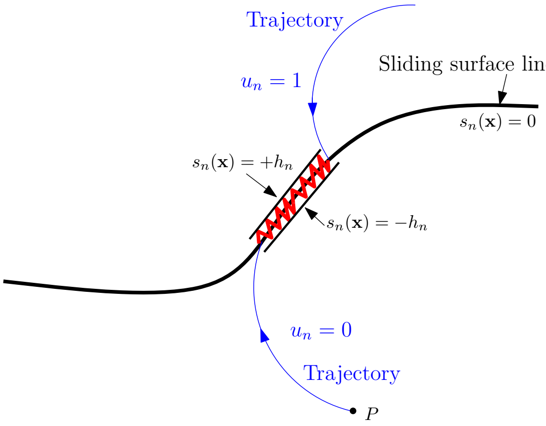

Figure 1.14: Actual sliding motion for a converter.

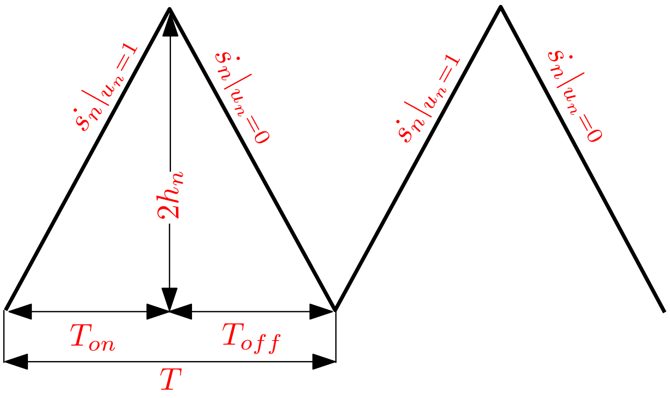

Figure 1.15: The switching time of the sliding surface.

$$f_n = \frac{1}{T} = \frac{1}{T_{on} + T_{off}} = \frac{1}{2h_n} \frac{\dot{s_n}|_{u_n=1} \dot{s_n}|_{u_n=0}}{\dot{s_n}|_{u_n=0} + \dot{s_n}|_{u_n=1}} \tag{1.13}$$

where $\dot{s_n}|_{u_n=1}$ and $\dot{s_n}|_{u_n=0}$ can be defined as follows

$$\dot{s_n}|_{u_n=1} = \mathbf{C}\dot{\mathbf{x}}|_{u_n=1} = \mathbf{C}(\mathbf{f}(\mathbf{x}, t) + \mathbf{g}(\mathbf{x}, t)\mathbf{u}(t)|_{u_n=1}) \tag{1.14}$$

$$\dot{s_n}|_{u_n=0} = \mathbf{C}\dot{\mathbf{x}}|_{u_n=0} = \mathbf{C}(\mathbf{f}(\mathbf{x}, t) + \mathbf{g}(\mathbf{x}, t)\mathbf{u}(t)|_{u_n=0}) \tag{1.15}$$

T_{on} and T_{off} are the ON and OFF time of the switch respectively and T is the period time as shown in Fig. 1.15. Note that the switching frequency depends on the amplitude of the hysteresis band h_n and system parameters.

The switching decision can be selected as follows

$$\text{if} \quad s_n(\mathbf{x}) > +h_n \Rightarrow u_n = 0 \tag{1.16}$$

$$\text{if} \quad s_n(\mathbf{x}) < -h_n \Rightarrow u_n = 1, \tag{1.17}$$

The main drawback of converters controlled by means of classical SMC with respect to PWM converters is the variable switching frequency. However there exist realization alternatives that allow to fix the switching frequency to a constant value He and Luo (2006), Yan et al. (2008), Hamoudi et al. (2011), Abrishamifar et al. (2012), Shtessel et al. (2014).

1.5 Canonical Elements for Power Processing

Power processing is a technical field whose main objective is to minimize energy loss in transforming the electrical power from one form into another according to certain control signals. The electrical architecture of power processing systems can be modeled by means of three ideal canonical elements and analyzed using the laws governing the interconnection of two-port circuits Suntio and Gadoura (2002). These canonical elements are the DC-transformer, the DC-gyrator and the DC loss-free resistor (LFR), which all belong to a class of ideal circuits named POPI (power output is equal to power input) Singer and Erickson (1992). The ideal schematic diagram of the three types of the canonical elements are shown in Fig. 1.16

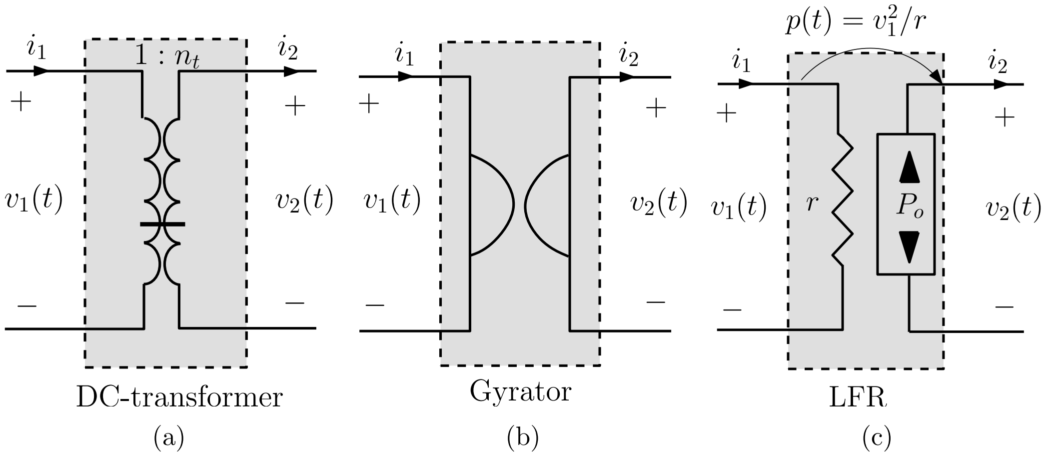

Figure 1.16: The ideal schematic diagrams of the three types of the canonical elements considered in this work: (a) DC-transformer (b) g-gyartor (c) loss-free resistor (LFR).

Canonical elements have been used in different contexts and applications in the last two decades. The two majors axes of application of the canonical elements concept are: first, the implementation of a specific function in energy processing such as power factor correction (PFC), voltage regulation and impedance matching Cid-Pastor et al. (2013), Jong-Lick et al. (2004). The second refers to the use of these elements in modeling dynamical systems, power processing systems and electric drives Hamill (1993), Du et al. (2011). Although other techniques of implementation exist Barazarte et al. (2010a), Erickson and Maksimovic (2001), a well known method for realization of the above canonical elements is the induction of certain sliding motions in appropriate converters Cid-Pastor et al. (2013), Martinez-Salamero et al. (2005), Martinez-Salamero and Cid-Pastor (2012).

As an example, the goal of the synthesis of a DC-transformer is to design a switching structure whose input and output variables in steady-state are related according to the following equation

$$V_2 = n_t V_1 \quad \text{and} \quad I_1 = n_t I_2 \tag{1.18}$$

where V_1, I_1, V_2 and I_2 are the steady-state averaged values of the instantaneous input and output port variables shown in Fig. 1.16(a) and n_t is the transformation ratio.

Similarly, the synthesis of a power gyrator requires a switching structure leading to the following set of relations between the steady-state input and output variables Cid-Pastor et al. (2007a), Cid-Pastor et al. (2009).

$$\text{g-gyrator type} \quad I_2 = gV_1, \quad I_1 = gV_2 \tag{1.19}$$

$$\text{r-gyrator type} \quad V_1 = r_g I_2, \quad V_2 = r_g I_1 \tag{1.20}$$

where g is the g-gyrator conductance and r_g is the r-gyrator resistance. Equation (1.19) defines a power gyrator of type g whereas Eq. (1.20) corresponds to a gyrator of type r Cid-Pastor et al. (2006a).

Finally, the synthesis of an LFR requires a switching structure guaranteing the following steady-state relationships between the steady-state input and output variables

$$V_1 = rI_1 \quad \text{and} \quad V_1 I_1 = V_2 I_2. \tag{1.21}$$

More details about synthesizing the canonical elements using SMC will be explained in the following chapters.

1.6 Objectives and Chapters Description

The main objective of this thesis is to present a framework for synthesizing, modeling, controlling and analyzing cascaded boost converters that work as canonical elements for power processing as shown in Fig. 1.17. These canonical elements are synthesized by imposing a certain relationship between the input and output variables. The relationship is imposed by using SMC with a suitable switching manifold. Although most of these structures have been previously analyzed individually in many previous works, there is no systematic study dealing with their design criteria and the stability problems derived from their cascade connection under SMC. In addition, the cascaded converters will be tackled from the side of achieving a high conversion ratio for PV applications.

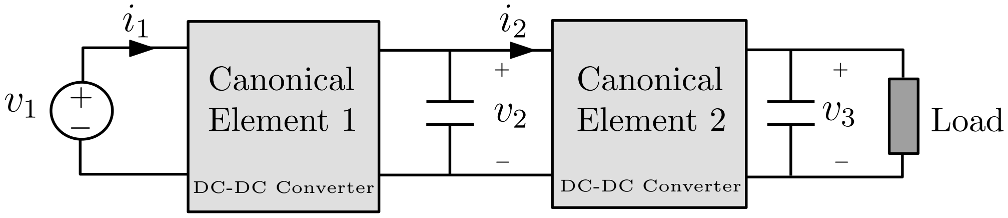

Figure 1.17: Two cascaded canonical elements based on DC-DC converters supplied from a voltage source.

The thesis consists mainly of eight chapters in addition to the introduction presented in this chapter. The content of the chapters can be summarized as follows:

Chapter 2 presents a brief survey about the DC-transformer, which will be used to connect two cascaded boost converters using SMC. Firstly, two cascaded DC-transformers, based on the application of a single sliding surface for each converter, will be synthesized. Secondly, a DC-transformer based on two cascaded boost converters will be synthesized using a single sliding surface. The numerical simulation, stability analysis and the associated dynamic performance will be studied in the same chapter.

Similarly to the DC-transformer, the same analysis will be carried out using the DC-gyrators and the LFRs in Chapter 3 and Chapter 4 respectively. Moreover, cascaded LFR- gyrator and gyrator-LFR, will be synthesized based on two sliding surfaces in Chapter 5. The numerical simulation, stability analysis and the associated dynamic performance of the different connections will be also presented.

In Chapter 6, two cascaded LFRs are used to connect a PV panel to a DC distribution system. The system will be analyzed theoretically and using numerical simulation. Moreover, the stability analysis of the system will be carried out using the PV and the MPPT models. In addition, the two cascaded LFRs will be used to connect a PV panel to an AC distribution system through a DC-AC H-bridge inverter. Other alternatives, such as Z-source converter and high gain coupled inductor boost converter, will be analyzed theoretically and using numerical simulation in Chapter 7 in order to show the advantages of the cascaded LFRs.

The cascaded LFRs will be used to synthesize an example of DC nanogrid in Chapter 8. This nanogrid consists of n output paralleled two-cascaded LFRs used to connect n PV panels to a DC voltage bus of 380 V. The DC nanogrid is regulated using a bidirectional converter connected to a battery which will be used also as a backup for the DC bus.

Finally, Chapter 9 summarizes the contributions of this work and proposes future research directions and applications of the new concepts introduced in this thesis.

Chapter 2

Cascaded Voltage Step-up DC-Transformers

According to Middlebrook's paradigm, a DC-DC switching converter can be modeled as an ideal DC-transformer, whose transformation ratio is a function of the duty cycle Middlebrook and Ćuk (1976). The ideal DC-transformer is used to represent the basic function of lossless conversion of DC and low-frequency AC voltage and current waveforms. The DC transformer, unlike AC transformer, does not exist as an individual component because the magnetic core transformer can not transform DC signals. Furthermore, in the last four decades it has become essential to model the DC-DC conversion characteristics of many converters. Particularly, with the advantage that using this equivalent circuit model, the switching ripple is neglected and only the most important low frequency components of the converter waveforms are considered. The DC-transformer is a canonical element whose its input current is proportional to its output current. This implies to that its input and output voltages are also proportional. The voltage conversion ratio is usually controlled, and hence the effective transformer ratio is dependent on the duty cycle. Exploitation of this duty cycle property allows the use of these converters not only in DC-DC voltage regulator applications, but also in AC applications such as DC-AC inverters and unity power factor AC-DC converters. In these applications, the voltage conversion ratio is continuously varied, such that the desired power waveforms are attained.

In this chapter, the DC-transformer based on the boost converter will be synthesized under a SMC using a suitable switching manifold. Firstly, two sliding surfaces will be used to synthesize two cascaded DC-transformers. Secondly, a DC-transformer will be synthesized based on two cascaded boost converters using a single sliding surface. Stability analysis is carried out for the two systems and stability conditions for each case are obtained. The theoretical results will be verified using numerical simulations and experimental results.

2.1 Synthesis of a DC-Transformer in SMC

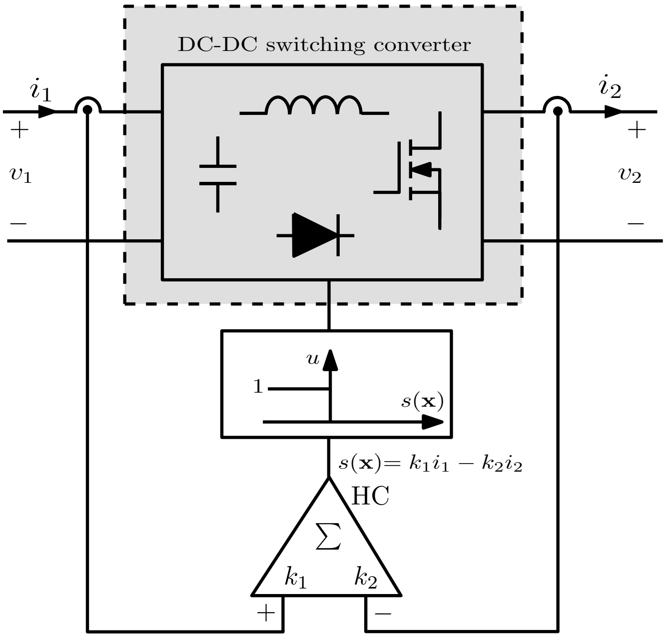

Figure 2.1: Block diagram of a switching converter to synthesize a DC-transformer as a canonical element for power processing.

In Giral et al. (1996), Martinez-Salamero et al. (2005), a detailed study has been carried out for the synthesis of a DC-transformer. The main objective is to design a switching structure whose equations in steady-state are given by

$$V_2 = n_t V_1 \tag{2.1}$$

$$I_2 = \frac{I_1}{n_t} \tag{2.2}$$

where V_1, I_1, V_2 and I_2 are the steady-state averaged values of input and output voltages and currents respectively. Equations (2.1), (2.2) define a DC-transformer, which can be synthesized as shown in the block diagram of Fig. 2.1. It consists of a switching converter, which is controlled by means of a sliding mode regulation loop Martinez-Salamero and Cid-Pastor (2012), in which the switching manifold is given by $\sum = \{\mathbf{x}|s(\mathbf{x}) = 0$, where $s(\mathbf{x}) = k_1 i_1 - k_2 i_2$ in such a way that, in steady state, the following equation holds

$$I_2 = \frac{k_1}{k_2} I_1 = \frac{I_1}{n_t} \tag{2.3}$$

where $n_t = k_2/k_1$. On the other hand, since the converter in Fig. 2.1 is ideal and a POPI structure (DC Power output=DC Power input) Singer and Erickson (1992), Eq. (2.1) will be automatically satisfied.

The sliding mode constraint requires that both i_1 and i_2 to be continuous function of time, this implies the existence of a series inductor in both ports Martinez-Salamero and Cid-Pastor (2012). The simplest converters with such a constraint at both ports are fourth order converters, namely, Buck with Input Filter (BIF), Boost with Output Filter (BOF), Ćuk converter and Ćuk converter with galvanic isolation. It has been shown in Giral et al. (1996), Martinez-Salamero et al. (2005), that a BIF converter under SMC yields to an unstable system. On the other hand, Ćuk converter has been proved to have stable dynamics with transformer characteristics if certain stability conditions are accomplished.

A similar analysis of a BOF converter controlled by the sliding function $s(\mathbf{x}) = k_1 i_1 - k_2 i_2$, yields to a stable system with transformer characteristics, i.e., the output voltage is proportional to the input voltage and the input current is proportional to the output current with the same proportionality factor in both relations. The sliding-mode feedback loop is illustrated in Fig. 2.1. It has been concluded in Giral et al. (1996), Martinez-Salamero et al. (2005) that the BOF converter exhibits unconditionally stable DC-transformer characteristic sliding modes over the surface $s(\mathbf{x}) = k_1 i_1 - k_2 i_2 = 0$ and therefore it can be considered a good candidate to synthesize a step-up DC-transformer.

The BOF converter will be used to synthesize two cascaded DC-transformers because it is a step-up voltage converter, has a high efficiency and unconditionally stable under SMC. Although the stability of a single step-up DC-transformer based on SMC has been demonstrated in previous works, the study of a cascade connection of DC-transformers has not been carried out before. In the following section, two cascaded DC-transformers will be studied theoretically and using numerical simulations.

2.2 Two Cascaded DC-Transformers Under SMC

Fig. 2.2(a) illustrates the cascade connection of two ideal DC-transformers implemented as described in the previous section. The equivalent model of the two cascaded ideal DC-transformers is shown in Fig. 2.2(b) as it will be studied in this section. In turn, Fig. 2.3 depicts the practical implementation of this cascade connection by means of two BOF-based DC-transformers. This section describes briefly the power stage and the control of the system.

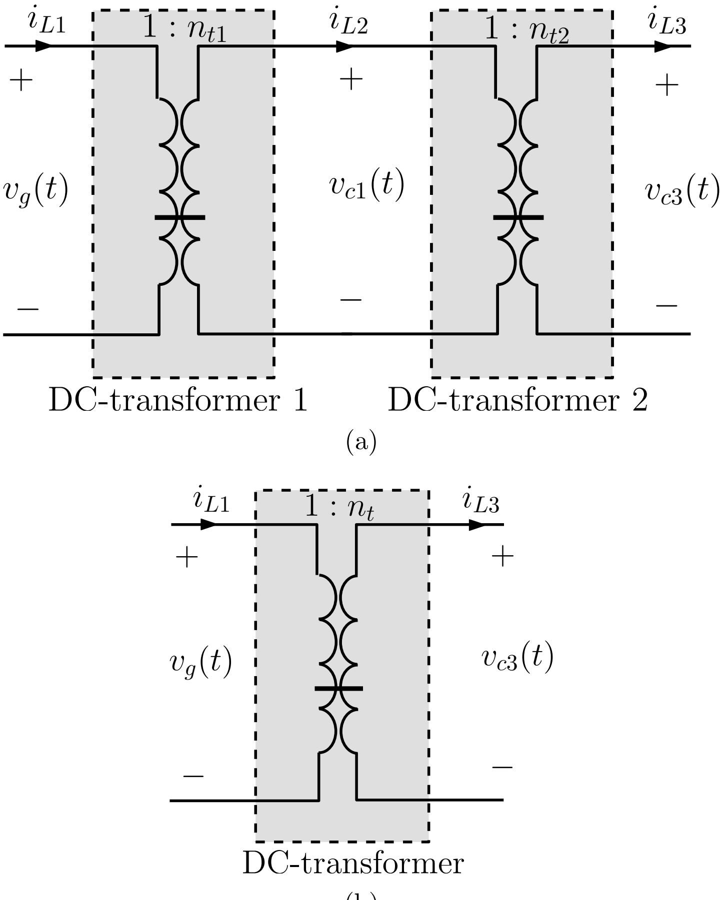

(a)

(b)

Figure 2.2: (a) Schematic diagram of two cascaded ideal DC-transformers. (b) Equivalent circuit model of the two cascaded ideal DC-transformers is a single DC-transformer $n_t = n_{t1}n_{t2}$.

2.2.1 System description

The system depicted in Fig. 2.3 is fed by a DC voltage source V_g, which is the input to the first stage giving the intermediate voltage V_{c1}, which is, in turn, the input of the second stage that gives the output voltage V_{c2}. The first stage consists of an inductor L_1, a diode D_1, a switch S_1 and a capacitor C_1 connected to an output filter with inductor L_f and capacitor C_f to be connected in parallel to the input of the second stage. The basic elements of the second stage consist of an inductor L_2, a switch S_2, a diode D_2, and an output capacitor C_2 which is connected to an output filter with inductor L_3 and capacitor C_3 to be connected in parallel with a resistive load R.

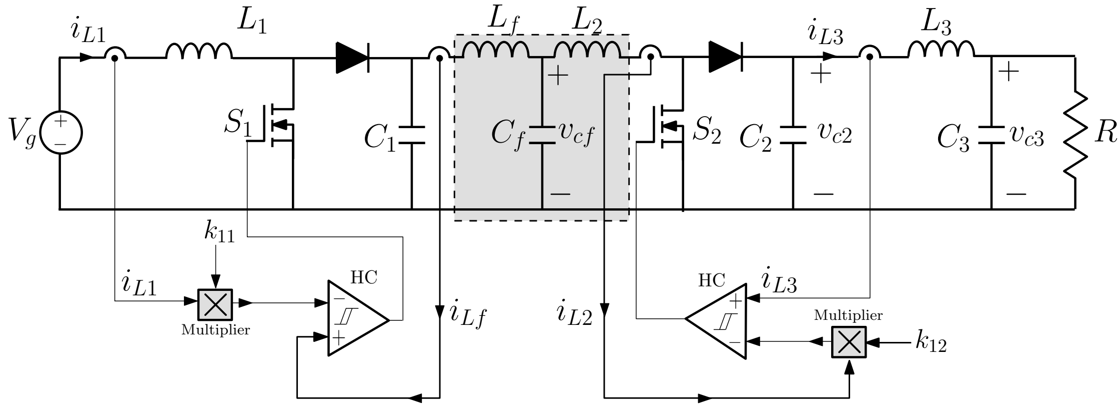

Figure 2.3: Schematic diagram of two cascaded DC-transformers under SMC using two BOF converters.

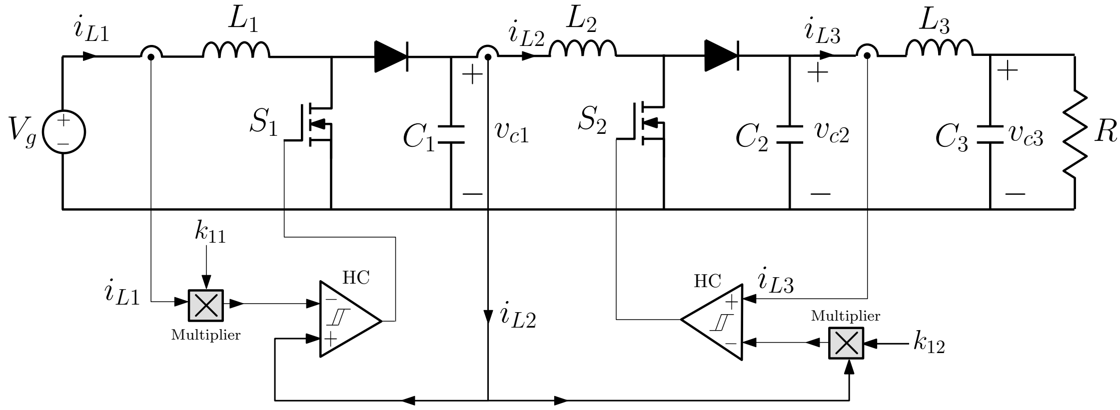

Figure 2.4: Simplified schematic diagram of two cascaded DC-transformers under SMC.

Indeed, the cascade connection of two BOF converters implies the presence, in the middle point v_{cf} of Fig. 2.3, of the output filter of the first stage formed by L_f and C_f and the input inductor L_2 of the second stage. This part of the circuit has been simplified to one single inductor L_2 in order to reduce the number of reactive elements as shown in Fig. 2.4. From now on, all the analysis will be carried out using the circuit depicted in Fig. 2.4.

The controller consists of two switching functions: $s_1(\mathbf{x}) = i_{L2} - k_{11}i_{L1}$ for the first stage converter and $s_2(\mathbf{x}) = i_{L3} - k_{12}i_{L2}$ for the second stage converter. In steady-state $s_1(\mathbf{x}) = 0$, *i.e.*, $I_{L2} = k_{11}I_{L1}$ with $n_{t1} = 1/k_{11}$. Furthermore, assuming that the first converter in Fig. 2.4 is ideal, Eq. (2.1) will be automatically satisfied ($V_{c1} = n_{t1}V_g$). In turn, $s_2(\mathbf{x}) = 0$, *i.e.*, $I_{L3} = k_{12}I_{L2}$ with $n_{t2} = 1/k_{12}$, like in the previous case, assuming the second stage ideal, Eq. (2.1) will be automatically satisfied ($V_{c3} = n_{t2}V_{c1}$). Therefore, a two-port network can be obtained in steady-state characterized by the the following equations

$$V_{c3} = n_t V_g \quad \text{and} \quad I_{L1} = n_t I_{L3} \tag{2.4}$$

Eq. (2.4) shows that a single DC-transformer can be implemented using two cascaded DC-transformers which is depicted in Fig. 2.2(b), with a transformation ratio n_t. It should be noted that the parameters k_{11} and k_{12}, which determine the transformer ratio of each stage, are multiplied respectively by currents i_{L1} and i_{L2} using a multiplier. These parameters (k_{11} and k_{12}) could be used to control the magnitude and/or shape of the signals at the input and output ports. This allows the implementation of some specific functions in power processing like impedance matching, voltage regulation and PFC Cid-Pastor et al. (2013), Jong-Lick et al. (2004).

2.2.2 Full-order switched model

By applying Kirchhoff's Voltage Law (KVL) and Kirchhoff's Current Law (KCL) to the circuit depicted in Fig. 2.4, and considering that both converters operate in CCM, the cascade connection of two BOF converters can be represented by the following set of differential equations

$$\frac{\mathrm{d}i_{L1}}{\mathrm{d}t} = \frac{V_g}{L_1} - \frac{(1-u_1)v_{c1}}{L_1} \tag{2.5}$$

$$\frac{\mathrm{d}i_{L2}}{\mathrm{d}t} = \frac{v_{c1}}{L_2} - \frac{(1-u_2)v_{c2}}{L_2} \tag{2.6}$$

$$\frac{\mathrm{d}i_{L3}}{\mathrm{d}t} = \frac{v_{c2}}{L_3} - \frac{v_{c3}}{L_3} \tag{2.7}$$

$$\frac{\mathrm{d}v_{c1}}{\mathrm{d}t} = \frac{(1-u_1)i_{L1}}{C_1} - \frac{i_{L2}}{C_1} \tag{2.8}$$

$$\frac{\mathrm{d}v_{c2}}{\mathrm{d}t} = \frac{(1-u_2)i_{L2}}{C_2} - \frac{i_{L3}}{C_2} \tag{2.9}$$

$$\frac{\mathrm{d}v_{c3}}{\mathrm{d}t} = \frac{i_{L3}}{C_3} - \frac{v_{c3}}{RC_3} \tag{2.10}$$

where $u_1 = 1$ for the first (resp. second) stage when the switch S_1 (resp. S_2) is closed and $u_1 = 0$ when the switch S_1 (resp. S_2) is open. All the parameters that appear in (2.5)-(2.10) are shown in Fig. 2.4.

2.2.3 Equivalent control

SMC can be classified as an order reduction control as mentioned in chapter 1, and ideally, the trajectories of the switched system are maintained on the switching boundary where the dynamics can be described by a reduced-order dynamical model. This model can be obtained by substituting the discontinuous control variables u_1 and u_2, belonging to the set $\{0,1\}$ by their equivalent continuous variables $u_{eq1}(\mathbf{x})$ and $u_{eq2}(\mathbf{x})$ that can take all the values between 0 and 1 Utkin (1978). These equivalent control variables can be obtained by imposing that the trajectories are evolving on the switching manifolds. The invariance conditions Sira-Ramirez (1987) implies that $s_1(\mathbf{x}) = \dot{s}_1(\mathbf{x}) = 0$ and $s_2(\mathbf{x}) = \dot{s}_2(\mathbf{x}) = 0$, where the overdot stands for the time derivative. Therefore, the dynamical behavior of i_{L1}, i_{L2} and i_{L3} is constrained by the following set of differential equations

$$\dot{s}_1(\mathbf{x}) = \frac{\mathrm{d}i_{L2}}{\mathrm{d}t} - k_{11}\frac{\mathrm{d}i_{L1}}{\mathrm{d}t} = 0 \tag{2.11}$$

$$\dot{s}_2(\mathbf{x}) = \frac{\mathrm{d}i_{L3}}{\mathrm{d}t} - k_{12}\frac{\mathrm{d}i_{L2}}{\mathrm{d}t} = 0 \tag{2.12}$$

From Eqs. (2.5)-(2.10) and (2.11)-(2.12), the following expressions are obtained for the equivalent control variables $u_{eq1}(\mathbf{x})$ and $u_{eq2}(\mathbf{x})$

$$u_{eq1}(\mathbf{x}) = 1 - \frac{1}{v_{c1}}(\alpha_1(v_{c3} - v_{c2}) + V_g) \tag{2.13}$$

$$u_{eq2}(\mathbf{x}) = 1 - \frac{1}{v_{c2}}(\alpha_2(v_{c3} - v_{c2}) - v_{c1}) \tag{2.14}$$

where $\alpha_1 = L_1/(L_3k_{11}k_{12})$ and $\alpha_2 = L_2/(L_3k_{12})$. These equivalent control variables represent the control laws that describe the behavior of the system restricted to the switching surface where the system motion takes place on the average Utkin (1978), Mattavelli et al. (1993). It is worth to note that these variables must be bounded by the minimum and maximum values of u_1 and u_2 respectively, i.e.

$$0 < u_{eq1}(\mathbf{x}) < 1 \quad \text{and} \quad 0 < u_{eq2}(\mathbf{x}) < 1 \tag{2.15}$$

These constraints on the equivalent control variables allow us to obtain the range of parameter values for which sliding-mode motion exists. From (2.13)-(2.14) one has

$$0 < 1 - \frac{1}{v_{c1}}(\alpha_1(v_{c3} - v_{c2}) - V_g) < 1 \tag{2.16}$$

$$0 < 1 - \frac{1}{v_{c2}}(\alpha_2(v_{c3} - v_{c2}) - v_{c1}) < 1 \tag{2.17}$$

In this case of the cascaded DC-transformers, the sliding-mode regime will exist provided that

$$v_{cr1} \quad < \quad v_{c1} \quad < \quad v_{cr2} \tag{2.18}$$

where $v_{cr1} = \alpha_1(v_{c3} - v_{c2}) - V_g$, $v_{cr2} = v_{c2} - \alpha_2(v_{c3} - v_{c2})$

2.2.4 Ideal sliding dynamics and sliding-mode conditions

Substituting, in Eqs. (2.5)-(2.10), the discontinuous control inputs u_1 and u_2 by their corresponding equivalent control variables $u_{eq1}(\mathbf{x})$ and $u_{eq2}(\mathbf{x})$ given in (2.13) and (2.14), and taking into account the order reduction imposed by the sliding manifolds defined in (2.11)-(2.12), the following reduced-order ideal sliding dynamics model is obtained

$$\frac{\mathrm{d}i_{L1}}{\mathrm{d}t} = \frac{v_{c2} - v_{c3}}{k_t L_3} \tag{2.19}$$

$$\frac{\mathrm{d}v_{c1}}{\mathrm{d}t} = \left(\frac{1}{v_{c1}}\left(\frac{\alpha_1 k_{12}}{k_{11}}(v_{c3} - v_{c2}) + V_g\right) - k_{11}\right)\frac{i_{L1}}{C_1} \tag{2.20}$$

$$\frac{\mathrm{d}v_{c2}}{\mathrm{d}t} = \left(\frac{\alpha_2 k_{12}}{k_{11}^2 v_{c2}}(v_{c3} - v_{c2}) + \frac{k_{11}v_{c1}}{v_{c2}} - k_{11}k_{12}\right)\frac{i_{L1}}{C_2} \tag{2.21}$$

$$\frac{\mathrm{d}v_{c3}}{\mathrm{d}t} = \frac{k_{11}k_{12}i_{L1}}{C_3} - \frac{v_{c3}}{RC_3} \tag{2.22}$$

Being a fourth order nonlinear system, the dynamical analysis of (2.19)-(2.22) is challenging. However, the linearization of the system in a given region around the equilibrium point allows to establish its local stability conditions. The equilibrium point can be obtained by forcing the time derivative of the ideal sliding dynamics state variables to be null. From (2.19)-(2.22), the equilibrium point of the system is given by

$$\mathbf{x}^* = [I_{L1}, I_{L2}, I_{L3}, V_{c1}, V_{c2}, V_{c3}]^\top = \left[\frac{V_g}{k_t^2 R}, \frac{V_g}{k_t k_{12} R}, \frac{V_g}{k_t R}, \frac{V_g}{k_{11}}, \frac{V_g}{k_t}, \frac{V_g}{k_t}\right]^\top \tag{2.23}$$

where $k_t = k_{11}k_{12}$ and $^\top$ stands for taking the transpose of a vector. It can be observed that $V_{c1} = V_g/k_{11}$ and $V_{c2} = V_{c1}/k_{12}$, which define the steady-state DC-transformer behavior of the cascaded circuit of Fig. 2.4. Similarly, $I_{L1} = I_{L2}/k_{11}$ and $I_{L2} = I_{L3}/k_{12}$ also corroborate the DC-transformer characteristics. Furthermore, the expressions of the equivalent controls $U_{eq1} := u_{eq1}(\mathbf{x}^*)$, and $U_{eq2} := u_{eq2}(\mathbf{x}^*)$ in the equilibrium point can be calculated by substituting (2.23) in (2.13) and (2.14). These steady-state equivalent controls can be expressed as follows

$$U_{eq1} = 1 - k_{11} \quad \text{and} \quad U_{eq2} = 1 - k_{12} \tag{2.24}$$

To ensure that U_{eq1} and U_{eq2} are bounded between 0 and 1, as mentioned in (2.15), the following conditions should be fulfilled

$$0 \; < \; k_{11} \; < \; 1 \quad \text{and} \quad 0 \; < \; k_{12} \; < \; 1 \tag{2.25}$$

These inequalities correspond to the intrinsic voltage step-up nature of the cascaded boost converters.

2.2.5 Stability analysis of the ideal sliding-mode dynamic model

The stability of the linearized system can be studied by using the Jacobian matrix $\mathbf{J}$ corresponding to (2.19)-(2.22) and evaluating it at the equilibrium point $\mathbf{x}^*$ given in (2.23). This matrix can be expressed as follows

$$\mathbf{J} = \begin{pmatrix} 0 & 0 & \dfrac{1}{k_t L_3} & -\dfrac{1}{k_t L_3} \\ 0 & \dfrac{-1}{k_{12}^2 R C_1} & \dfrac{-\alpha_1}{k_t k_{12} R C_1} & \dfrac{\alpha_1}{k_t k_{12} R C_1} \\ 0 & \dfrac{1}{k_{12} R C_2} & -\dfrac{\alpha_2}{k_{12} R C_2} - \dfrac{1}{R C_2} & \dfrac{\alpha_2}{k_{12} R C_2} \\ \dfrac{k_t}{C_3} & 0 & 0 & -\dfrac{1}{R C_3} \end{pmatrix} \tag{2.26}$$

The characteristic polynomial of the linearized system is $p_J(s) = \det(\mathbf{J} - s\mathbf{I})$, where $\mathbf{I}$ is the unitary matrix which can be written in the following form

$$p_J(s) = s^4 + a_1 s^3 + a_2 s^2 + a_3 s + a_4. \tag{2.27}$$

The coefficients a_i, $(i = 1 \ldots 4)$ are given by the following expressions

$$\begin{aligned} a_1 &= \frac{L_3 C_2 \mathcal{C}_{13} + C_3 C_1 L}{k_{12}^2 R L_3 C_1 C_2 C_3} \\ a_2 &= \frac{b_1 + C_3 \mathcal{L}_{12}}{k_t^2 k_{12}^2 R^2 L_3 C_1 C_2 C_3} \\ b_1 &= k_t^2 (k_{12}^2 R^2 C_1 C_2 + C_3 L_3 + \mathcal{L}_{23} C_1 + L_3 C_2) \\ a_3 &= \frac{k_t^2 k_{12}^2 (R^2 \mathcal{C}_{12} + L_3) + \mathcal{L}_{12}}{k_t^2 k_{12}^2 R^3 L_3 C_1 C_2 C_3} \\ a_4 &= \frac{1}{k_{12}^2 R^2 L_3 C_1 C_2 C_3} \end{aligned}$$

Table 2.1: The used parameter values for two cascaded DC-transformers.

$L_1 = L_2$	L_3	$C_1 = C_2 = C_3$	R	h_1	h_2	$r_{L1} = r_{L2}$	$r_{on1} = r_{on2}$
220 μH	30 μH	100 μF	32 Ω	0.5	0.25	0.1 Ω	0.1 Ω

where the parameters $\mathcal{L}_{12}$, $\mathcal{L}_{23}$, $\mathcal{C}_{12}$ and $\mathcal{C}_{13}$ can be expressed as follows

$$\begin{array}{lcl} \mathcal{L}_{12} = L_1 + k_{11}^2 L_2, & \mathcal{L}_{23} & = & L_2 + k_{12}^2 L_3 \\ \mathcal{C}_{12} = C_2 + k_{12}^2 C_1, & \mathcal{C}_{13} & = & C_3 + k_{12}^2 C_1 \end{array}$$

By applying the Routh-Hurwitz criterion to $p_J(s)$ in (2.27), it is found that all the terms in the first column of the Routh-Hurwitz array are positive and therefore all the conditions of the stability are fulfilled. This will guarantee the convergence of the system trajectories to the operating equilibrium point for small disturbances in its vicinity.

2.2.6 Numerical simulations and experimental validation

Based on the previous analysis, the two cascaded DC-transformers are stable. However, achieving a high conversion ratio is quietly hard because there is a common state variable between the two switching functions which is the intermediate current i_{L2}. This common state variable presents difficulties in applying the sliding control for all the selected parameter values. The two cascaded boost-based DC-transformer is simulated using PSIM with the following set of parameter values: $k_{11} = k_{12} = 0.5$, and an input voltage $V_g = 6$ V. These values have been chosen so that they fulfill the conditions obtained previously in (2.25) and in order to achieve an input power P_{in} =18 W, an intermediate voltage V_{c1} =12 V, an output voltage V_{c2} =24 V and a nominal switching frequency of 20 kHz. We have to point out that $k_{11} = 1/n_{t1}$ and $k_{12} = 1/n_{t2}$, where n_{t1}, n_{t2} are the transformation ratio of the first and second DC-transformer, respectively. Table 2.1 shows the rest of parameter values used in numerical simulations. The internal resistances of the inductors r_{L1}, r_{L2} and the ON resistance of the MOSFETs r_{on1}, r_{on2} which have been included in the PSIM simulation are shown in the same table. Two prototypes of boost converter with an output filter, working as a DC-transformer, have been implemented to validate the simulation results. These prototypes are connected in cascade with the set of parameter values shown in Table 2.1 (for more details about the experimental results, see Appendix A).

First, the validity of the ideal sliding-mode dynamic model is checked with numerical simulation using the full-order model (2.5)-(2.10). For this purpose, the system has been simulated from a certain initial condition P within the sliding

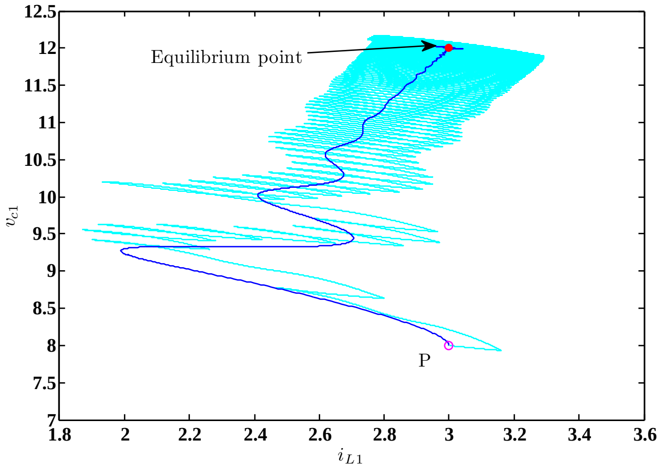

Figure 2.5: Trajectories obtained from the ideal sliding dynamics model and from the full-order switched model using PSIM for DC-transformer starting from a certain initial condition P in the state plane (i_{L1}, v_{c1}) selected within the sliding manifold.

manifold using the two different models, and the result is shown in Fig. 2.5. As observed from this figure, the trajectories obtained from the switched model and the reduced-order model are in perfect agreement, which validate the use of the last one for studying the dynamical behavior and the stability of the system.

Second, Fig. 2.6 shows the time-domain response of two cascaded DC-transformers during start-up and steady-state. Fig. 2.6(a) shows the transient start-up of the system from zero initial conditions. Note that after a short transient time of 5 ms, the state variables reach their steady-state values given in Eq. (2.23). Fig. 2.6(b) shows that the two stages are behaving as a DC-transformer in steady-state, because the ratio between the currents, namely i_{L1}/i_{L2} and i_{L2}/i_{L3}, equal to the transformation ratios established by the respective switching functions.

Fig. 2.7 shows the simulation and experimental response of the system due to an input voltage variation from 6 V to 8 V respectively. When the input voltage increases, the capacitor voltages and the inductor currents increase as well. Fig. 2.8 shows the simulation and experimental steady-state waveforms during the load variation from 32 Ω to 16 Ω. In this case, when the load resistance decreases, the capacitor voltages decrease with a small value while the inductor currents increase. Note that when the load changes, the input power changes from 18 W to 36 W, because the input current increases while the input voltage is constant. This can be considered a disadvantage for this connection for RES application. In all these tests, the POPI nature of the system and its DC-transformer behavior in steady-state are verified. Furthermore, in the ideal case, the steady-state values of

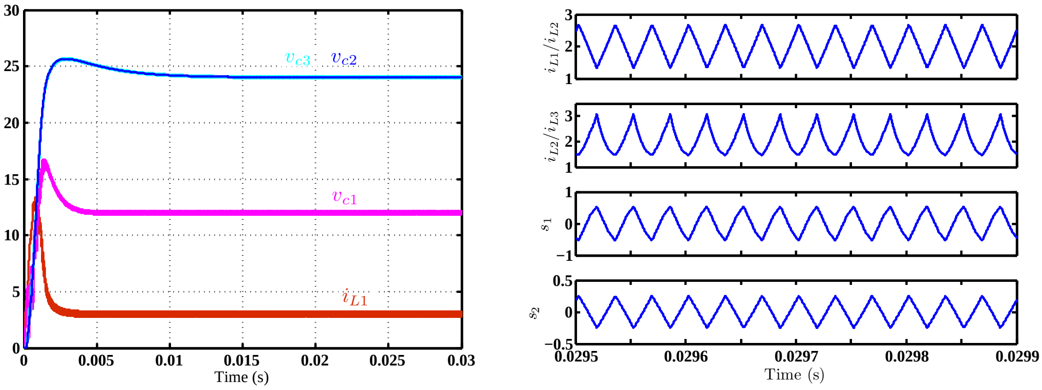

(a) (b)

Figure 2.6: Time domain response of two cascaded boost-based DC-transformer (a) Simulated capacitor voltages v_{c3} , v_{c2}, v_{c1} and inductor current i_{L1} (respectively from up to down) during start-up (b) The ratios i_{L1}/i_{L2}, i_{L2}/i_{L3} and the switching functions $s_1(\mathbf{x})$ and $s_2(\mathbf{x})$ in the steady-state.

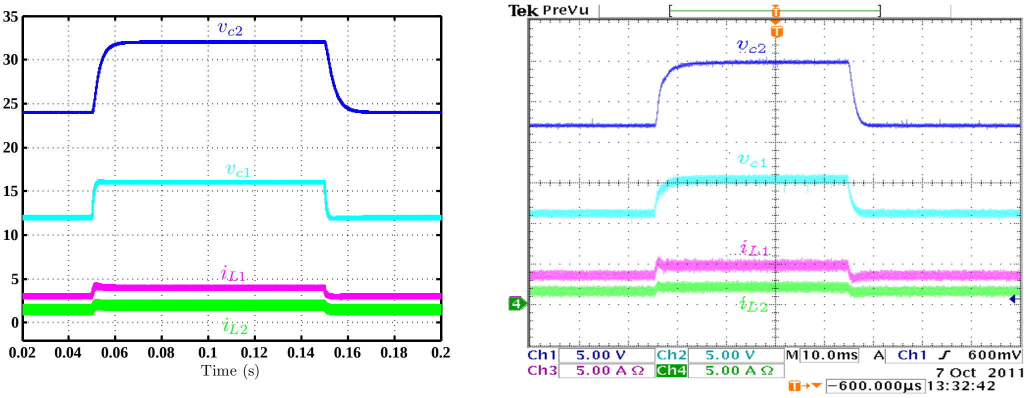

(a) (b)

Figure 2.7: Simulated and experimental waveforms of the capacitor voltages v_{c2}, v_{c1} and the inductor currents i_{L1}, i_{L2} (respectively from up to down) for two cascaded DC-transformers for $k_{11} = k_{12} = 0.5$ under input voltage change from 6 V to 8 V.

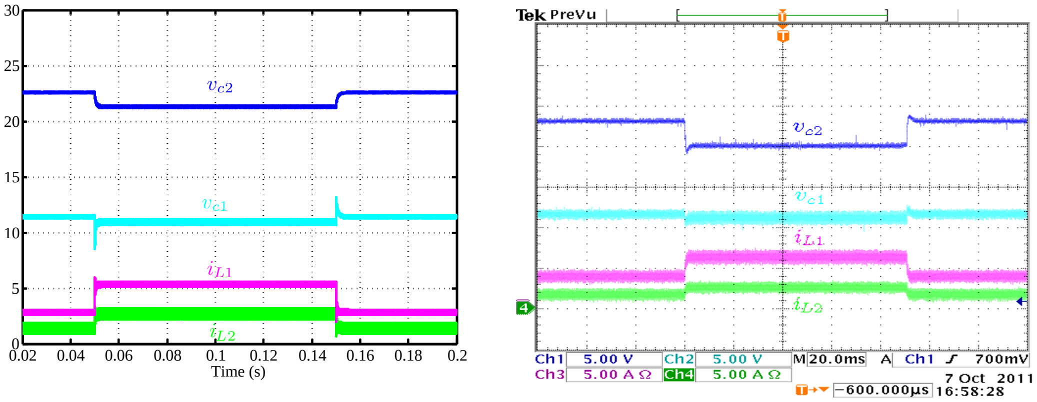

(a) (b)

Figure 2.8: Simulated and experimental waveforms of the capacitor voltages v_{c2}, v_{c1} and the inductor currents i_{L1}, i_{L2} (respectively from up to down) for two cascaded DC-transformers for $k_{11} = k_{12} = 0.5$ under load change from 32 Ω to 16 Ω.

the output voltage V_{c2} and the intermediate voltage V_{c1} are insensible to load resistance variations as it has been predicted theoretically in (2.23). However, due to the existence of parasitic elements in the components (diode voltage drop, ESR of inductor...) the intermediate output voltage presents in steady-state a deviation with respect to the ideal case. This deviation is amplified by the second DC-transformer resulting in a supplementary deviation with respect to the expected ideal value as shown in Fig. 2.8(b). Therefore, although the DC-transformer connection seems to be the most appropriate choice to implement a voltage regulator, the parasitic elements of the components will impose the presence of an additional voltage feedback loop to achieve high-quality load regulation. It should be noted that the transient time that the waveforms take to reach the steady-state for this case is relatively small (2 ms).

2.3 DC-Transformer Based on Cascaded Boost Converters Using a Single Sliding Surface

In this section, a DC-transformer based on two cascaded boost converters will be synthesized using a single sliding surface. For that, there are two possibilities for the switch activation of the two boost converters. The first one implies an identical gate drive signal for the two controlled switches of the boost converters. The second one is through the complementary activation of the second controlled switch. The conversion ratio of the two cascaded boost converters for the two cases can be expressed as follows:

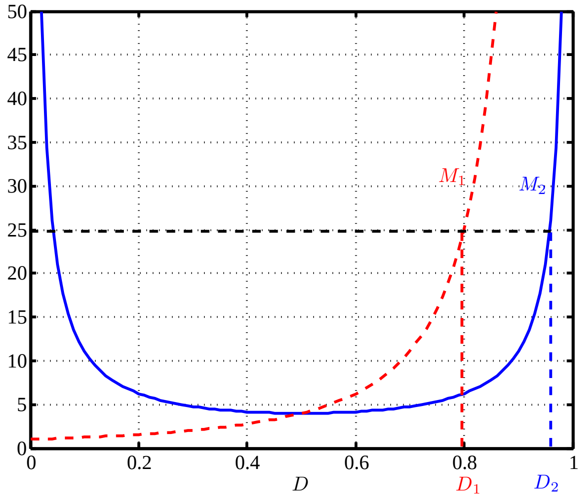

Figure 2.9: The conversion ratio in terms of the duty cycle.

$$M_1 = \frac{1}{D(1-D)} \quad \text{case 1} \tag{2.28}$$

$$M_2 = \frac{1}{(1-D)^2} \quad \text{case 2} \tag{2.29}$$

The conversion ratio of the two cascaded boost converters in terms of the duty cycle is shown in Fig. 2.9. It can be noted that the conversion ratio in case of using the same gate signal increases when the duty cycle increases. For instance a conversion ratio around 25 can be achieved using a duty cycle 0.78 for the two boost converters. However, when the complementary signal is used, the curve becomes symmetrical around a duty cycle 0.5. A high conversion ratio can be achieved in two points in the curve. The first point, is to use a duty cycle 0.05 for the first stage and 0.95 for the second stage and viceversa for the second case. This is undesired practically, because of using a very high duty cycle for one of the two stages which yields to high stress on one of the two MOSFETs.

Therefore, a DC-transformer based on two cascaded boost converters will be synthesized using the same gate signal for the two stages. The power stage of this circuit is similar to the one described in the previous section. Figure 2.10 shows the schematic diagram of a DC-transformer based on two cascaded boost converters using SMC. To synthesize this kind of connection using a single sliding surface, the

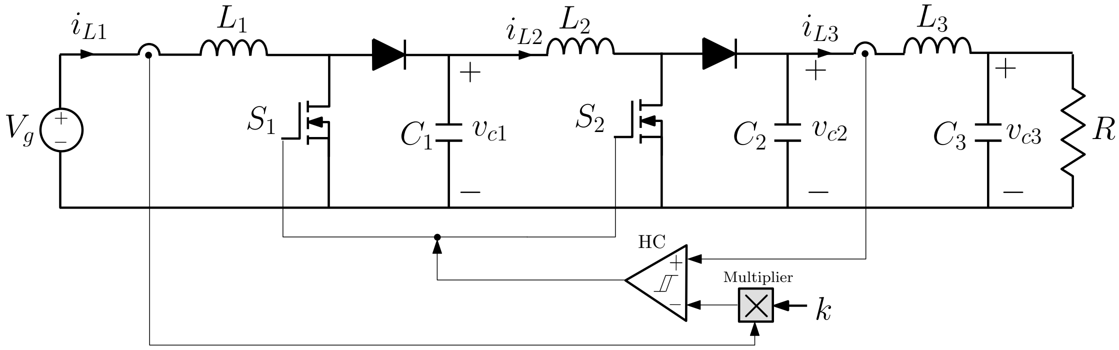

Figure 2.10: The schematic circuit diagram of a DC-transformer based on two cascaded boost converters using a single sliding surface.

switching function can be selected as a relationship between two inductor currents which are the input and output inductors and can be expressed by $s(\mathbf{x}) = ki_{L1} - i_{L3}$.

2.3.1 Full-order switched model

The two cascaded boost converters can be represented by the following differential equations:

$$\frac{\mathrm{d}i_{L1}}{dt} = \frac{V_g}{L_1} - \frac{(1-u)v_{c1}}{L_1} \tag{2.30}$$

$$\frac{\mathrm{d}i_{L2}}{dt} = \frac{v_{c1}}{L_2} - \frac{(1-u)v_{c2}}{L_2} \tag{2.31}$$

$$\frac{\mathrm{d}i_{L3}}{dt} = \frac{v_{c2}}{L_3} - \frac{v_{c3}}{L_3} \tag{2.32}$$

$$\frac{\mathrm{d}v_{c1}}{dt} = \frac{(1-u)i_{L1}}{C_1} - \frac{i_{L2}}{C_1} \tag{2.33}$$

$$\frac{\mathrm{d}v_{c2}}{dt} = \frac{(1-u)i_{L2}}{C_2} - \frac{i_{L3}}{C_2} \tag{2.34}$$

$$\frac{\mathrm{d}v_{c3}}{\mathrm{d}t} = \frac{i_{L3}}{C_3} - \frac{v_{c3}}{RC_3} \tag{2.35}$$

where $u = 1$ when the switch S_1 and S_2 are closed and $u = 0$ when the switch S_1 and S_2 are open. All the parameters that appear in (2.30)-(2.35) are shown in Fig. 2.10.

2.3.2 Equivalent control

As mentioned before, a single sliding surface will be used to synthesize a DC-transformer for the two cascaded boost converters. Therefore, the dynamical behavior of i_{L1} and i_{L3} is constrained by the following equations

$$\begin{aligned} s(\mathbf{x}) &= k i_{L1} - i_{L3} = 0 && (2.36)\\ \dot{s}(\mathbf{x}) &= k\frac{\mathrm{d}i_{L1}}{\mathrm{d}t} - \frac{\mathrm{d}i_{L3}}{\mathrm{d}t} = 0 && (2.37)\end{aligned}$$

The equivalent control $u_{eq}(\mathbf{x})$ can be obtained from Eqs. (2.30)-(2.35) and (2.36)-(2.37), and can be expressed in the following form

$$u_{eq}(\mathbf{x}) = 1 - \frac{kL_3V_g - L_1(v_{c3} - v_{c2})}{kL_3v_{c1}} \qquad (2.38)$$

As mentioned before, this variable must be bounded by the minimum and maximum values of u_{eq}, i.e.

$$0 \ < \ u_{eq}(\mathbf{x}) \ < \ 1. \qquad (2.39)$$

These constraints on the equivalent control variable allow us to obtain the range of parameter values for which sliding-mode motion exists. From (2.38)-(2.39), sliding mode regime will exist in the region of the state space defined by the following inequality

$$V_g - \frac{L_1}{kL_3}(v_{c3} - v_{c2}) \ < \ v_{c1}. \qquad (2.40)$$

2.3.3 Ideal sliding dynamics and sliding-mode conditions

Substituting (2.38) in the switching model (Eqs. (2.30)-(2.35)) of the two boost converters, and taking into account (2.36)-(2.37), the following ideal sliding-mode reduced-order model is obtained

$$\begin{aligned} \frac{\mathrm{d}i_{L1}}{dt} &= \frac{V_g}{L_1} - \frac{kL_3V_g - L_1(v_{c3} - v_{c2})}{kL_3v_{c1}}\frac{v_{c1}}{L_1} && (2.41)\\ \frac{\mathrm{d}i_{L2}}{dt} &= \frac{v_{c1}}{L_2} - \frac{kL_3V_g - L_1(v_{c3} - v_{c2})}{kL_3v_{c1}}\frac{v_{c2}}{L_2} && (2.42)\\ \frac{\mathrm{d}v_{c1}}{dt} &= \frac{kL_3V_g - L_1(v_{c3} - v_{c2})}{kL_3v_{c1}}\frac{i_{L1}}{C_1} - \frac{i_{L2}}{C_1} && (2.43)\\ \frac{\mathrm{d}v_{c2}}{\mathrm{d}t} &= \frac{kL_3V_g - L_1(v_{c3} - v_{c2})}{kL_3v_{c1}}\frac{i_{L2}}{C_2} - \frac{i_{L3}}{C_2} && (2.44)\\ \frac{\mathrm{d}v_{c3}}{\mathrm{d}t} &= \frac{i_{L3}}{C_3} - \frac{v_{c3}}{RC_3} && (2.45)\end{aligned}$$

As mentioned before, the equilibrium point can be obtained by forcing the time derivative of the state variables of the reduced order model to be null. From (2.41)-(2.45) taking into account the sliding surface equations (2.36)-(2.37), the equilibrium point of the system can be expressed by:

$$\mathbf{x}^* = [I_{L1}, I_{L2}, I_{L3}, V_{c1}, V_{c2}, V_{c3}]^\top = \left[\frac{V_g}{k^2R}, \frac{V_g}{k\sqrt{k}R}, \frac{V_g}{kR}, \frac{V_g}{\sqrt{k}}, \frac{V_g}{k}, \frac{V_g}{k}\right]^\top \quad (2.46)$$

It can be observed that $V_{c1} = V_g/\sqrt{k}$ and $V_{c2} = V_{c1}/k$, which define the steady-state of two cascaded DC-transformers. Therefore, a single sliding surface could be sufficient to implement two cascaded DC-transformers.

Similarly, the expression of the equivalent control $U_{eq} := u_{eq}(\mathbf{x}^*)$, in the equilibrium point can be calculated by substituting (2.46) in (2.38). These steady-state equivalent control can be expressed as follows

$$U_{eq} = 1 - \sqrt{k}. \quad (2.47)$$

This steady-state value U_{eq} must be bounded between 0 and 1, as mentioned before in (2.39). This implies that the following condition should be fulfilled

$$0 < k < 1. \quad (2.48)$$

2.3.4 Stability analysis of the ideal sliding-mode dynamic model

As in the previous case, the model given by (2.41)-(2.45) that represents the ideal sliding dynamics is nonlinear. In order to study the stability of the system, the model (2.41)-(2.45) is first linearized around the equilibrium point $\mathbf{x}^*$ given by Eq. (2.46). Using the Jacobian matrix $\mathbf{J}$ corresponding to (2.41)-(2.45) and evaluating it at the equilibrium point $\mathbf{x}^*$. This matrix can be expressed as follows

$$\mathbf{J} = \begin{pmatrix} 0 & 0 & 0 & \dfrac{1}{kL_3} & -\dfrac{1}{kL_3} \\ 0 & 0 & \dfrac{2}{L_2} & -\dfrac{k^2L_3 - L_1}{k^{3/2}L_2L_3} & -\dfrac{L_1}{k^{3/2}L_2L_3} \\ \dfrac{\sqrt{k}}{C_1} & -\dfrac{1}{C_1} & -\dfrac{1}{kRC_1} & -\dfrac{L_1}{k^{5/2}RL_3C_1} & \dfrac{L_1}{k^{5/2}RL_3C_1} \\ -\dfrac{k}{C_2} & \dfrac{\sqrt{k}}{C_2} & -\dfrac{1}{\sqrt{k}RC_2} & -\dfrac{L_1}{k^2RL_3C_2} & \dfrac{L_1}{k^2RL_3C_2} \\ \dfrac{k}{C_3} & 0 & 0 & 0 & -\dfrac{1}{RC_3} \end{pmatrix} \tag{2.49}$$

The characteristic polynomial of the linearized system is $p_J(s) = \det(\mathbf{J} - s\mathbf{I})$ and can be expressed as follows

$$p_J(s) = s^5 + a_1s^4 + a_2s^3 + a_3s^2 + a_4s + a_5. \tag{2.50}$$

The coefficients a_i, $(i = 1 \ldots 5)$ are given by the following expressions

$$\begin{aligned} a_1 &= \frac{k^2L_3C_1C_2 + (kL_3C_2 + L_1C_1)C_3}{k^2RL_3C_1C_2C_3} \\ a_2 &= \frac{kR^2C_3(C_1(kL_2 + k^2L_3 - L_1) + 2kL_3C_2) + kL_2C_2(kR^2C_1 + L_3) + L_1L_2C_1}{k^2R^2L_2L_3C_1C_2C_3} \\ a_3 &= \frac{kL_2(2C_3 + C_2) + 2C_3(k^2L_3 + L_1) + k^2(L_3(2C_2 + kC_1) + L_2C_1) - kC_1L_1}{k^2RL_2L_3C_1C_2C_3} \\ a_4 &= \frac{2(L_1 + kL_2) + 2k^2(L_3 + R^2C_2) + k^3R^2C_1}{k^2R^2L_2L_3C_1C_2C_3} \\ a_5 &= \frac{1}{RL_2L_3C_1C_2C_3} \end{aligned}$$

By applying the Routh-Hurwitz criterion to $p_J(s)$ in (2.50), the following stability conditions can be deduced to be expressed as follows

$$k^2L_3C_1C_2 + (kL_3C_2 + L_1C_1)C_3 > 0 \tag{2.51}$$

$$\begin{aligned} &k^2L_3^2C_2C_3(L_2C_2C_{13} + kR^2C_3C_{12}) + kR^2C_1^2(kL_2C_2\tau_3 - L_1^2C_3^2) \\ &+R^2k^2L_1L_3C_1C_3^2(L_1C - kL_2C_2) + L_1L_2C_1(C_3\tau_2 + k^2L_3C_1\tau_1) > 0 \end{aligned} \tag{2.52}$$

where $\tau_1 = R^2C_3^2 + L_3C_2, \tau_2 = L_1C_1 + 2kL_3C_2, C = kC_1 - C_2, \tau_3 = k^2L_3C_2 + L_1C_3, C_{12} = 2C_2 + kC_1, C_{13} = kC_1 + C_3$. For a stable system, the previous conditions must be fulfilled.

Table 2.2: The used parameter values for a DC-transformer based on two cascaded boost converters under SMC.

V_g	L_1	L_2	$C_1 = C_2$	R	h	$r_{L1} = r_{L2}$	$r_{on1} = r_{on2}$
6 V	200 μH	2 mH	100 μF	32 Ω	0.2	0.1 Ω	0.1 Ω

2.3.5 Numerical simulations

For achieving a high conversion ratio, the parameter k should be selected equals 0.04. However, for this high conversion ratio parameter, the condition of (2.52) is not valid which yields to an unstable system. In order to verify the theoretical results predicted in the previous subsection, the circuit depicted in Fig. 2.10 has been simulated using PSIM for $k = 0.25$. This value has been chosen to satisfy the condition of (2.48) and in order to achieve an input power P_{in} =18 W, an intermediate voltage V_{c1} =12 V, an output voltage V_{c2} =24 V and a nominal switching frequency 20 kHz. Note that, as mentioned before, $n_t = 1/k$ where n_t is the transformation ratio of the two cascaded boost converters. Table 2.2 shows the rest of parameter values and the parasitic elements values used in numerical simulations. As mentioned before, the same gate signal has been used to activate the two MOSFETs for the two stages.

Fig. 2.11 shows the time-domain response of the system during start-up and steady-state. Fig. 2.11(a) shows the response of the system starting from zero initial conditions until reaching steady-state. Note that after a transient time of 7 ms, the state variables reach their steady-state values which are in good agreement with the theoretical values given in Eq. (2.46). Note that the transient time during start-up for this system is higher than the transient time for the two cascaded DC-transformers. Fig. 2.11(b) shows that the two stages behave as a DC-transformer in steady-state because the ratio between the currents, namely i_{L1}/i_{L2} is equal to the transformation ratio established for the first stage.

Fig. 2.12 shows the response of the system under input voltage variation. Fig. 2.12(a) shows the effect of input voltage variation from 6 V to 8 V. When the input voltage increases from 6 V to 8 V, the inductor currents and the capacitor voltages increase. In turn, Fig. 2.12(b) shows the waveforms during a load variation from 32 Ω to 16 Ω. In this case, when the load resistance decreases, the inductor currents increase which yields to increasing the losses in the system. This losses change leads to a small decrease in the capacitor voltages. Note that

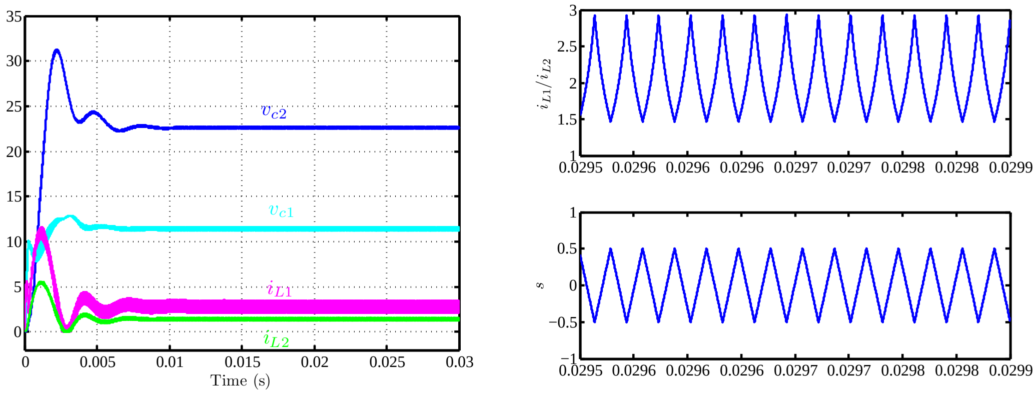

(a) (b)

Figure 2.11: Time domain response of a DC-transformer based on two cascaded boost converters (a) Simulated capacitor voltages v_{c3}, v_{c2}, v_{c1} and inductor current i_{L1} (respectively from up to down) during start-up (b) The ratios i_{L1}/i_{L2} and the switching functions $s(\mathbf{x})$ in steady-state.

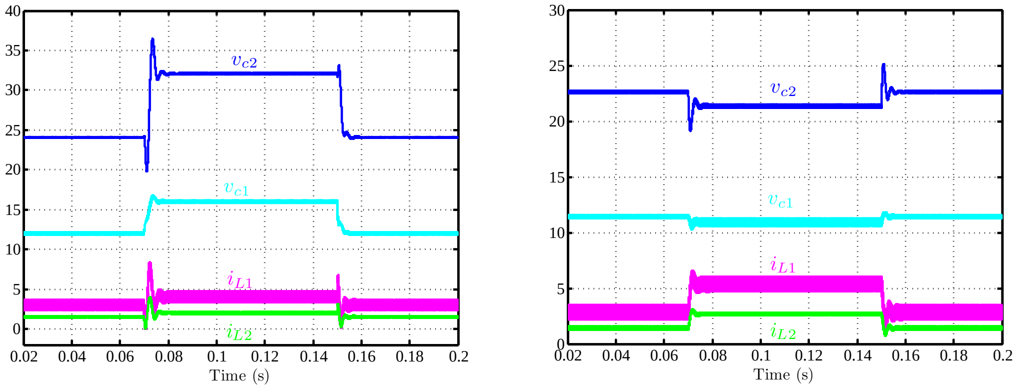

(a) (b)

Figure 2.12: The capacitor voltages v_{c2}, v_{c1} and the inductor currents i_{L1}, i_{L2} (respectively from up to down) of a DC-transformer based on two cascaded boost converters using one sliding surface for $k = 0.25$ and for (a) Input voltage change from 6 V to 8 V (b) Load change from 32 Ω to 16 Ω.

ideally, the capacitor voltages are not depend on the load resistance according to Eq. (2.46). In turn, the input power increases from 18 W to 36 W due to the increase of the inductor currents. The transient time for this case is around 7 ms which is higher than the case of two cascaded DC-transformers.

2.4 Conclusion

Two cascaded DC-transformers using two sliding surfaces, one for each boost converter, have been studied in this chapter. The analysis has verified that the system is unconditionally stable. Moreover, a DC-transformer based on two cascaded boost converters using a single sliding surface has been studied in this chapter as well. The analysis has verified that the system is stable with certain conditions. The behavior of the two systems under the input voltage variation and the load variation are similar. When the input voltage increases, the inductor currents and the capacitor voltages for the two systems increase. In addition, when the load decreases, the inductor currents increase which increases the copper losses. This leads to a slightly decrease in the capacitor voltages. However, the transient time of the waveforms to reach steady-state of the DC-transformer based on two cascaded converters system (one sliding surface) is higher than the two cascaded DC-transformers (two sliding surfaces). The main advantage of the two systems is that the capacitor voltages for both systems are not sensible to the load change. The disadvantage of the two studied systems is that the load variation yields to input current variation which consequently leads to input power changes. This behavior is not suitable for RES applications where it is not suitable that the load variations affect, for example the MPPT of a PV generator. In addition, the two cascaded DC-transformers have the disadvantage that the two switching functions have a common state variable (intermediate current) which limits the sliding-mode control. This implies to an inability to obtain a high conversion ratio from the two cascaded DC-transformers this type. For the DC-transformer based on cascaded boost converters, a high conversion ratio cannot be obtained from this system because the stability conditions are not fulfilled for high voltage conversion ratio case. Although, the two systems are not suitable for high conversion ratio applications, they can be used for low conversion ratio applications.

Chapter 3

Cascaded Voltage Step-up DC-Gyrators

The concept of power gyrator was firstly introduced in Singer (1987, 1988), Singer and Erickson (1992). The notion of DC gyrators was related to a general class of circuits named POPI (DC power output = DC power input), which characterized the ideal behavior of a DC-DC switching converter.

Although, the DC gyrator approach is not a new idea Singer (1987, 1988), its use has been constrained to some practical realizations in different contexts Singer (1988), Shmilovitz et al. (1998), its notion was specially useful to model some complex structures such as dual converters Ehsani et al. (1993a), double bridge converters Ehsani et al. (1993b), multiport converter systems Barazarte et al. (2010b) and the integrated magnetics of a zero-ripple isolated Ćuk converter Hamill (1993).

From a circuit standpoint, a power gyrator is a two-port structure characterized by the fact that the output current is proportional to the input voltage, and that, in turn, the input current is proportional to the output voltage with the same proportionality factor. It was shown in Cid-Pastor et al. (2006a) that power gyrators can be classified by the manner in which they transform an excitation source at one port to its dual representation at the output port. The procedure shown in Cid Pastor (2005), Cid-Pastor et al. (2005) to synthesize a power gyrator starts from a generic switching converter structure and then continues by the imposition of its defining function by means of a sliding-mode regulation loop.

In this chapter, the cascade connection of two DC-gyrators based on the boost converter will be analyzed with the aim of obtaining a power stage with a high voltage conversion ratio. For that, the stability criteria for the design of such a system will be described analytically and verified through simulations and experimental prototypes. Moreover, the design of a power gyrator based on the cascade connection of two boost converters sharing the same gate signal and having only one current sensor will be presented as an alternative to the cascaded gyrators that needs two sliding surfaces and two current sensors.

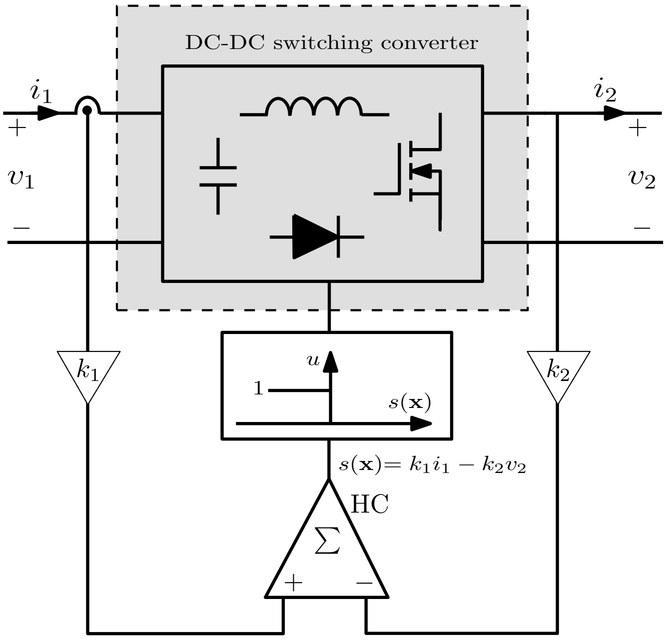

Figure 3.1: Block diagram of a switching converter acting as a power g-gyrator for power processing with controlled input current.

3.1 Synthesis of Power Gyrators in SMC

The main objective is to design a switching structure whose equations in steady-state are given by

$$I_1 = gV_2, \quad I_2 = gV_1 \qquad \text{g-gyrator} \tag{3.1}$$

$$V_1 = r_g I_2, \quad V_2 = r_g I_1 \qquad \text{r-gyrator} \tag{3.2}$$

where g (r_g) is the gyrator conductance (resistance) and V_1, I_1, V_2 and I_2 are the steady-state averaged values of the instantaneous input and output port variables. The power g-gyrator can be synthesized as shown in the block diagram of Fig. 3.1. Eqs (3.1) and (3.2) define the two types gyrators. It consists of a switching converter controlled by means of a SMC Cid-Pastor et al. (2006b), in which the switching manifold is the set $\sum = \{\mathbf{x}|s(\mathbf{x}) = 0\}$, where $s(\mathbf{x}) = k_1 i_1 - k_2 v_2$ in such a way that, in steady state the following equation $I_1 = (k_2/k_1)V_2 = gV_2$ is fulfilled. Note that in this case the gyrator parameter is given by $g = k_2/k_1$. Imposing a sliding-mode regime requires that the input current i_1 to be a continuous function of time, that implying the existence of a series inductor at the input port.

It was shown in Cid-Pastor et al. (2006a), Cid Pastor (2005) that both BIF and Ćuk converter, behaving as g-gyrators with controlled output current, can exhibit stable g-gyrator characteristics if capacitive damping are inserted and certain parametric conditions are satisfied. In particular, in Cid Pastor (2005), Cid-Pastor et al. (2006b), it has been demonstrated that boost converters, behaving as g-gyrators with controlled input current, can exhibit a sliding regime with unconditionally stable equilibrium point with higher efficiencies compared to the BIF and Ćuk converter g-gyrators. Therefore, in this study boost converters acting as g-gyrators with controlled input current have been selected for the cascaded connection because of their higher efficiency when compared with other fourth order structures having the same sliding and stability characteristics.

3.2 Two Cascaded G-gyrators Operating in SMC

The cascaded connection of two ideal g-gyrators is depicted in Fig. 3.2(a). The ideal equivalent circuit model of the two cascaded gyrators, which is equivalent to a single DC-transformer is shown in Fig. 3.2(b) as it will be shown in this section. In turn, the circuit model corresponding to a cascade connection of two g-gyrators under SMC is illustrated in Fig. 3.3. The two stage converters and the control of system will be briefly explained in this section.

3.2.1 System description

The power stage of the described system of Fig. 3.3 is similar to the system studied previously in Section 2.2. The system is supplied from a DC voltage source V_g and loaded with a resistive load R. However, in this case, an output LC filter is not required like in the DC-transformer, because the sliding surface depends on the input current (which is continuous for boost converter) and the output voltage. Similarly to the previous chapter, the same study will be carried out for the two cascaded g-gyrators with controlled input current.

In this case, the controller consists of two switching functions $s_1(\mathbf{x}) = i_{L1} - g_1 v_{c1}$ for the first stage converter and $s_2(\mathbf{x}) = i_{L2} - g_2 v_{c2}$ for the second stage converter. In steady-state $s_1(\mathbf{x}) = 0$, *i.e.*, $I_{L1} = g_1 V_{c1}$. Furthermore, assuming that the first stage in Fig. 3.3 is ideal and therefore is a POPI structure ($V_g I_{L1} = V_{c1} I_{L2}$), Eq. (3.1) will be automatically satisfied ($I_{L2} = g_1 V_g$). In turn, the steady-state switching condition imposes that $s_2(\mathbf{x}) = 0$, *i.e.*, $I_{L2} = g_2 V_{c2}$ and, like in the previous case, considering that the second stage is ideal, Eq. (3.1) will be automatically

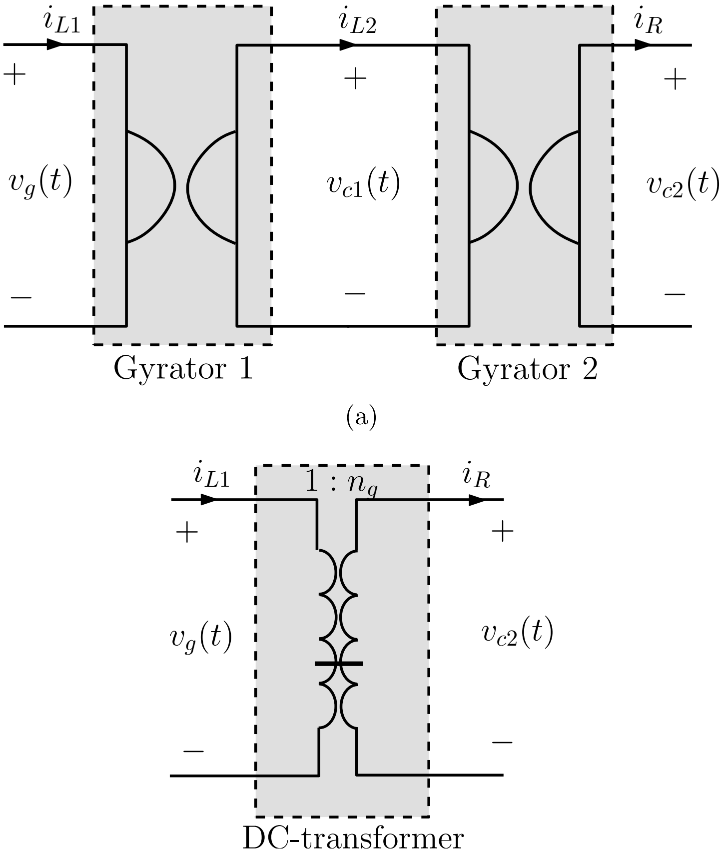

(a)

(b)

Figure 3.2: (a) The schematic diagram of two cascaded ideal g-gyrators. (b) The equivalent circuit model of the two cascaded ideal g-gyrators is a DC-transformer.

satisfied ($I_R = g_2 V_{c1}$). Finally, combining the steady-state expressions of both gyrators, the following relationship is obtained

$$V_{c2} = \frac{g_1}{g_2} V_g \quad \text{and} \quad I_R = \frac{g_2}{g_1} I_{L1}. \tag{3.3}$$

Eq. (3.3) corresponds to the definition of a DC-transformer with a transformation ratio $n_g = g_1/g_2$. This result is in agreement with the straightforward fact that a DC-transformer could be implemented by means of a cascade connection of two gyrators Singer and Erickson (1992). Like in the case of DC-transformer, a multiplier is used to implement the sliding surfaces allowing the possibility to vary the parameters g_1 and/or g_2 and employ them as control variables to realize specific functions in energy processing.

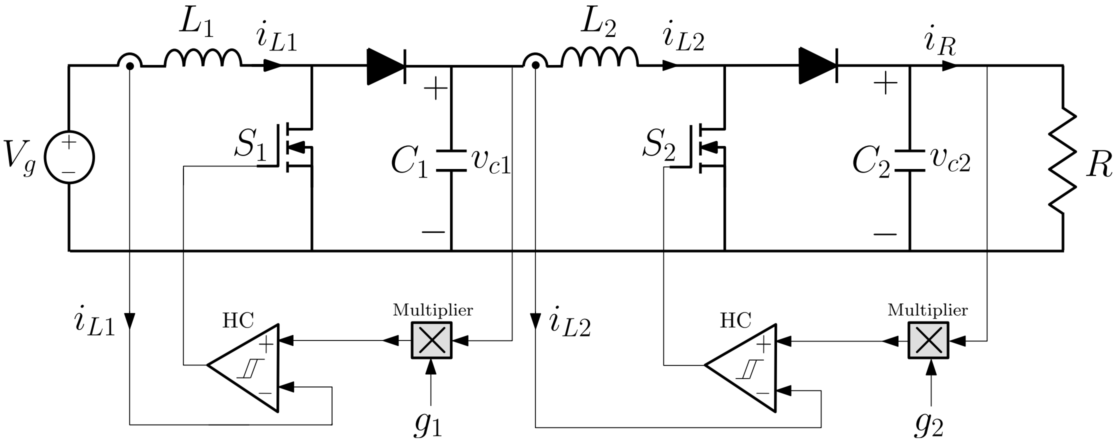

Figure 3.3: Schematic diagram of two cascaded g-gyrators operating in SMC.

3.2.2 Full-order switched model

By analogy with chapter 2 and considering that both converters operate in CCM, the cascade connection of two g-gyrators of Fig. 3.3 can be represented by the following set of differential equations

$$\frac{\mathrm{d}i_{L1}}{\mathrm{d}t} = \frac{V_g}{L_1} - \frac{v_{c1}}{L_1}(1-u_1) \tag{3.4}$$

$$\frac{\mathrm{d}i_{L2}}{\mathrm{d}t} = \frac{v_{c1}}{L_2} - \frac{v_{c2}}{L_2}(1-u_2) \tag{3.5}$$

$$\frac{\mathrm{d}v_{c1}}{\mathrm{d}t} = \frac{i_{L1}}{C_1}(1-u_1) - \frac{i_{L2}}{C_1} \tag{3.6}$$

$$\frac{\mathrm{d}v_{c2}}{\mathrm{d}t} = \frac{i_{L2}}{C_2}(1-u_2) - \frac{v_{c2}}{RC_2}. \tag{3.7}$$

where u_1 and u_2 are the discontinuous control variables for the first and second stage respectively.

3.2.3 Equivalent control

The dynamical behavior of i_{L1}, v_{c1} and i_{L2} is constrained by the following set of differential equations

$$\dot{s}_1(\mathbf{x}) = \frac{\mathrm{d}i_{L1}}{\mathrm{d}t} - g_1\frac{\mathrm{d}v_{c1}}{\mathrm{d}t} = 0 \tag{3.8}$$

$$\dot{s}_2(\mathbf{x}) = \frac{\mathrm{d}i_{L2}}{\mathrm{d}t} - g_2\frac{\mathrm{d}v_{c2}}{\mathrm{d}t} = 0 \tag{3.9}$$

Following the same procedure used for the DC-transformer, the equivalent control variables $u_{eq1}(\mathbf{x})$ and $u_{eq2}(\mathbf{x})$ can be obtained. Their expressions are given by

$$\begin{aligned} u_{eq1}(\mathbf{x}) &= 1 - \frac{1}{v_{c1}}(\beta_1 V_g + \beta_2 v_{c2}) && (3.10)\\ u_{eq2}(\mathbf{x}) &= 1 - \beta_3 \frac{v_{c1}}{v_{c2}} - \beta_4 && (3.11) \end{aligned}$$

where, $\beta_1 = C_1/(g_1^2 L_1 + C_1)$, $\beta_2 = g L_1/(g_1^2 L_1 + C_1)$, $g = g_1 g_2$, $\beta_3 = C_2/(g_2^2 L_2 + C_2)$ and $\beta_4 = g_2 L_2/(R(g_2^2 L_2 + C_2))$. From these expressions, the existence conditions of sliding regimes can be obtained. As mentioned before, the limits of $u_{eq1}(\mathbf{x})$ and $u_{eq2}(\mathbf{x})$ are 0 and 1. In the case of the g-gyrator, the sliding-mode regime will exist provided that

$$v_{cr1} < v_{c1} < v_{cr2} \tag{3.12}$$

where the critical values v_{cr1} and v_{cr2} are given by

$$\begin{aligned} v_{cr1} &= \beta_1 V_g + \beta_2 v_{c2} && (3.13)\\ v_{cr2} &= \frac{1-\beta_4}{\beta_3} v_{c2}. && (3.14) \end{aligned}$$

3.2.4 Ideal sliding dynamics and sliding-mode conditions

Replacing the discontinuous control variables u_1 and u_2 by their respective equivalent expressions $u_{eq1}(\mathbf{x})$ and $u_{eq2}(\mathbf{x})$ in the switching model, and taking into account the invariance conditions imposed by the switching surface, the ideal sliding dynamics can be obtained. Constrained on the sliding manifold, the motion of the system is described by the following reduced-order ideal sliding-mode dynamics model

$$\begin{aligned} \frac{\mathrm{d}v_{c1}}{\mathrm{d}t} &= \frac{g_1 V_g}{g_1^2 L_1 + C_1} + (\beta_2 g_1 - g_2)\frac{v_{c2}}{C_1} && (3.15)\\ \frac{\mathrm{d}v_{c2}}{\mathrm{d}t} &= \frac{g_2 v_{c1}}{g_2^2 L_2 + C_2} + (\beta_4 g_2 - 1)\frac{v_{c2}}{RC_2}. && (3.16) \end{aligned}$$

The coordinates of the equilibrium point of the system are given by

$$\mathbf{x}^* = [I_{L1}, I_{L2}, V_{c1}, V_{c2}]^\top = \left[\frac{g_1^2}{g_2^2 R} V_g, g_1 V_g, \frac{g_1}{g_2^2 R} V_g, \frac{g_1}{g_2} V_g\right]^\top. \tag{3.17}$$

It should be mentioned that the steady state values of I_{L1} and V_{c1} depend on the load resistance. Moreover, note that

$$I_{L1} = \frac{g_1}{g_2}\frac{V_{c2}}{R} = \frac{g_1}{g_2} I_R \quad \text{and} \quad V_{c2} = \frac{g_1}{g_2} V_g \tag{3.18}$$

Table 3.1: The used parameter values for the two cascaded g-gyrators.

L_1	L_2	$C_1 = C_2$	R	h_1	h_2	f_s
200 μH	2 mH	10 μF	2500 Ω	0.27 A	0.13 A	100 kHz

The expressions in (3.18) define the DC-transformer behavior as it has been previously anticipated in (3.3).

The equivalent control variables at the equilibrium point can be obtained by substituting (3.17) in (3.10) and (3.11). In steady-state, these control variables are given by

$$U_{eq1} = 1 - \frac{g_2^2 R}{g_1} \quad \text{and} \quad U_{eq2} = 1 - \frac{1}{g_2 R} \tag{3.19}$$

Since U_{eq1} and U_{eq2} must be bounded between 0 and 1, the following condition must be fulfilled

$$\frac{1}{g_2} < R < \frac{g_1}{g_2^2} \tag{3.20}$$

It can be observed that this condition depends on the load resistance and under load change, the sliding motion can be lost. This is a disadvantage of this type of cascade connection.

3.2.5 Stability analysis of the ideal sliding-mode dynamic model

In order to study the stability of the system, the Jacobian matrix has been obtained. This matrix can be expressed as follows

$$\mathbf{J} = \begin{pmatrix} 0 & -\dfrac{g_2\beta_1}{C_1} \\ \dfrac{g_2\beta_3}{C_2} & -\dfrac{\beta_4}{g_2 L_2} \end{pmatrix} \tag{3.21}$$

whose characteristic polynomial equation is given by

$$s^2 + \frac{\beta_4}{g_2 L_2} s + \frac{\beta_1 \beta_3 g_2^2}{C_1 C_2} = 0 \tag{3.22}$$

which has two complex conjugates poles in the left half plane resulting in an unconditionally stable system.

3.2.6 Numerical simulations and experimental results

The two cascaded gyrators have been simulated using PSIM. The selected conductances are $g_1 = 0.05$ S and $g_2 = 0.002$ S. These values have been chosen to achieve an input power $P_{in} = 60$ W, an intermediate voltage $V_{c1} = 80$ V, an output voltage $V_{c2} = 380$ V and a nominal switching frequency of 100 kHz. This switching frequency can be achieved using the hysteresis widths h_1 and h_2 for the first and second sliding surfaces respectively, whose values are listed in Table 3.1. The rest of parameters of the circuit and their values used in the numerical simulations are shown in Table 3.1. It is worth mentioning that the parasitic elements have been included in the PSIM simulation. These are the internal resistance of the inductors (r_{L1}=60 mΩ and r_{L2}=130 mΩ), the ON resistance of the MOSFETs (r_{on1}=60 mΩ and r_{on2}=165 mΩ) and the equivalent series resistances (ESR) of the capacitors $r_{c1} = r_{c2} = 0.1\ \Omega$.

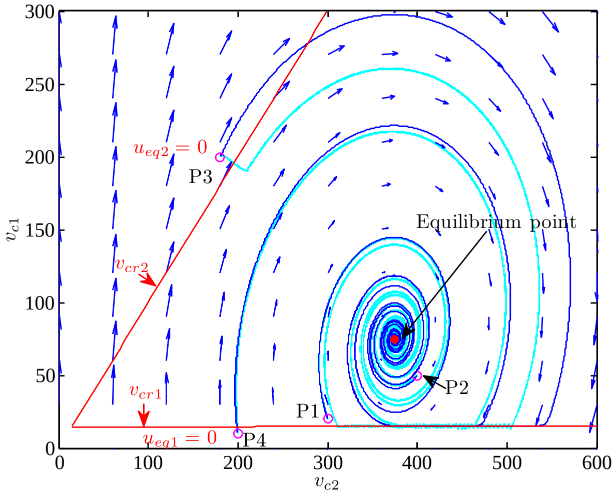

Figure 3.4: Trajectories obtained from the ideal sliding dynamics model and from the full-order switched model for two cascaded g-gyrators using PSIM starting from different initial conditions in the plane (v_{c1}, v_{c2}).

First, the validity of the ideal sliding dynamic model is checked with numerical simulations from the full-order model in different regions of the state space. Four different initial conditions P1-P4 are considered, the system is simulated using the two different models and the results are shown in Fig. 3.4. The sliding-mode boundaries defined by v_{cr1} and v_{cr2} given in (3.13) and (3.14) are also plotted. It can be observed from this figure that the system trajectories converge to the equilibrium point in all cases. Furthermore, when starting from the points P1-P2, the corresponding trajectories are in perfect agreement with the full-order simulations from PSIM based on the switched model. However, concerning the points P3 and P4, the mismatching between the trajectories from the ideal sliding dynamics model and the full-order model is due to the fact that these points are outside the sliding-mode domain described previously in closed-form.

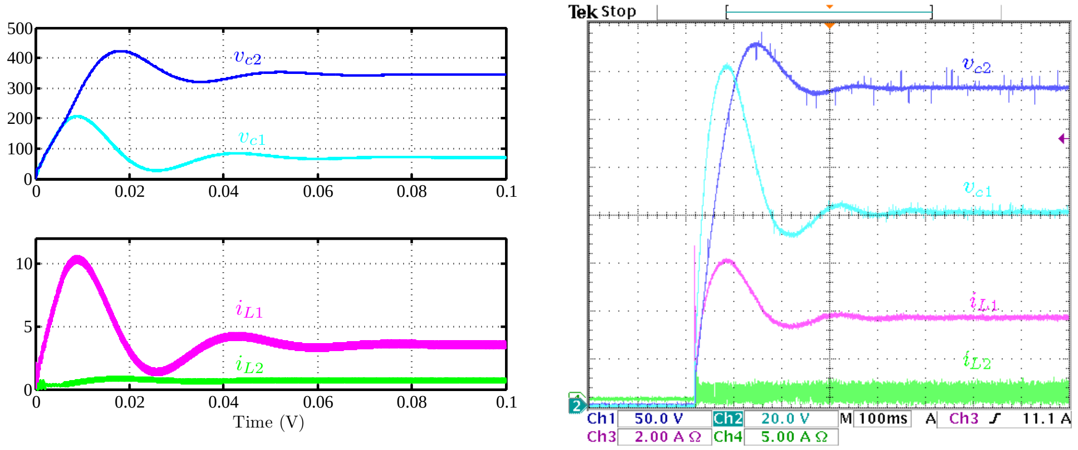

(a) (b)

Figure 3.5: Time domain responses of simulated and experimental waveforms of capacitor voltages v_{c2}, v_{c1} and inductor currents i_{L1}, i_{L2} (respectively from up to down) for two cascaded g-gyrators during start-up.

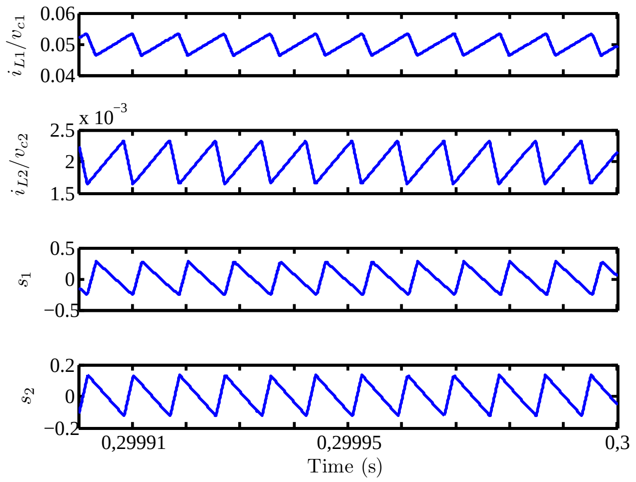

Figure 3.6: The ratios i_{L1}/v_{c1}, i_{L2}/v_{c2} and the switching function s_1 and s_2 in the steady-state.

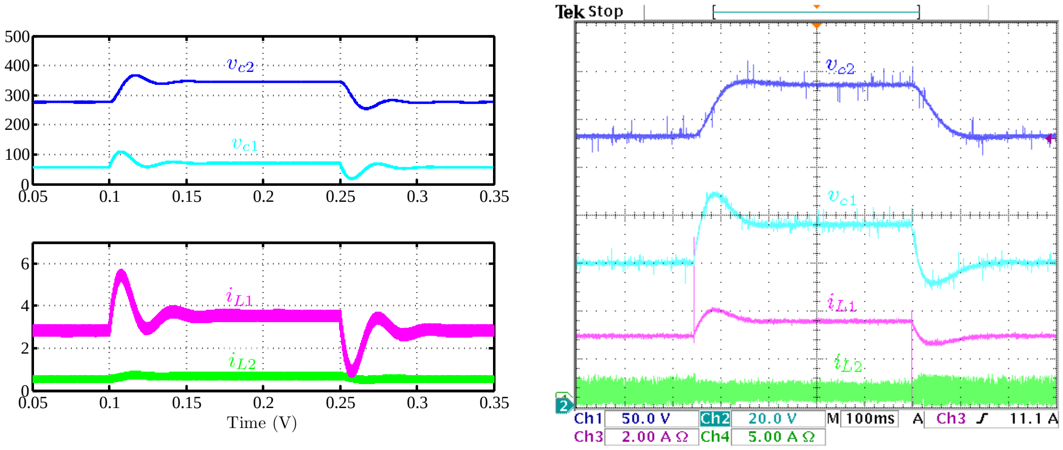

(a) (b)

Figure 3.7: Simulated and experimental waveforms of capacitor voltages v_{c2}, v_{c1} and inductor currents i_{L1}, i_{L2} (respectively from up to down) for $g_1 = 0.05$ S and $g_2 = 0.002$ S under input voltage step change from 12 V to 15 V.

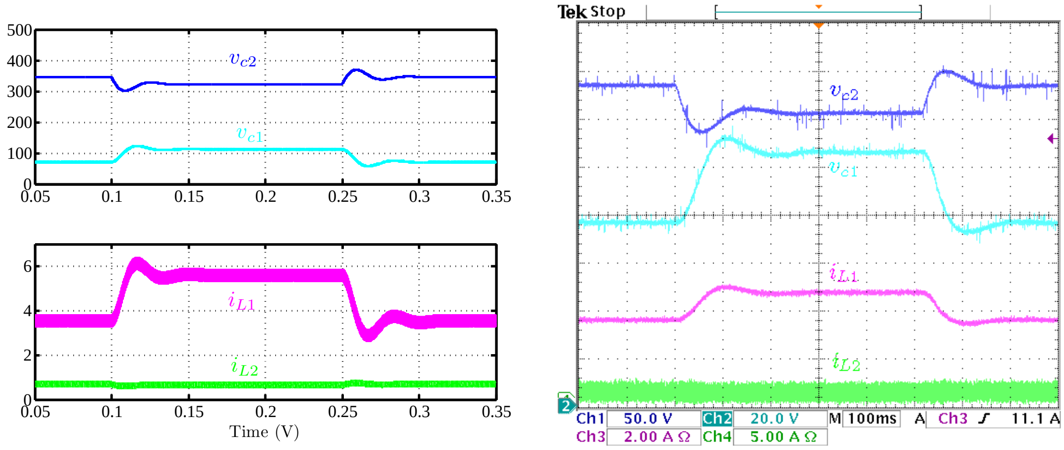

(a) (b)

Figure 3.8: Simulated and experimental waveforms of capacitor voltages v_{c2}, v_{c1} and inductor currents i_{L1}, i_{L2} (respectively from up to down) for $g_1 = 0.05$ S and $g_2 = 0.002$ S under load step change from 2500 Ω to 1500 Ω.

Figs. 3.5 shows the simulated and experimental waveforms during the transient start-up of the system from zero initial conditions of the circuit of Fig. 3.3. Note that after a long transient response of 60 ms, the state variables reach their steady-state values which are given in Eq. (3.17) and both stages are behaving as a gyrator in steady-state due to the constraints imposed by the switching functions $s_1(\mathbf{x})$ and $s_2(\mathbf{x})$. In particular, Fig. 3.6 shows that the two stages are behaving as a g-gyrator in steady-state because the ratios i_{L1}/v_{c1} and i_{L2}/v_{c2}, equal the conductances of the two converters defined by their respective switching functions.

Fig. 3.7 shows the simulated and experimental responses under input voltage variation. When the input voltage increases from 12 to 15 V, the capacitor voltages and the inductor currents increase with a large transient time of 60 ms. Fig. 3.8 shows the simulated and experimental responses under load variation. When the load changes from 2500 Ω to 1500 Ω, the inductor current i_{L2} is constant and the intermediate voltage v_{c1} increases and the inductor current i_{L1} increases which are in agreement with the expression of the equilibrium point in (3.17), which increases the the switching losses and the copper losses in the first stage due to the existence of parasitic elements in the components. This leads to a slightly decrease in the output capacitor voltage v_{c2}. However, ideally, this voltage should be constant as deduced in (3.17). On the other hand, the capacitor voltage v_{c1} and inductor current i_{L1} increase as they are depending on the load resistance also in concordance with Eq. (3.17). The input power increases form 60 W to 75 W for this load change.

3.3 G-Gyrator Based on Cascaded Boost Converters Using a Single Sliding Surface

Similarly to the DC-transformer case, a g-gyrator synthesized from the cascade connection of two boost converters having the same gate drive signals is analyzed in this section. This approach has the advantage of having only one current sensor and a single sliding surface.

3.3.1 System description

Fig. 3.9 depicts the circuit description corresponding to a g-gyrator based on two cascaded boost converters. The gyrator characteristics can be implemented by means of a SMC as described in the previous section. The sliding surface imposes that the input current of the first converter is proportional to the output voltage of the second converter. The sliding surface can be described by the following switching function.

$$s(\mathbf{x}) = i_{L1} - g v_{c2}. \tag{3.23}$$

In steady-state $s(\mathbf{x}) = 0$, i.e., $I_{L1} = gV_{c2}$. Therefore, the two cascaded boost converters behave as a g-gyrator with controlled input current. Furthermore, by

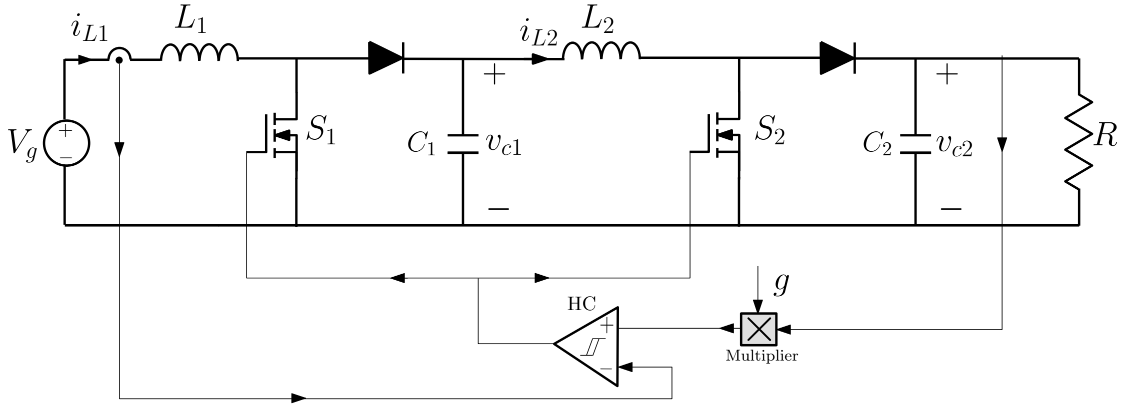

Figure 3.9: The schematic diagram of a power gyrator with controlled input current based on two cascaded boost converters.

considering that the two converters in Fig. 3.1 are ideal, one will have $V_g I_{L1} = V_{c2} I_R$ and therefore, (3.2) will be automatically satisfied and the following relationship between the output current and the input voltage holds

$$I_R = gV_g \tag{3.24}$$

3.3.2 Full-order switched model

By applying standard KVLs and KCLs to the circuit depicted in Fig. 3.9. The two cascaded boost converters can be represented by the following differential equations

$$\frac{\mathrm{d}i_{L1}}{\mathrm{d}t} = \frac{V_g}{L_1} - \frac{(1-u)v_{c1}}{L_1} \tag{3.25}$$

$$\frac{\mathrm{d}i_{L2}}{\mathrm{d}t} = \frac{v_{c1}}{L_2} - \frac{(1-u)v_{c2}}{L_2} \tag{3.26}$$

$$\frac{\mathrm{d}v_{c1}}{\mathrm{d}t} = \frac{(1-u)i_{L1}}{C_1} - \frac{i_{L2}}{C_1} \tag{3.27}$$

$$\frac{\mathrm{d}v_{c2}}{\mathrm{d}t} = \frac{(1-u)i_{L2}}{C_2} - \frac{v_{c2}}{RC_2} \tag{3.28}$$

All the other parameters that appear in (3.25)-(3.28) are shown in Fig. 3.9. The signal u is the control variable used to drive the switches for both converters. $u = 1$ during the period T_{ON} and $u = 0$ during the period T_{OFF}.

3.3.3 Equivalent control

The equivalent control variable is obtained by imposing that the trajectories are evolving on the switching manifold. To synthesize a g-gyrator based on two cascaded boost converters, the switching function can be selected as follows: $s(\mathbf{x}) = i_{L1} - g v_{c2}$. By imposing the invariance conditions Sira-Ramirez (1987), one has $s(\mathbf{x}) = \dot{s}(\mathbf{x}) = 0$. Therefore, the dynamical behavior of i_{L1} is constrained by the following differential equation

$$\dot{s}(\mathbf{x}) \quad = \quad \frac{\mathrm{d}i_{L1}}{\mathrm{d}t} - g\frac{\mathrm{d}v_{c2}}{\mathrm{d}t} = 0 \tag{3.29}$$

From Eqs. (3.25), (3.28) and (3.29), the following expression is obtained for the equivalent control variable $u_{eq}(\mathbf{x})$

$$u_{eq}(\mathbf{x}) = 1 - \frac{V_g R C_2 + g v_{c2} L_1}{v_{c1} R C_2 + g i_{L2} R L_1} \tag{3.30}$$

Note that $u_{eq}(\mathbf{x})$ must be bounded by the minimum and maximum value of u Utkin (1978), Mattavelli et al. (1993), i.e

$$0 \ < \ u_{eq}(\mathbf{x}) \ < \ 1 \tag{3.31}$$

For this system, the sliding-mode regime will implies that

$$v_{c1} > V_g + \frac{g v_{c2} L_1 - g i_{L2} R L_1}{R C_2} \tag{3.32}$$

3.3.4 Ideal sliding dynamics and sliding-mode conditions

Substituting (3.30) in Eqs. (3.25)-(3.28) and taking into account (3.29), the following ideal sliding dynamics reduced-order model is obtained

$$\frac{\mathrm{d}i_{L2}}{\mathrm{d}t} \quad = \quad \frac{v_{c1}}{L_2} - \frac{V_g R C_2 + g v_{c2} L_1}{R L_2 (v_{c1} C_2 + g i_{L2} L_1)} v_{c2} \tag{3.33}$$

$$\frac{\mathrm{d}v_{c1}}{\mathrm{d}t} \quad = \quad \frac{g(V_g R C_2 + g v_{c2} L_1) v_{c2}}{RC1(v_{c1} C_2 + g i_{L2} L_1)} - \frac{i_{L2}}{C_1} \tag{3.34}$$

$$\frac{\mathrm{d}v_{c2}}{\mathrm{d}t} \quad = \quad \frac{V_g R C_2 + g v_{c2} L_1}{R C_2 (v_{c1} C_2 + g i_{L2} L_1)} i_{L2} - \frac{v_{c2}}{R C_2} \tag{3.35}$$

Being a third order nonlinear system, the dynamical analysis of (3.33)-(3.35) is challenging. However, the linearization of the system near the operating point reveals that the system is stable with certain conditions as will be shown later. The equilibrium point can be obtained by forcing the time derivative of the state variables of the ideal sliding mode model to be null. From (3.33)-(3.35) and taking into account the sliding surface equation and that, ideally, the input power equals the output power, the equilibrium point of the ideal sliding dynamics is given by

$$\mathbf{x}^* = [I_{L1}, I_{L2}, V_{c1}, V_{c2}]^\top = \left[g^2 V_g R, g V_g \sqrt{Rg}, V_g \sqrt{Rg}, g V_g R\right]^\top . \tag{3.36}$$

It can be observed that $I_{L1} = gV_{c2}$, which defines the steady-state gyrator behavior and that $I_{L2} = gV_{c1}$, which defines a steady-state Loss-Free Resistor (LFR) characteristics that means that the input port of the second boost converter has natural LFR characteristics. Note that the steady-state values of all the state variables are depending on the load resistance.

The control law at the equilibrium point can be obtained by substituting (3.36) in (3.30). In doing so, one obtains the following steady state value U_{eq} of the control variable $u_{eq}(\mathbf{x})$

$$U_{eq} := u_{eq}(\mathbf{x}^*) \quad = \quad 1 - \frac{1}{\sqrt{R\, g}} \tag{3.37}$$

As mentioned before in (3.31), U_{eq} is bounded between 0 and 1 which implies that, the following condition must be fulfilled

$$R\, g \quad > \quad 1 \tag{3.38}$$

3.3.5 Stability analysis of the ideal sliding-mode dynamic model

As mentioned in the previous cases, the stability of the linearized system can be studied by using the Jacobian matrix $\mathbf{J}$ corresponding to (3.33)-(3.35) and evaluating it at the equilibrium point $\mathbf{x}^*$. This matrix can be expressed as follows

$$\mathbf{J} = \begin{pmatrix} \dfrac{L_1 g}{L_2 C} & \dfrac{2C_2 + g^2 L_1}{L_2 C} & -\dfrac{2g^2 L_1 + C_2}{\sqrt{Rg} L_2 C} \\[2ex] -\dfrac{2g^2 L_1 + C_2}{C_1 C} & -\dfrac{C_2 g}{C_1 C} & -\dfrac{g(2g^2 L_1 + C_2)}{\sqrt{Rg} C_1 C} \\[2ex] \dfrac{1}{\sqrt{Rg} C} & -\dfrac{g}{\sqrt{Rg} C} & -\dfrac{1}{RC} \end{pmatrix} \tag{3.39}$$

where $C = C_2 + g^2 L_1$. The characteristic polynomial of the linearized system is $\det(\mathbf{J} - s\mathbf{I}) = 0$, where $\mathbf{I}$ is the unitary matrix as defined before. Developing this

Table 3.2: The used parameter values for g-gyrator based on cascaded converters using a single sliding surface.

L_1	L_2	$C_1 = C_2$	R	h	f_s
200 μH	2 mH	10 μF	2500 Ω	0.25 A	100 kHz

equation, the characteristic polynomial can be written in the following form

$$s^3 + \frac{L_2C_1 + Rg\Delta\tau}{RL_2C_1C}s^2 + \frac{2L_2g^2 + 2RgC + C_1}{RgL_2C_1C}s + \frac{2}{RL_2C_1C} \tag{3.40}$$

where $\Delta\tau = C_2L_2 - L_1C_1$. The stability of this system can be checked by using Routh-Hurwitz criterion to get the following stability conditions

$$L_2C_1 + Rg\Delta\tau > 0 \tag{3.41}$$

$$(L_2C_1 + Rg\Delta\tau)(2g^2L_2 + C_1) + 2R^2g^2C\Delta\tau > 0 \tag{3.42}$$

It can be noted that all the terms are positive except $\Delta\tau = C_2L_2 - L_1C_1$. Therefore, the system will be stable if L_2C_2 is higher than L_1C_1.

3.3.6 Numerical simulations and experimental results

In order to verify the theoretical results predicted in Section 3.4, the circuit depicted in Fig. 3.9 has been simulated by using PSIM software with the set of parameter values depicted in Table 3.2 that satisfies the stability conditions of Section 3.4. It is worth mentioning here that the parasitic elements have been included in the PSIM simulation. These are the internal resistance of the inductors (r_{L1}=60 mΩ and r_{L2}=130 mΩ), the ON resistance of the MOSFETs (r_{on1}=60 mΩ and r_{on2}=165 mΩ) and the equivalent series resistances (ESR) of the capacitors $r_{c1} = r_{c2} = 0.1\ \Omega$. Moreover, a gyrator based on two boost converters has been implemented to validate the simulation results using the set of parameters shown in Table 3.2 (for more details see Appendix A).

First, the validity of the ideal sliding dynamics model (3.33)-(3.35) will be checked using numerical simulation from the full order model. The system is simulated from two certain initial points P1 and P2 using the two different models. As shown in Fig. 3.10, the trajectories of the reduced-order model are in perfect agreement with the full-order model for both cases.

Fig. 3.11 shows the simulated and experimental waveforms for the transient start-up and steady state responses of the system from zero initial conditions. Note, that after a long transient time of 80 ms, the state variables reach their steady state values which are in agreement with Eq. (3.36). The cascade connection of the

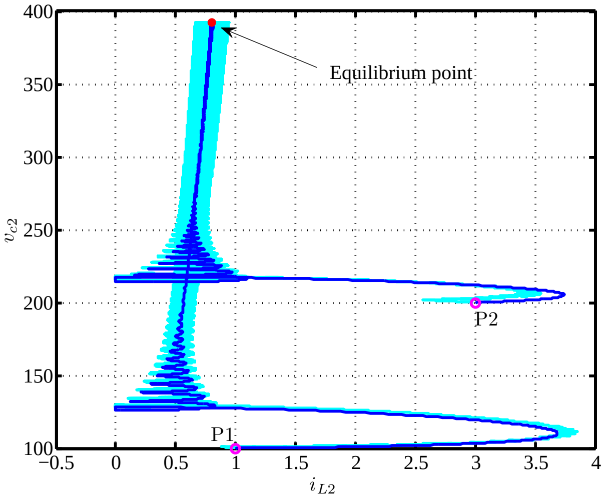

Figure 3.10: Trajectories obtained from the reduced-order ideal sliding-mode dynamics model and from the full-order switched model using PSIM starting from different initial conditions P1 and P2 in the state plane (i_{L2}, v_{c2}).

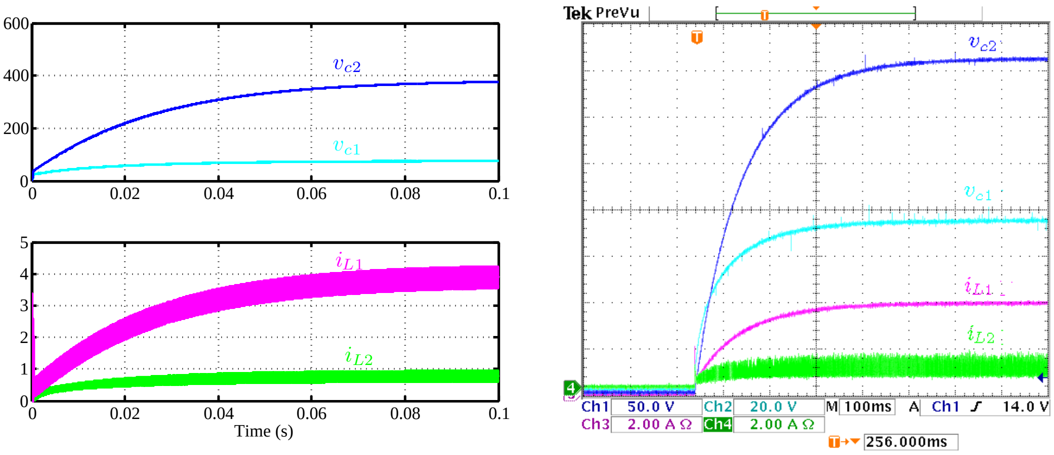

(a) (b)

Figure 3.11: Simulated and experimental waveforms of the capacitor voltages v_{c2}, v_{c1} and the inductor currents i_{L1}, i_{L2} (respectively from up to down) showing the start-up of the g-gyrator with controlled input current based on two cascaded boost converters for $g = 0.0105$ S.

two converters is behaving as g-gyrator in steady state and the second converter behaves as an LFR in the intermediate point of the two cascaded boost converters, due to the constraints imposed by the switching function $s(\mathbf{x})$.

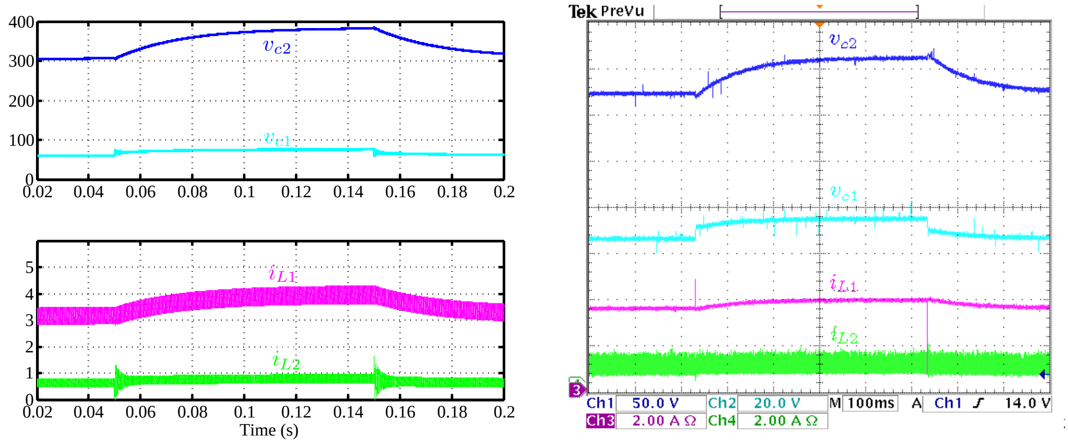

(a) (b)

Figure 3.12: Simulated and experimental waveforms of the capacitor voltages v_{c2}, v_{c1} and the inductor currents i_{L1}, i_{L2} (respectively from up to down) for g-gyrator with controlled input current based on two cascaded boost converters for $g = 0.0105$ S and under input voltage change from 12 V to 15 V.

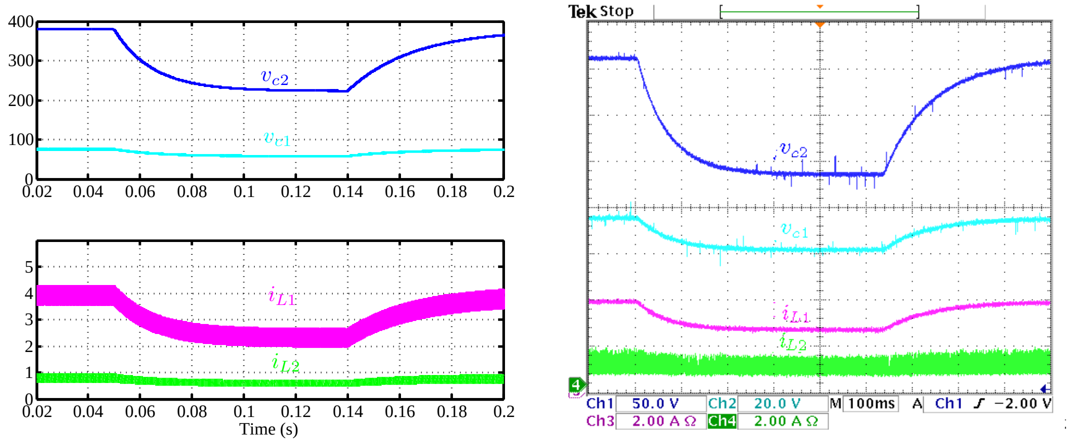

(a) (b)

Figure 3.13: Simulated and experimental waveforms of the capacitor voltages v_{c2}, v_{c1} and the inductor currents i_{L1}, i_{L2} (respectively from up to down) for g-gyrator with controlled input current based on two cascaded boost converters for $g = 0.0105$ S and under load change from 2500 Ω to 1500 Ω.

Fig. 3.12 shows the simulated and experimental responses in case of an input voltage variation from 12 V to 15 V. By increasing the input voltage, the output capacitor voltages and the inductor currents increase. However, when the the load R changes from 2500 to 1500 Ω, the capacitor voltages and the inductor currents decrease as shown in Fig. 3.13. As a consequence, the input power decreases from 60 W to 40 W in a good agreement with Eq. (3.36).

3.4 Conclusion

In this chapter, the gyrator has been defined as a type of canonical element for power processing. Firstly, two cascaded g-gyrators based on two sliding surfaces have been synthesized. The analysis has verified that the system is unconditionally stable. However, this system can lost the sliding motion when the load changes because of the restrictive existence condition. Moreover, the steady state value V_{c1} depends on the load resistance which can change the conversion ratio of each converter if the load changes. However, the steady state value of the output voltage V_{c2} is not sensible for the load change.

Secondly, the gyrator based on two cascaded boost converters using a single sliding surface has been synthesized to reduce the number of components which will help to decrease the cost and to increase the efficiency. The analysis has been verified that the system is stable with certain conditions. The existence condition of the system has been obtained, however, it is less restrictive than the two cascaded gyrators. In addition, the equilibrium point for all the state variables depend on the resistive load. Moreover, the transient time of the gyrator based two cascaded boost converters system is higher than the transient time of the two cascaded gyrators. Furthermore, the two systems have been tested for input voltage and load variation. It has been shown that the two systems can be used for achieving a high voltage conversion ratio. However, in both cases the existence conditions of sliding regimes depend on the output load resistance, hence, limiting its applicability to many energy processing systems.

Chapter 4

Cascaded Voltage Step-up Loss-Free Resistors

The notion of LFR was introduced first in Singer (1990, 1991) and then modeled in Singer and Erickson (1992). The LFR is modeled by a two-port element with a resistor at the input port and a power source at the output port, so that all the input power absorbed by the input resistor is transferred to the output. The LFR is characterized by a current at the input port proportional to the voltage at the same port. Ideally, this element transfer energy without losses, i.e, its power output is equal to its power input (POPI) Singer (1990). Initially, this notion was limited to the recognition that, when certain switching converters working in discontinuous conduction mode (DCM), under PWM operation, they exhibit resistive input impedance in steady-state Singer (1990), Singer and Erickson (1992). Later, the concept of the LFR was employed to model PFC circuits that use input voltage feedback to obtain switching converter with resistive input characteristic. Many techniques have been reported on the design of switching circuits with an input current proportional to input voltage Erickson and Maksimovic (2001), Flores-Bahamonde et al. (2014).

In this chapter, the LFR based on the boost converter will be synthesized using SMC. Firstly, two cascaded LFRs based on two sliding surfaces will be synthesized. Secondly, a single LFR will be synthesized based on two cascaded boost converters using only one sliding surface. The two systems will be analyzed theoretically and using numerical simulation. Stability analysis is carried out for the two systems in order to obtain their stability conditions and sliding conditions. The theoretical results will be verified using numerical simulations and experimental results.

4.1 Synthesis of Loss-Free Resistors in SMC

The LFR element does not exist naturally but its synthesis can be carried out by using a switched mode converter as depicted in Fig. 4.1. Under specific conditions regarding sliding mode operation and stability, the proportionality between the voltage and the current at the input port can be guaranteed in steady state in different power converter topologies. The following equations define the LFR canonical element

$$V_1 = rI_1 \tag{4.1}$$

$$V_1I_1 = V_2I_2 \tag{4.2}$$

where r is the resistance of the LFR and I_1, V_1, I_2 and V_2 are the steady-state averaged values of input and output currents and voltages respectively. Fig. 4.1 shows the block diagram of a switching converter which under an appropriate SMC would behave as an LFR Martinez-Salamero (2009). In this figure, the switching function is given by

$$s(\mathbf{x}) = k_i i_1 - k_v v_1 = 0 \tag{4.3}$$

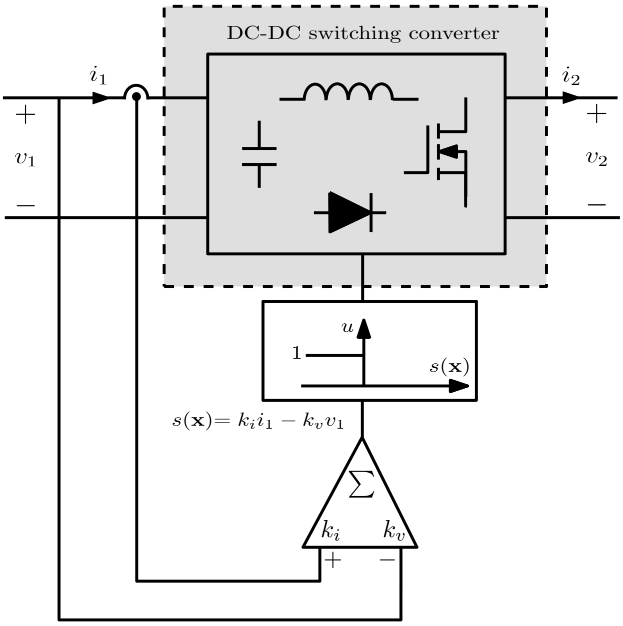

Figure 4.1: Block diagram of a switching converter acting as an LFR for power processing.

The switching function will be designed to impose an LFR behavior in steady state operation. If the switching surface, defined by $s(\mathbf{x}) = 0$ in steady-state, is reached, we will have the following relationship between the parameters and the variables defining the switching manifold

$$s(\mathbf{x}) = 0 \Rightarrow V_1 = \frac{k_i}{k_v} I_1 = rI_1 \tag{4.4}$$

where $r = k_i/k_v$. It can be observed that Eq. (4.4) establishes the same relationship given by Eq. (4.1) defining the LFR canonical element. On the other hand, since ideally the switching converter in Fig. 4.1 is a POPI system, the DC output power is equal to the DC input power Singer and Erickson (1992) and therefore Eq. (4.2) will be automatically satisfied. As mentioned before, ideally, the power absorbed by the input port is transmitted to the output port without losses. Hence, the output port behaves as a constant power source. In Singer and Erickson (1992), Cid-Pastor et al. (2010) a detailed analysis of an LFR synthesized using boost, buck-boost converters, working in discontinuous conduction mode, and Ćuk converter, working in continuous conduction mode (CCM), can be found.

4.2 Two Cascaded LFRs Operating in SMC

Fig. 4.2(a) shows the ideal schematic diagram of the two cascaded LFRs. The equivalent circuit model of the ideal two cascaded LFRs is a DC-transformer or an LFR as shown in Fig. 4.2(b), 4.2(c) respectively. Fig. 4.3 illustrates the circuit description of the cascade connection of two LFRs based on the boost converter. Likewise in previous chapter, this system do not require an LC filter at the output port of the second converter because the switching surface is defined by the inductor current (which is continuous) and the input voltage of each converter.

4.2.1 System description

The power stage of the two cascaded boost converters is the same one described in details in Fig. 2.4 of Chapter 2. The SMC technique is used to impose the LFR characteristic at the input port of both converters. Namely, the switching functions are $s_1(\mathbf{x}) = i_{L1} - g_{r1}V_g$ and $s_2(\mathbf{x}) = i_{L2} - g_{r2}V_{c1}$ in which g_{r1} and g_{r2} are the input conductance of the LFRs 1 and 2 respectively ($g_{r1} = 1/r_1$ and $g_{r1} = 1/r_2$) where r_1 and r_2 are the resistances of the LFRs. As it can be deduced from Fig. 4.3, the first converter is loaded by the input resistance of the second converter. In

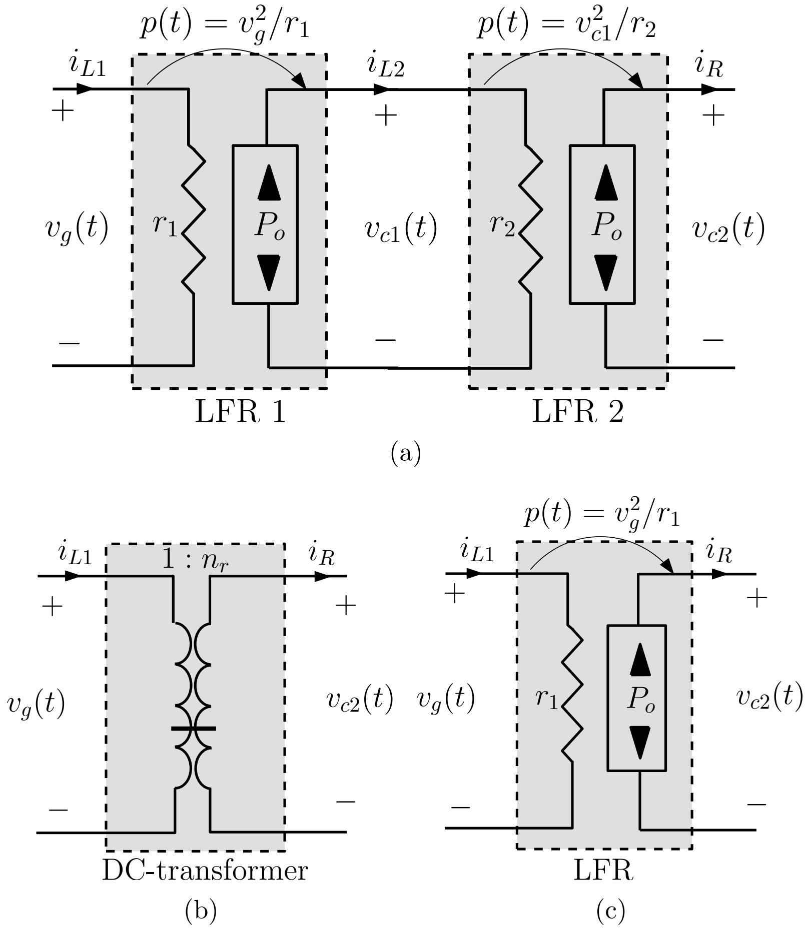

Figure 4.2: (a) The schematic diagram of two cascaded ideal LFRs (b) The equivalent circuit model of the two cascaded ideal LFRs is a DC-transformer. (c) The equivalent circuit model for the two cascaded ideal LFRs is a LFR.

steady-state $s_1(\mathbf{x}) = s_2(\mathbf{x}) = 0$, *i.e.*, $I_{L1} = g_{r1}V_g, I_{L2} = g_{r2}V_{c1}$ which implies that

$$\begin{aligned} V_{c1} &= V_g\sqrt{\frac{g_{r1}}{g_{r2}}} && (4.5)\\ V_{c2} &= V_g\sqrt{Rg_{r1}} && (4.6)\\ I_R &= I_{L1}\frac{1}{\sqrt{Rg_{r1}}}. && (4.7) \end{aligned}$$

Equations (4.5), (4.6) show that the output voltage depends on three parameters: the input voltage V_g, the conductance g_{r1} of the first LFR and the load resistance R. Furthermore, the intermediate voltage V_{c1} depends on the conductances g_{r1},

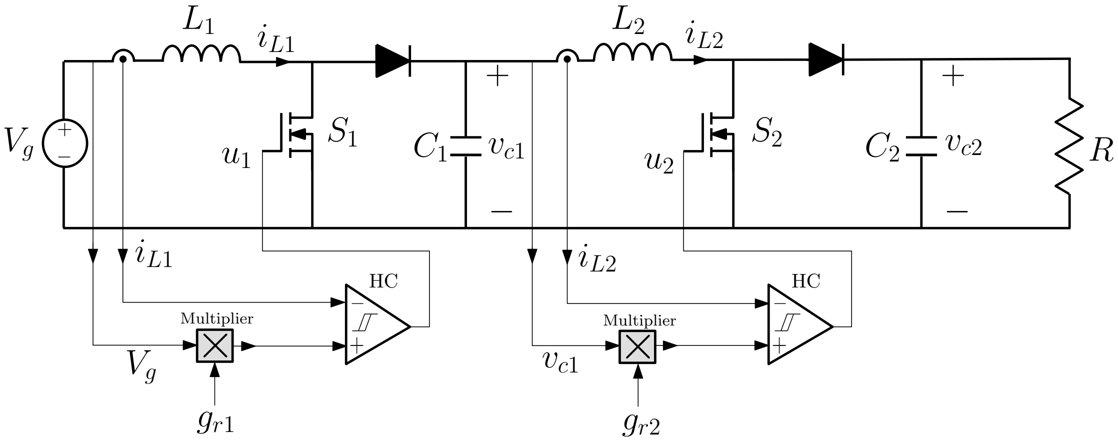

Figure 4.3: Schematic diagram of two cascaded LFRs by using SMC.

g_{r2} of both LFRs and the input voltage. Therefore, in a potential application of this structure, the conductance of the first LFR could be used to regulate the output voltage while the conductance of the second LFR could be used to regulate the intermediate voltage V_{c1}. It is worth to note also, that Eq. (4.6) and (4.7) correspond to the definition of a DC-transformer with a transformation ratio n_r equals $n_r = \sqrt{Rg_{r1}}$. That means a DC-transformer could be used as a model of the cascade connection of two LFRs as shown in Fig. 4.2(b). However, the conversion ratio has a nonlinear dependence on the load and on the conductance of the first LFR.

4.2.2 Full-order switched model

By applying KVL and KCL to the circuit depicted in Fig. 4.3, and considering that both converters operate in CCM, the two cascaded LFRs can be represented by the following set of differential equations

$$\frac{di_{L1}}{dt} = \frac{V_g}{L_1} - \frac{v_{c1}}{L_1}(1-u_1) \tag{4.8}$$

$$\frac{di_{L2}}{dt} = \frac{v_{c1}}{L_2} - \frac{v_{c2}}{L_2}(1-u_2) \tag{4.9}$$

$$\frac{dv_{c1}}{dt} = \frac{i_{L1}}{C_1}(1-u_1) - \frac{i_{L2}}{C_1} \tag{4.10}$$

$$\frac{dv_{c2}}{dt} = \frac{i_{L2}}{C_2}(1-u_2) - \frac{v_{c2}}{RC_2}. \tag{4.11}$$

where u_1 and u_2 are the discontinuous control variables for the first and second stage respectively as defined previously in Chapter 3. All the parameters that appear in (4.8)-(4.11) are shown in Fig. 4.3.

4.2.3 Equivalent control

The dynamical behavior of i_{L1}, v_{c1} and i_{L2} is constrained by the following set of differential equations

$$\dot{s}_1(\mathbf{x}) = \frac{\mathrm{d}i_{L1}}{\mathrm{d}t} = 0 \tag{4.12}$$

$$\dot{s}_2(\mathbf{x}) = \frac{\mathrm{d}i_{L2}}{\mathrm{d}t} - g_{r2}\frac{\mathrm{d}v_{c1}}{\mathrm{d}t} = 0 \tag{4.13}$$

Using the same procedure of Chapters 2 and 3, the equivalent control variables $u_{eq1}(\mathbf{x})$ and $u_{eq2}(\mathbf{x})$ can be expressed by

$$u_{eq1}(\mathbf{x}) = 1 - \frac{V_g}{v_{c1}} \tag{4.14}$$

$$u_{eq2}(\mathbf{x}) = 1 - \gamma_1\frac{v_{c1}}{v_{c2}} + \gamma_2\frac{V_g^2}{v_{c1}v_{c2}} \tag{4.15}$$

where $\gamma_1 = (C_1 + g_{r2}^2 L_2)/C_1$ and $\gamma_2 = g_{r1}g_{r2}L_2/C_1$. Like in the case of cascaded gyrators, the sliding-mode domain can be plotted in the plane (v_{c2}, v_{c1}). In this case, the sliding-mode regime will exist provided that

$$V_g < v_{c1} < v_{c1L}, \tag{4.16}$$

where the critical value v_{c1L} is given by

$$v_{c1L} = \frac{v_{c2}}{2\gamma_1} + \sqrt{\frac{v_{c2}^2}{4\gamma_1^2} + \frac{V_g^2\gamma_2}{\gamma_1}}. \tag{4.17}$$

Theoretically, other boundaries also exist, but the expression given by (4.17) is the most restrictive.

4.2.4 Ideal sliding dynamics and sliding-mode conditions

Replacing the discontinuous control variables u_1 and u_2 by their respective equivalent expressions $u_{eq1}(\mathbf{x})$ and $u_{eq2}(\mathbf{x})$ in the switching model, and taking into account the invariance conditions imposed by the switching surface, the ideal sliding dynamics model can be obtained as follows

$$\frac{\mathrm{d}v_{c1}}{\mathrm{d}t} = \frac{V_g}{v_{c1}}\frac{i_{L1}}{C_1} - \frac{i_{L2}}{C_1} \tag{4.18}$$

$$\frac{\mathrm{d}v_{c2}}{\mathrm{d}t} = \frac{i_{L2}}{C_2}\left(\gamma_1\frac{v_{c1}}{v_{c2}} - \gamma_2\frac{V_g^2}{v_{c1}v_{c2}}\right) - \frac{v_{c2}}{RC_2}. \tag{4.19}$$

The equilibrium point corresponding to (4.18)-(4.19) is given by

$$\mathbf{x}^* \;=\; [I_{L1}, I_{L2}, V_{c1}, V_{c2}]^\top = \left[g_{r1}V_g, V_g\sqrt{g_{r1}g_{r2}}, V_g\sqrt{\frac{g_{r1}}{g_{r2}}}, V_g\sqrt{Rg_{r1}}\right]^\top . \quad (4.20)$$

Note that, $I_{L1} = g_{r1}V_g$ and $I_{L2} = g_{r2}V_{c1}$. These results confirm the LFR behavior of the cascaded connection of two LFRs in steady-state as deduced in (4.5). It should be mentioned, that the steady state variable V_{c1} is not depending on the resistive load. However, V_{c2} depends on the load resistance as mentioned before.

The equivalent control variables at the equilibrium point can be obtained by substituting (4.20) in (4.14) and (4.15) to obtain the following equations

$$U_{eq1} = 1 - \sqrt{\frac{g_{r2}}{g_{r1}}} \quad \text{and} \quad U_{eq2} = 1 - \frac{1}{\sqrt{Rg_{r2}}} \qquad (4.21)$$

U_{eq1} and U_{eq2} must be bounded between 0 and 1 and therefore the following conditions must be fulfilled:

$$g_{r1} > g_{r2} \quad \text{and} \quad Rg_{r1} > 1 \qquad (4.22)$$

The second condition depends on the load resistance as in the case of the g-gyrator. However, the condition corresponding to the LFR is less restrictive comparing to the two cascaded gyrators case.

4.2.5 Stability analysis of the ideal sliding-mode dynamic model

The Jacobian matrix of the system can be expressed as follows

$$\mathbf{J} = \begin{pmatrix} -\dfrac{g_{r2}}{C_1} & 0 \\ \dfrac{2g_{r2}(C_1 + L_2 g_{r2}^2)}{\sqrt{Rg_{r2}}C_1C_2} & -\dfrac{2}{RC_2} \end{pmatrix} \qquad (4.23)$$

whose characteristic polynomial is the following

$$(s + \frac{2g_{r2}}{C_1})(s + \frac{2}{RC_2}) = 0 \qquad (4.24)$$

Its roots $-2g_{r2}/C_1$ and $-2/(RC_2)$ are located in the left half plane and hence, the system is unconditionally stable.

Table 4.1: The used parameter values for two cascaded LFRs.

L_1	L_2	$C_1 = C_2$	R	h_1	h_2	f_s
200 μH	2 mH	10 μF	2500 Ω	0.27 A	0.14 A	100 kHz

4.2.6 Numerical simulations and experimental results

According to (4.22), the selected conductances are $g_{r1} = 0.27$ S and $g_{r2} = 0.01$ S. These values have been chosen to achieve an input power $P_{in} = 60$ W, an intermediate voltage $V_{c1} = 80$ V, an output voltage $V_{c2} = 380$ V and a nominal switching frequency 100 kHz, the rest of parameters are shown in Table. 4.1. The parasitic elements have been included in the simulation similar to the gyrator case. These are the internal resistance of the inductors (r_{L1}=60 mΩ and r_{L2}=130 mΩ), the ON resistance of the MOSFETs (r_{on1}=60 mΩ and r_{on2}=165 mΩ) and the equivalent series resistances (ESR) of the capacitors $r_{c1} = r_{c2} = 0.1\ \Omega$. Moreover, a prototype of two cascaded boost-based LFRs has been implemented. The system is supplied from a DC voltage source of 15 V and loaded with a resistance (for more details about the experimental prototypes, see Appendix A).

Firstly, the validity of ideal sliding dynamic model is checked by numerical simulation from the full-order model in different regions of the state space. As depicted in Fig. 4.4, different initial conditions P1-P4 are considered and the system is simulated using the two different models. The sliding-mode boundaries given by $v_{c1} > V_g$ and $v_{c1} < v_{c1L}$ established in (4.17) are also plotted in the same figure. It can be observed from this figure that the system trajectories converge to the equilibrium point in all cases. Moreover, for the points P1-P3, the corresponding trajectories are in perfect agreement with the full-order simulations obtained with the switched model. Concerning the point P4, the mismatching between the trajectories from the ideal sliding dynamics model and the full-order model is mainly due to the fact that this point is outside the sliding-mode domain.

Secondly, Fig. 4.5 shows the simulated and experimental waveforms during the transient start-up response of the system from zero initial conditions. Note, that after a short transient time of 30 ms, the state variables reach their steady-state values which are in perfect agreement with their theoretical values given in Eq. (4.20) and both stages are behaving as LFR, due to the constraints imposed by the switching functions $s_1(\mathbf{x})$ and $s_2(\mathbf{x})$. In particular, Fig. 4.6 shows that the two stages are behaving as an LFR in steady-state because the ratios i_{L1}/v_g and i_{L2}/v_{c1}, are equal to the conductances of the LFRs established by the respective switching functions.

Fig. 4.7 shows the simulated and experimental results corresponding to the input voltage variation on the response of the system. When the input voltage

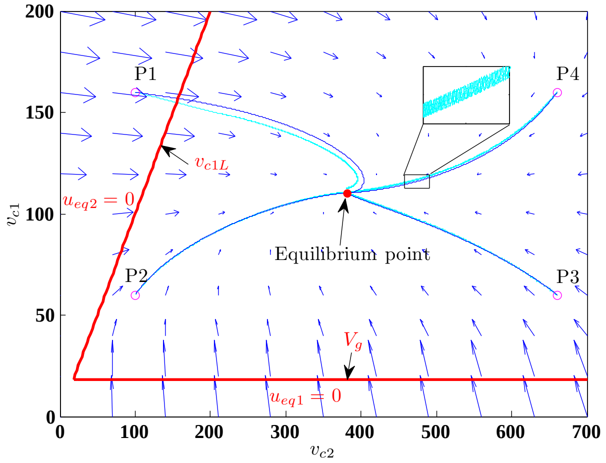

Figure 4.4: Trajectories of two cascaded boost-based LFRs obtained from the ideal sliding dynamics model and from the full-order switched model using PSIM starting from different initial conditions in the plane (v_{c1}, v_{c2}).

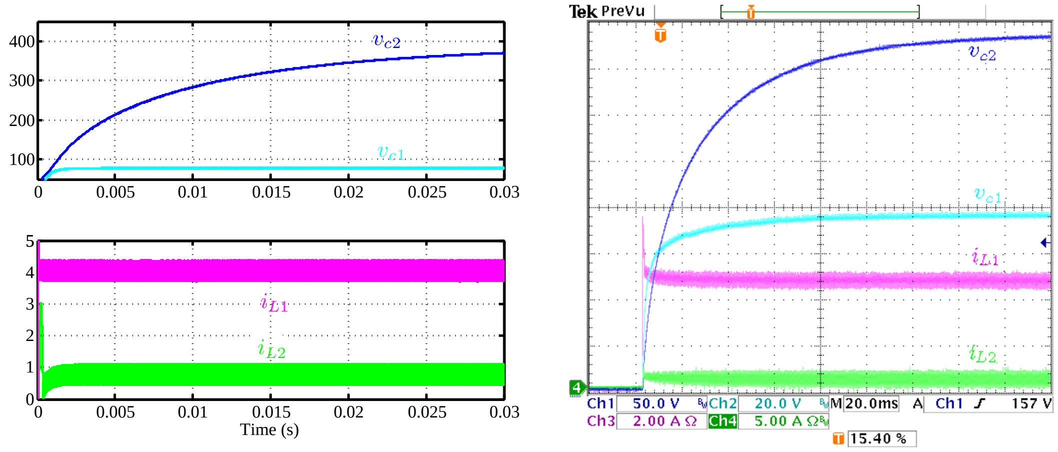

(a) (b)

Figure 4.5: Simulated and experimental waveforms of the capacitor voltages v_{c2}, v_{c1} and the inductor currents i_{L1}, i_{L2} (respectively from up to down) for two cascaded LFRs during start-up.

increases from 12 V to 15 V, the capacitor voltages and the inductor currents increase. When the load changes from 2500 Ω to 1500 Ω, the inductor currents remain constant, in turn, the output capacitor voltage V_{c2} decreases because of

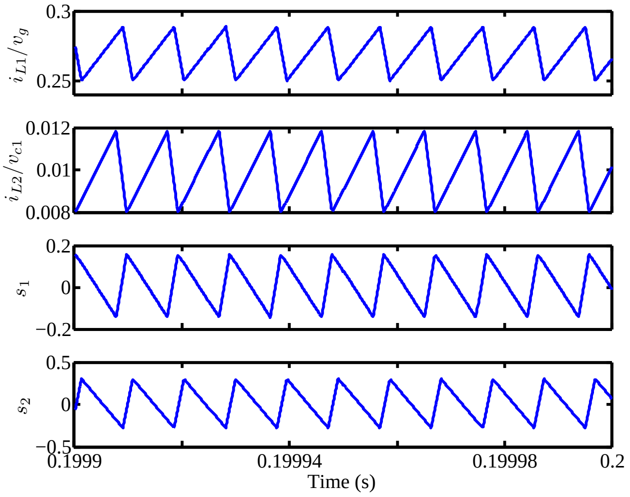

Figure 4.6: The ratios i_{L1}/v_g and i_{L2}/v_{c1} and the switching functions $s_1(\mathbf{x})$ and $s_2(\mathbf{x})$ in the steady-state.

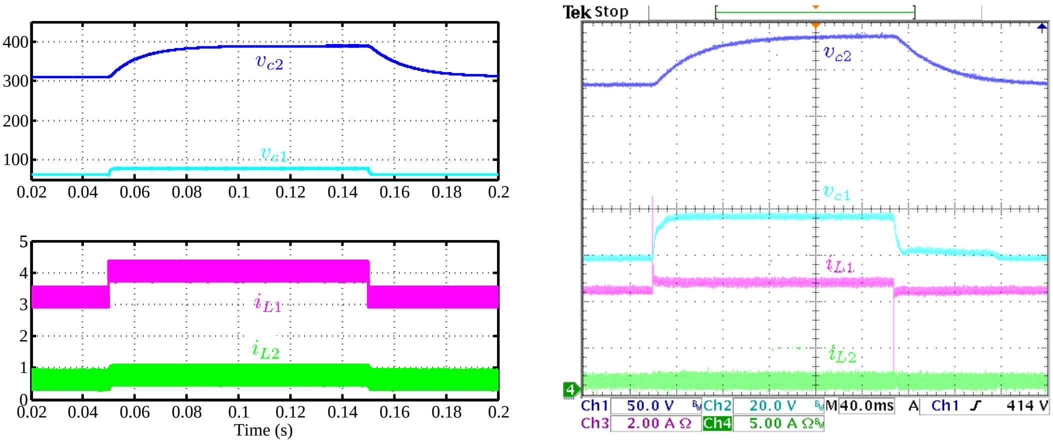

(a) (b)

Figure 4.7: Simulated and experimental waveforms of the capacitor voltages v_{c2}, v_{c1} and the inductor currents i_{L1}, i_{L2} (respectively from up to down) for two cascaded LFRs at $g_{r1} = 0.27$ S and $g_{r2} = 0.01$ S under input voltage change from 12 V to 15 V.

its dependance on the load resistance as shown in Fig. 4.8. This change of V_{c2} has an effect on the switching losses which leads to a slightly decrease in the capacitor voltage V_{c1}. Note that ideally the voltage V_{c1} is not depending on the load resistance as given in (4.20). In addition, unlike the DC-transformer and

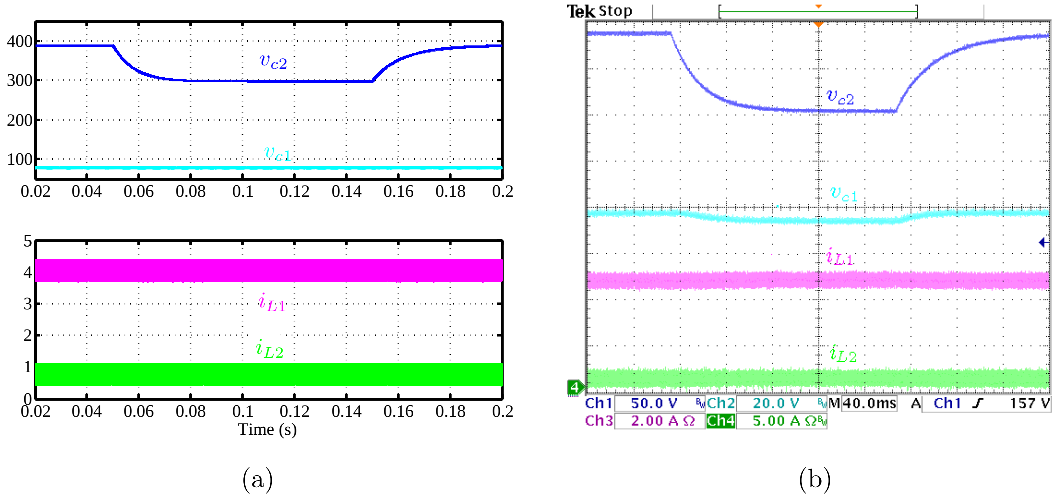

(a) (b)

Figure 4.8: Simulated and experimental waveforms of the capacitor voltages v_{c2}, v_{c1} and the inductor currents i_{L1}, i_{L2} (respectively from up to down) for two cascaded LFRs under load change from 2500 Ω to 1500 Ω.

g-gyrator systems, the absorbed input power is constant when the load resistance varies. All these simulation and experimental results are in perfect agreement with steady-state predictions given in (4.20).

4.3 Two Cascaded LFRs with an Output Filter

The output current of the two cascaded LFRs is discontinuous one. Therefore, if this system is required to supply a certain load with a continuous current, an output filter will be necessary. For that purpose, in this section , an LC filter will be connected at the output port of the two cascaded LFRs.

Fig. 4.9 shows the schematic diagram of the two cascaded LFRs with an LC

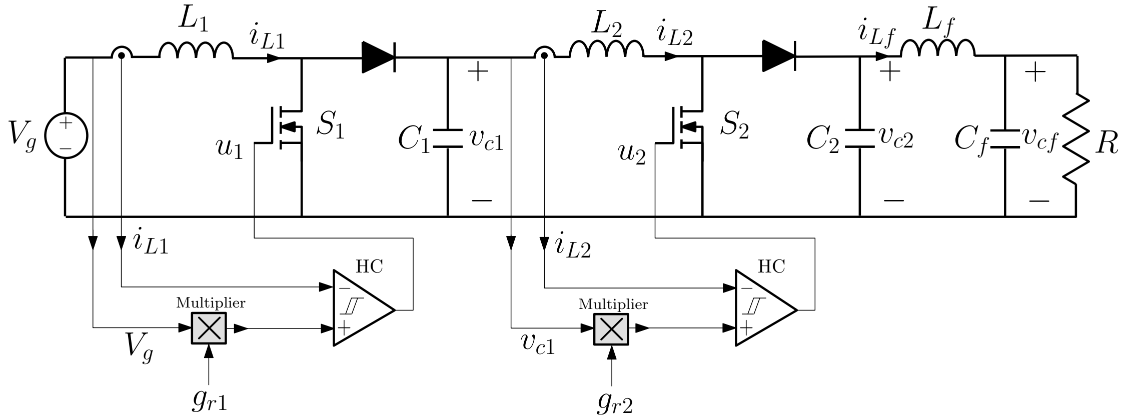

Figure 4.9: Schematic diagram of two cascaded LFRs with an LC filter by using SMC.

filter. The system can be represented by the following set of equations

$$\frac{\mathrm{d}i_{L1}}{\mathrm{d}t} = \frac{V_g}{L_1} - \frac{v_{c1}}{L_1}(1-u_1) \tag{4.25}$$

$$\frac{\mathrm{d}i_{L2}}{\mathrm{d}t} = \frac{v_{c1}}{L_2} - \frac{v_{c2}}{L_2}(1-u_2) \tag{4.26}$$

$$\frac{\mathrm{d}i_{Lf}}{\mathrm{d}t} = \frac{v_{c2}}{L_f} - \frac{v_{cf}}{L_f} \tag{4.27}$$

$$\frac{\mathrm{d}v_{c1}}{\mathrm{d}t} = \frac{i_{L1}}{C_1}(1-u_1) - \frac{i_{L2}}{C_1} \tag{4.28}$$

$$\frac{\mathrm{d}v_{c2}}{\mathrm{d}t} = \frac{i_{L2}}{C_2}(1-u_2) - \frac{i_{Lf}}{C_2} \tag{4.29}$$

$$\frac{\mathrm{d}v_{cf}}{\mathrm{d}t} = \frac{i_{Lf}}{C_f} - \frac{v_{cf}}{RC_f} \tag{4.30}$$

The same switching functions of Eq. (4.12), (4.13) will be used for imposing SMC.

Following the same previous analysis, the equivalent control variables of the system $u_{eq1}(\mathbf{x})$ and $u_{eq2}(\mathbf{x})$ can be expressed by the same equations of the two cascaded LFRs (Eqs. (4.14), (4.15)). This means that the existence conditions are also similar to the conditions of the previous system (Eq. (4.22)).

The equilibrium point corresponding to the system is given by

$$\begin{aligned}\mathbf{x}^* &= [I_{L1}, I_{L2}, I_{Lf}, V_{c1}, V_{c2}, V_{cf}]^\top \\ &= \left[g_{r1}V_g, V_g\sqrt{g_{r1}g_{r2}}, V_g\sqrt{\frac{g_{r1}}{R}}, V_g\sqrt{\frac{g_{r1}}{g_{r2}}}, V_g\sqrt{Rg_{r1}}, V_g\sqrt{Rg_{r1}}\right]^\top\end{aligned} \tag{4.31}$$

It can be noted that the corresponding steady-state values $I_{L1}, I_{L2}, V_{c1}, V_{c2}$ are the same for the two cascaded LFRs given in (4.31).

The characteristic polynomial equation can be expressed as follows

$$(s+\frac{2g_{r2}}{C_1})(s^3R^2L_fC_2C_f+s^2RL_fC+s(L_f+R^2C)+2R) \tag{4.32}$$

where $C = C_2 + C_f$. By applying the Routh-Hurwitz criterion, it can be found that the system is unconditionally stable.

4.4 LFR Based on Cascaded Boost Converters Using a Single Sliding Surface

In this section, one LFR is synthesized based on two cascaded boost converters using a single sliding surface by sensing the input voltage and input current for the first converter. The power stage of the system is similar to the described previously. Figure (4.10) shows the schematic diagram of the two cascaded connection using a single LFR based on SMC. The two cascaded converters will be driven with the same control signal.

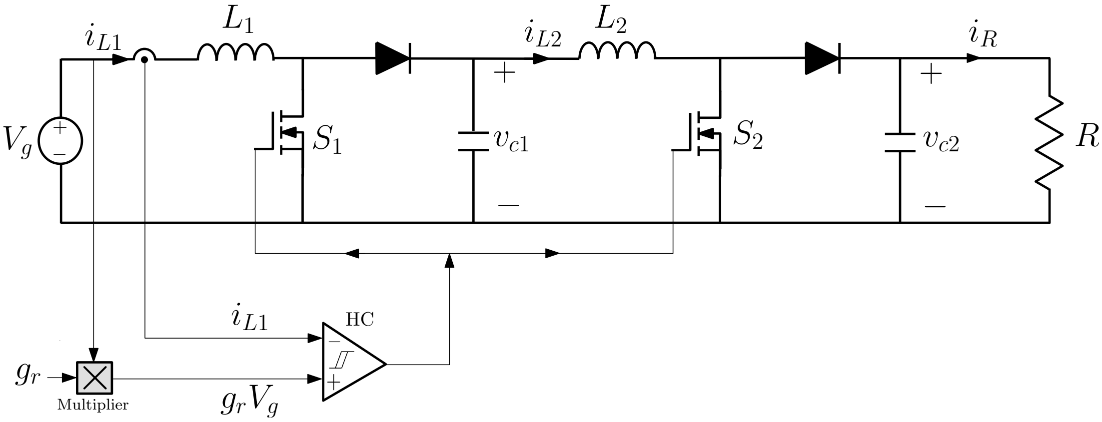

Figure 4.10: Schematic diagram of an LFR based on two cascaded boost converters using one sliding surface.

The switching surface can be selected as $s(\mathbf{x}) = i_{L1} - g_rV_g$. By imposing the invariance conditions $s(\mathbf{x}) = 0$ and $\dot{s}(\mathbf{x}) = 0$ in the last equations, we obtain

$$s(\mathbf{x}) \; = \; i_{L1} - g_rV_g = 0 \tag{4.33}$$

$$\dot{s}(\mathbf{x}) \; = \; g_r\frac{\mathrm{d}i_{L1}}{\mathrm{d}t} = 0 \tag{4.34}$$

4.4.1 Full-order switched model and equivalent control

The two cascaded boost converters can be represented by the same differential equations of the two cascaded LFRs (4.8), (4.11), by using $u_1 = u_2 = u$, where u is the discontinuous control variable for the two stages.

Following the same procedure used for the DC-transformer and gyrator, the equivalent control variable $u_{eq}(\mathbf{x})$ can be obtained. Its expression is given by

$$u_{eq}(\mathbf{x}) = 1 - \frac{V_g}{v_{c1}} \tag{4.35}$$

As mentioned before, this variable must be bounded by the minimum and maximum values of u, i.e.

$$0 \ < \ u_{eq}(\mathbf{x}) \ < \ 1. \tag{4.36}$$

These constraints on the equivalent control variable allow us to obtain the range of parameter values for which sliding-mode motion exists. From (4.35)-(4.36) one has

$$V_g \ < \ v_{c1} \tag{4.37}$$

which implies that sliding-mode regime will exist only when v_{c1} reaches it minimum value V_g.

4.4.2 Ideal sliding dynamics and sliding-mode conditions

Constrained on the sliding manifold, the motion of the system is described by the following ideal reduced order sliding-mode dynamics model

$$\frac{\mathrm{d}i_{L2}}{dt} = \frac{v_{c1}}{L_2} - \frac{V_g v_{c2}}{v_{c1} L_2} \tag{4.38}$$

$$\frac{\mathrm{d}v_{c1}}{dt} = \frac{g_r V_g^2}{v_{c1} C_1} - \frac{i_{L2}}{C_1} \tag{4.39}$$

$$\frac{\mathrm{d}v_{c2}}{dt} = \frac{V_g i_{L2}}{v_{c1} C_2} - \frac{v_{c2}}{R C_2} \tag{4.40}$$

The coordinates of the equilibrium point are given by

$$\mathbf{x}^* = [I_{L1}, I_{L2}, V_{c1}, V_{c2}]^\top = \left[g_r V_g, \frac{g_r V_g}{(R g_r)^{\frac{1}{4}}}, V_g (R g_r)^{\frac{1}{4}}, V_g \sqrt{R g_r} \right]^\top \tag{4.41}$$

Note that the steady state values for all the state variables are depending on the input voltage V_g and the resistive load R.

The equivalent control variable at the equilibrium point can be obtained in the following equations

$$U_{eq} = 1 - \frac{1}{(Rg_r)^{\frac{1}{4}}}. \tag{4.42}$$

U_{eq} must be bounded between 0 and 1 and therefore, the following condition must be fulfilled:

$$Rg_r > 1. \tag{4.43}$$

This condition is less restrictive than the condition of the two cascaded g-gyrators.

4.4.3 Stability analysis of the ideal sliding-mode dynamic model

The stability of the linearized system can be studied using the Jacobian matrix $\mathbf{J}$ corresponding to (4.38)-(4.40) and evaluating it at the equilibrium point $\mathbf{x}^*$. This matrix can be expressed as follows

$$\mathbf{J} = \begin{pmatrix} 0 & \frac{2}{L_2} & -\frac{1}{(Rg_r)^{\frac{1}{4}}L_2} \\ -\frac{1}{C_1} & -\frac{g_r}{\sqrt{Rg_r}C_1} & 0 \\ \frac{1}{(Rg_r)^{\frac{1}{4}}C_2} & -\frac{g_r}{(Rg_r)^{\frac{3}{4}}C_2} & -\frac{1}{RC_2} \end{pmatrix} \tag{4.44}$$

The characteristic polynomial can be represented as follows

$$s^3 + \frac{C_1 + \sqrt{Rg_r}C_2}{RC_1C_2}s^2 + \frac{2RC_2\sqrt{Rg_r} + RC_1 + L_2g_r}{RC_1C_2L_2\sqrt{Rg_r}}s + \frac{4}{RC_1C_2L_2} \tag{4.45}$$

By applying Routh-Hurwitz criterion for this equation, the stability condition can be written in the following form.

$$2R^2C_2^2g_r + RC_1^2 + L_2g_rC_1 + L_2g_rC_2\sqrt{Rg_r} > RC_1C_2\sqrt{Rg_r} \tag{4.46}$$

Table 4.2: The used parameter values for the LFR based on cascaded converters using a single sliding surface.

L_1	L_2	$C_1 = C_2$	R	h	f_s
200 μH	2 mH	10 μF	2500 Ω	0.27 A	100 kHz

4.4.4 Numerical simulations and experimental results

A single LFR based on two cascaded boost converters has been simulated using PSIM to validate the previous analysis. Table 4.2 shows the parameter values used in numerical simulations. Moreover, the system is implemented in the laboratory and supplied from a DC voltage source of 15 V and loaded with a resistive load (for more details about the prototypes, see Appendix A). The parasitic elements have been included in the PSIM simulation. These are the internal resistance of the inductors (r_{L1}=60 mΩ and r_{L2}=130 mΩ), the ON resistance of the MOSFETs (r_{on1}=60 mΩ and r_{on2}=165 mΩ) and the equivalent series resistances (ESR) of the capacitors $r_{c1} = r_{c2} = 0.1$ Ω.

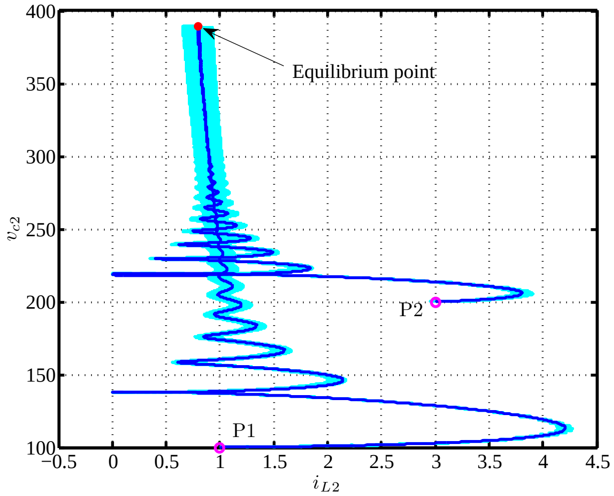

Figure 4.11: Trajectories obtained from the reduced-order ideal sliding-mode dynamics model and from the full-order switched model using PSIM starting from different initial conditions in the state plane (i_{L2}, v_{c2}).

Firstly, the validity of ideal sliding dynamic model is checked by numerical simulation from the full-order model in different regions of the state space. As depicted in Fig. 4.11, two different initial conditions P1, P2 are considered and the system is simulated using the two different models. It can be observed from

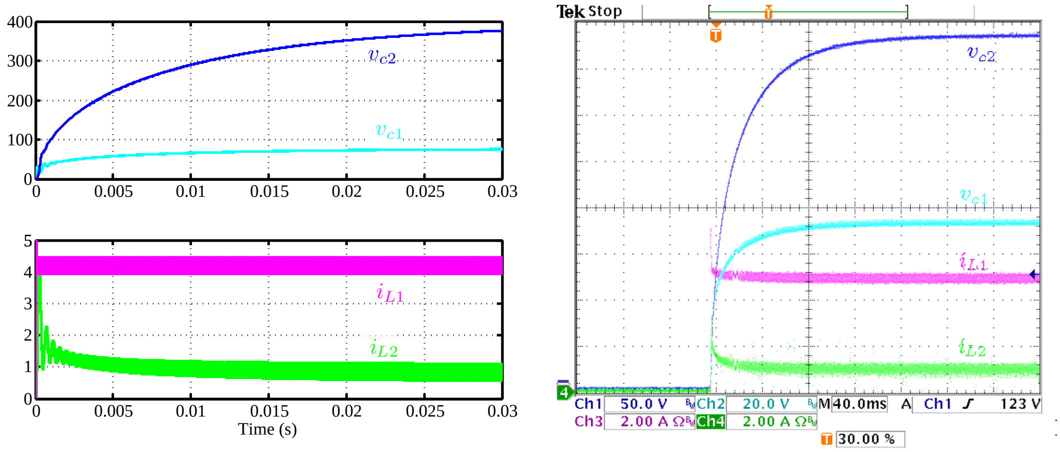

(a) (b)

Figure 4.12: Simulated and experimental waveforms of the capacitor voltages v_{c2}, v_{c1} and the inductor currents i_{L1}, i_{L2} (respectively from up to down) for an LFR based on two cascaded boost converters for $g_r = 0.27$ S during start-up.

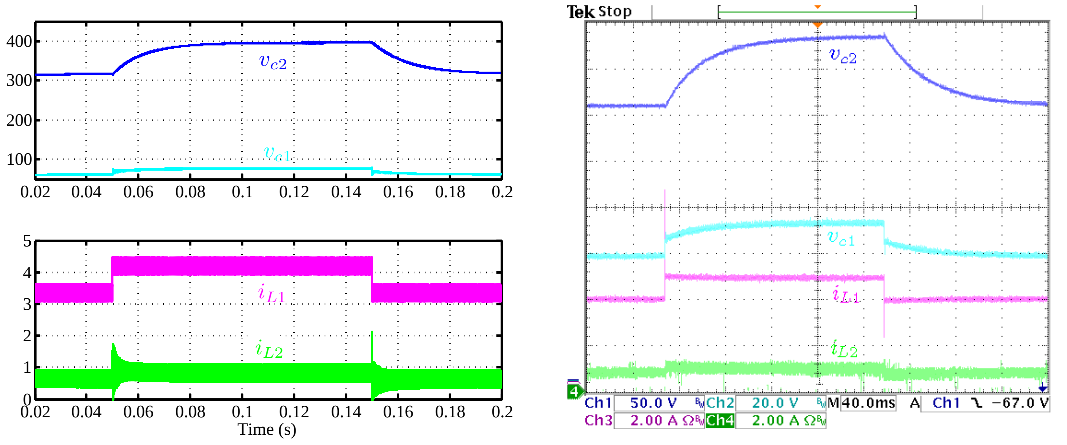

(a) (b)

Figure 4.13: Simulated and experimental waveforms of the capacitor voltages v_{c2}, v_{c1} and the inductor currents i_{L1}, i_{L2} (respectively from up to down) for an LFR based two cascaded boost converters for $g_r = 0.27$ S and input voltage change from 12 V to 15 V.

this figure that the reduced order model trajectories converge to the equilibrium point. Moreover, the corresponding trajectories are in perfect agreement with the full-order simulations obtained with the switched model.

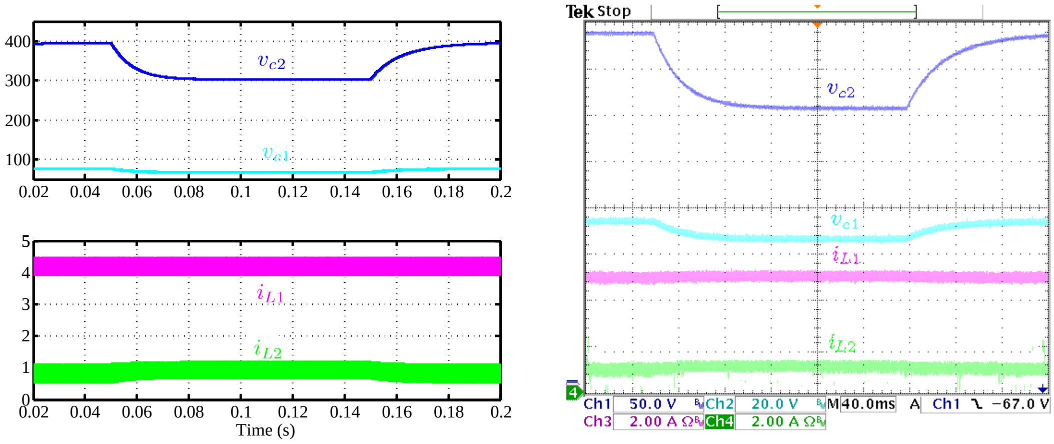

(a) (b)

Figure 4.14: Simulated and experimental waveforms of the capacitor voltages v_{c2}, v_{c1} and the inductor currents i_{L1}, i_{L2} (respectively from up to down) for an LFR based on two cascaded boost converters under load change from 2500 Ω to 1500 Ω.

Secondly, Fig. 4.12 shows the simulated and experimental waveforms during the transient start-up of the system from zero initial conditions. Note that after a transient time of 30 ms, the state variables reach their steady-state values which are in agreement with the steady-state predictions given in Eq. (4.41).

Fig. 4.13 shows the simulated and experimental waveforms corresponding to the input voltage variations effect on the response of the system. When the input voltage increases from 12 V to 15 V, the output capacitor voltages and the inductor currents increase. When the load changes from 2500 Ω to 1500 Ω, the inductor currents remain constant and the capacitor voltages v_{c1} and v_{c2} decrease as depicted in Fig. 4.14. Note that the input power is constant when the load resistance decreases. All these simulation and experimental results are in perfect agreement with steady-state predictions given in (4.41).

4.5 Synthesis of m cascaded LFRs

In this section, a general procedure for synthesizing m cascaded converters (Fig. 4.15) behaving as LFRs will be explained. Using the switched model of the two cascaded LFRs represented in Eq. (4.8)-(4.11), a generalized switched model of m cascaded LFRs can be represented with the same equation of (1.1) in Chapter 1

$$\dot{\mathbf{x}} = f(\mathbf{x}) + g(\mathbf{x})\mathbf{u} \tag{4.47}$$

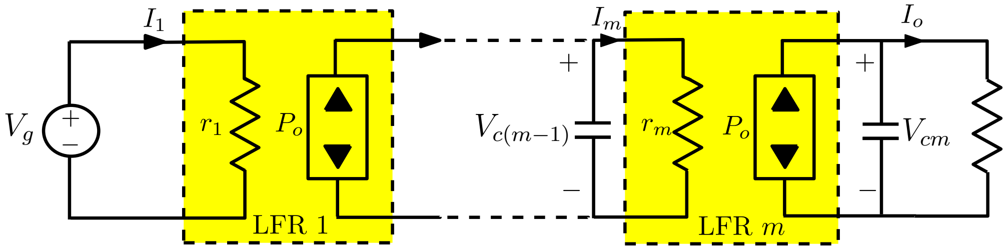

Figure 4.15: Schematic diagram of m cascaded converters working as LFRs.

where, the matrixes $\mathbf{f}$ and $\mathbf{g}$ are not depending on the time as in the general system of Eq. (1.1). While, $\mathbf{x}$ is the vector of state variables and $\mathbf{u}$ is the vector of command signals for the switches, which can be written respectively as follows $\mathbf{x} = [i_{L1}, i_{L2}.....i_{Lm}, v_{c1}, v_{c2}, ..., v_{cm}]^\top$ and $\mathbf{u} = [u_1, u_2, ...u_m]^\top$, where m is the number of the connected converters.

The switching function s_n corresponding to stage n can be described by

$$s_n(\mathbf{x}) = g_{rn}v_{c,n-1} - i_{L,n} := \rho_n - \mathbf{C}_n\mathbf{x}, \;\; n = 1\dots m \tag{4.48}$$

where $\rho_1 = g_{r1}V_g$, $\rho_n = 0 \; \forall n > 1$, $i_{L,n}$ and $v_{c,n}$ are the inductor current and the output voltage of the stage number n respectively and $\mathbf{C}_1 = [1, \;\; 0, \dots \;\; 0, \dots 0]$,... $\mathbf{C}_m = [0, \dots 0, \;\; 1 \;\; 0, \dots 0, \;\; -g_m, \;\; 0]$. The switching functions can be grouped as follows

$$\mathbf{s}(\mathbf{x}) = \mathbf{r} - \mathbf{C}\mathbf{x} \tag{4.49}$$

where $\mathbf{r}$ is a suitable reference vector whose first element is g_1V_g and all other elements are zero, $\mathbf{C}$ is a matrix whose entries are dependent on the proportionality factors g_n of the LFR and $\mathbf{s} = [s_1, \; s_2, \dots s_m]^\top$. The time derivative of the switching function vector, $\mathbf{s}(\mathbf{x})$ is $\dot{\mathbf{s}}(\mathbf{x}) = -\mathbf{C}\dot{\mathbf{x}}$ which after substituting it in (4.47), one obtains

$$\frac{\mathrm{d}\mathbf{s}}{\mathrm{d}t} = -\mathbf{C}(f(\mathbf{x}) + g(\mathbf{x})\mathbf{u}) \tag{4.50}$$

According to the equivalent control method which has been explained previously in Chapter 1, the expression of the equivalent control can be derived as

$$\mathbf{u}_{eq} = -(\mathbf{C}g(\mathbf{x}))^{-1}\mathbf{C}f(\mathbf{x}) \tag{4.51}$$

Using the reduced order model and the equivalent control, the equilibrium point can be expressed as

$$\begin{aligned} \mathbf{x}^* &= [I_{L1}, I_{L2}....I_{Lm}, V_{c1}, V_{c2}....., V_{c(m-1)}, V_{cm}]^\top \\ &= \left[g_{r1}V_g, V_g\sqrt{g_{r1}g_{r2}}...V_g\sqrt{g_{r(m-1)}g_{rm}}, V_g\sqrt{\frac{g_{r1}}{g_{r2}}}, V_g\sqrt{\frac{g_{r1}}{g_{r3}}}..., V_g\sqrt{\frac{g_{r1}}{g_{rm}}}, V_g\sqrt{Rg_{r1}}\right]^\top \end{aligned} \tag{4.52}$$

A necessary condition for the existence of sliding mode on the manifold $\{\mathbf{x}|s_n(\mathbf{x}) = 0\}$ is that all the elements of the equivalent control vector must be bounded between 0 and 1. By applying theses constraints, the following inequalities for the conductances g_{r1}, g_{r2}... and g_{rm} should be achieved

$$g_{r1} > g_{r2} > g_{r3}.... > g_{rm} \tag{4.53}$$

The ideal sliding dynamics can be linearized and its stability can be studied using standard techniques. The Jacobian matrix can be expressed as follows

$$\mathbf{J} = \begin{pmatrix} -\frac{2g_{r2}}{C_1} & 0 & 0 & .... & 0 \\ 2\sqrt{g_{r2}g_{r3}}\frac{C_1 + L_2 g_{r2}^2}{C_1C_2} & -\frac{2g_{r3}}{C_2} & 0 & ... & 0 \\ \vdots & \vdots & \ddots & \ddots & \vdots \\ * & * & \cdots & -\frac{2g_{rm}}{C_{m-1}} & 0 \\ * & * & \cdots & 2\sqrt{\frac{g_{r(m-1)}}{R}}\frac{C_{m-1} + L_m g_{rm}^2}{C_{m-1}C_m} & -\frac{2}{RC_m} \end{pmatrix} \tag{4.54}$$

It can be observed that the the matrix $\mathbf{J}$ is a lower triangular matrix Axler (1997). Thus, the characteristic polynomial of the linearized system, $p_J(s) = \det(\mathbf{J} - s\mathbf{I})$, depends only on the diagonal of the matrix, irrespective of the lower diagonal terms marked with an asterisk $*$ in (4.54). The characteristic polynomial equation can be expressed as follows

$$(s + \frac{2g_{r2}}{C_1})(s + \frac{2g_{r3}}{C_2})...(s + \frac{2g_{rm}}{C_{m-1}})(s + \frac{2}{RC_m}) = 0 \tag{4.55}$$

It can be observed that all the roots are located in the left half plane and hence, the system is unconditionally stable.

4.6 Conclusion

In this chapter, the LFR concept has been used to design a DC-DC power stage with a high conversion ratio. First, the cascade connection of two LFRs based on the boost converter has been analyzed in detail theoretically, by numerical simulations and experimentally. The system is unconditionally stable and the conditions for sliding motions have been obtained. The steady state value of the intermediate voltage V_{c1} is not sensitive to the load unlike the output voltage

V_{c2} which depends on the load resistance. Furthermore, an LC filter has been connected at the output of the system without any effect on the stability.

In addition, an LFR has been synthesized based on two cascaded boost converters using a single sliding surface. This structure has the advantage of reducing the number of components which in turn decreases the cost and increases the efficiency. The analysis has verified that the system is stable with a certain condition and the sliding conditions have been obtained. The equilibrium point of this system is depending on the resistive load. It has been noticed that the transient time of the two cascaded LFRs is less than the transient time for the LFR based on two cascaded converters system. Moreover, the two systems have been tested under input voltage and load variation. As shown in this chapter, the two systems can be used to solve the problem of achieving a high voltage conversion ratio of 25. However, the two cascaded LFRs system is better than the LFR based on two cascaded boost converters in terms of the dynamic performance and the stability. Moreover, it has been demonstrated that the cascade connection of m LFR based on the boost converter is stable irrespective of the number of cascaded elements.

Chapter 5

Cascade Connection of LFR and Gyrator

The three types of canonical elements for power processing, namely DC-transformer, DC gyrator and LFR, have been employed for the design of a power stage with a high conversion ratio in the previous chapters. The cascade connection of similar canonical elements was carried out using two sliding surfaces. In this chapter, in turn, the cascade connection of different canonical elements such as a LFR and a gyrator and vice versa will be analyzed. However the DC-transformer has been excluded from this study because its stability problems and disability to increase the conversion ratio to 25 as it had been shown in chapter 2. Therefore, the two possible cascade connections of a LFR and a power gyrator will be analyzed, i.e., a LFR supplying a gyrator and viceversa. Each connection will be analyzed theoretically and using numerical simulations which in turn will be also verified experimentally.

5.1 Cascaded LFR with G-gyrator

The ideal schematic diagram of the cascaded LFR-gyrator are depicted in Fig. 5.1(a). The equivalent model of the cascaded ideal LFR-gyrator is a DC-transformer or an LFR as depicted in Fig. 5.1(b) and 5.1(c), respectively. The practical implantation for the cascaded LFR-gyrator has been shown in Fig. 5.2.

Fig. 5.2 depicts the circuit diagram corresponding to a cascade connection LFR-gyrator under SMC. In this case, the controller consists of two switching functions, $s_1(\mathbf{x}) = i_{L1} - g_{r1}V_g$ for the first stage converter and $s_2(\mathbf{x}) = i_{L2} - g_2 v_{c2}$ for the second stage converter. In steady-state $s_1(\mathbf{x}) = 0$, *i.e.*, $I_{L1} = g_{r1}V_g$. In turn, the steady-state switching condition imposes that $s_2(\mathbf{x}) = 0$, *i.e.*, $I_{L2} = g_2 V_{c2}$. Finally, combining the steady-state expressions of both LFR-gyrator, the following relationship is obtained

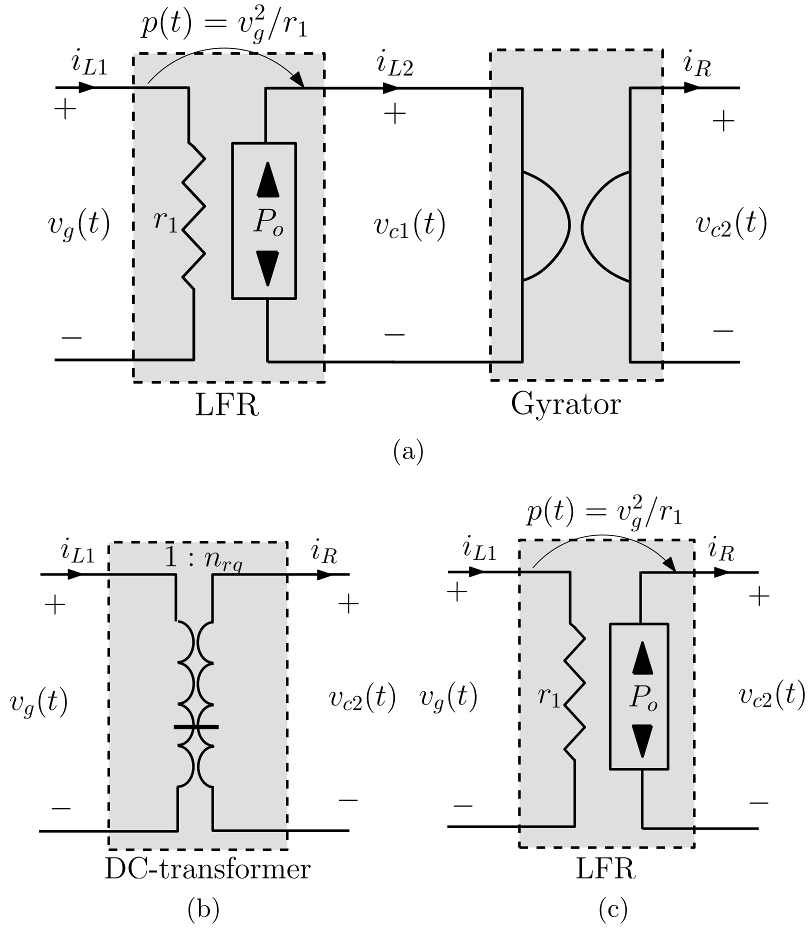

Figure 5.1: (a) The schematic diagram of cascaded ideal LFR-gyrator. (b) The equivalent circuit model of the cascaded ideal LFR-gyrator is a DC-transformer (c) The equivalent circuit model of the cascaded ideal LFR-gyrator is a LFR.

$$V_{c2} = \sqrt{Rg_{r1}}V_g \quad \text{and} \quad I_R = \frac{1}{\sqrt{Rg_{r1}}}I_{L1} \tag{5.1}$$

$$p_o = \frac{V_{c2}^2}{R} = g_{r1}V_g^2 \tag{5.2}$$

where p_o is the output power. Eq. (5.1) corresponds to the definition of a DC-transformer with a transformation ratio $n_{rg} = \sqrt{Rg_{r1}}$. Note, that n_{rg} for this case is equal to the transformation ratio for the two cascaded LFRs case which depends on the load resistance and the conductance of the LFR. Moreover, the output power can be defined in Eq. (5.2) which is the input power for the cascaded converters.

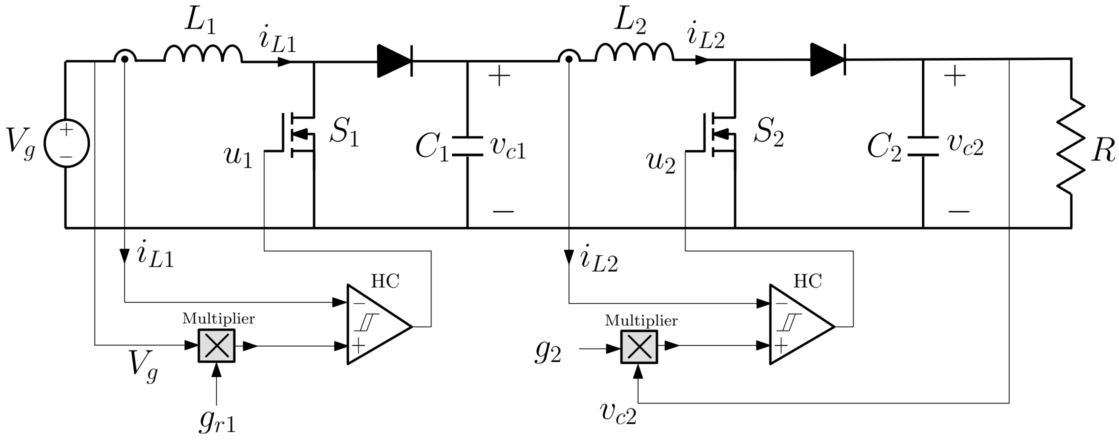

Figure 5.2: Schematic diagram of cascaded LFR and a g-gyrator with controlled input current by imposing SMC.

Therefore, the cascaded LFR-gyrator can be modeled by a DC-transformer or an LFR which are depicted in Figs. 5.1(b) and 5.1(c).

5.1.1 Full-order switched model

Considering that both converters operate in CCM, the cascade connection of the LFR-gyrator of Fig. 5.2 can be represented by the following set of differential equations

$$\frac{\mathrm{d}i_{L1}}{\mathrm{d}t} = \frac{V_g}{L_1} - \frac{v_{c1}}{L_1}(1-u_1) \tag{5.3}$$

$$\frac{\mathrm{d}i_{L2}}{\mathrm{d}t} = \frac{v_{c1}}{L_2} - \frac{v_{c2}}{L_2}(1-u_2) \tag{5.4}$$

$$\frac{\mathrm{d}v_{c1}}{\mathrm{d}t} = \frac{i_{L1}}{C_1}(1-u_1) - \frac{i_{L2}}{C_1} \tag{5.5}$$

$$\frac{\mathrm{d}v_{c2}}{\mathrm{d}t} = \frac{i_{L2}}{C_2}(1-u_2) - \frac{v_{c2}}{RC_2}. \tag{5.6}$$

where u_1 and u_2 are the discontinuous control variables for the first and second stage respectively as defined previously in Chapter 4.

5.1.2 Equivalent control

The dynamical behavior of i_{L1}, i_{L2} and v_{c2} is constrained by the following set of differential equations

$$\dot{s}_1(\mathbf{x}) = \frac{\mathrm{d}i_{L1}}{\mathrm{d}t} = 0 \tag{5.7}$$

$$\dot{s}_2(\mathbf{x}) = \frac{\mathrm{d}i_{L2}}{\mathrm{d}t} - g_2\frac{\mathrm{d}v_{c2}}{\mathrm{d}t} = 0 \tag{5.8}$$

Following the same procedure, the equivalent control variables $u_{eq1}(\mathbf{x})$ and $u_{eq2}(\mathbf{x})$ can be obtained. Their expressions are given by

$$u_{eq1}(\mathbf{x}) = 1 - \frac{V_g}{v_{c1}} \tag{5.9}$$

$$u_{eq2}(\mathbf{x}) = 1 - \frac{C_2 v_{c1} + L_2 g_2^2 v_{c2}}{v_{c2} C_{m2}} \tag{5.10}$$

where $C_{m2} = g_2^2 L_2 + C_2$. From these expressions, the existence conditions of sliding regimes can be obtained. As mentioned before, the limits of $u_{eq1}(\mathbf{x})$ and $u_{eq2}(\mathbf{x})$ are 0 and 1. In this case, the sliding-mode regime will exist provided that

$$v_{cr1} < v_{c1} < v_{cr2} \tag{5.11}$$

where the critical values v_{cr1} and v_{cr2} are given by

$$v_{cr1} = \frac{v_{c2}(RC_{m2} - L_2 g_2)}{RC_2} \tag{5.12}$$

$$v_{cr2} = \frac{L_2 g_2 v_{c2}}{RC_2}. \tag{5.13}$$

5.1.3 Ideal sliding dynamics and sliding-mode conditions

The motion of the system can be described by the following reduced-order ideal sliding-mode dynamics model

$$\frac{\mathrm{d}v_{c1}}{\mathrm{d}t} = \frac{g_{r1} V_g^2}{C_1 v_{c1}} - \frac{g_2 v_{c2}}{C_1} \tag{5.14}$$

$$\frac{\mathrm{d}v_{c2}}{\mathrm{d}t} = \frac{R v_{c1} g_2 - v_{c2}}{RC_{m2}}. \tag{5.15}$$

The coordinates of the equilibrium point are given by

$$\mathbf{x}^* = [I_{L1}, I_{L2}, V_{c1}, V_{c2}]^\top = [g_{r1}V_g, g_2 V_g\sqrt{Rg_{r1}}, \frac{V_g}{g_2}\sqrt{\frac{g_{r1}}{R}}, V_g\sqrt{Rg_{r1}}]^\top. \tag{5.16}$$

As in the previous cases, the steady-state variables have been obtained taking into account that in steady-state one has $s_1(\mathbf{x}^*) = s_2(\mathbf{x}^*) = 0$, thus obtaining $I_{L1} = g_{r1}V_g$ and $I_{L2} = g_2V_{c2}$. Note that the voltage V_{c1} depends on the conductance of the LFR g_{r1} and the conductance of the gyrator g_2. In turn, the voltage V_{c2} depends on the conductance of the LFR g_{r1}. It can be noticed that, in certain application of this structure, the voltage V_{c2} can be controlled using the conductance g_{r1} of the LFR and the voltage V_{c1} can be controlled using the conductance g_2 of the g-gyrator. Moreover, both steady-state values of the voltages V_{c1} and V_{c2} depend on the load resistance which can be considered as a disadvantage for this system.

The equivalent control variables at the equilibrium point can be expressed as follows

$$U_{eq1} = 1 - g_2\sqrt{\frac{R}{g_{r1}}} \quad \text{and} \quad U_{eq2} = 1 - \frac{1}{g_2R}. \tag{5.17}$$

Since U_{eq1} and U_{eq2} must be bounded between 0 and 1, the following condition must be fulfilled

$$\frac{1}{g_2} < R < \frac{g_{r1}}{g_2^2}. \tag{5.18}$$

It can be observed that load resistance is bounded between two certain values which limit the sliding region. Therefore, the sliding motion can be lost when the load changes and this is similar to the condition of the two cascaded g-gyrators (considering g_{r1} of the first LFR of this system replaced with g_1 for the first gyrator of the two cascaded gyrators system).

5.1.4 Stability analysis of the ideal sliding-mode dynamics model

The Jacobian matrix of the system can be expressed as follows

$$\mathbf{J} = \begin{pmatrix} \dfrac{Rg_2^2}{C_1} & -\dfrac{g_2}{C_1} \\ \\ \dfrac{g_2}{C_{m2}} & -\dfrac{1}{RC_{m2}} \end{pmatrix}. \tag{5.19}$$

Using the Jacobian matrix, the characteristic polynomial equation is given by the following expression

$$s^2 + \frac{Rg_2^2(C_1 + C_{m2})}{C_1C_{m2}}s + \frac{2g_2^2}{C_1C_{m2}} = 0 \tag{5.20}$$

which has two complex conjugates poles in the left half plane and hence, the system is unconditionally stable.

Table 5.1: The used parameter values for the cascaded LFR-gyrator.

L_1	L_2	$C_1 = C_2$	R	h_1	h_2	f_s
200 μH	2 mH	10 μF	2500 Ω	0.27 A	0.15 A	100 kHz

5.1.5 Numerical simulations and experimental results

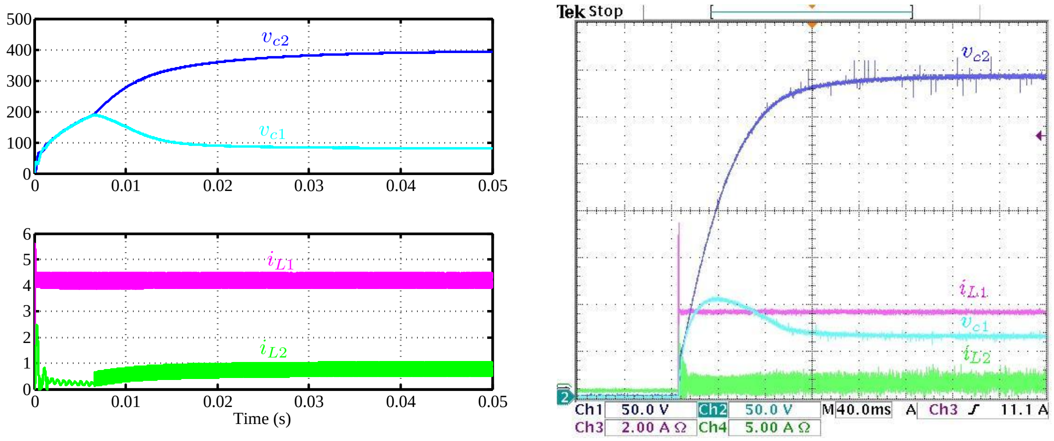

(a) (b)

Figure 5.3: Experimental and simulated waveforms of the capacitor voltages v_{c2}, v_{c1} and the inductor currents i_{L1}, i_{L2} (respectively from up to down) of the cascaded LFR-gyrator during start-up.

The cascaded LFR-gyrator has been simulated using PSIM simulation. The selected conductances are $g_{r1} = 0.27$ S for the LFR and $g_2 = 0.002$ S for the g-gyrator. As in the previous cases, these values have been chosen to achieve an input power $P_{in} = 60$ W, an intermediate voltage $V_{c1} = 80$ V, an output voltage $V_{c2} = 380$ V and a nominal switching frequency 100 kHz which can be adjusted using h_1 and h_2. Table 5.1 shows the rest of parameters of the circuit and their values used in the numerical simulations. The parasitic elements have been included in the PSIM simulation. These are the internal resistance of the inductors (r_{L1}=60 mΩ and r_{L2}=130 mΩ), the ON resistance of the MOSFETs (r_{on1}=60 mΩ and r_{on2}=165 mΩ) and the equivalent series resistances (ESR) of the capacitors $r_{c1} = r_{c2} = 0.1$ Ω. Moreover, cascaded LFR-gyrator have been implemented and supplied from a DC voltage source of 15 V and loaded with a resistive load (for more details about the prototypes, see Appendix A).

Fig. 5.3 shows the simulated and experimental waveforms during the start-up

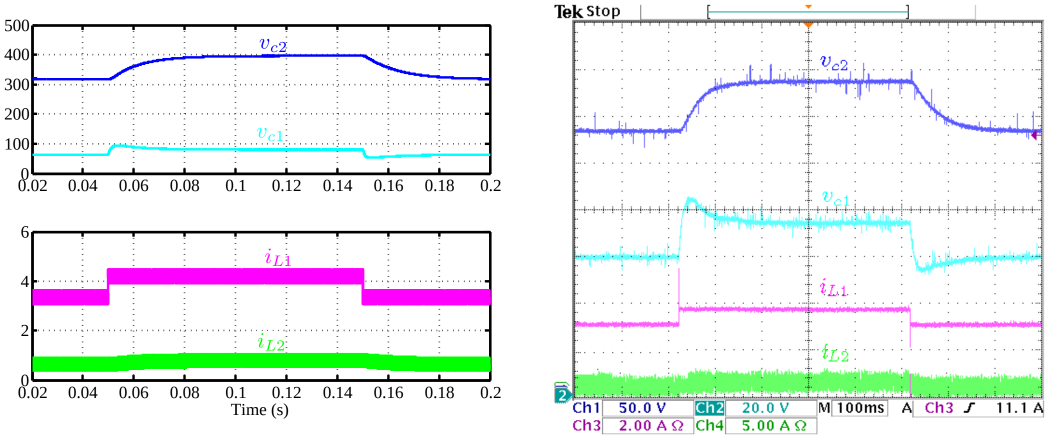

(a) (b)

Figure 5.4: Experimental and simulated waveforms of the capacitor voltages v_{c2}, v_{c1} and the inductor currents i_{L1}, i_{L2} (respectively from up to down) for $g_{r1} = 0.27$ S and $g_2 = 0.002$ S under input voltage step change from 12 V to 15 V.

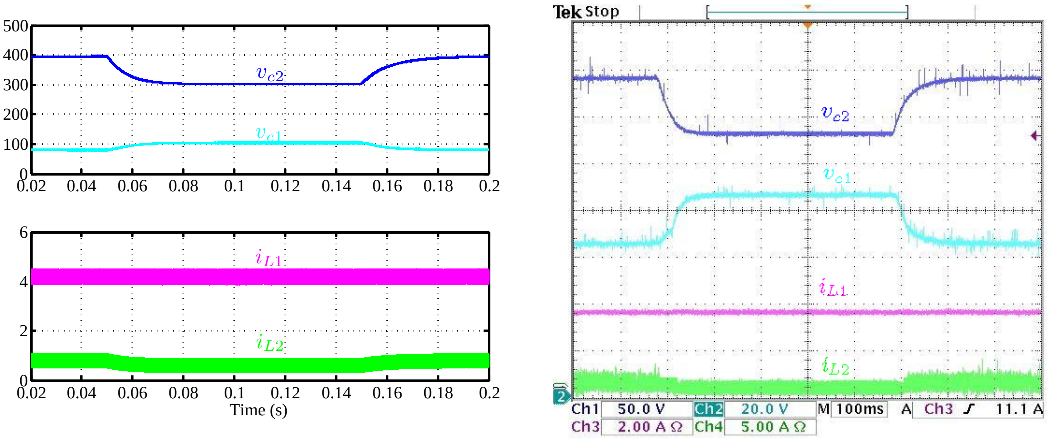

(a) (b)

Figure 5.5: Experimental and simulated waveforms of the capacitor voltages v_{c2}, v_{c1} and the inductor currents i_{L1}, i_{L2} (respectively from up to down) for $g_{r1} = 0.27$ S and $g_2 = 0.002$ S under load step change from 2500 Ω to 1500 Ω.

of the system from zero initial conditions of the circuit of Fig. 5.2. Note that after a long transient response of 20 ms, the state variables reach their steady-state values which are given in Eq. (5.16). Moreover, the g-gyrator takes about 10 ms for reaching the sliding surface as shown in the output capacitor voltages v_{c2} and the inductor currents i_{L2}.

Fig. 5.4 shows the simulated and experimental waveforms corresponding to the input voltage variation. When the input voltage increases from 12 to 15 V, the output capacitor voltages and the inductor currents increase. Fig. 5.5 show, in turn, the simulated and experimental waveforms during the load variation. When the load changes from (2500 Ω to 1500 Ω), the inductor current i_{L1} is constant as deduced from the equilibrium point. On the other hand, the capacitor voltage v_{c2} and inductor current i_{L2} decrease. However, the capacitor voltage v_{c1} increases which are in a good agreement to the equilibrium point given in (5.16). It should be highlighted that, when the load changes, the input power does not change because this system can be modeled with an LFR, however, the operating point of the system will be changed.

5.2 Cascaded G-gyrator with LFR

Conversely, Fig. 5.6(a) depicts the ideal circuit diagram for the cascaded gyrator-LFR. The equivalent diagram of the ideal cascaded gyrator-LFR is shown in Fig. 5.6(b) as it will be derived in this section. While, Fig. 5.7 depicts the circuit diagram corresponding to a cascade connection of gyrator-LFR under SMC.

The controller of this system consists of two switching functions $s_1(\mathbf{x}) = i_{L1} - g_1 v_{c1}$ for the first stage converter and $s_2(\mathbf{x}) = i_{L2} - g_{r2} v_{c1}$ for the second stage converter. In steady-state $s_1(\mathbf{x}) = 0$, *i.e.*, $I_{L1} = g_1 V_{c1}$. In turn, the steady-state switching condition imposes that $s_2(\mathbf{x}) = 0$, *i.e.*, $I_{L2} = g_{r2} V_{c1}$. Finally, combining the steady-state expressions of both gyrator-LFR, the following relationship is obtained

$$V_{c2} = g_1 V_g \sqrt{\frac{R}{g_{r2}}} \quad \text{and} \quad I_R = \frac{1}{g_1}\sqrt{\frac{g_{r2}}{R}} I_{L1}. \tag{5.21}$$

Eq. (5.21) corresponds to the definition of a DC-transformer with a transformation ratio $n_{gr} = g_1 \sqrt{\frac{R}{g_{r2}}}$. Note that n_{gr} depends on the load resistance and the conductances of the gyrator g_1 and the LFR g_{r2}. Therefore, the cascaded gyrator-LFR can be modeled by a DC transformer with a conversion ratio n_{gr}.

5.2.1 Full-order switched model and equivalent control

By applying standard KVLs and KCLs to the circuit depicted in Fig. 5.7. The two cascaded boost converters can be represented also by Eqs. (5.3)-(5.6) corresponding to the system depicted in Fig. 5.7.

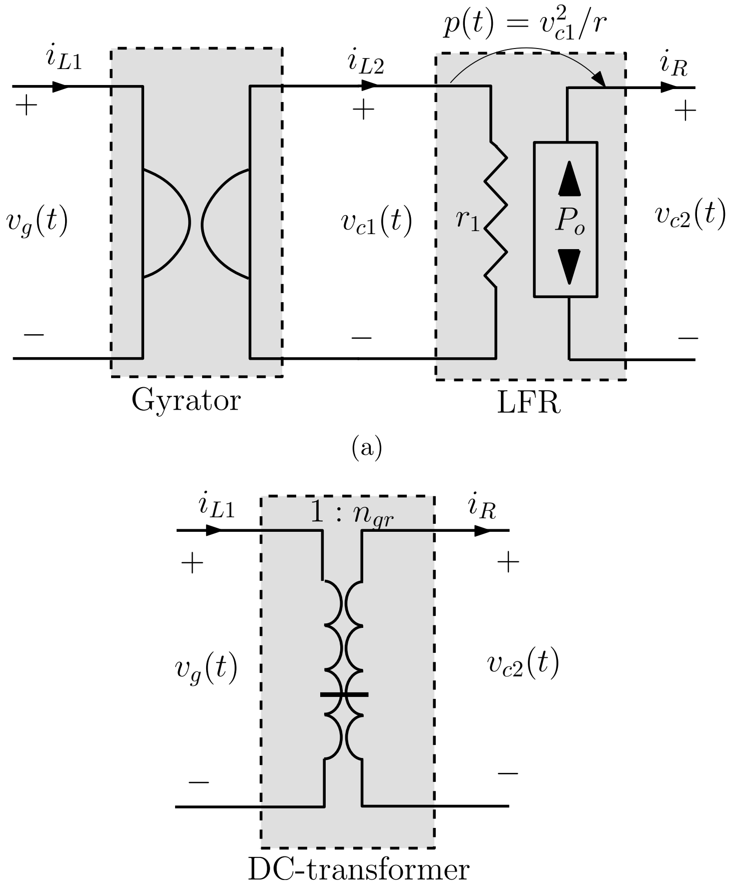

(a)

(b)

Figure 5.6: (a) The schematic diagram of two cascaded ideal gyrator-LFR. (b) The equivalent circuit model of the two cascaded ideal gyrator-LFR is a DC-transformer.

Following the same procedure employed in the previous chapters, the equivalent control variables $u_{eq1}(\mathbf{x})$ and $u_{eq2}(\mathbf{x})$ can be obtained. Their expressions are given by

$$u_{eq1}(\mathbf{x}) = 1 - \frac{C_1 V_g + g_1 g_{r2} L_1 v_{c1}}{v_{c1} C_{m1}} \tag{5.22}$$

$$u_{eq2}(\mathbf{x}) = 1 - \frac{C_{m1} v_{c1} + L_2 g_{r2}(g_{r2} v_{c1} - g_1 V_g)}{v_{c2} C_{m1}} \tag{5.23}$$

where $C_{m1} = C_1 + g_1^2 L1$. The sliding-mode regime will exist provided that

$$v_{cr1} < v_{c1} < v_{cr2} \tag{5.24}$$

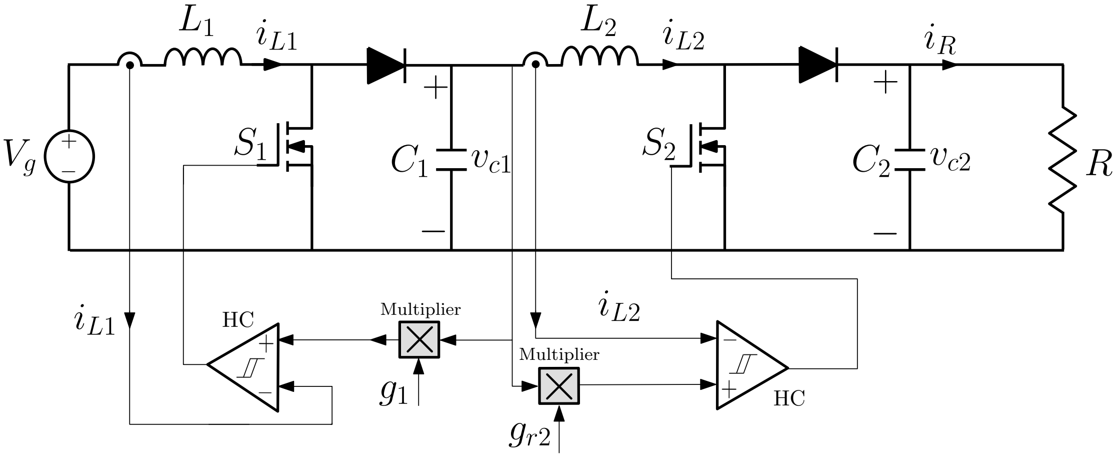

Figure 5.7: Schematic diagram of cascaded gyrator-LFR under SMC.

where the critical values v_{cr1} and v_{cr2} are given by

$$v_{cr1} = \frac{v_{c2}C_{m1} + g_1 g_{r2} L_2 V_g}{C_{m1} + L_2 g_{r2}^2} \tag{5.25}$$

$$v_{cr2} = \frac{g_1 g_{r2} L_2 V_g}{C_{m1} + L_2 g_{r2}^2}. \tag{5.26}$$

5.2.2 Ideal sliding dynamics and sliding-mode conditions

Substituting (5.22)-(5.23) in Eqs. (5.3)-(5.6) and taking into account the switching functions, the following ideal sliding dynamics reduced-order model is obtained

$$\frac{\mathrm{d}v_{c1}}{\mathrm{d}t} = \frac{g_1 V_g}{C_{m1}} - \frac{g_{r2} v_{c1}}{C_{m1}} \tag{5.27}$$

$$\frac{\mathrm{d}v_{c2}}{\mathrm{d}t} = \frac{g_{r2} v_{c1}^2}{C_2 v_{c2}} - \frac{v_{c2}}{RC_2} - \frac{g_{r2}^2 v_{c1} L_2 (g_1 V_g - g_{r2} v_{c1})}{C_2 v_{c2} C_{m1}} \tag{5.28}$$

The equilibrium point of the system can be expressed by

$$\mathbf{x}^* = [I_{L1}, I_{L2}, V_{c1}, V_{c2}]^\top = [\frac{{g_1}^2}{g_{r2}} V_g, g_1 V_g, \frac{g_1}{g_{r2}} V_g, g_1 V_g \sqrt{\frac{R}{g_{r2}}}]^\top \tag{5.29}$$

As in the previous cases, the steady-state variables have been obtained taking into account that in steady-state one has $s_1(\mathbf{x}^*) = s_2(\mathbf{x}^*) = 0$, thus obtaining $I_{L1} = g_1 V_{c1}$ and $I_{L2} = g_{r2} V_{c1}$. Although, the voltage V_{c1} is not depending on the load resistance ,which can be an advantage for this system, it can be noticed that the steady state of the capacitor voltages V_{c1} and V_{c2} are depending on the conductance values g_1 for the g-gyrator and g_{r2} for the LFR. For certain application, this makes difficulties in the control of the steady-state variables. Because, any change of g_1 or g_{r2} changes the equilibrium point of the system. The control laws at the equilibrium point can be expressed by

$$U_{eq1} = 1 - \frac{g_{r2}}{g_1} \tag{5.30}$$

$$U_{eq2} = 1 - \sqrt{\frac{1}{Rg_{r2}}} \tag{5.31}$$

Since U_{eq1} and U_{eq2} must be bounded between 0 and 1, the following condition must be fulfilled

$$g_1 > g_{r2}, \qquad Rg_{r2} > 1 \tag{5.32}$$

As observed, the condition of Eq. (5.32) is similar to the two cascaded LFRs in Eq. (4.22). However, for this case, the load resistance depends on g_{r2} which is the smallest conductance in the system, While, in the two cascaded LFRs, the load resistance depends on g_{r1} which is the largest conductance in the system. This yields that the range of the sliding region of the two cascaded LFRs is wider than the sliding region of the cascaded gyrator-LFR system.

5.2.3 Stability analysis of the ideal sliding-mode dynamic model

The Jacobian matrix of the system can be expressed as follows

$$\mathbf{J} = \begin{pmatrix} -\dfrac{g_{r2}}{C_{m1}} & 0 \\ \dfrac{L_2 g_{r2}^2 + 2C_{m1}}{\sqrt{\dfrac{R}{g_{r2}}} C_2 C_{m1}} & -\dfrac{2}{RC_2} \end{pmatrix} \tag{5.33}$$

Using the Jacobian matrix, the characteristic polynomial can be written in the following form

$$(s + \frac{2}{RC_2})(s + \frac{g_{r2}}{C_{m1}}) \tag{5.34}$$

Its roots $-g_{r2}/C_{m1}$ and $-2/(RC_2)$ are located in the left half plane and hence, the system is unconditionally stable. As observed, that the characteristic polynomial equation is similar to the previously one of the two cascaded LFRs in Eq. (4.24).

Table 5.2: The used parameter values for the cascaded gyrator-LFR.

L_1	L_2	$C_1 = C_2$	R	h_1	h_2	f_s
200 μH	2 mH	10 μF	2500 Ω	0.2 A	0.1 A	100 kHz

5.2.4 Numerical simulations and experimental results

In order to verify the theoretical results, the circuit depicted in Fig. 5.7 has been simulated by using PSIM software with the set of parameter values depicted in Table 5.2 that satisfies the stability conditions for the system. It is worth mentioning also that the parasitic elements have been included in the PSIM simulation similar to the previous cases. These are the internal resistance of the inductors (r_{L1}=60 mΩ and r_{L2}=130 mΩ), the ON resistance of the MOSFETs (r_{on1}=60 mΩ and r_{on2}=165 mΩ) and the equivalent series resistances (ESR) of the capacitors $r_{c1} = r_{c2} = 0.1\ \Omega$. Moreover, cascaded gyrator-LFR has been implemented in the laboratory to validate the simulation results using the set of parameters shown in Table 5.2 (for more details about the prototypes, see Appendix A).

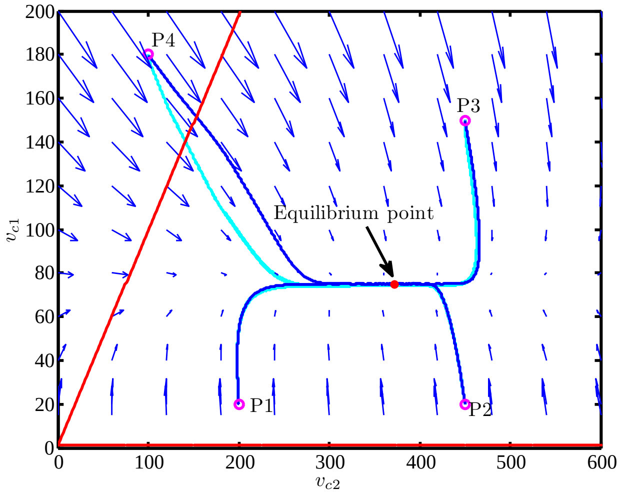

Figure 5.8: Trajectories of two cascaded gyrator-LFR obtained from the ideal sliding dynamics model and from the full-order switched model using PSIM starting from different initial conditions in the plane (v_{c1}, v_{c2}).

Firstly, the validity of ideal sliding dynamic model is checked by numerical simulations from the full-order model in different regions of the state space. As depicted in Fig. 5.8, different initial conditions P1-P4 are considered and the system is simulated using the two different models. The sliding-mode boundaries given by $v_{c1} > v_{cr1}$ and $v_{c1} < v_{cr2}$ established in (5.24) are also plotted in the same figure. It can be observed from this figure that the system trajectories converge to the equilibrium point in all cases. Moreover, for the points P1-P3, the corresponding trajectories are in perfect agreement with the full-order simulations obtained with the switched model. Concerning the point P4, the mismatching between the trajectories from the ideal sliding dynamics model and the full-order model is mainly due to the fact that this point is outside the sliding-mode domain.

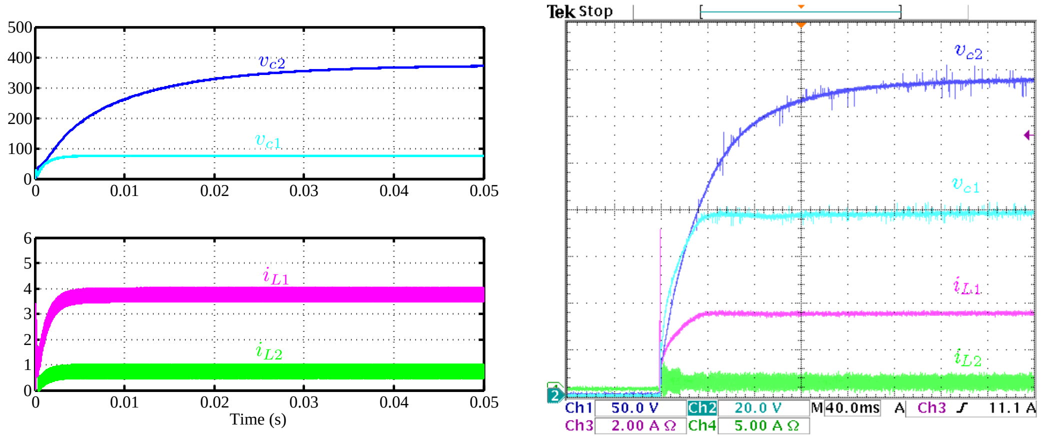

(a) (b)

Figure 5.9: Simulated and experimental waveforms of the capacitor voltages v_{c2}, v_{c1} and the inductor currents i_{L1}, i_{L2} (respectively from up to down) showing the start-up of for cascaded gyrator-LFR for $g_1 = 0.05$ S, $g_{r2} = 0.01$ S.

Secondly, Fig. 5.9 shows the simulated and experimental results for the transient start up and steady state responses of the system from zero initial conditions. Note, that after a long transient time of 50 ms, the state variables reach their steady state values which are in agreement with (5.29).

Fig. 5.10 shows the simulated and experimental results for the input voltage variation effect. When the input voltage increases from 12 V to 15 V, the output capacitor voltages and the inductor currents increase. However, when the load resistance changes from 2500 Ω to 1500 Ω, the inductor currents are constants, while,the capacitor voltage v_{c2} decreases as shown in Fig. 5.11. This reduce in v_{c2} change the switching losses which yields that the voltage v_{c1} slightly reduced. Note that, ideally, v_{c1} is constant because it is not sensible to the load resistance. This can also be deduced from the equilibrium point (5.29). Note that, when the load changes, the input power is constant because of the existence of the LFR.

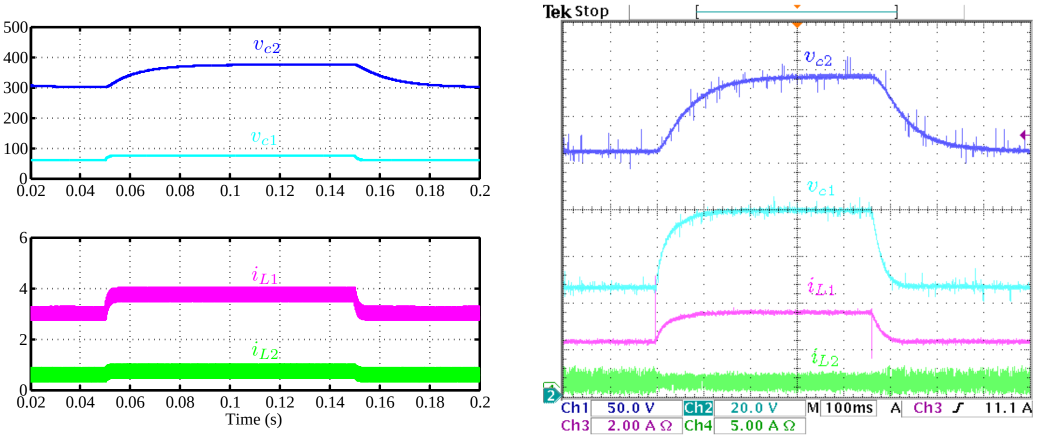

(a) (b)

Figure 5.10: Simulated and experimental waveforms of the capacitor voltages v_{c2}, v_{c1} and the inductor currents i_{L1}, i_{L2} (respectively from up to down) for cascaded gyrator-LFR for $g_1 = 0.05$ S, $g_{r2} = 0.01$ S and under input voltage change from 12 V to 15 V.

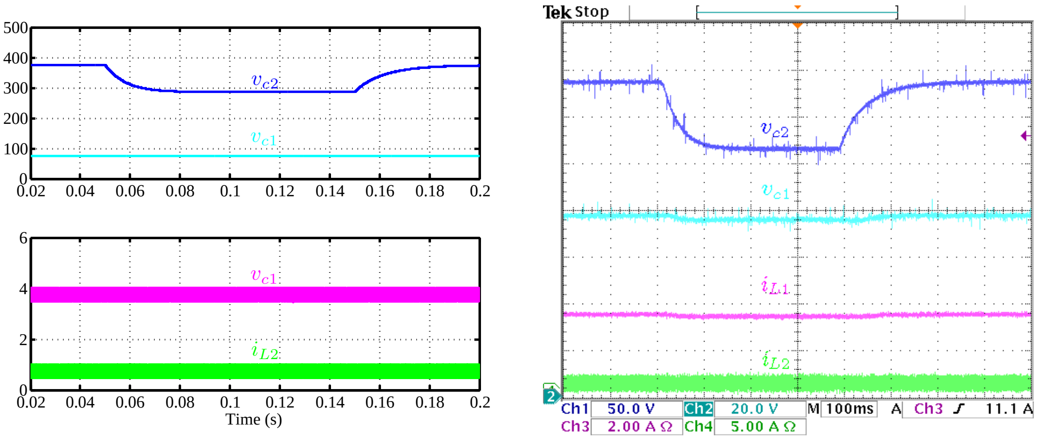

(a) (b)

Figure 5.11: Simulated and experimental waveforms of the capacitor voltages v_{c2}, v_{c1} and the inductor currents i_{L1}, i_{L2} (respectively from up to down) for cascaded gyrator-LFR for $g_1 = 0.05$ S, $g_{r2} = 0.01$ S and under load change from 2500 Ω to 1500 Ω.

5.3 Conclusion

In this chapter, two different canonical elements have been connected in cascade. First, a cascaded LFR-gyrator based on two sliding surfaces has been synthesized.

The analysis has verified that the system is unconditionally stable. However, the condition for sliding motion is restricted for the resistive load between two certain values. This means that the system can lost the sliding when the load changes. Moreover, the equilibrium point of the state variables depends on the resistive load. This system has been analyzed theoretically and using numerical simulations which have been verified with the experimental results.

Second, cascaded gyrator-LFR using two sliding surfaces has been synthesized. This system has been analyzed theoretically and using PSIM simulations. The analysis has verified that the system is unconditionally stable and the sliding conditions have been obtained. It should be noted that the dynamics of this system is similar to the two cascaded LFRs. It has been explained that the sliding regime of the two cascaded LFRs is wider than the cascaded gyrator with LFR. Moreover, the equilibrium point of the two cascaded LFRs is more controllable than the cascaded gyrator-LFR.

Chapter 6

Impedance Matching Using Cascaded LFRs in PV Applications

In the previous chapters, different types of cascaded canonical elements have been analyzed. It has been demonstrated that some of them cannot be used for obtaining a high conversion ratio such as the two cascaded boost-based DC-transformers.

The systems of two cascaded boost converters based on a single sliding surface result in a stable system with certain conditions. The existence conditions for the two systems depend on the resistive load which limits the sliding regime for the two systems. In addition, the steady state value of the intermediate voltage V_{c1} and output voltage V_{c2}, for the two systems, depend on the resistive load.

In turn, the two cascaded g-gyrators and the cascaded LFR-gyrator systems have the ability to operate with a high conversion ratio with an unconditionally stable behavior. The existence condition of sliding-mode regimes are more difficult to accomplish for the two mentioned systems. Moreover, the steady state value of the intermediate voltage V_{c1}, for the two systems, depends on the load resistance which varies the conversion ratio of the two stages when the load changes.

The two cascaded LFRs and the cascaded gyrator-LFR result in an unconditionally stable system. The steady-state values of the capacitor voltages, in the cascaded gyrator-LFR, depend on the conductance of the g-gyrator and the conductance of the LFR which make controlling these steady-state values difficult. On the contrast, for the two cascaded LFRs, the steady-state value of output capacitor voltage V_{c2} depends only on conductance of the second LFR g_{r2}, while the steady-state value of the intermediate voltage V_{c1} depends on the conductances of the first and second LFR g_{r1} and g_{r2} respectively. This makes the two cascaded LFRs system more controllable than the others. In addition, the range of the sliding regime for the two cascaded LFRs is wider than the cascaded gyrator-LFR.

Therefore, in this chapter, two cascaded LFRs system is used for impedance matching between a PV panel and a (DC and AC) distribution system. The modeling, simulation and design of the systems are addressed. First, an ideal reduced-order sliding-mode dynamics model is derived from the full-order switched model taking into account the sliding constraints, the nonlinear characteristic of the PV module and the dynamics of the MPPT controller. From this model, a design-oriented averaged model is obtained and its dynamic behavior showing that the system is asymptotically globally stable. Numerical simulations and experimental results corroborate the theoretical analysis and illustrate the advantages of this architecture in PV systems.

6.1 System Overview

The proposed conversion system is based on two cascaded boost converters behaving as LFRs as shown in Fig. 6.1. This section describes briefly the different parts of the system, the impedance matching of the PV characteristic and the MPPT circuit. The realization of a sliding-mode controller to obtain the LFR characteristic has been explained previously.

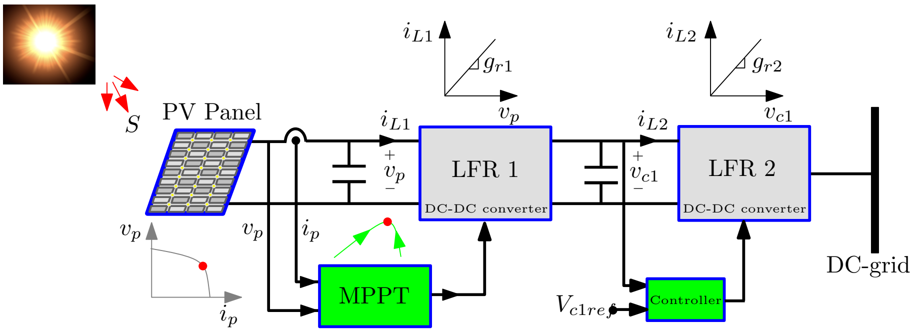

Figure 6.1: Grid connected with a PV module through cascaded DC-DC converters.

6.1.1 Impedance matching in PV systems

The switching converters can be used as an interface element to connect a PV generator to a load. Fig. 6.2 illustrates the problem of matching a PV generator to a DC load using two cascaded boost converters working as LFRs. The output power can be expressed as a function of the LFR conductance $g_{r1} = 1/r_1$:

$$P_o = P_i = g_{r1} v_p^2. \tag{6.1}$$

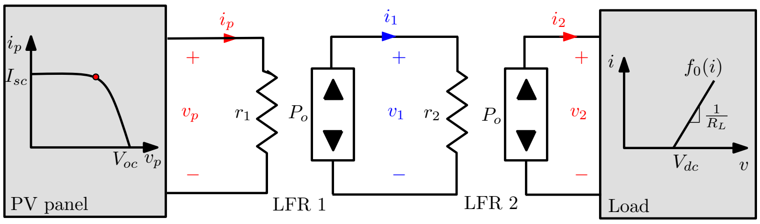

Figure 6.2: Impedance matching of a PV module generator to a DC load using two cascaded boost-based LFRs.

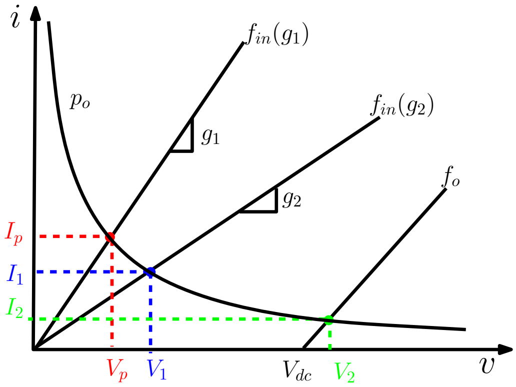

Figure 6.3: Power source characteristics of the LFR output port.

As a consequence, the output power is not influenced by the output port variables as it can be shown in Fig. 6.3 Singer and Erickson (1994). This inherent characteristic of LFRs is of high importance to avoid the influence of the load variations in the impedance matching of PV systems. Both PV generator and load have been modeled in the first quadrant $i - v$ characteristic. The DC load can be modeled by means of a function $i_2 = f_o(v_2)$, which corresponds to the one-port description of the usual DC loads such as batteries, LED lamps, electrolytic cells, etc. and can be expressed generally by:

$$v_2 = f_o(i_2) = V_{dc} + i_2 R_L, \tag{6.2}$$

where $V_{dc} > 0$ and $R_L > 0$. The analysis of the impedance matching will be carried out by considering a very small equivalent series resistance ($R_L \simeq 0$) and with a nominal DC voltage V_{dc} much greater than the open circuit voltage V_{oc} of the PV module.

The PV module current-voltage characteristic and the LFR steady-state input impedance are depicted in Fig. 6.4. Note that there is no operating point that would result from the direct connection of the PV generator and the DC bus since there is no intersection between their respective characteristics ($V_{dc} >> V_{oc}$). It can be observed also that the operating point of the PV generator depends on the

LFR conductance g. The variation of this parameter changes the operating point of the PV module as illustrated in Fig. 6.4. Operating points A and B correspond respectively to conductances g_a and g_b with $g_a > g_b$. The LFR converters can operate at the optimal value of the conductance that leads to an intersection of the PV $i - v$ characteristic curve and the LFR load line ($i = gv$) described by $f_{in}(g_{opt})$ at the MPP.

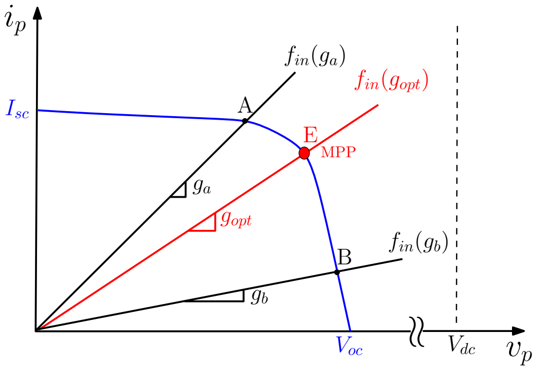

Figure 6.4: PV module operating points for an impedance matching between the PV generator and the LFR.

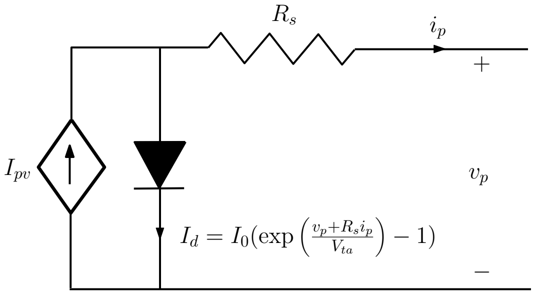

Figure 6.5: Equivalent circuit diagram of the PV module model.

According to the current-voltage characteristic of the PV module, Fig. 6.5 shows an equivalent circuit whose output current can be expressed as follows Walker (2001), Petrone et al. (2007), Ropp and Gonzalez (2009), Villalva et al. (2009):

$$i_p = I_{pv} - I_0 \left(\exp\left(\frac{v_p + R_s i_p}{V_{ta}} \right) - 1 \right), \tag{6.3}$$

where v_p is the voltage of the module, I_{pv} and I_0 are the photogenerated and saturation currents respectively, V_{ta} is the thermal voltage which is given by $V_{ta} = N_s AKT/q$ where A is the diode quality factor, K is Boltzmann constant, q is the charge of the electron, T is the PV module temperature and N_s is the number of the cells connected in series.

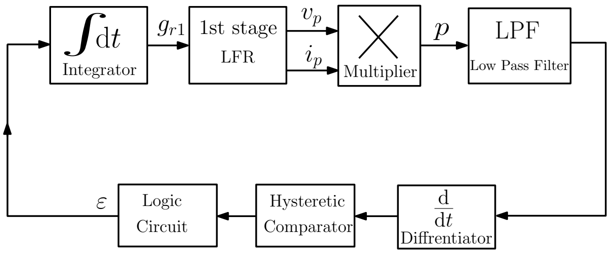

Figure 6.6: Generation of the conductance g_{r1} by means of an MPPT scheme based on ESC.

In addition, the photogenerated current I_{pv} depends on the irradiance and temperature as follows

$$I_{pv} \quad = \quad I_{sc}\frac{S}{S_n} + C_t(T - T_n), \tag{6.4}$$

being I_{sc} the short circuit current, T_n and S_n the nominal temperature and irradiance, S the ambient irradiance and C_t the temperature coefficient.

The implicit equation (6.3) can be transformed to an explicit relation using the Lambert-W function, as in Petrone et al. (2007). In this way, a nonlinear relationship between the current i_p and the voltage v_p at the basic PV unit terminals can be obtained and expressed as follows

$$i_p = I_{pv} + I_0 - \frac{V_{ta}}{R_s}\mathcal{W}\left(\frac{R_s I_0}{V_{ta}} \exp\left(\frac{v_p + R_s(I_{pv} + I_0)}{V_{ta}}\right)\right), \tag{6.5}$$

where $\mathcal{W}$ stands for the Lambert-W function. This equation is used in the analysis of the system that follows.

6.1.2 Maximum power point tracking

The goal of the MPPT is to ensure that the PV module always operates at its MPP regardless of the temperature, insolation and load variation. A number of tracking algorithms have been applied for different types of DC-DC converter topologies Veerachary et al. (2002), Noguchi et al. (2002), Leyva et al. (2006), Esram and Chapman (2007), Kjaer (2012), Femia et al. (2005), A.G. de Brito et al. (2013). Extremum Seeking Control (ESC) is one of the commonly used types of MPPT which can force the PV system to approach the MPP by increasing or decreasing a suitable control variable Leyva et al. (2006).

Fig. 6.6 shows the block diagram corresponding to ESC MPPT subsystem. The power supplied by the panel p is calculated by means of a multiplier. This signal is filtered using a low pass filter (LPF) to remove the switching ripple and then

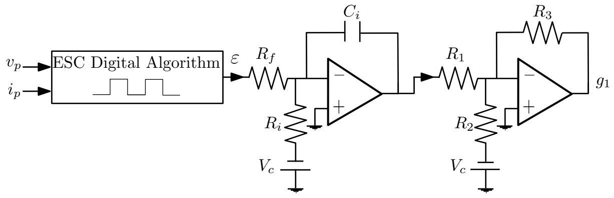

Figure 6.7: Simplified description of an ESC MPPT: a digital algorithm, an integrator and a gain Leyva et al. (2006).

processed by a differentiator to calculate the power time-derivative. The output signal of the differentiator is processed by an HC which provides together with a logic circuit a binary signal ε to indicate whether the power time-derivative is positive or negative. The binary signal ε is introduced into a logic circuit with an inhibition delay τ_d which establishes, after a fixed time interval, if the direction of maximum searching has to be maintained or should be changed. The waiting interval ensures that the converter is operating in steady-state when the decision on the change or maintenance of the control law sign is made. Thus, in the proposed scheme the settling time of the PV voltage and current will be directly related to the capacitor C_p and the loss-free resistance r_1. Therefore, the minimum time delay τ_d could be defined theoretically as $5\max(r_1)C_p$. Note that r_1 is a variable parameter whose maximum value depends on the characteristics of the PV generator, the irradiation level and temperature. Moreover, an additional waiting time should be added to eliminate the negative effects of the noise in the experimental prototype Sullivan et al. (2013), Latham et al. (2013). The output signal ε of the logic circuit is integrated and multiplied by a gain in order to obtain the triangular signal g_{r1} which is the required conductance by the LFR.

The ESC can be modeled by a square wave generator that can be implemented by a microcontroller and an integrator as shown in Fig. 6.7. From this figure, the following equation describes the ESC MPPT controller

$$g_{r1} = k_1 V_c - \frac{k_2}{\tau_1}\int_0^t v_s(\zeta)\mathrm{d}\zeta \tag{6.6}$$

where $v_s = k_3 V_c - \varepsilon$, $\tau_1 = R_f C_i$, $k_1 = R_3/R_2$, $k_2 = R_3/R_1$, $k_3 = R_f/R_i$ and V_c is a constant voltage source. The variable ε depends mainly on the derivative of the filtered power and its value is 0 or 1. If $\varepsilon = 0$, g_{r1} decreases based on (6.6) and when $\varepsilon = 1$, g_{r1} increases based on the same equation. Fig. 6.8 describes the flow chart of the ESC algorithm and illustrates the sequence for selecting the parameter ε. If the derivative of the filtered power is positive, ε will not be changed. However, if this derivative is negative and the time delay is achieved, the value of ε changes from 0 to 1 or viceversa. In the following section, both PV panel model

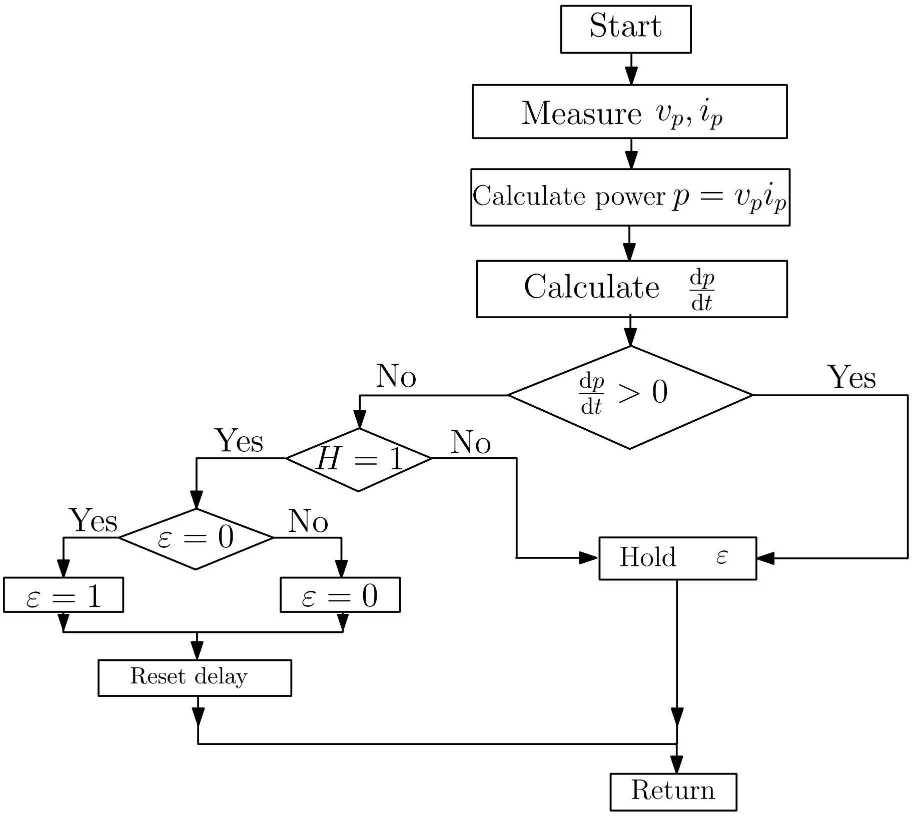

Figure 6.8: Flow chart for ESC algorithm ($H = 1$ means that the time delay is achieved).

and MPPT model will be used in the analysis of the whole system. First, the two cascaded LFRs will be used to connect a PV panel to a DC distribution system as depicted in Fig. 6.9. Second, the two cascaded LFRs will be used to connect a PV panel to an AC distribution system. This analysis will be carried out by using a reduced-order ideal sliding-mode dynamics model.

6.2 Impedance Matching Between a PV and a DC Distribution System

6.2.1 Switched model

By applying KVLs and KCLs to the circuit depicted in Fig. 6.9, the following set of differential equations describing the system dynamical behavior are obtained

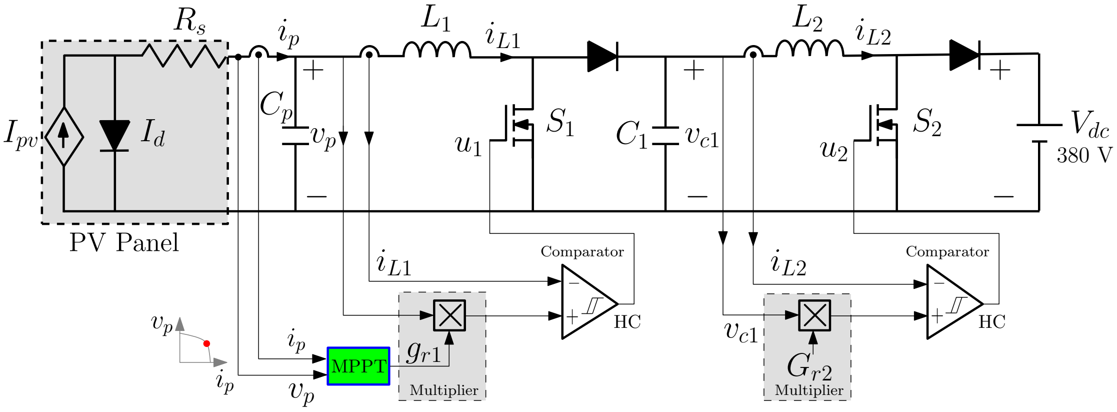

Figure 6.9: Schematic diagram of two cascaded boost-based LFRs under SMC.

$$\frac{\mathrm{d}i_{L1}}{\mathrm{d}t} = \frac{v_p}{L_1} - \frac{v_{c1}}{L_1}(1-u_1) \tag{6.7}$$

$$\frac{\mathrm{d}i_{L2}}{\mathrm{d}t} = \frac{v_{c1}}{L_2} - \frac{V_{dc}}{L_2}(1-u_2) \tag{6.8}$$

$$\frac{\mathrm{d}v_p}{\mathrm{d}t} = \frac{i_p}{C_p} - \frac{i_{L1}}{C_p} \tag{6.9}$$

$$\frac{\mathrm{d}v_{c1}}{\mathrm{d}t} = \frac{i_{L1}}{C_1}(1-u_1) - \frac{i_{L2}}{C_1}, \tag{6.10}$$

where for the first stage (resp. second stage) $u_1 = 1$ when the switch S_1 (resp. S_2) is closed and $u_1 = 0$ when the switch S_1 (resp. S_2) is open. All the parameters that appear in (6.7)-(6.10) are shown in Fig. 6.9.

6.2.2 Equivalent control

The sliding-mode dynamics at steady state are defined with the following equations:

$$s_1(\mathbf{x}) = g_{r1}v_p - i_{L1} = 0 \tag{6.11}$$

$$s_2(\mathbf{x}) = G_{r2}v_{c1} - i_{L2} = 0 \tag{6.12}$$

$$\dot{s}_1(\mathbf{x}) = g_{r1}\frac{\mathrm{d}v_p}{\mathrm{d}t} + v_p\frac{\mathrm{d}g_{r1}}{\mathrm{d}t} - \frac{\mathrm{d}i_{L1}}{\mathrm{d}t} = 0 \tag{6.13}$$

$$\dot{s}_2(\mathbf{x}) = G_{r2}\frac{\mathrm{d}v_{c1}}{\mathrm{d}t} - \frac{\mathrm{d}i_{L2}}{\mathrm{d}t} = 0. \tag{6.14}$$

Under sliding mode conditions, the equivalent control variables $u_{eq1}(\mathbf{x})$ and $u_{eq2}(\mathbf{x})$ represent the control laws that describe the behavior of the system restricted to the switching surfaces where the system motion takes place on the average as mentioned previously. Hence, from Eqs. (6.7)-(6.10) and (6.13)-(6.14), $u_{eq1}(\mathbf{x})$ and $u_{eq2}(\mathbf{x})$ can be expressed as follows

$$\begin{aligned} u_{eq1} &= 1-\frac{v_d}{v_{c1}}-\frac{v_m}{v_{c1}} && (6.15)\\ u_{eq2} &= 1-\frac{1}{V_{dc}}\left(v_{c1}+\alpha_2\left(G_{r2}v_{c1}+\frac{g_{r1}v_p}{v_{c1}}v_d\right)\right), && (6.16)\end{aligned}$$

where $\alpha_1 = g_{r1}L_1/C_p$, $\alpha_2 = G_{r2}L_2/C_1$, $v_d = v_p - \alpha_1(i_p - g_{r1}v_p)$ and $v_m = v_pL_1(k_2(k_3V_c - \varepsilon)/\tau_1)$. Note that the equivalent control variables u_{eq1} and u_{eq2} must be bounded between the minimum and maximum values of u_1 and u_2 respectively as mentioned before, i.e.:

$$0 \leq u_{eq1} \leq 1 \text{ and } 0 \leq u_{eq2} \leq 1. \qquad (6.17)$$

6.2.3 Ideal sliding dynamics and sliding-mode conditions

By imposing the existence conditions given by Eq. (6.17), the sliding-mode domain can be obtained. For instance, in the plane (v_p, v_{c1}) and based on (6.15), (6.16) and (6.17), the sliding-mode regime exists provided that $v_{c1L} < v_{c1} < v_{c2L}$ where the critical values v_{c1L} and v_{c2L} are given by

$$\begin{aligned} v_{c1L} &= v_d + v_m && (6.18)\\ v_{c2L} &= \frac{V_{dc}+\sqrt{V_{dc}^2+4\alpha_2 g_{r1}v_p(1-\alpha_2G_{r2})(v_d+v_m)}}{2(1-\alpha_2G_{r2})}. && (6.19)\end{aligned}$$

Other boundaries also exist but the ones expressed by (6.18), (6.19) are the most restrictive. The equivalent control variables $u_{eq1}(\mathbf{x})$ and $u_{eq2}(\mathbf{x})$ depend on g_{r1}, which is the output of the MPPT algorithm. Introducing (6.15) and (6.16) into Eqs. (6.7)-(6.10) and considering Eqs. (6.11)-(6.14) result in the following reduced-order model for the ideal sliding-mode dynamics:

$$\begin{aligned} \frac{\mathrm{d}v_p}{\mathrm{d}t} &= \frac{i_p}{C_p}-\frac{g_{r1}v_p}{C_p} && (6.20)\\ \frac{\mathrm{d}v_{c1}}{\mathrm{d}t} &= \frac{g_{r1}v_p^2}{C_1v_{c1}}\beta_2+\frac{\alpha_1 g_{r1}v_p}{C_1v_{c1}}(g_{r1}v_p-i_p)-\frac{G_{r2}v_{c1}}{C_1} && (6.21)\\ \frac{\mathrm{d}g_{r1}}{\mathrm{d}t} &= -k_2\frac{k_3V_c-\varepsilon}{\tau_1}, && (6.22)\end{aligned}$$

where $\beta_2 = 1 + k_2v_sL_1/\tau_1$. The large-signal ideal sliding-mode dynamics given in (6.20)-(6.22) can be represented by the circuit depicted in Fig. 6.10. This model will be used for numerical simulations after its validation by the full-order switched

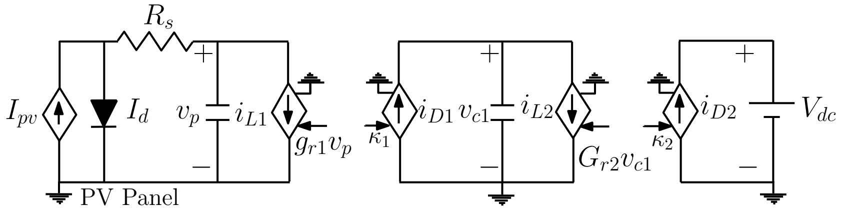

Figure 6.10: Large-signal circuit corresponding to the ideal sliding dynamics where $\kappa_1 = g_{r1}v_p^2\beta_2/v_{c1}$, $\kappa_2 = G_{r2}v_{c1}^2/V_{dc}$.

model given in (6.7)-(6.10). The advantage of using this large-signal reduced-order model is the significant consumption time reduction if compared to the switched model. The inductor currents can be modeled by voltage controlled current sources which are governed by $g_{r1}v_p$ and $G_{r2}v_{c1}$ as mentioned on the switching surface equations. It is worth showing that the second term in (6.21) is very small. Therefore, to simplify the large-signal model block diagram, this term has been neglected.

6.2.4 Design-oriented averaged model

The previous model (6.20)-(6.22) is a switched model whose dynamical behavior characterization is challenging due to the presence of the MPPT dynamics which introduce a switching variable ε and also due to nonlinearities. As a first step for stability analysis, averaging of the previous equations (6.20)-(6.22) over one period $2\tau_d$ is carried out, where τ_d is the delay period used in the MPPT controller. Let $\overline{v}_p$, $\overline{i}_p$, $\overline{v}_{c1}$, $\overline{v}_s$, $\overline{g}_{r1}$ and $\overline{\varepsilon}$ stand for averaged quantities, i.e,

$$\overline{\varepsilon} = \frac{1}{2\tau_d}\int_t^{t+2\tau_d} \varepsilon(\zeta)\mathrm{d}\zeta \tag{6.23}$$

with similar expressions for the rest of averaged variables. Therefore, we obtain the following $2\tau_d-$averaged equations

$$\begin{aligned}
\frac{\mathrm{d}\overline{v}_p}{\mathrm{d}t} &= \frac{\overline{i}_p}{C_p} - \frac{\overline{g}_{r1}\overline{v}_p}{C_p} && (6.24)\\
\frac{\mathrm{d}\overline{v}_{c1}}{\mathrm{d}t} &= \frac{\overline{g}_{r1}\overline{v}_p^2}{C_1\overline{v}_{c1}}\beta_2 + \frac{\alpha_1\overline{g}_{r1}\overline{v}_p}{C_1\overline{v}_{c1}}(\overline{g}_{r1}\overline{v}_p - \overline{i}_p) - \frac{G_{r2}\overline{v}_{c1}}{C_1} && (6.25)\\
\frac{\mathrm{d}\overline{g}_{r1}}{\mathrm{d}t} &= -k_2\frac{k_3V_c - \overline{\varepsilon}}{\tau_1}. && (6.26)
\end{aligned}$$

The next step in our study will be the determination of the equilibrium point of the averaged model defined in (6.24) - (6.26).

Equilibrium point

The equilibrium point can be obtained by forcing the time derivative of the state variables of the averaged model to be null. In order to get an explicit expression of the equilibrium point, let us suppose that $R_s = 0$ in Eq. (6.3) which becomes

$$i_p = I_{pv} - I_0(\exp(\frac{v_p}{V_{ta}}) - 1). \tag{6.27}$$

From (6.24)-(6.26) and taking into account Eqs. (6.11) and (6.12), the equilibrium point of the averaged-model is given by

$$\mathbf{x}^* = [\overline{V}_p, \overline{V}_{c1}, \overline{G}_{r1}]^\top = \left[\frac{\overline{I}_e}{\overline{G}_{r1}}, \frac{\overline{I}_e}{\sqrt{\overline{G}_{r1} G_{r2}}}, k_1 V_c\right]^\top, \tag{6.28}$$

where $\overline{I}_e$ can be expressed as follows

$$\overline{I}_e = I_{pv} + I_0 - \overline{G}_{r1} V_t \mathcal{W}\left(\frac{I_0}{\overline{G}_{r1} V_{ta}} \exp\left(\frac{I_{pv} + I_0}{\overline{G}_{r1} V_t}\right)\right). \tag{6.29}$$

In order to validate the previous analytical expression for the equilibrium point, it has been calculated numerically by an iterating procedure with the exact expression (6.5) and using the analytical approximated expression given in (6.28) and a good agreement has been obtained for a wide range of practical parameter values.

The averaged values of the control variables at the equilibrium point can be obtained by substituting (6.28) in (6.15) and (6.16) and leads to the following expressions

$$\overline{U}_{eq1}(\mathbf{x}^*) = 1 - \sqrt{\frac{G_{r2}}{\overline{G}_{r1}}} \tag{6.30}$$

$$\overline{U}_{eq2}(\mathbf{x}^*) = 1 - \frac{\overline{I}_p}{V_{dc}}\left(\frac{1}{\sqrt{\overline{G}_{r1} G_{r2}}} - 2\alpha_2 \sqrt{\frac{G_{r2}}{\overline{G}_{r1}}}\right). \tag{6.31}$$

As mentioned previously in (6.17), $\overline{u}_{eq1}(\mathbf{x}^*)$ and $\overline{u}_{eq2}(\mathbf{x}^*)$ must be bounded between 0 and 1. Moreover, in steady-state, $\overline{I}_p = \overline{I}_{L1}$. Therefore, from (6.17) the following condition must be satisfied

$$\overline{G}_{r1} > \max(G_{r2}, \frac{(1 - 2\alpha_2 G_{r2})^2 I_p^2}{G_{r2} V_{dc}^2}). \tag{6.32}$$

It is worth to note that the previous condition (6.32) has been derived considering that $\overline{I}_p - \overline{G}_{r1}\overline{V}_p = 0$ at the equilibrium point.

Small-signal stability analysis

In order to study the stability of the system, the nonlinear equations (6.24)-(6.26) are first linearized around the equilibrium point $\mathbf{x}^*$ given by (6.28), obtaining the following expression of the Jacobian matrix $\mathbf{J}$

$$\mathbf{J} = \begin{pmatrix} -\delta & 0 & -\dfrac{\overline{V}_p}{C_p} \\ \beta_3 + \beta_1(2\overline{v}_s + \dfrac{\partial\overline{\varepsilon}}{\partial\overline{v}_p}) & -\beta_4 & \dfrac{\overline{V}_p^2}{C_1\overline{V}_{c1}}(\beta_2 + \alpha_1\overline{G}_{r1}) \\ -\dfrac{k_2}{\tau_1}\dfrac{\partial\overline{\varepsilon}}{\partial\overline{v}_p} & 0 & 0 \end{pmatrix} \tag{6.33}$$

where the parameters δ, $\mathcal{L}$, β_1, β_2, β_3 and β_4 are given by

$$\delta = \frac{R_s\overline{G}_{r1}(1+\mathcal{L}) + \mathcal{L}}{R_sC_p(1+\mathcal{L})} \tag{6.34}$$

$$\mathcal{L} = \mathcal{W}\left(\frac{R_sI_0}{V_{ta}}\exp\left(\frac{\overline{V}_p + R_s(I_{pv}+I_0)}{V_{ta}}\right)\right) \tag{6.35}$$

$$\beta_1 = \frac{\sqrt{\overline{G}_{r1}G_{r2}}L_1k_2}{C_1\tau_1}, \quad \beta_2 = (1 + k_2\overline{V}_s\frac{L_1}{\tau_1}) \tag{6.36}$$

$$\beta_3 = \frac{1}{C_1}(2\overline{G}_{r1} - \sqrt{\overline{G}_{r1}G_{r2}\delta}), \ \beta_4 = \frac{2G_{r2}}{C_1} + \sqrt{\frac{G_{r2}}{\overline{G}_{r1}}}\beta_1. \tag{6.37}$$

The characteristic polynomial equation of the linearized system is given by $\det(\mathbf{J} - s\mathbf{I}) = 0$. Developing this equation, the characteristic polynomial can be written in the following form:

$$s^3 + (\delta+\beta_4)s^2 + \delta\beta_4 s - \frac{\overline{v}_p}{C_p}\frac{k_2}{\tau_1}\frac{\partial\overline{\varepsilon}}{\partial\overline{v}_p}s - \frac{\overline{v}_p}{C_p}\frac{k_2}{\tau_1}\frac{\partial\overline{\varepsilon}}{\partial\overline{v}_p}\beta_4 = 0. \tag{6.38}$$

Observe that we cannot study the stability of the system using the previous characteristic polynomial due to the non availability of an explicit mathematical expression of $\overline{\varepsilon}$ in terms of $\overline{v}_p$ allowing a general result. It might be possible, however, to treat the system using numerical simulations. This has the advantage of not requiring such a mathematical expression as in the case of an analytical stability analysis. Fortunately, in our system, the averaged variable $\overline{\varepsilon}$ changes very slowly with respect to $\overline{v}_p$. Therefore, it can be considered that $\partial\overline{\varepsilon}/\partial\overline{v}_p \approx 0$ which implies that the characteristic polynomial can be simplified as follows

$$s^2 + (\delta+\beta_4)s + \delta\beta_4. \tag{6.39}$$

This new simplified expression of the characteristic polynomial has two roots δ and β_4 located both in the left half plane, and hence, the equilibrium point of the averaged system is asymptotically stable. Note, that the previous stability analysis is only valid locally near enough to the equilibrium point. However, as the MPPT controller is included in the dynamical model, the equilibrium point corresponds to the MPP. This is because at the MPP one has $\mathrm{d}\overline{p}/\mathrm{d}v_p \approx 0$, which implies that $\mathrm{d}\overline{p}/\mathrm{d}t \approx 0$, i.e, $\mathrm{d}\overline{v}_p/\mathrm{d}t \approx 0$ and $\mathrm{d}\overline{i}_p/\mathrm{d}t \approx 0$. If the stability is guaranteed for this point, it becomes inherently an attractor of the system. As the equilibrium point is unique, this ensures that it is a global attractor for the system. The following section provides numerical simulations showing that the basin of attraction of this equilibrium point is indeed very large.

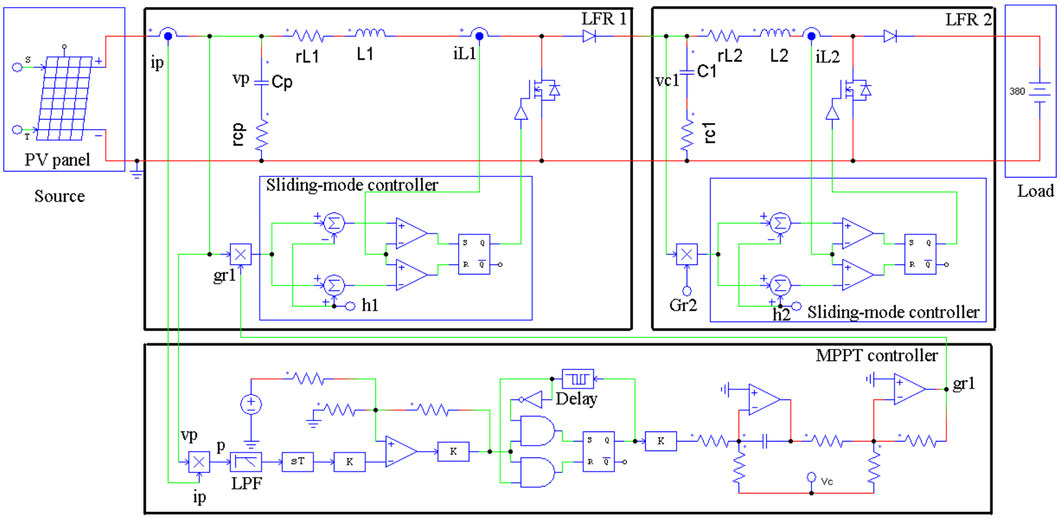

Figure 6.11: PSIM schematic diagram of the two cascaded boost-based LFRs connected to a PV module operating with an ESC MPPT controller.

6.2.5 Numerical simulation and experimental results

In order to verify the previous theoretical results, the original switched-mode system is simulated in PSIM using the schematic shown in Fig. 6.11. The PSIM solar module BP585 is used, being its internal parameters shown in Table 6.1. Table 6.2 shows the rest of the parameter values of the system. Moreover, the two cascaded boost based LFRs have been implemented in the laboratory supplied from a PV panel BP585 and loaded with a dynamic load working as a constant DC voltage 380 V, for more details (see Appendix A). Conductance G_{r2} has been selected in such a way that both stages work with the same duty cycle, which in this case corresponds to a conversion ratio of 5 at each stage, or equivalently an intermediate voltage v_{c1} around 80 V. The period of oscillation of the MPP tracker has

Table 6.1: Parameters of the PV module.

Parameter	Value
Number of cells N_s	36 cell
Standard light intensity S_0	1000 W/m^2
Ref temperature T_{ref}	25 ^{o}C
Series resistance R_s	0.008 Ω
Short circuit current I_{sc0}	5 A
Saturation current I_{s0}	$3.8074{\cdot}10^{-8}$ A
Band energy E_g	1.12
Ideality factor A	1.2
Temperature coefficient C_t	0.00065 A/C

Table 6.2: The used parameter values for two cascaded LFR connected to a DC distribution system.

V_{dc}	L_1	L_2	C_p	C_1	G_{r2}	h_1
380 V	200 μH	2 mH	100 μF	10 μF	0.008 S	0.25 V
h_2	k_1	k_2	k_3	τ_1	V_c	f_s
0.15 V	0.05	0.167	0.5	0.1 s	5 V	100 kHz

been fixed by means of the integrator gain and the time delay τ_d. This delay period has been fixed to 5 ms taking into account the aforementioned settling time of the system and the presence of noise in the prototype Sullivan et al. (2013), Latham et al. (2013). In turn, the integrator gain has been tuned in order to obtain a good tradeoff between the static MPPT efficiency and the tracking speed at both low and rated power levels. It is worth mentioning also that the parasitic elements have been included in the PSIM simulation shown in Fig. 6.11. They are the internal resistance of the inductors (r_{L1}=60 mΩ and r_{L2}=130 mΩ), the ON resistance of the MOSFETs (r_{on1}=60 mΩ and r_{on2}=165 mΩ) and the equivalent series resistances (ESR) of the capacitors $r_{cp} = r_{c1} = 0.1\ \Omega$.

6.2.6 Steady-state results

The efficiency of the system has been checked analytically and using experimental results. Analytically, the power loss of the two cascaded LFRs can be expressed as follows:

$$
\begin{aligned}
&\text{Inductor Copper Losses:} \\
P_{Li} &= I_{L_i}^2 r_{L_i} \\
&\text{Diode Losses:} \\
P_d &= V_{D_i} I_{L_i}(1-D_i) + f_s T_{rD_i} I_{L_i} V_{C_i} + 0.5 f_s T_{rD_i} I_{rD_i} V_{C_i} \\
&\text{MOSFET Losses:} \\
P_s &= I_{L_i}^2 R_{on_i} D_i + 0.5 f_s C_{ds_i} V_{c_i}^2.
\end{aligned}
$$

where i indicates for the number of the cascaded converters, for this case $i = 1, 2$. r_{L_i} is the inductor DC resistance, R_{on_i} is the ON resistance of the MOSFETs and f_s is the switching frequency. The remaining diode and MOSFET parameters, such as V_{D_i}, T_{rD_i}, I_{rD_i} and C_{ds_i} can be obtained from datasheets. Fig. 6.12 shows the efficiency of the two cascaded LFRs in terms of the intermediate voltage v_{c1}. It can be noted that, the efficiency is a semiconcave function depending on the steady-state intermediate capacitor voltage value V_{c_1}. Moreover, the maximum efficiency with respect to v_{c1} is changing when the power changes as shown in Fig. 6.12. Based on Fig. 6.12, it has been selected a value of v_{c1} of 80 V, to be close from the maximum efficiency for different input power.

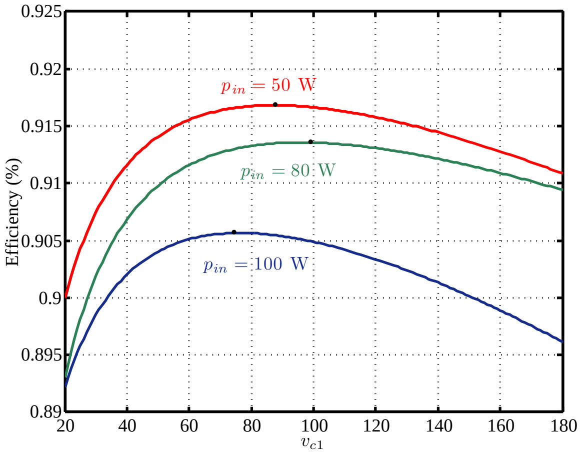

Figure 6.12: Conversion efficiency of the two-cascaded boost converters in terms of intermediate voltage v_{c1}.

The analytical expressions and experimental steady-state measurements showing the cascaded system efficiency with respect to output power for three different PV module voltages are shown in Fig. 6.13(a), Fig. 6.13(b) respectively. Note that the analysis and experimental results present efficiencies above 90 % for a wide

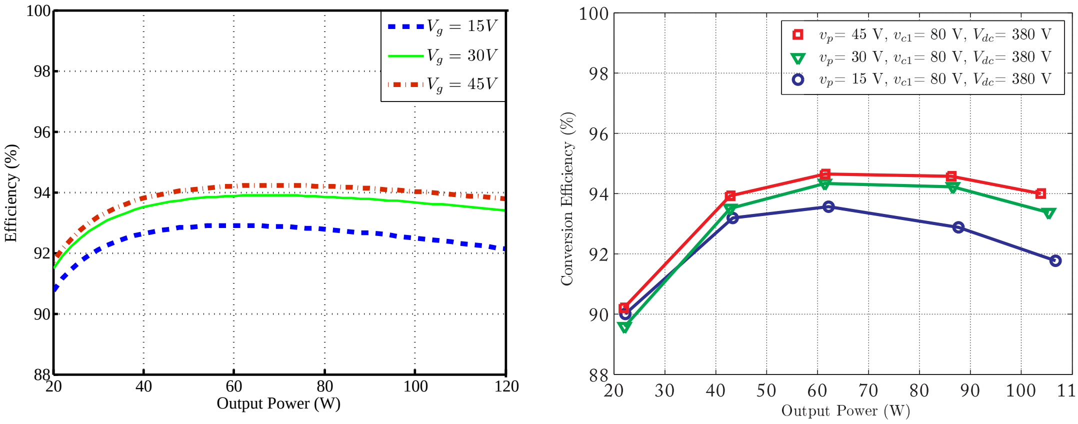

(a) (b)

Figure 6.13: Conversion efficiency of the two-cascaded boost converter in terms of output power (a) Analytical (b) Experimental.

range of output powers and input voltages, achieving a peak efficiency close to 95 % for a conversion ratio between output and input voltages above 25. It should be noted that there is a good matching between the analytical expressions and the experimental results.

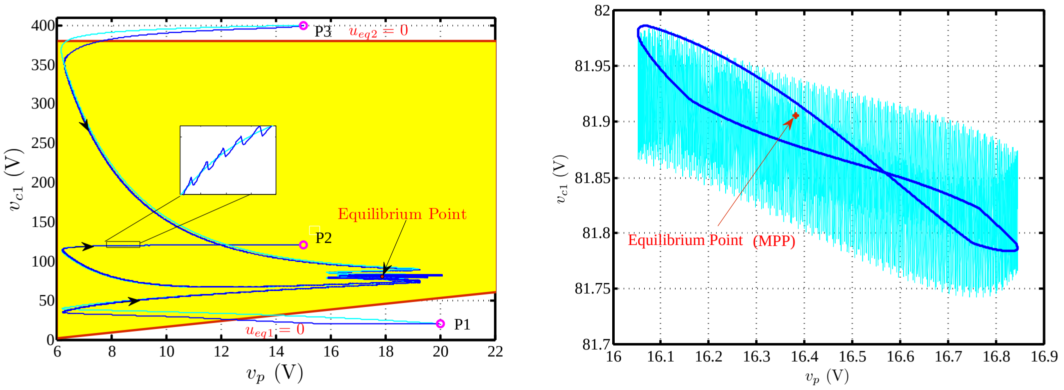

(a) (b)

Figure 6.14: Transient response of the system. (a) Trajectories from different initial conditions in the plane (v_p, v_{c1}) obtained from the full-order switched model and the ideal sliding-mode dynamics model. (b) The steady-state response in the plane (v_p, v_{c1}) form the full-order switched model and the reduced-order ideal sliding-mode dynamics.

The validity of the ideal sliding-mode dynamics model has been checked in

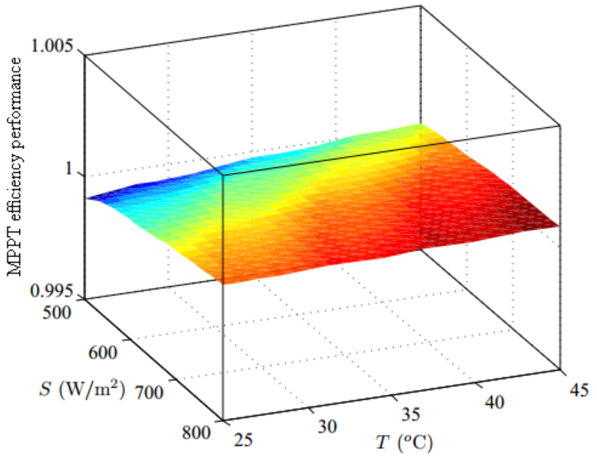

Figure 6.15: Static MPPT efficiency performance η_{MPPT} under temperature and irradiance variations.

Fig. 6.14(a), where the trajectories of both the ideal sliding-mode and switched-mode are shown. Three different initial condition points P1-P3 are considered, where the sliding-mode boundaries defined by $v_{c1} = v_{c1L}$ and $v_{c1} = v_{c2L}$, as defined in (6.18) and (6.19), are also plotted. It can be observed that the system trajectories converge to the limit cycle in the vicinity of the MPP in all the cases. For point P2, the ideal and switched-mode trajectories are in perfect agreement. For points P1 and P3, the mismatch between the ideal and switched trajectories is due to the fact that these points are outside the sliding-mode domain described previously. Fig. 6.14(b) shows the steady-state behavior of the system in the state plane (v_p, v_{c1}) using the full-order switched model and the reduced-order ideal sliding-mode dynamics model. The concordance between the results obtained from the different models is remarkable. Moreover, it can be noticed that the system converges to a limit cycle in the vicinity of the MPP in all the cases.

In order to check the MPPT effectiveness of the system, the efficiency of the MPPT η_{MPPT}, defined as the ratio between the power delivered by the PV module and its theoretical maximum value obtained form the characteristic curve Lim and Hamill (2000), has been computed for a wide range of temperature (20 to 50 °C) and irradiance (500 to 800 W/m^2) and the result is depicted in Fig. 6.15. It can be noticed that the minimum value of this MPPT efficiency is 0.995 which confirms the robustness of the system.

Fig. 6.16(a), 6.16(b) show the simulated and experimental steady-state time domain waveforms of the system. It can be noticed that the output voltage and the output current for the PV module have triangular waveforms and they are 180^o out of phase. The frequency of the instantaneous power p is twice the frequency of the current or voltage. Therefore, each half period of the current or voltage,

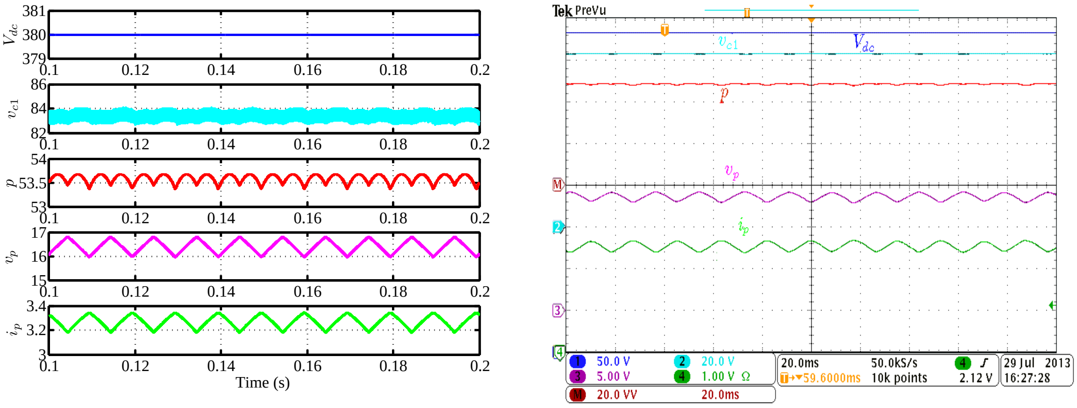

(a) (b)

Figure 6.16: Simulated and experimental waveforms of the two cascaded converters behaving as LFRs supplied from a PV module operating with an MPPT controller corresponding to steady-state.

the maximum value of the power p is reached. It can be observed that the slope changes in both current and voltage takes place between two maximum of power because the frequency of the power oscillations is twice the frequency of these variables. The efficiency of the MPPT has been measured using the measured ripple of the input power of Fig. 6.16(b), to be equal 99%.

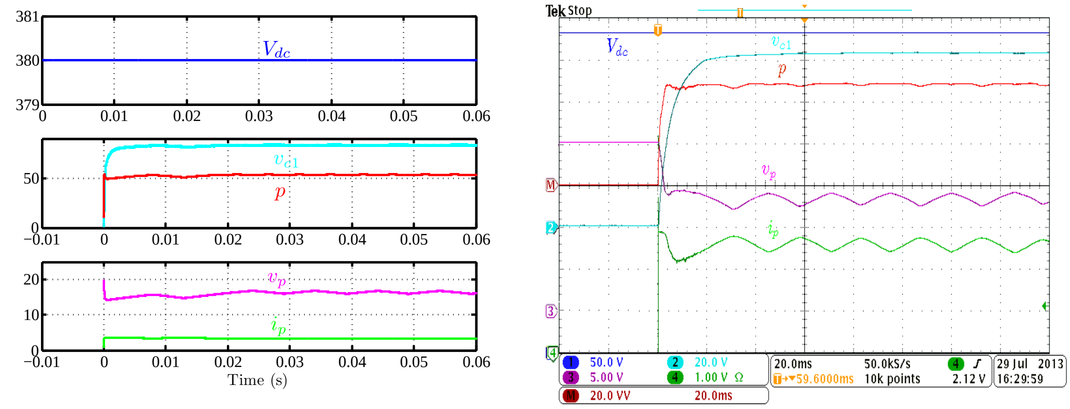

(a) (b)

Figure 6.17: Simulated and experimental waveforms of the two cascaded converters behaving as LFRs supplied from a PV module operating with an MPPT controller corresponding to start up.

6.2.7 Transient behavior

The simulated and experimental transient behavior of the PV module during startup is depicted in Fig. 6.17. The starting point of the PV module is at zero current and open circuit voltage 20 V. The voltage of the module decreases during the start up while the current and the power increase. It can be noticed that the settling time is small and that the system behaves as an LFR at steady-state.

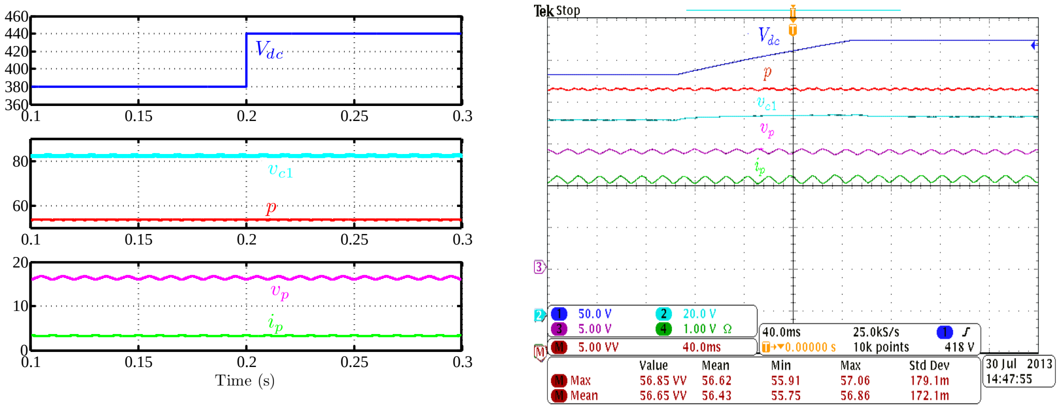

(a) (b)

Figure 6.18: Simulated and experimental waveforms of the system showing the effect of load increase from 380 V to 420 V.

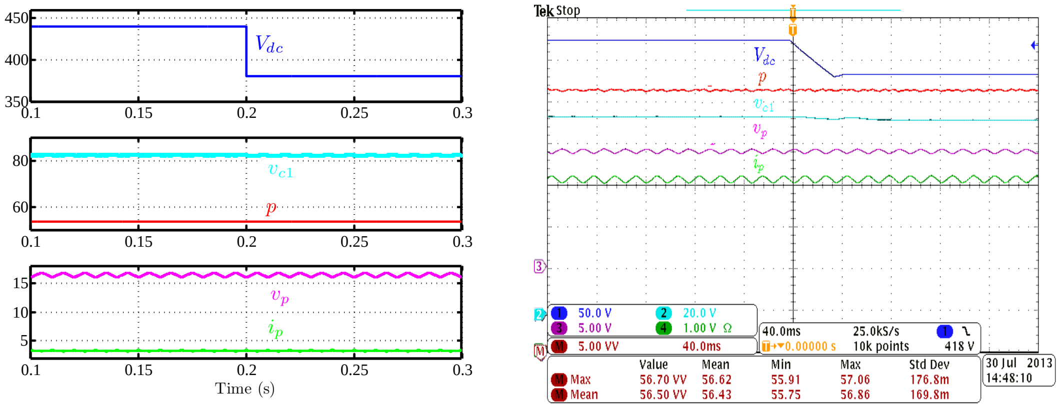

(a) (b)

Figure 6.19: Simulated and experimental waveforms of the system showing the effect of load decrease from 420 V to 380 V.

The system has been tested under several disturbances. Fig. 6.18 shows the simulated and experimental waveforms for the system under a step change of the output voltage form 380 V to 420 V. It can be noticed that increasing the output voltage has no effect on the input variables v_p and i_p of the PV module and consequently it does not alter the tracking of the input power, given the inherent power source characteristic of the LFRs that has been previously discussed in Section II.A. However, because of the losses, a small increase in the intermediate voltage v_{c1} can be noticed. Similarly, Fig. 6.19 shows the simulated and experimental waveforms of the system under a decrease of the output voltage. It can be noticed that in this case no effect on the PV power tracking can be observed. Note that the DC voltage V_{dc} in the experimental has a slope which is not exist in

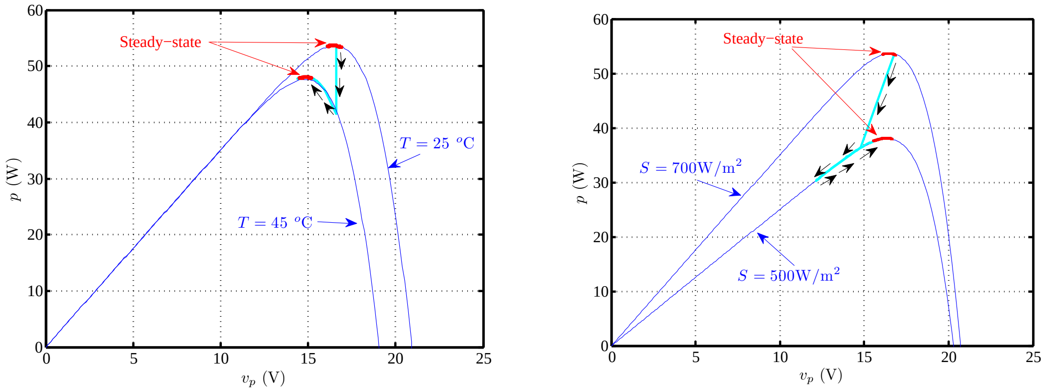

(a) Temperature effect at $S = 700$ W/m^2 (b) Irradiance effect at $T = 25^o$ C

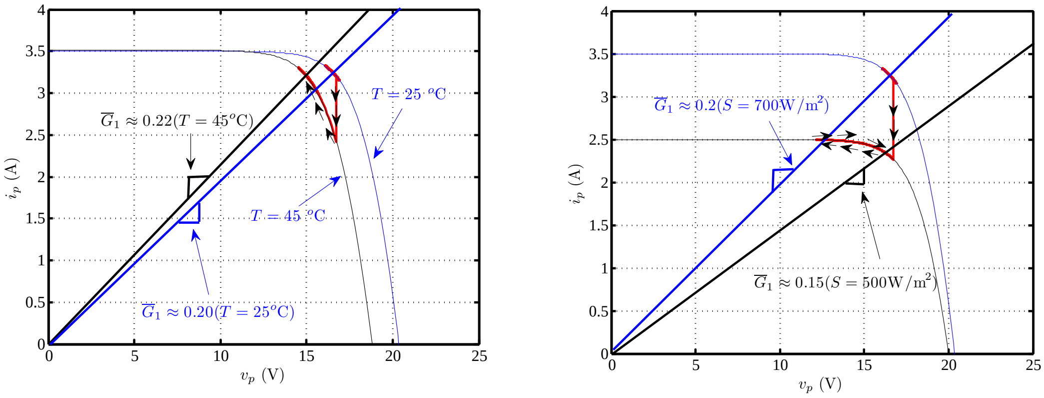

(c) Temperature effect at $S = 700$ W/m^2 (d) Irradiance effect at $T = 25^o$ C

Figure 6.20: Response of the cascaded LFR system supplied by the PV module with the MPPT controller under temperature and irradiation changes.

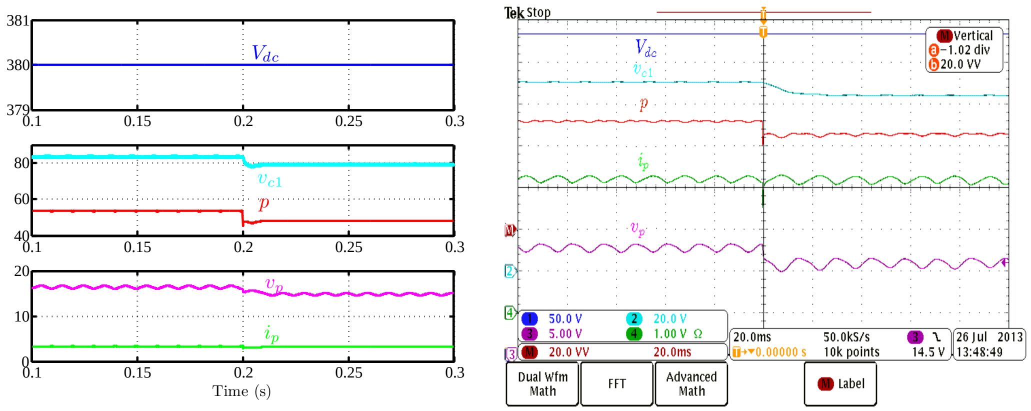

(a) (b)

Figure 6.21: Simulated and experimental waveforms of the system showing the effect of temperature changes at $S = 700$ W/m^2.

the simulation, this slope is coming from the dynamic load (SPS800X13).

The response of the two cascaded boost-based LFRs connected to the PV module with an MPPT have been checked also under the change of temperature T and irradiance S. In order to control such changing conditions, a PV emulator E4360A has been used as a source for the following experimental measurements. Fig. 6.20(a) depicts the response under step change of temperature with the same irradiance $S = 700$ W/m^2. When the temperature increases from 25 ^{o}C to 45 ^{o}C, the power decreases but the system still works at the MPP for this temperature. Similarly, Fig. 6.20(b) illustrates the response of the system under a step irradiance change from $S = 700$ W/m^2 to $S = 500$ W/m^2 at constant temperature $T = 25^o$C. It can be noticed that, the system is able to maintain the power in the vicinity of the MPP under the variation of the external conditions. The PV $i - v$ characteristic curve and the LFR load line are depicted in Fig. 6.20(c) and Fig. 6.20(d) for the same step change in the temperature and irradiance respectively. It can be noticed that, when the temperature increases from 25 ^{o}C to 45 ^{o}C, the average conductance $\overline{G}_{r1}$ changes from 0.2 S to 0.22 S to extract the maximum power as shown in Fig. 6.20(c). However, when the irradiance changes from $S = 700$ W/m^2 to S =500 W/m^2, the conductance $\overline{G}_{r1}$ changes from 0.2 S to 0.15 S for achieving the MPP steady-state for the new conditions as shown in Fig. 6.20(d).

The transient waveforms of the system also are depicted under temperature T and irradiance S changes in Fig. 6.21, 6.22. Figure 6.21(a), 6.21(b) show the response of the system under a step change of temperature with the same irradiance level $S = 700$ W/m^2. When the temperature increases from 25 ^{o}C to 45 ^{o}C, the power decreases but the system converges to the MPP for this temperature after

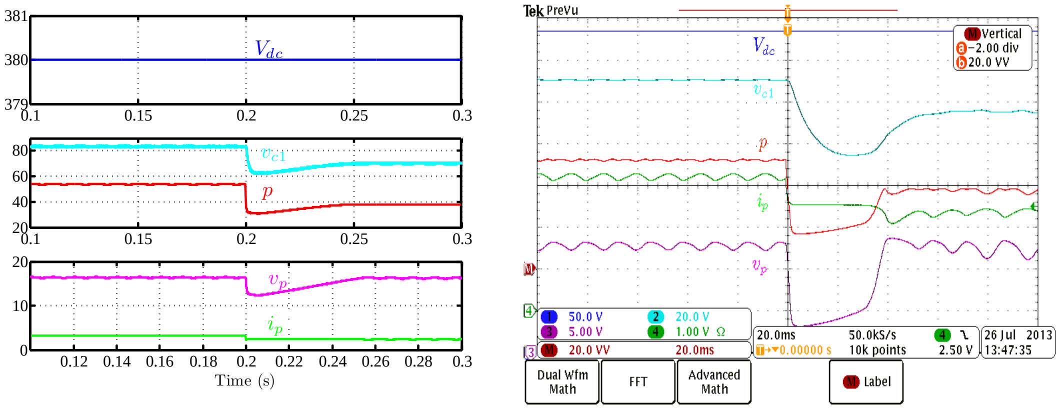

(a) (b)

Figure 6.22: Simulated and experimental waveforms of the system showing the effect of irradiance changes at $T = 25^oC$.

a short transient period of about 10 ms. On the other hand, Fig. 6.22(a), 6.22(b) show the response under a step change of irradiance with the same temperature $T = 25\ ^oC$. When the irradiance decreases from 700 W/m^2 to 500 W/m^2, the power decreases but the system steady state is at the MPP for this temperature after a small transient time of about 30 ms.

6.3 Impedance Matching Between a PV panel and an AC Distribution System

In the previous section, two cascaded LFRs have been used to connect a PV panel to a DC distribution system with a nominal voltage of 380 V. Although many studies suggest the use of a DC distribution bus in the framework of the future distribution system Fahimi et al. (2011), Chang et al. (2013), the AC distribution system is still used as an standard in the current electrical energy distribution and generation system. In this section, two cascaded LFRs will be used to connect a PV generator of 85 W to an AC grid (230 Vrms/ 50Hz) through an H-bridge inverter Camur et al. (2006), Naumanen et al. (2010), as shown in Fig. 6.23.

The used two cascaded LFRs are the same described in section 6.2 in addition to an inverter. The output of the two cascaded LFRs is used to supply an inverter with a minimum DC voltage 340 V. The inverter, in turn, converts the voltage from DC to an AC voltage of 230 V (rms). The inverter is controlled using the LFR concept under SMC as shown in Fig. 6.24. The inverter is controlled using

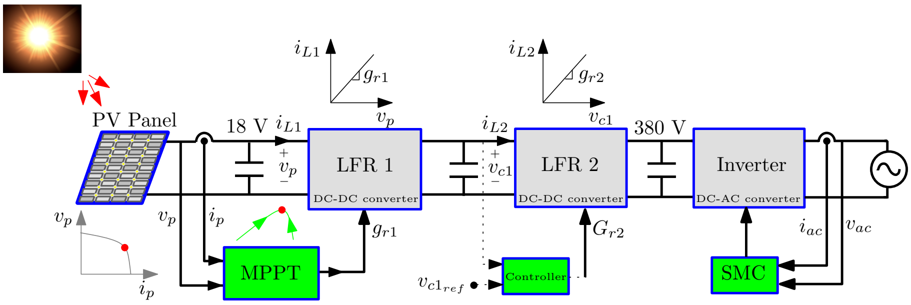

Figure 6.23: Grid connected with PV panel through cascaded DC-DC converters and an inverter.

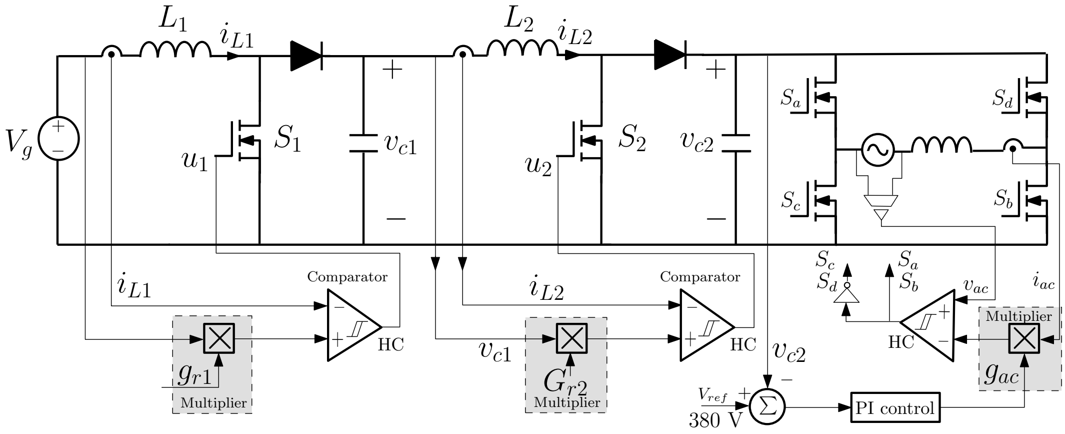

Figure 6.24: Schematic diagram of the three-stage inverters which consist of two cascaded boost converters and an inverter under SMC.

SMC with a switching function that can be expressed as follows

$$s(\mathbf{x}) = g_{ac}v_{ac} - i_{ac} = 0 \tag{6.40}$$

where v_{ac}, i_{ac} are the voltage and the current of the AC grid and g_{ac} is the conductance of the LFR at the grid side. It should be mentioned that the conductance g_{ac} is used to regulate the output capacitor voltage v_{c2} to 380 V. Moreover, it is used for determining the direction of the power flow in the bidirectional converter. The drawing current by the inverter has the fundamental part which is a DC current and some additional harmonics. For simplifying the analysis, the additional harmonics will be neglected to model the inverter as a current source I_d as shown in Fig. 6.25. It has been demonstrated in section 6.2, that the nonlinear characteristic of the PV panel has no effect on the stability of the system. Therefore, the input voltage will be considered a constant voltage V_g for the following analysis.

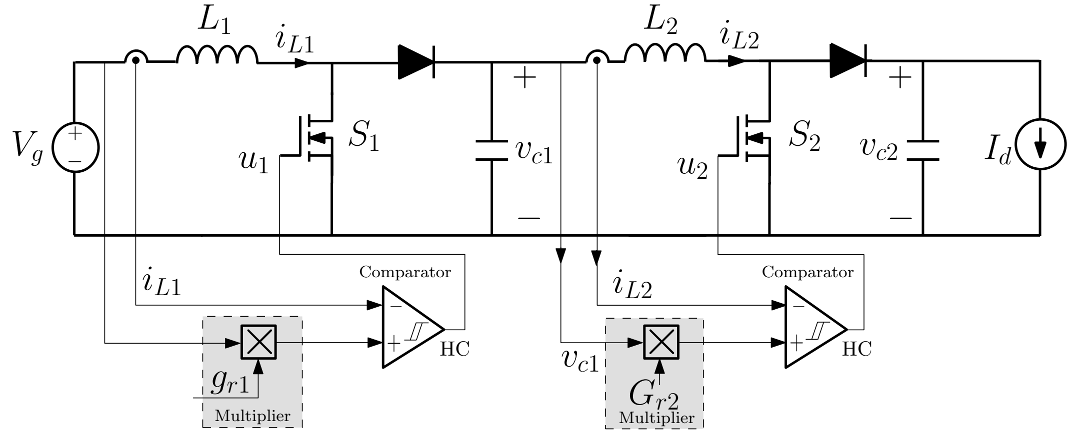

Figure 6.25: Schematic diagram of two cascaded boost converters under SMC loaded by a current source.

Using the same switching functions as Section 6.2, the following reduced-order model can be obtained

$$\frac{\mathrm{d}v_{c1}}{\mathrm{d}t} = \frac{g_{r1}V_g^2}{C_1 v_{c1}} - \frac{G_{r2}v_{c1}}{C_1} \tag{6.41}$$

$$\frac{\mathrm{d}v_{c2}}{\mathrm{d}t} = \frac{v_{c1}^2}{v_{c2}}\left(\frac{G_{r2}}{C_2}(1+\frac{G_{r2}^2 L_2}{C_1})\right) - \frac{G_{r2}}{C_2}\frac{V_g^2}{v_{c2}}\frac{g_{r1}G_{r2}L_2}{C_1} - \frac{I_d}{C_2} \tag{6.42}$$

The equilibrium point of the system can be expressed as follows

$$\mathbf{x}^* = [I_{L1}, I_{L2}, V_{c1}, V_{c2}]^\top = \left[g_{r1}V_g, \sqrt{g_{r1}G_{r2}}V_g, \sqrt{\frac{g_{r1}}{G_{r2}}}V_g, \frac{g_{r1}V_g^2}{I_d}\right]^\top. \tag{6.43}$$

Note that, the output capacitor voltage V_{c2} depends on the drawing current by the inverter I_d and the conductance g_{r1}. It should noted that the steady state value of the intermediate capacitor voltage V_{c1} is depending on g_{r1}/G_{r2}. This voltage can be regulated if we consider $G_{r2} = ag_{r1}$ to assure the ratio $g_{r1}/G_{r2} = a$ where a is a constant value, considering the input voltage is constant. On the other hand, the regulation of the output capacitor voltage v_{c2} is carried out using the control of the inverter using the conductance g_{ac}.

6.3.1 Numerical simulation

In order to verify the previous analytical results, two cascaded boost converters supplied from PV panel with LFR characteristics connected to the AC grid using an H-bridge inverter based on LFR under SMC have been simulated. Table 6.3

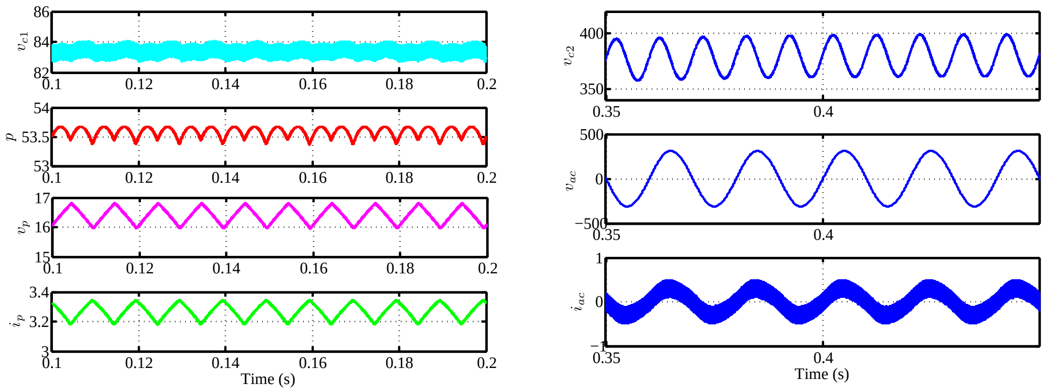

(a) (b)

Figure 6.26: (a) The steady state waveforms v_{c1}, p, v_p and i_p of the two cascaded boost converters. (b) The steady-state waveforms of the input voltage of the inverter v_{c2} and the grid signals v_{ac} and i_{ac}.

Table 6.3: The used parameter values for two cascaded LFR connected to an AC distribution system.

L_1	L_2	$C_1 = C_2$	g_{r1}	G_{r2}
200 μH	2 mH	10 μF	MPPT output	0.043 g_{r1}

shows the parameters of the circuit and their values. The parameters g_{r1}, G_{r2}, L_1, L_2, C_1 and C_2 are chosen to meet steady state and transient performances. It can be noticed that the system has a stable behavior as shown in Fig. 6.26. The steady-state behavior of different variables are shown in Fig. 6.26(a). Note that the PV current and the PV voltage are 180^o out of phase as it can be deduced from the $i - v$ characteristics of the PV panel. It can be observed that the slope change in both current and voltage takes place between two maximum of power because the frequency of the power is twice the frequency of these variables. Moreover, the intermediate voltage frequency is the same like the input current which means that the system is stable. The steady state waveforms of the AC grid are depicted in Fig. 6.26(b) with a frequency 50 Hz and the input voltage of the inverter v_{c2} has a frequency of 100 Hz which is the double frequency of the AC grid. Note that the output voltage v_{c2} is regulated to 380 V. The PI controller has been designed to assure fast response for the system and less transient time in case of occurring any disturbance.

The steady-state waveforms of the system are also depicted under temperature

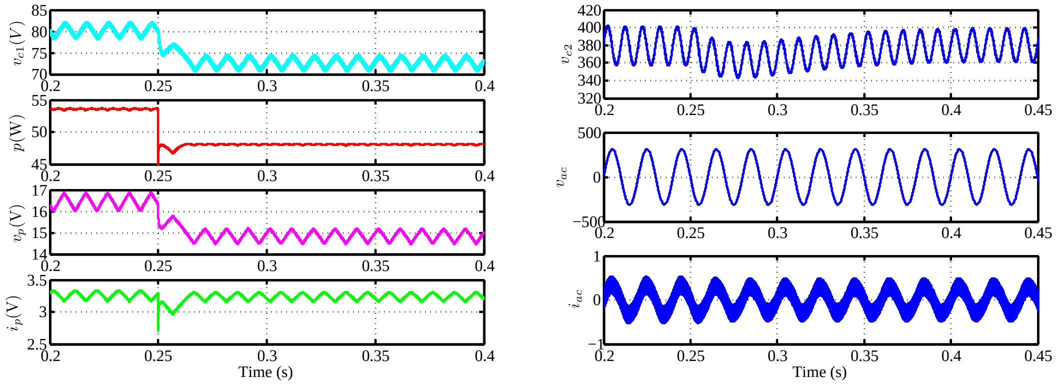

(a) (b)

Figure 6.27: The effect of temperature changes at $S = 700$ W/m^2 (a) The steady state waveforms v_{c1}, p, v_p and i_p of the two cascaded boost converters. (b) The steady-state waveforms of the input voltage of the inverter v_{c2} and the grid signals v_{ac} and i_{ac}.

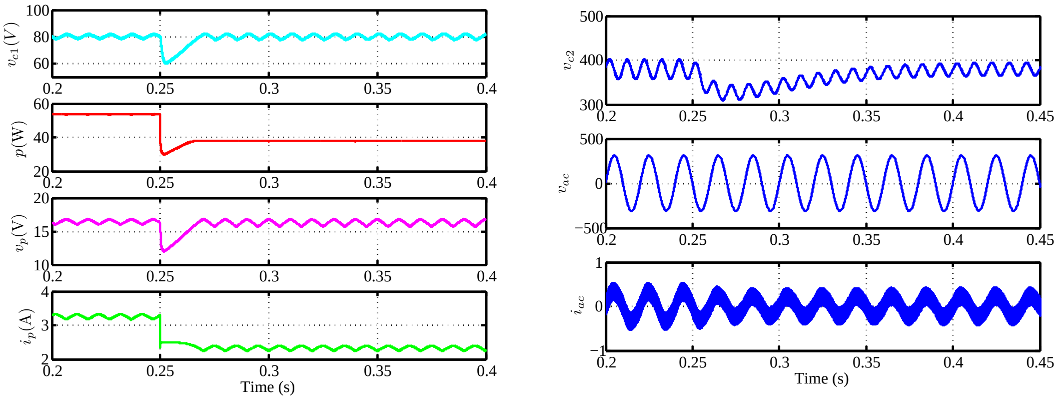

(a) (b)

Figure 6.28: The effect of irradiance changes at $T = 25^o$C (a) The steady state waveforms v_{c1}, p, v_p and i_p of the two cascaded boost converters. (b) The steady-state waveforms of the input voltage of the inverter v_{c2} and the grid signals v_{ac} and i_{ac}.

T and irradiance S changes in Fig. 6.27, 6.28. Figure 6.27 shows the response of the system under a step change of temperature with the same irradiance level $S = 700$ W/m^2. When the temperature increases from 25 ^{o}C to 45 ^{o}C, the power decreases but the system converges to the MPP for this temperature and the PV panel voltage v_p and the intermediate voltage v_{c1} decrease while the output voltage v_{c2} has a transient variation with a settling time around 100 ms keeping the average value regulated around 380 V. On the other hand, Fig. 6.28 shows the response of the system under a step change of irradiance with the same temperature $T = 25\ ^{o}$C. When the irradiance decreases from 700 W/m^2 to 500 W/m^2, the power decreases but the system steady state is at the MPP for this temperature and the PV panel voltage v_p and the intermediate voltage v_{c1} are remaining constant while the output voltage v_{c2} has a transient variation with a settling time around 100 ms. As the power decreases the current injected to the AC grid has also to diminish. For that, the PI control modifies the conductance g_{ac} in order to regulate the voltage V_{c2} around 380 V.

6.4 Conclusion

The cascade connection of two LFRs, has been used in order to step up the low voltage of a PV module to the DC voltage of a DC grid (380 V). The operation of the circuit has been analyzed theoretically and with numerical simulations using the PV and MPPT models which are plugged in the ideal sliding-mode dynamic model. This model, which has been validated by using the full-order switched model, has the advantage of faster simulation time. Moreover, the ideal sliding-mode dynamic model allows to develop a design-oriented description which facilitates the stability analysis of the system. This stability analysis shows that the system exhibits stable LFR characteristics without any conditions. Using the LFR canonical element with SMC in the cascade connection adds simplicity for the stability analysis and the implementation. The experimental tests carried out in the laboratory are in good agreement with the theoretical predictions and show that the extraction of the maximum power can be achieved robustly even in the presence of climate (temperature or irradiance) or load changes. As observed for the proposed system, a high conversion ratio can be achieved together with a very fast tracking speed, high efficiency for the converters and high static MPPT efficiency, which allows to obtain the maximum available energy from the PV module in order to supply a DC distribution system.

Moreover, the two cascaded LFRs have been used to connect a PV panel to an AC grid through an inverter. This system results in unconditionally stable system. The inverter was controlled using LFR under SMC. The output voltage of the two cascaded LFRs has been regulated to 380 V using a PI controller, for supplying the inverter stage. More analysis and experimental work has to be carried out for this cascaded LFRs supplying an AC distribution system as a future work.

Chapter 7

Comparison with Existing High Gain Step-Up Converters

Two cascaded LFRs have been used for impedance matching between a PV panel and a DC or AC distribution system in the previous chapter. In this chapter, other converters with high gain conversion ratio will be studied in order to be compared with the proposed two cascaded LFRs. The two converters which will be studied are the Z-source converter and the high step-up converter based coupled-inductor reported in Wai and Duan (2005). The Z-source converter under SMC will be analyzed theoretically and using numerical simulation. The high step-up converter using coupled-inductor will be analyzed using numerical simulations. The advantages and the disadvantages of each converter will be addressed. Finally, these systems will be compared with the two cascaded LFRs system in terms of size, number of components, dynamic performance and efficiency.

7.1 Z-source Converter Under SMC

The Z-source converter is a power converter with both buck and boost capabilities which has been first proposed in 2002 Peng (2002). Various Z-source topologies have been presented in numerous diversified studies Peng (2002), Peng et al. (2003), Shen et al. (2004, 2006), Liu et al. (2007), Gao et al. (2010), Hanif et al. (2011), Anderson and Peng (2008), Gao et al. (2011), Gajanayake et al. (2009), Nguyen et al. (2010), Cao et al. (2011), Galigekere and Kazimierczuk (2012). Some of the studies are focused on applications, modeling, controls and modulation strategies Peng (2002), Shen et al. (2006), Liu et al. (2007), Gao et al. (2010), Hanif et al. (2011) whereas others are focused on the development of new topologies Anderson and Peng (2008), Gao et al. (2011), Gajanayake et al. (2009), Nguyen et al. (2010).

On the other hand, the Z-source converter has been proposed as an efficient way of obtaining high conversion ratio with relatively low values of the duty cycles. Although, Z-source structure can be used in all these types of power conversions such as AC-DC rectifiers, DC-DC converters, DC-AC inverters and AC-AC converters. Most of the researchers are using the Z-source as an inverter Liu et al. (2007), Cao et al. (2011). The main operation principles of Z-source structure and application of Z-source inverter are investigated in detail in Peng (2002), Peng et al. (2003).

The high gain conversion ratio can be handled either by using a simple step-up converter with high duty cycle, using cascaded converters or using a step-up transformer. The use of a single stage like one boost converter in performing this conversion ratio will imply working with a high duty cycle and therefore the losses will be increased which will in turn jeopardize the system efficiency and reduce the voltage conversion ratio. Moreover, the use of an individual power converter with a high duty cycle to obtain high voltage conversion ratios has some design limitations due to the finite commutation times of the power devices and the size of the passive elements. Besides, the use of a step-up transformer limits the operating frequencies and increases the problems of switching surges. If galvanic isolation is not required, the cascade connection of two boost converters can be a good alternative to obtain high voltage step-up ratios. Moreover, the Z-source converter works with a low duty cycle form 0 to 0.5 for the boost mode. Fig. 7.1 shows the conversion ratio for the boost, two cascaded boost and Z-source converters in terms of duty cycle. These conversion ratios can be expressed as follows

$$M_1 = \frac{1}{1-d} \quad \text{for the boost converter} \tag{7.1}$$

$$M_2 = \frac{1}{(1-d)^2} \quad \text{for the two cascaded boost converters} \tag{7.2}$$

$$M_3 = \frac{1-d}{1-2d} \quad \text{for the Z-source converter} \tag{7.3}$$

For achieving a conversion ratio of 25, the boost converter should work at duty cycle equal to 0.95 which will imply significant losses and would consequently degrade the efficiency of the converter. The use of cascaded boost converters and the Z-source converter can remedy this problem. The two cascaded boost converter should work with a duty cycle of 0.78 for each converter with the assumption that the two gate drive signals are equal to make the same conversion ratio for each boost converter (5 for each one). However the Z-source converter should work with a duty cycle around 0.48 which is very small comparing to the others.

Thus, by controlling the duty ratio D, the output voltage of the z-source converter can be bucked or boosted. In addition, the output voltage can be in-phase or out-of-phase with the input voltage depending on operating regions of the duty

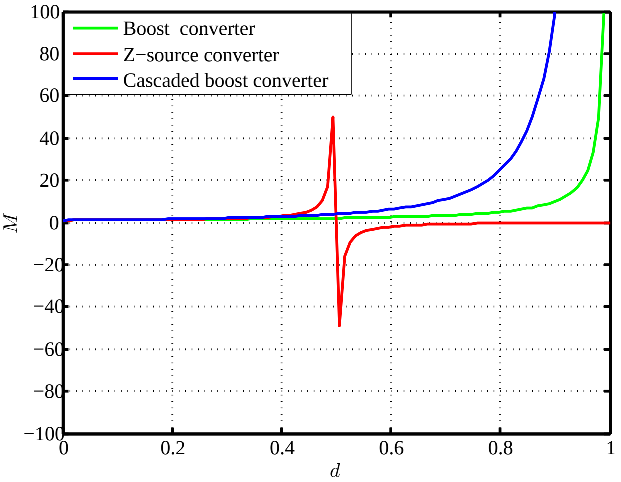

Figure 7.1: The conversion ratio $M(d)$ in terms of the duty cycle d of the boost, two cascaded boost and the Z-source converters.

cycle. In this section, the Z-source will be used as a DC-DC converter based SMC for achieving a high conversion ratio of 25. This Z-source converter will be compared with the previously studied two cascaded LFRs in terms of the static and dynamic performance.

7.1.1 System description

Fig. 7.2 depicts the circuit description corresponding to the Z-source converter under SMC. A single control variable is used to drive the switch of the Z-source converter. The sliding surface imposes that the inductor current i_{Lz1} is proportional to the input voltage of the Z-source converter. The sliding surface can be described with the switching function: $s(\mathbf{x}) = gV_g - i_{Lz1}$. In steady-state $s(\mathbf{x}) = 0$, i.e., $I_{Lz1} = gV_g$. To use the symmetrical behavior of Z-source structure, the Z-source capacitors (C_z) are set equal to each other and Z-source inductors, (L_z) are chosen such as their inductance values and sizes are the same. Then, by the symmetry, the voltage waveforms on the Z-source inductors are identical. The current waveforms through Z-source capacitors are also identical.

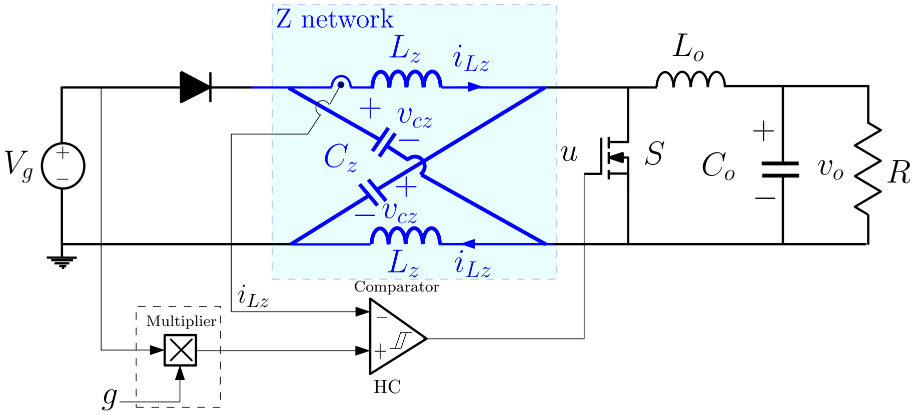

Figure 7.2: The schematic diagram of a Z-source converter under SMC.

7.1.2 Switched model

By applying standard KVLs and KCLs to the circuit depicted in Fig. 7.2, the Z-source converter can be represented by the following differential equations

$$\frac{\mathrm{d}i_{Lz1}}{\mathrm{d}t} = \frac{(1-u)V_g}{L_z} + \frac{(u-1)v_{cz1} + uv_{cz2}}{L_z} \tag{7.4}$$

$$\frac{\mathrm{d}i_{Lz2}}{\mathrm{d}t} = \frac{(1-u)V_g}{L_z} + \frac{(u-1)v_{cz2} + uv_{cz1}}{L_z} \tag{7.5}$$

$$\frac{\mathrm{d}i_{Lo}}{\mathrm{d}t} = \frac{(u-1)V_g - i_{Lo}R}{L_o} + \frac{(1-u)(v_{cz1} + v_{cz2})}{L_o} \tag{7.6}$$

$$\frac{\mathrm{d}v_{cz1}}{\mathrm{d}t} = \frac{(1-u)i_{Lz2} - ui_{Lz1}}{C_z} - \frac{(1-u)i_{Lo}}{C_z} \tag{7.7}$$

$$\frac{\mathrm{d}v_{cz2}}{\mathrm{d}t} = \frac{(1-u)i_{Lz1} - ui_{Lz2}}{C_z} - \frac{(1-u)i_{Lo}}{C_z} \tag{7.8}$$

where V_g is a voltage source which is considered constant. All the other parameters that appear in (7.4)-(7.8) are shown in Fig. 7.2. The signal u is the control variable used to drive the switch of Z-source converter. $u = 1$ during the period T_{ON} and $u = 0$ during the period T_{OFF}.

7.1.3 Equivalent control

The equivalent control variable for the Z-source converter under SMC can be obtained by taking into account the following set of equations defining the sliding mode dynamics

$$s(\mathbf{x}) = gV_g - i_{Lz1} = 0 \tag{7.9}$$

$$\dot{s}(\mathbf{x}) = -\frac{\mathrm{d}i_{Lz1}}{\mathrm{d}t} = 0 \tag{7.10}$$

From (7.4)-(7.8) and (7.9)-(7.10), the following expression is obtained for the equivalent control variable $u_{eq}(\mathbf{x})$

$$u_{eq}(\mathbf{x}) = 1 - \frac{v_{cz2}}{v_{cz1} + v_{cz2} - V_g} \tag{7.11}$$

Note that $u_{eq}(\mathbf{x})$ must be bounded by the minimum and maximum value of u Utkin (1978), Mattavelli et al. (1993), i.e.

$$0 < u_{eq}(\mathbf{x}) < 1 \tag{7.12}$$

By imposing the existence conditions given by (7.12), the sliding domain in the parameter and in the state spaces can be obtained. For instance, in the plane (i_{Lo}, v_{cz1}) and based on (7.11) and (7.12), the sliding mode regime will exist provided that $V_g < v_{cz1}$.

7.1.4 Ideal sliding dynamics and sliding-mode conditions

Substituting (7.11) in (7.4)-(7.8) and taking into account (7.9)-(7.10), the following ideal sliding dynamics reduced-order model is obtained

$$\frac{\mathrm{d}i_{Lz2}}{\mathrm{d}t} = \frac{v_{cz2} - v_{cz1}}{L_z} \tag{7.13}$$

$$\frac{\mathrm{d}i_{Lo}}{\mathrm{d}t} = \frac{v_{cz1} - i_{Lo}R}{L_o} \tag{7.14}$$

$$\frac{\mathrm{d}v_{cz1}}{\mathrm{d}t} = \frac{v_{cz1}(i_{Lz2} - i_{Lo}) + gV_g(V_g - v_{cz2})}{(v_{cz1} + v_{cz2} - V_g)C_z} \tag{7.15}$$

$$\frac{\mathrm{d}v_{cz2}}{\mathrm{d}t} = \frac{v_{cz1}(gV_g - i_{Lo}) + i_{Lz2}(V_g - v_{cz2})}{(v_{cz1} + v_{cz2} - V_g)C_z} \tag{7.16}$$

The equilibrium point can be obtained by forcing the time derivative of the state variables of the averaged model to be null. From (7.13)-(7.16) and taking into account Eq. (7.10), the equilibrium point of the system is given by

$$\mathbf{x}^* = [I_{Lz1}, I_{Lz2}, I_{Lo}, V_{cz1}, V_{c2z}]^\top = V_g \left[g, g, \sqrt{\frac{g}{R}}, \sqrt{Rg}, \sqrt{Rg} \right]^\top \tag{7.17}$$

The control variable $u_{eq}(\mathbf{x})$ at the equilibrium point can be obtained by substituting (7.17) in (7.11). In doing so, one obtains the following steady state value U_{eq} of the control variable $u_{eq}(\mathbf{x})$

$$U_{eq} := u_{eq}(\mathbf{x}^*) \ = \ \frac{1}{2}\frac{\sqrt{R\ g}-1}{\sqrt{R\ g}-1} \tag{7.18}$$

As mentioned before in (7.12) that U_{eq} is bounded between 0 and 1, the following condition should be fulfilled

$$R\ g > 1 \tag{7.19}$$

7.1.5 Stability analysis of the ideal sliding-mode dynamic model

In order to study the stability of the system, the nonlinear model (7.13)-(7.16) is linearized around the equilibrium point $\mathbf{x}^*$ given by (7.17). The Jacobian matrix $\mathbf{J}$ can be expressed as follows

$$\mathbf{J} = \begin{pmatrix} 0 & 0 & -\frac{1}{L_2} & -\frac{1}{L_2} \\ 0 & -\frac{R}{L_o} & \frac{1}{L_o} & 0 \\ a & -a & -b & c \\ d & a & -b & c \end{pmatrix} \tag{7.20}$$

where the parameters a, b, c and d can be defined as follows

$$\begin{aligned} a &= \frac{-\sqrt{Rg}}{C_z(2\sqrt{Rg}-1)}, \quad d = \frac{\sqrt{Rg}-1}{C_z(2\sqrt{Rg}-1)}, \\ b &= \frac{d(\sqrt{\frac{g}{R}}-2g)}{2\sqrt{Rg}-1}, \quad c = \frac{a(\sqrt{\frac{g}{R}}-2g)}{2\sqrt{Rg}-1} \end{aligned} \tag{7.21}$$

The local stability analysis of the system can be carried out by using the characteristic polynomial equation $p(s) = \det(\mathbf{J} - s\mathbf{I}) = 0$ of the linearized system as mentioned previously. Developing this equation, $p(s)$ can be written in the following form

$$p(s) = s^4 + a_3 s^3 + a_2 s^2 + a_1 s + a_0 \tag{7.22}$$

where a_3, a_2, a_1 and a_0 can be defined as follows

$$\begin{aligned} a_3 &= \frac{L_o(b-c)+R}{L_o}, \quad a_2 = \frac{R(b-c)+a}{L_o} + \frac{a-d}{L_z} \\ a_1 &= \frac{a_3(a-d)}{L_z}, \quad a_0 = \frac{((R(b-c)+a)(a-d)}{L_o L_z} \end{aligned} \tag{7.23}$$

Using Routh-Hurwitz criterion, four conditions for stability are obtained, three of them are always fulfilled which are

$$\begin{aligned} a_3 &> 0 \quad (7.24)\\ a_0 &> 0 \quad (7.25)\\ a_2 a_3 - a_1 &> 0 \quad (7.26) \end{aligned}$$

while another one establishes that for stability to be guaranteed, a certain function c that depends on many parameters of the system must be positive. The expression of $c(R)$ of this condition can be expressed as follows:

$$(a_2 a_3 - a_1)\frac{a_1}{a_3} - a_0 a_3 > 0 \quad (7.27)$$

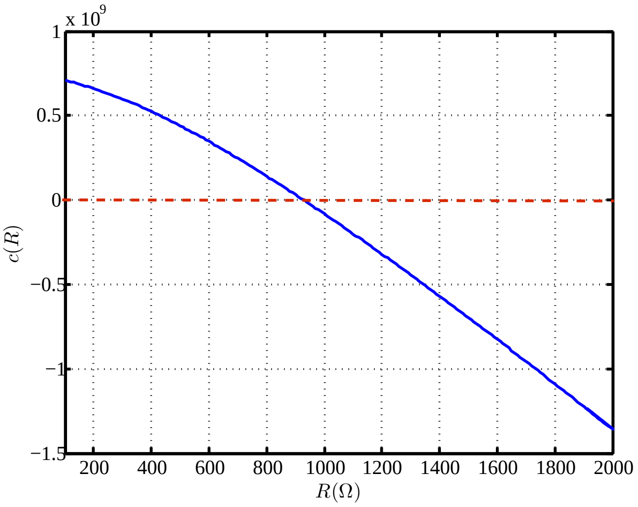

Figure 7.3: The function $c(R)$ establishing the stability condition with respect to the load resistance R. The system is stable if $c(R) < 0$.

However this expression is shown in Fig. 7.3 in terms of the load resistance. The critical value of the load resistance for stability boundary is about 927 Ω, for $R < 927$ the system is stable while for $R > 927$ Ω, the system becomes unstable. It should be noted that the Z-source converter is stable with certain conditions, while the two cascaded LFRs system is unconditionally stable as deduced previously.

7.1.6 Static performances

The static performances can be represented in terms of many figures of merits. The efficiency is considered as the main figure of merit to be compared for the

Z-source converter and two cascaded boost converters based LFRs. Other aspects such as size, weight and cost will be discussed. The efficiency of a switching converter depends mainly on the losses in the parasitic parameters which have been considered ideal in the previous sections. The main losses of the system are due to the inductors (conduction losses), diodes and MOSFETs (conduction/switching losses) while capacitor losses can be neglected because of their small effect. The power lost in the different components of the Z-source converter can be expressed as follows Galigekere and Kazimierczuk (2012), Nguyen et al. (2012)

$$\begin{aligned}
&\text{Inductor Copper Losses:}\\
P_{Lz} &= 2\frac{P_o}{R}\frac{1-D}{1-2D}r_{Lz} \qquad (7.28)\\
P_{Lo} &= 2\frac{P_o}{R}r_{Lo} \qquad (7.29)\\
&\text{Diode Losses:}\\
P_d &= \left[\frac{r_f(1-D)^3}{R(1-2D)^2}+\frac{V_f(1-D)^2}{V_o(1-2D)}\right]P_o \qquad (7.30)\\
&\text{MOSFET Losses:}\\
P_s &= P_o\frac{r_{on}D}{R(1-2D)}+0.5f_sC_{ds}P_oR. \qquad (7.31)
\end{aligned}$$

where r_{Lz} and r_{Lo} are the internal resistances of the inductors L_z and L_o respectively. r_{on} is the ON resistance of the MOSFET, r_f and V_f are the ON resistance and the forward voltage of the Diode respectively and f_s is the switching frequency. Fig. 7.4 shows the Z-source converter efficiency in terms of the duty cycle, it can

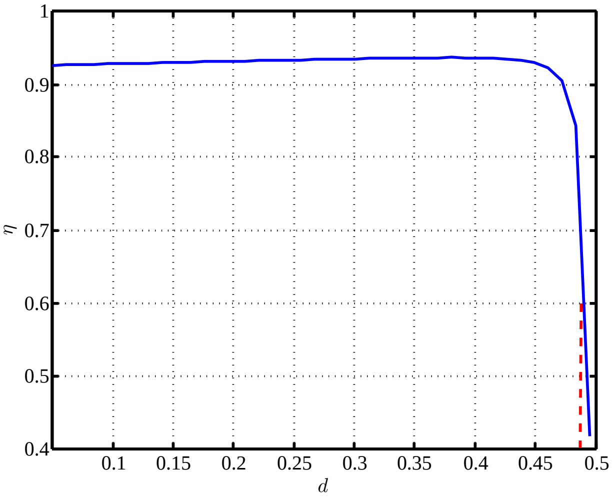

Figure 7.4: Conversion efficiency of the Z-source converter in terms of duty cycle.

be shown that the efficiency is about 60% for duty cycle equals 0.49 (which is the suitable duty cycle for achieving a conversion ratio about 25). This result is confirmed also in Nguyen et al. (2012), Galigekere and Kazimierczuk (2012) and they consider that the maximum duty cycle that the Z-source converter can work is 0.35. Therefore, The Z-source converter has not been implemented, because, in the simulation, the required duty cycle is about 0.49.

For the Z-source converter, although the system is working with a duty cycle less than 50%, the efficiency obtained with the used parameter values is low. The low value of the efficiency can be attributed to the the copper losses of the three inductors. Furthermore, the MOSFET current is equal to the inductor current which increases the switching losses.

On the other hand, the efficiency of the two cascaded LFRs is above 90 % for a wide range of output powers and input voltages as mentioned before. The relatively better efficiency is due to the fact that this system uses only two inductors with different values of currents and two MOSFETs. The switching current in the first MOSFET is large and its switching voltage is the intermediate voltage v_{c1}. For the second MOSFET, its switching voltage is high 380 V but its switching current is relatively small.

From a size point of view, the Z-source converter has three inductors, three capacitors, one MOSFET and one diode, while the two cascaded LFR has two inductors, two capacitors, two switches and two diodes. According to this, the size of the two cascaded LFRs could be smaller than the volume of the Z-source converter.

7.1.7 Numerical simulations

In order to verify the theoretical results predicted in previous Section, the Z-source converter has been simulated by using PSIM software with the set of parameter values depicted in Table 7.1.

Table 7.1: The used parameter values for the Z-source converter.

V_g	V_{cz2}	L_z	C_z	g	R
18 V	380 V	1 mH	100 μF	0.3 S	1500 Ω

The Z-source converter under SMC has been simulated to confirm the previous stability conditions. The system has been tested for two values of the load resistance. Fig. 7.5(a) shows that the system is stable for load resistance R =300 Ω, and it becomes unstable for a load resistance 1500 Ω as it is depicted in Fig. 7.5(b) where it can be observed that a small amplitude and low frequency oscillation appears in the inductor currents and the capacitor voltages.

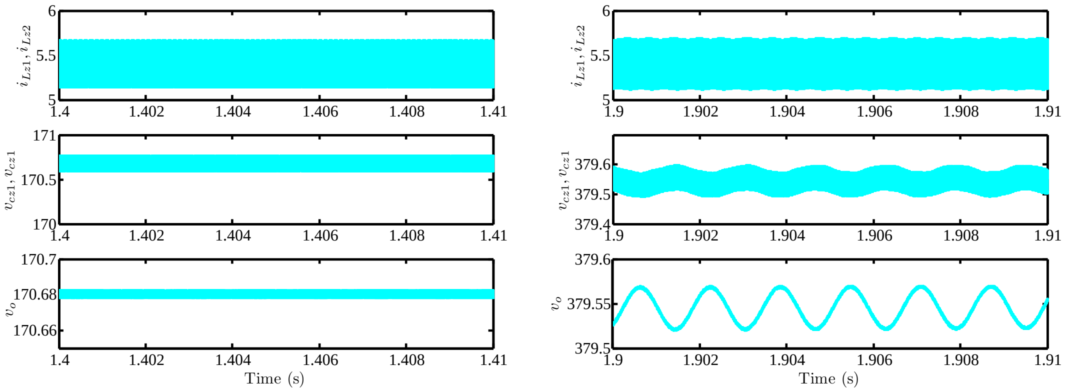

(a) Stable case at load 300 Ω.

(b) Unstable case at 1500 Ω.

Figure 7.5: The inductor current i_L and the capacitor voltages v_c and v_o of the Z-source converter for $g = 0.3$.

7.2 High Step-up Converter Wai and Duan (2005)

Many other converters use coupled-inductor technique to achieve a high gain conversion ratio Wai and Duan (2005), Wai et al. (2008). These converters have high efficiencies above 95% using only one controllable switch. This efficiency is slightly higher than the efficiency obtained by two cascaded LFRs. In this section, the converter proposed in Wai and Duan (2005) has been selected to be compared with the two cascaded LFRs in terms of dynamic performance, size and volume. In order to compare the dynamic performance properly, this coupled-inductor converter was shown to deal with the same problem of interfacing PV modules with a high DC voltage in Wai et al. (2008), and has the benefits of high efficient power conversion with only one controllable switch.

The coupled-inductor converter, which is shown in Fig. 7.6, using a conventional Proportional Integral (PI) controller scheme has been simulated in the same conditions of the two cascaded LFRs connected to a DC distribution system described in Chapter 6. The values of the gain G and the time constant τ_c of the PI controller are mentioned in Table 7.2. Similarly, the same ESC MPPT algorithm has been used to generate the reference for the current controller. Table 7.2 shows the set of parameter values of the converter, which are the same that were reported in Wai et al. (2008) with the exception of the input capacitance C_p. This parameter, which was equal to 3.3 mF in Wai et al. (2008), has been reduced to 100 μF in order to match the input capacitance of the cascaded boost converters.

Figure 7.7 shows the waveforms of a transient simulation of the coupled-

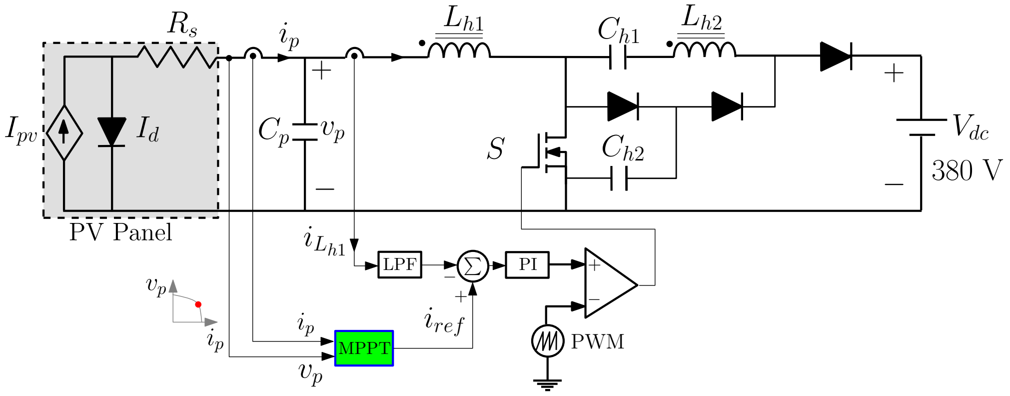

Figure 7.6: Circuit diagram of the coupled-inductor high step-up converter of Wai and Duan (2005) with PI controller.

Table 7.2: The used parameter values for the coupled-inductor converter Wai and Duan (2005).

V_{dc}	L_{h1}	L_{h2}	C_p	C_{h1}	C_{h2}	G	τ_c	f_s
380 V	16 μH	470 μH	100 μF	14 μF	20 μF	0.5 s	0.1 ms	50 kHz

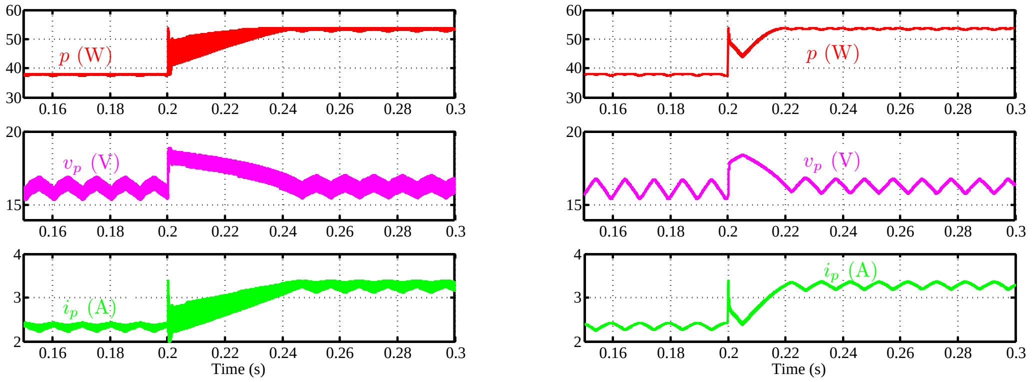

(a) (b)

Figure 7.7: Waveforms of the PV power, voltage and current during an irradiance change from $S = 500$ W/m^2 to $S = 700$ W/m^2 at constant temperature 25^o C (a) Coupled-inductor converter (b) Two cascaded boost converters.

inductor and cascaded boost converters during a step change in irradiance at t = 200 ms. It can be observed in the figure that the settling time of the cascaded boost converters is more than twice faster than the coupled-inductor converter. Furthermore, the much larger input voltage and input current ripples of the coupled-inductor converter do not allow to increase the MPPT gain, because a higher deviation from the MPP would be expected under those conditions. It is worth to remark that a very large and bulky coupled inductance would be required in order to have a switching ripple similar to the one achieved with the cascaded boost converters.

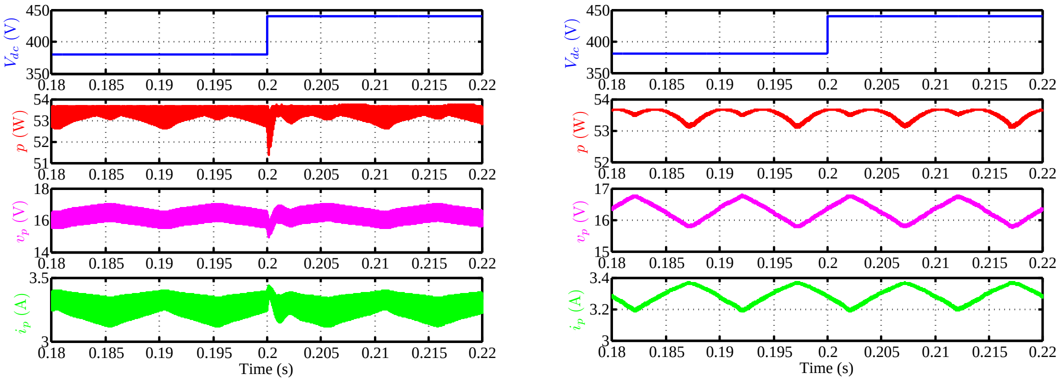

(a) (b)

Figure 7.8: Waveforms of the PV power, voltage and current during an output voltage change from 380 V to 440 V at constant temperature 25^o C (a) Coupled-inductor converter (b) Two cascaded boost converters.

Fig. 7.8 shows the two compared systems response under a step change of the output voltage from 380 V to 440 V. It can be noticed that increasing the output voltage has no effect on the input variables v_p and i_p of the PV module in the two cascaded LFRs system. However, in case of the coupled inductor single-stage converter, the change on the output voltage yields the interruption in the input voltage, input current and extracted input power causing a decrease of the energy production.

In terms of cost and size, the coupled-inductor converter requires three diodes, three capacitors, a MOSFET and a coupled-inductor (i.e.: two inductors on the same core). In turn, the cascaded boost converters needs two diodes, two capacitances, two MOSFETs and two inductors, which for the same input current ripple, they will have smaller volume with respect to the coupled inductor. In general, the two cascaded LFRs system should have less volume and less number of components compared to the high step-up gain converter. The two cascaded LFRs system is more simple than the coupled inductor converter as regards the implementation or the stability analysis. With regard to the drawbacks, the cascaded boost converter requires some additional external circuitry for the sliding mode control and more driver circuitry due to the presence of two MOSFETs, and it presents slightly lower conversion efficiency if a high conversion ratio (around 25) is needed.

7.3 Conclusion

In this chapter, different alternatives to the proposed cascaded approach have been studied and analyzed theoretically and with numerical simulations using PSIM software. The studied converters in this chapter are the Z-source converter and the high gain converter based coupled-inductor. Firstly, large-signal dynamical models and stability analysis of the Z-source converter has been presented out to obtain the conditions for sliding motions and for stability boundary in their design parameter space. The behavior of the Z-source converter has been compared with the two cascaded LFRs which have been studied in a chapter 6. It has been shown that two cascaded LFRs system is better than the Z-source converter in terms of the stability, dynamic, static performances and the efficiency.

Secondly, high gain converter based coupled-inductor, reported in Wai and Duan (2005), has been studied using numerical simulations. It has been shown that the two cascaded LFRs is a better solution than the high gain converter in terms of the dynamic behavior, size and volume. However, the two cascaded LFRs has an efficiency slightly lower than the high gain converter. Therefore, two cascaded boost converters can be considered the best candidate for making the impedance matching between a PV panel and DC distribution system if a high conversion ratio (around 25) is required.

Chapter 8

Output-Parallel-Connected Cascaded LFRs For DC Nanogrid Applications

The nanogrid is a combination of various RESs, is emerging as an alternative electric power supply for remote areas having benefits in terms of both economical and technical viewpoints Boroyevich et al. (2013). A nanogrid is capable of operating in two modes namely Grid connected and Stand-alone Planas et al. (2013), de Souza Ribeiro et al. (2011) (Fig. 8.1). The key components in integration of RESs in the same field of a nanogrid are the power electronic converters and their sophisticated controllers. Different power converter topologies and their control methods for grid-connected operation of a nanogrid are surveyed in Dasgupta et al. (2011a,b). The research on stand-alone operation of a nanogrid for providing electric power supply to household appliances is gaining paramount importance. The focus in this study is on DC systems because most RESs inherently produce DC current facilitating the integration of most modern electronic loads and energy storage devices.

The fluctuation nature of most RES, like wind and solar, makes them unsuitable for standalone operation as they are the sole source of power. A common solution to overcome this problem is the use an energy storage device beside the RES to compensate these fluctuations and maintain a regulated voltage and a smooth and continuous power flow to the load. As the most common and economical energy storage devices in medium-power range are batteries and super-capacitors, a DC-DC converter is always required to allow energy exchange between storage device and the rest of system. These kind of converters must have bidirectional power flow capability with flexible control in all operating modes Sun et al. (2011), Sintupatsuk et al. (2012).

An example of nanogrid will be studied in this chapter. The complete scheme considered in this study is shown in Fig. 8.1. This nanogrid consists of n PV panels

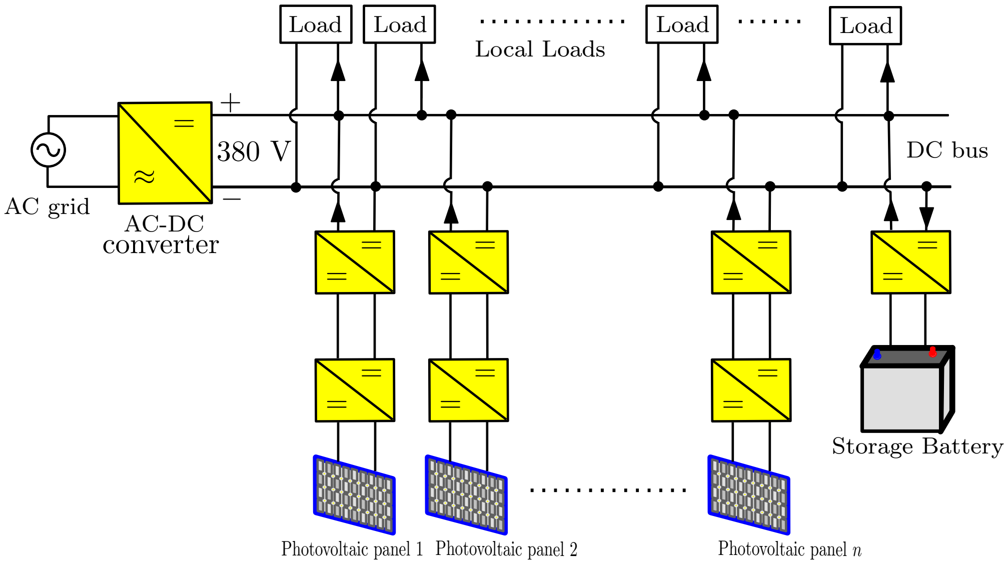

Figure 8.1: Possible DC nanogrid architecture.

with their respective maximum power point (MPP) controllers feeding n output-parallel-connected two-stage boost converters behaving as LFRs. A storage battery connected to a DC grid and behaving also as an LFR is added as a backup for the system. Moreover, the bidirectional converter has another important function which is achieving the regulation for the DC bus.

8.1 Problem Statement

Let us consider a DC nanogrid consisting of n PV panels and a storage battery connected in parallel to a DC bus. Each PV panel is connected to the DC bus through a high conversion ratio converter. A storage battery is connected to the DC grid through a bidirectional DC-DC converter which charges the storage battery in the buck-mode and it provides the stored energy, in the boost-mode, to the bus in case of emergency or a drop of the production of the PV panels. Fig. 8.2 illustrates the problem of load matching in PV generators connected to a DC bus through a switching converter as an interface element. The PV generator and the load have been modeled in the first quadrant $i-v$ characteristic as shown previously.

As mentioned before, the most widely used model for a PV panel is a current source in parallel with a diode, and a series resistance R_s. The current of the PV panel in branch m can be expressed as follows

$$i_{p,m} = I_{pv,m} + I_{0,m} - \frac{V_{ta,m}}{R_{s,m}}\mathcal{L}_m \tag{8.1}$$

where $m = 1, 2, .., n$, $v_{p,m}$ is the voltage of the panel, $I_{pv,m}$ and $I_{0,m}$ are the photovoltaic and saturation currents of the panel respectively, $V_{ta,m}$ is the thermal voltage which is given by $V_{ta,m} = N_s AKT/q$ where A is the diode quality factor, K is Boltzmann constant, q is the charge of the electron, T is the PV panel temperature and N_s is the number of the cells connected in series and $\mathcal{L}_m$ is given by

$$\mathcal{L}_m = \mathcal{W}\left(\frac{R_{s,m}I_{0,m}}{V_{ta,m}}\exp\left(\frac{V_{p,m} + R_{s,m}(I_{pv,m} + I_{0,m})}{V_{ta,m}}\right)\right) \tag{8.2}$$

where $\mathcal{W}$ stands for the Lambert-W function as defined before.

8.2 Output-Parallel-Connected Two-Stage Boost Converter Under SMC

8.2.1 Synthesis of n output-parallel-connected two-stage boost-based LFRs

The goal is to synthesize a system that in steady-state will have the scheme depicted in Fig. 8.2. Each PV panel is connected to a DC bus through a high conversion ratio two-stage LFR. The outputs of the second stage of all the LFRs are connected in parallel to feed the DC grid. Fig. 8.3 depicts a possible practical implementation of this system by means of two-stage DC-DC boost converters under SMC. Each branch of the circuit in Fig. 8.3 consists of two-stage boost converter with two sliding surfaces, one surface for each stage.

8.2.2 Mathematical modeling and stability analysis

A reduced-order model for ideal sliding dynamics for the branch m can be obtained, following the same procedure described in chapter 6, and it can be expressed as follows

$$\begin{aligned}\frac{\mathrm{d}v_{p,m}}{\mathrm{d}t} &= \frac{i_{p,m}}{C_{p,m}} - \frac{g_{1,m}v_{p,m}}{C_{p,m}} && (8.3)\\ \frac{\mathrm{d}v_{c,m}}{\mathrm{d}t} &= \frac{g_{1,m}v_{p,m}^2}{C_m v_{c,m}} - \frac{g_{2,m}v_{c,m}}{C_m} \\ &+ \frac{\alpha_{1,m}g_{1,m}v_{p,m}}{C_m v_{c,m}}(g_{1,m}v_{p,m} - i_{p,m}) && (8.4)\end{aligned}$$

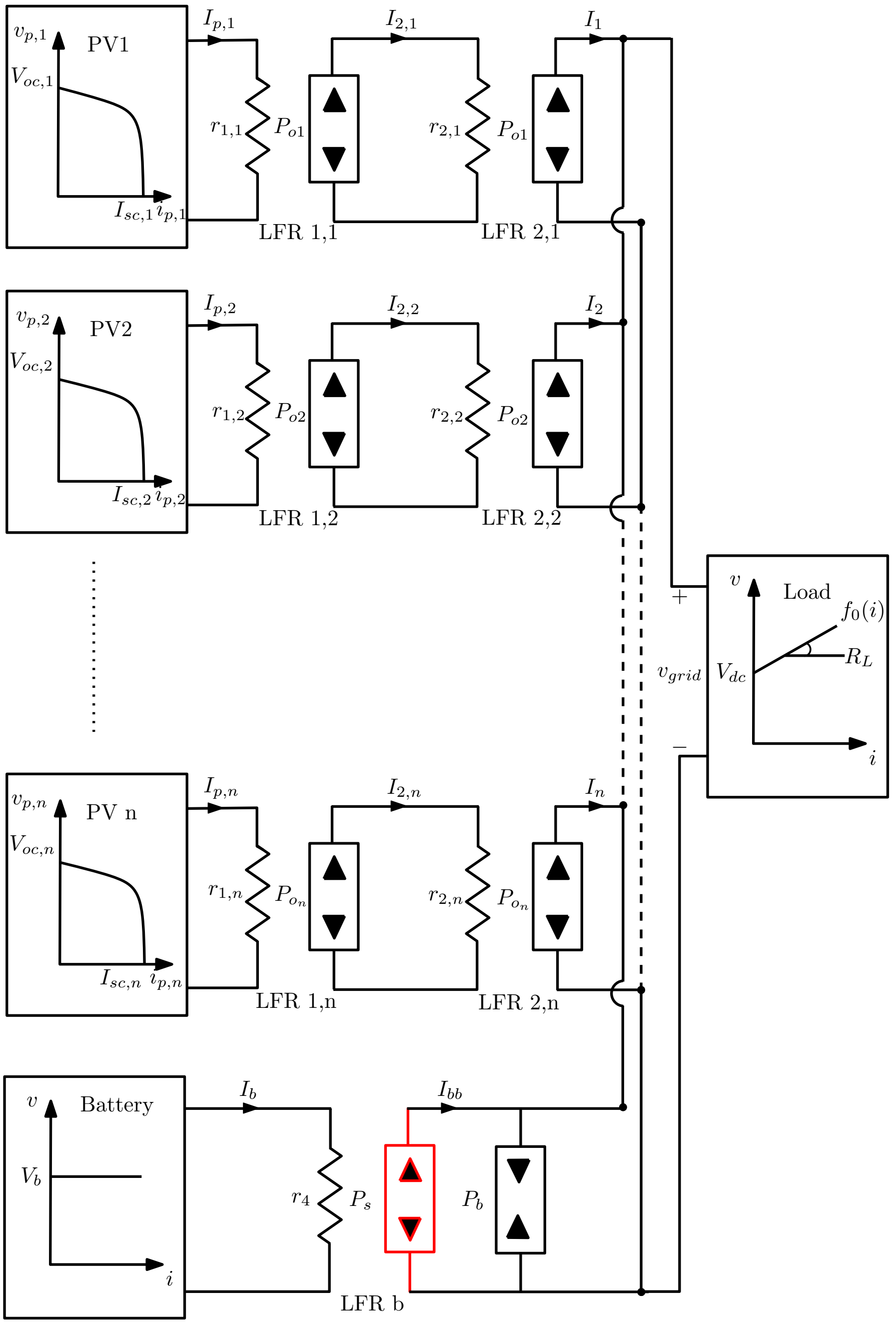

Figure 8.2: Impedance matching of a DC load to a PV panel generator using two cascaded boost-based LFRs and to a DC battery using a bidirectional converter.

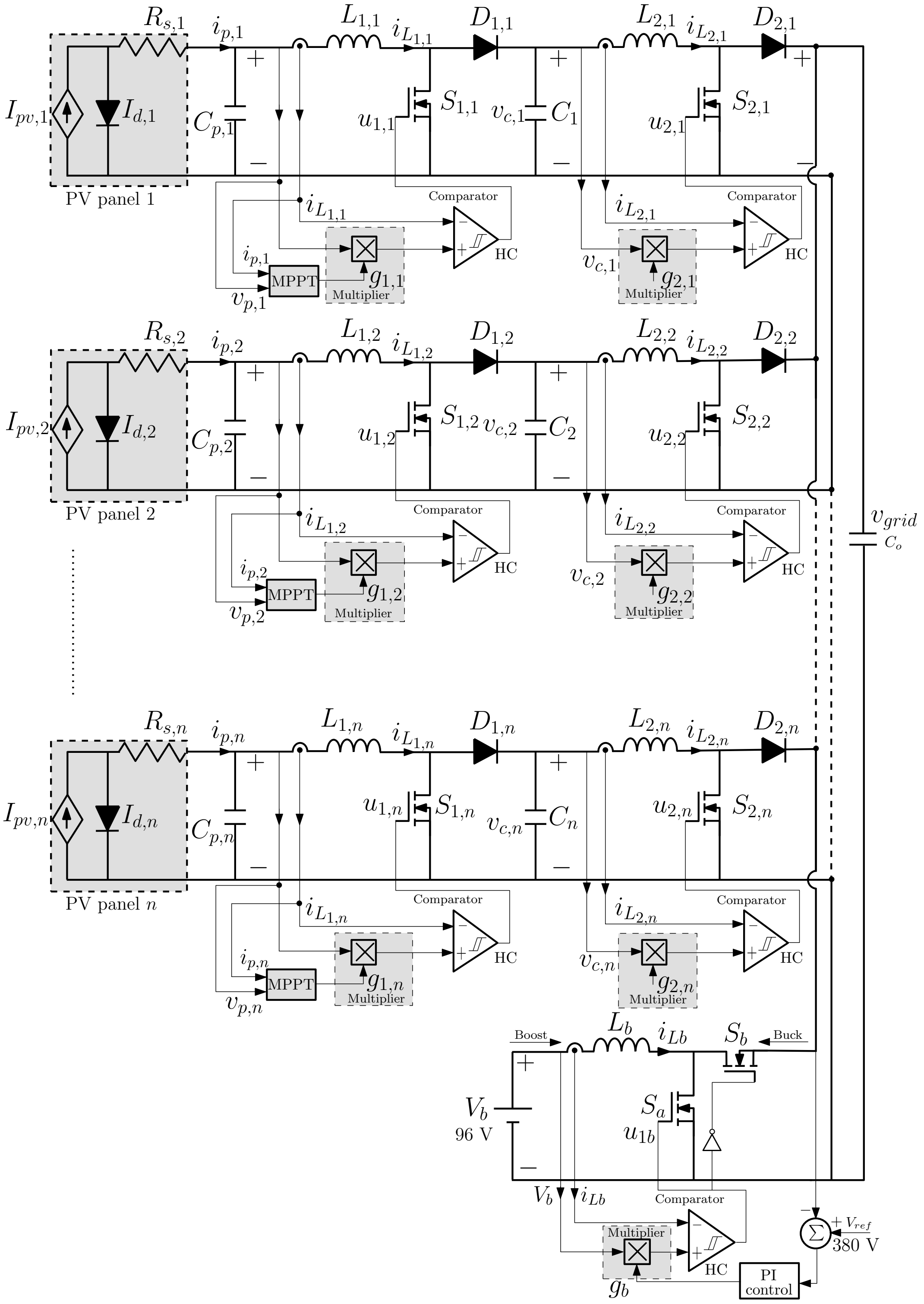

Figure 8.3: Schematic diagram of a nanogrid consisting of n PV panels and a storage battery connected to a regulated DC bus of 380 V.

All the parameters that appear in (8.3)-(8.4) are shown in Fig. 8.3. The next step in our study will be the determination of the equilibrium point of model defined in Eqs. (8.3) and (8.4) and its local stability analysis. In order to get an explicit expression of the equilibrium point, let us suppose that $R_{s,m} = 0$. Therefore, Eq. (8.1) becomes

$$i_{p,m} = I_{pv,m} + I_{0,m} - I_{0,m} \exp(\frac{v_{p,m}}{V_{ta,m}}) \tag{8.5}$$

From (8.3), (8.4) and taking into account the switching functions, the equilibrium point of the ideal sliding dynamics is given by

$$\mathbf{x}^* = [V_{p,m}, V_{C,m}]^\top = \left[\frac{I_{L_{1,m}}}{g_{1,m}}, \frac{I_{L_{1,m}}}{\sqrt{g_{1,m}g_{2,m}}}\right]^\top \tag{8.6}$$

where $I_{L_{1,m}}$ can be expressed as follows

$$\begin{aligned} I_{L_{1,m}} &= I_{pv,m} + I_{0,m} \\ &- g_{1,m}V_{t,m}\mathcal{W}\left(\frac{I_{0,m}}{g_{1,m}V_{ta,m}}\exp\left(\frac{I_{pv,m}+I_{0,m}}{g_{1,m}V_{t,m}}\right)\right) \end{aligned} \tag{8.7}$$

It can be observed that $I_{L_{1,m}} = g_{1,m}V_{p,m}$ and $I_{L_{2,m}} = g_{2,m}V_{C,m}$ which is a result of imposing an LFR behavior to each branch and each stage of the circuit of Fig. 8.3. The characteristic polynomial equation of the linearized system can be obtained from $\det(\mathbf{J} - s\mathbf{I}) = 0$, where $\mathbf{J}$ is the Jacobian matrix of (8.3)-(8.4). Developing this equation, the characteristic polynomial equation corresponding to a branch m can be written in the flowing form

$$(s + \mathcal{M}_m)\left(s + \frac{2g_{2,m}}{C_m}\right) = 0 \tag{8.8}$$

where $\mathcal{M}_m$ is given by

$$\mathcal{M}_m = \frac{R_{s,m}g_{1,m}(1+\mathcal{L}_m) + \mathcal{L}_m}{R_{s,m}C_{p,m}(1+\mathcal{L}_m)} \tag{8.9}$$

The characteristic equation corresponding to the branch m has two roots located in the left half plane, and hence, each branch is unconditionally stable. Note that the dynamics of the branches are uncoupled from each other and therefore the overall system consisting of n output-parallel-connected two-stage boost converters behaving as LFRs is also unconditionally stable. It should be mentioned that the two cascaded LFRs output voltage depend on the load and is not regulated. Therefore, in this analysis, the voltage of the grid has been considered constant at 380 V. This voltage actually can be regulated using a bidirectional converter connected to a DC battery which can be considered as a back-up as will be described in the following section.

8.3 Bidirectional Converter Based on a LFR for DC Bus Voltage Regulation

The bidirectional DC-DC power converter is part of the nanogrid Boroyevich et al. (2010). The aim of using the bidirectional DC-DC power converter is to regulate the DC bus voltage despite the interactions of all the sources and loads. In the nanogrid and microgrid, the load, which can be another converter, is considered a Constant Power Load (CPL). In Lenz Cesar and Pagano (2013), Stramosk and Pagano (2013), the bidirectional converter loaded with a CPL has been studied using different kind of controls (Passivity-Based Control (PBC), Immersion & Invariance (I&I) and Sliding Mode Control (SMC). Moreover, a lot of studies have been carried out for converters loaded with a CPL Emadi et al. (2006), Rahimi et al. (2006), Veerachary and Sudhakar (2009), Onwuchekwa and Kwasinski (2010, 2011). The stability analysis shows that the system can exhibit a kind of instability, if certain conditions are not achieved.

A bidirectional DC-DC converter connected to a 380 V DC bus and supplied from a 96 V storage back-up battery is depicted in Fig. 8.4. One of the main functions of this converter is to regulate the DC bus voltage. This converter works in the buck-mode (power sink) in case of charging the battery when the input power p_{in} is lower than the absorbed power p_b. In turn, it works in the boost-mode (power source) in order to supply the DC grid in case of emergency when p_{in} is higher than p_b. In this work, this bidirectional converter is also controlled using an SMC strategy imposing an LFR at the port connected to the battery. To impose an LFR behavior, its switching condition is selected as follows

$$s_b(\mathbf{x}) \quad = \quad g_b V_b - i_{L_b} \tag{8.10}$$

where V_b is the storage battery voltage. The derivative of the switching condition can be expressed as follows

$$\dot{s}_b(\mathbf{x}) \quad = \quad -\frac{\mathrm{d}i_{L_b}}{\mathrm{d}t} = 0 \tag{8.11}$$

By controlling the sign of parameter g_b, the direction of the power flow of the bidirectional converter can be fixed. If g_b is positive, the converter works in the charging boost-mode delivering the power for the grid, and if it is negative, it works in the charging buck-mode. The parameter g_b is the responsible for regulating the DC bus, and it is generated by using a PI controller as shown in Fig. 8.4. The design of this controller should be carried out in such a way to reduce the charging time of the battery. More information about the design of PI controller with LFR can be found in Cid-Pastor et al. (2010) The circuit depicted in Fig. 8.4 can be expressed using the following differential equation

$$\frac{\mathrm{d}i_{L_b}}{\mathrm{d}t} = \frac{V_b}{L_b} - \frac{v_{grid}}{L_b}(1-u_b) \tag{8.12}$$

$$\frac{\mathrm{d}v_{grid}}{\mathrm{d}t} = \frac{i_{L1}}{C_o}(1-u_b) - \frac{P_b}{v_{grid}C_o} \tag{8.13}$$

$$\frac{\mathrm{d}g_b}{\mathrm{d}t} = \frac{\kappa_p}{\tau}(V_{ref}-v_{grid}) - \kappa_p(\frac{i_{L1}}{C_o}(1-u_b) - \frac{P_b}{v_{grid}C_o}) \tag{8.14}$$

where κ_p is the proportional gain and τ is the time constant of the PI controller.

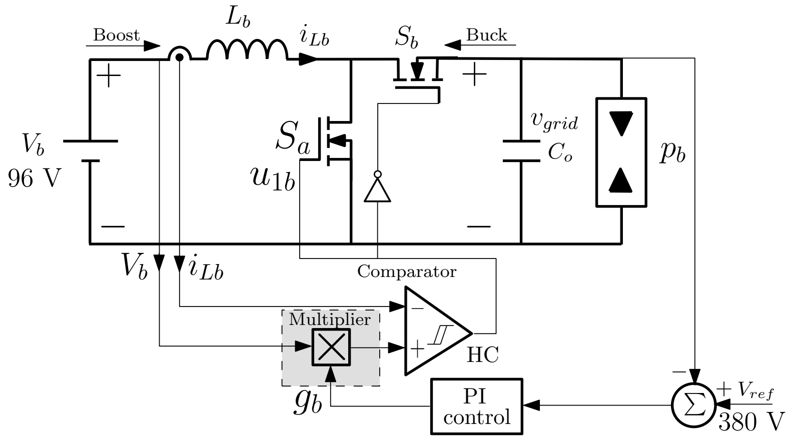

Figure 8.4: Bidirectional converter under a SMC strategy imposing an LFR behavior.

Following the same procedure mentioned in the Section 8.3 and from Eqs.(8.10), (8.11) and (8.12)-(8.14), the equivalent control $u_{b_{eq}}$ for the bidirectional converter can be expressed as follows

$$u_{b_{eq}} = 1 - \frac{V_b}{v_{grid}} \tag{8.15}$$

From (8.12), (8.14) and taking into account the switching function, the reduced order model is as follows

$$\frac{\mathrm{d}v_{grid}}{\mathrm{d}t} = \frac{g_b}{C_o}\frac{V_b^2}{v_{grid}} - \frac{P_b}{v_{grid}C_o} \tag{8.16}$$

$$\frac{\mathrm{d}g_b}{\mathrm{d}t} = \frac{\kappa_p}{\tau}(V_{ref}-v_{grid}) - \kappa_p(\frac{g_bV_b^2 - P_b}{v_{grid}C_o}) \tag{8.17}$$

Using the reduced order model (8.16)-(8.17) and the switching function, the equilibrium point of the system is given by

$$\mathbf{x}^* = [I_{L_b}, V_{grid}, G_b]^\top = \left[G_bV_b, V_{ref}, \frac{P_b}{V_b^2}\right]^\top \tag{8.18}$$

The characteristic polynomial corresponding to the bidirectional converter can be written in the flowing form

$$\tau C_1^2 V_{ref}^3 s^2 + \tau \kappa_p C_1 V_b V_{ref}^2 (2V_{ref} - V_b)s + \kappa_p V_b^2 (V_{ref}^2 C_1 + 2\tau P_b) \qquad (8.19)$$

If the bidirectional converter works as a boost converter, the load is considered a constant power load and the system will be stable. If the bidirectional converter works as a buck converter, the grid will be modeled as a power sink $P_b = -P_s$. Therefore, the following stability condition should be achieved

$$P < \frac{V_{ref}^2 C_1}{2\tau} \qquad (8.20)$$

It can be concluded that the bidirectional converter is stable when it works as a boost converter and stable with condition when it works a a buck converter.

Table 8.1: The used parameter values for the DC nanogrid example.

$L_{1,m}$	$L_{2,m}$	$C_{p,m}$	C_m	$g_{2,m}$	h_1	h_2
200 μH	2 mH	100 μF	10 μF	0.008 S	0.25 A	0.17 A

8.4 Numerical Simulations

In order to verify the previous theoretical results, a system consisting of four PV panels and a storage battery are connected to synthesize a DC nano-grid and simulated using PSIM. Table 8.1 shows the parameter values used in the numerical simulations. The variables $g_{1,m}$ for all the branches are generated by performing an MPPT in all the PV generators. The system has been checked under a partial change of irradiance S of only two branches. Fig. 8.5 depicts the response of the system under a step change of the irradiance which was increased from 700 W/m^2 to 900 W/m^2 in the third branch while it was decreased from 700 W/m^2 to 500 W/m^2 in the fourth branch. The temperature has been maintained at 25^{o}C for all the tests. It can be noticed that, while the extracted power from the third PV panel increases and the extracted power of the fourth PV panels decreases due to the simulated effect of partial shadowing, it still works at its MPP and that the power in the first and the second branches is not affected by the change of the irradiance in the other branches.

The system has been also checked under the same temperature and irradiance for the four PV panels, when connecting a 200 W load to the DC grid at time 0.25 s as shown in Fig. 8.6. It is clear, that connecting the load has no effect

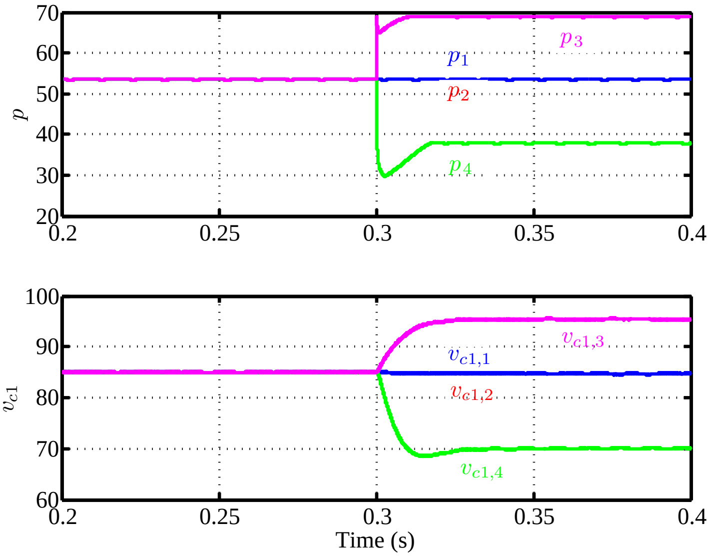

Figure 8.5: Response of the system supplied by the PV panel with the MPPT controller under a step change in the irradiation for the third PV panel from 700 W/m^2 to 900 W/m^2 and for the fourth PV panel from 700 W/m^2 to 500 W/m^2.

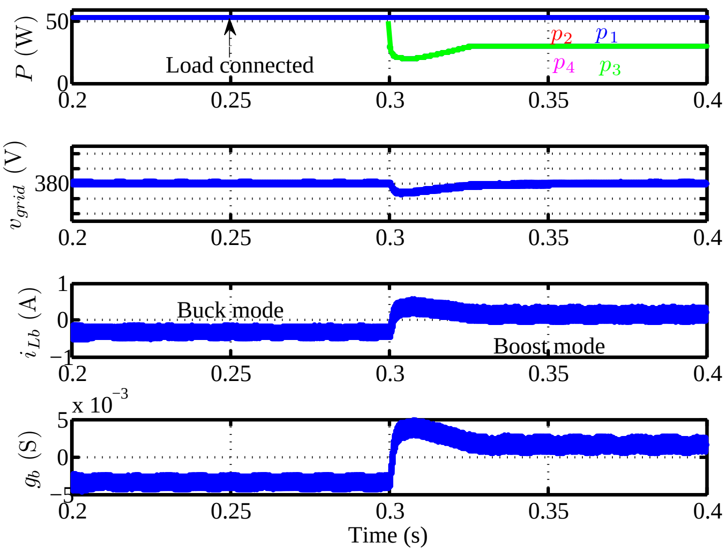

Figure 8.6: Waveforms of the bidirectional converter when the irradiance for the third and fourth PV panels changes from 700 W/m^2 to 500 W/m^2.

on the steady-state waveforms of the PV panels. After that, the irradiance of the third and fourth PV panels changes from 700 W/m^2 to 400 W/m^2 at 0.3 s which consequently changes the delivered power by the four PV panels to the DC grid form 220 W to 180 W. It can be noticed that the bidirectional converter works in the buck-mode at 700 W/m^2 irradiance level. The extracted power from the panel is enough for supplying the load and the extra generated power is used to charge the battery through the bidirectional converter. When the irradiance for two PV panels changes from 700 W/m^2 to 500 W/m^2, the total generated power (180 W) is not enough for supplying the load and in this case the sign of the parameter g_b is inverted automatically by using the PI control and therefore the power flow in the bidirectional converter is changed being working in the boost-mode to supply the load with the necessary power. Although, the voltage of the grid is affected by the change of the irradiance of the PV panels, It is still regulated around 380 V. However, as mentioned before in the load test, changing the voltage of the grid has no effect on the extracted input power from the PV generators.

8.5 Conclusions

In this chapter, the cascade connection of LFRs has been used to design a DC nanogrid constituted by n PV modules, a battery and a DC distribution bus of 380 V. It has been used n output-parallel-connected converters behaving as LFRs to connect n PV panels to a DC distribution bus of 380 V. A storage battery connected to a DC bus through a bidirectional converter is also aggregated as a backup for the system and for regulating the DC bus of 380 V. An extremum seeking MPPT controller is used for each PV panel which are connected to the DC grid using two cascaded LFRs to step up the low voltage of the PV panel to the DC voltage of the grid (380 V). Mathematical modeling and stability analysis of the system have been addressed. This stability analysis shows that the overall system is stable whenever the two-stage subsystems in each branches are in turn stable. The stability of each branch can be guaranteed by imposing an LFR behavior at the input port of each stage. This can be achieved by a SMC strategy applied to all the stages and branches. The storage battery dynamics can also be controlled by the same strategy. The direction of the power flow can be dictated by comparing the grid voltage and the reference voltage using a PI controller which in turn determine the signum of the parameter g_b. In addition, the bidirectional converter is responsible for achieving the regulation for the DC bus using a PI controller. Numerical simulations have been carried out for a system consisting of four branches corroborate the theoretical derivations.

Chapter 9

Summary and Conclusions

This chapter presents a summary of the contributions and final remarks of this thesis and suggests future research directions.

9.1 Summary of Contributions

In this thesis, the cascaded connection of canonical elements for energy processing such as gyrator, DC-transformer and loss-free resistor based on SMC has been tackled in a general context of power electronics in Chapter 2, Chapter 3, Chapter 4 and Chapter 5. The cascaded connection has been used for impedance matching between a PV panel and a DC or AC distribution system in Chapter 6 using high conversion ratio. In order to evaluate this cascaded system in this kind of applications, some alternatives for high gain conversion ratios have been studied in Chapter 7. Then, the cascaded connection has been used to synthesize a nanogrid based on a DC distribution system. The main DC bus of the DC nanogrid is regulated to 380 V using a bidirectional converter connected to a battery as an energy storage element in Chapter 8. Next, A brief summary of the main points considered in this thesis are listed.

Cascade connection of canonical elements

An approach is proposed to connect in cascade DC-DC switching converters to obtain a high voltage conversion ratios by using the concept of canonical elements in power processing. These canonical elements, named DC-transformers, power gyrators and LFRs, have been implemented by means of the SMC technique. It has been found that the two cascade DC-transformers results in a fourth-order unconditionally stable system. In turn a DC-transformer based on two cascaded boost converters using a single sliding surface result in a fifth-order stable system with certain stability conditions detailed in Chapter 2. The presence of the inductors in the input and output port is necessary for synthesizing the DC-transformer in SMC. In both systems, neither the existence of the sliding-mode regimes, nor the output voltage depends on the load resistance variations. Although the two structures could be using for obtaining high voltage regulators from low voltage sources such as PV panels, they cannot be used for high conversion ratio applications. Furthermore, when the load resistance decreases in the two mentioned systems, the input current increases, that yields to an input power increase, for a constant input voltage, which is not suitable for renewable energy sources (RES) applications. For low gain conversion ratio application, the two cascaded DC-transformers will be preferable than the DC-transformer based on two cascaded boost in terms of dynamic performance. Also it is worth to mention, that two cascaded (similar or different) canonical elements can be modeled using a single DC-transformer.

Furthermore, the two cascaded gyrators and the cascaded LFR-gyrator systems yield to a second-order unconditionally stable system. However, the existence conditions of sliding-mode regimes for the two systems are more difficult to accomplish than in the case of DC-transformers because the load resistance should be confined between two certain values (Table. 9.1). Moreover, the steady-state of the intermediate voltage V_{c1} in both cases depends on the load resistance and input voltage variations which could complicate the implementation of a high voltage regulator. Additionally, it has been found that the dynamic performance during the start-up and under input voltage disturbances, corresponds to a highly under-damped behavior with large transient period for the two cascaded gyrators. However, this transient time is smaller in case of the cascaded LFR-gyrator.

The two cascaded boost converters based on one canonical element (g-gyrator or LFR) under a single sliding surface have been analyzed theoretically and using numerical simulations and validated by experimental measurements. It has been shown that the two systems can work for high conversion ratio applications. The interconnections result in a third order stable system with certain conditions. Moreover, the existence condition of sliding-mode regime of the two systems depends on the load resistance but this condition is less restrictive than the case of the two cascaded gyrators. However, the steady-state variables V_{c1} and V_{c2} for the two systems depend on the load resistance and the input voltage and the response of the systems based on one canonical element is slower than the previous cases.

In addition, the two cascaded LFRs and the cascaded gyrator-LFR systems have been analyzed theoretically and using numerical simulations and validated by experimental measurements.. The two systems result in a second-order unconditionally stable systems. The characteristic equations of the two systems have two real poles resulting in an over-damped transient response with shorter transient period than the obtained in the previous mentioned cases. In this case, the existence conditions of sliding-mode regime of the two systems depend on the load resistance but are less restrictive than in the case of the two cascaded gyrators interconnection (Table. 9.1). However, the sliding regime of the two cascaded LFRs is wider than the cascaded gyrator-LFR. In addition, the response of the two cascaded LFRs is faster than the cascaded gyrator-LFR. Another particular feature of the cascaded LFRs is that the intermediate voltage V_{c1} and the input current of the first LFR are not sensible to output load variations. This detail suggests that the cascade connection of boost-based LFRs is a good candidate for the implementation of an adaptation stage between a PV generator (18 V) and a 380 V DC bus voltage. The fact that the disturbances that might occur at the output port are not transferred to the input port would allow the implementation of a fast MPPT of the PV generator irrespective of the output port disturbances. Based on this discussion, the cascade connection of two LFRs could be considered as the best candidate to obtain high voltage conversion ratios with good dynamic and good line and load regulation performances. Moreover, it has been demonstrated that the cascade connection of m LFR based on the boost converter is stable irrespective of the number of cascaded elements.

Impedance matching in DC or AC distribution system

As discussed before, the cascade connection of LFRs is the most promising approach in terms of dynamic response and stability to obtain a power stage with a high conversion ratio. For that, it has been studied in deep in the case of impedance matching between a low voltage PV generator and a DC bus of 380 V. The system has been analyzed theoretically and using numerical simulations using the nonlinear PV model and the MPPT model. It has been deduced that the system is a second order unconditionally stable. This system has been tested under temperature, irradiance and load variations. It has been shown that the system can extract the maximum power from the PV panel regardless the temperature or irradiance variation. All the simulation results have been confirmed by means of experimental results.

Many alternative converters for high gain conversion ratio applications exist in the literature and can be used for impedance matching. In order to compare with the cascaded LFRs, the Z-source converter under SMC has been analyzed theoretically and using numerical simulations. However, the Z-source converter results in a stable system with certain conditions. Furthermore, it has a very low efficiency comparing to the two cascaded LFRs.

The high gain converter based on coupled-inductor reported in Wai and Duan (2005) has a high efficiency about 95% which is slightly higher than the efficiency of the two cascaded LFRs in the same power level. Therefore, this converter

Table 9.1: The main results of the analysis of two cascaded converters with different canonical elements.

Canonical elements	Switching functions	Conversion ratio	SM conditions
Two DC-transformers	$s_1(\mathbf{x}) = i_{L2} - k_{11} i_{L1}$ $s_2(\mathbf{x}) = i_{L3} - k_{12} i_{L2}$	$\frac{V_{c2}}{V_g} = \frac{k_{11}}{k_{12}}$	$k_{11} k_{12} < 1$ $k_{11} < 1$
One DC-transformer	$s(\mathbf{x}) = k i_{L1} - i_{L2}$	$\frac{V_{c2}}{V_g} = \frac{1}{k}$	$0 < k < 1$
Two Gyrators	$s_1(\mathbf{x}) = g_1 v_{c1} - i_{L1}$ $s_2(\mathbf{x}) = g_2 v_{c2} - i_{L2}$	$\frac{V_{c2}}{V_g} = \frac{g_1}{g_2}$	$\frac{1}{g_2} < R < \frac{g_1}{g_2^2}$
One Gyrator	$s(\mathbf{x}) = i_{L1} - g v_{c2}$	$\frac{V_{c2}}{V_g} = gR$	$R\, g > 1$
Two LFRs	$s_1(\mathbf{x}) = i_{L1} - g_{r1} V_g$ $s_2(\mathbf{x}) = i_{L2} - g_{r2} v_{c1}$	$\frac{V_{c2}}{V_g} = \sqrt{R g_{r1}}$	$R > \frac{1}{g_{r1}}$ $g_{r1} > g_{r2}$
One LFR	$s(\mathbf{x}) = i_{L1} - g V_g$	$\frac{V_{c2}}{V_g} = \sqrt{R g_{r1}}$	$R\, g_r > 1$
LFR and gyrator	$s_1(\mathbf{x}) = i_{L1} - g_{r1} V_g$ $s_2(\mathbf{x}) = i_{L2} - g_2 v_{c2}$	$\frac{V_{c2}}{V_g} = \sqrt{R g_{r1}}$	$\frac{1}{g_2} < R < \frac{g_{r1}}{g_2^2}$
gyrator and LFR	$s_1(\mathbf{x}) = i_{L1} - g_1 v_{c1}$ $s_2(\mathbf{x}) = i_{L2} - g_{r2} v_{c1}$	$\frac{V_{c2}}{V_g} = g_1 \sqrt{\frac{R}{g_{r2}}}$	$R > \frac{1}{g_{r2}}$ $g_1 > g_{r2}$

has been studied in detail for impedance matching between a PV panel and a DC distribution system under the same conditions of the two cascaded LFRs. The dynamic behavior of this system has been checked during load change and start-up. It has been shown that the transient time for the coupled-inductor boost converter is higher than the two cascaded LFRs, while the load variation is perturbing the input power, input voltage and input current in case of the coupled-inductor boost converter. On the contrary, the load change has no effect in the input power, input voltage and input current for the two cascaded LFRs.

Moreover, the structure based on two cascaded LFRs has less volume and number of components compared to the Z-source converter or the coupled-inductor boost converter. This confirms that the two cascaded LFRs is the best candidate for the impedance matching, high conversion ratio application and for extracting the maximum power from the RESs. However, a disadvantage of this system is that the output voltage V_{c2} is sensible to the load variation which results in a non regulated output voltage. This problem can be solved by regulating the DC bus using another converter.

Standalone nanogrid

A nanogrid consisting of n output-parallel-connected converters behaving as LFRs for PV applications in DC nanogrids has been considered in Chapter 8. A storage battery connected to a DC bus through a bidirectional converter is also aggregated as back-up for the system and for achieving the regulation of the DC bus. An extremum seeking MPPT controller is used for each PV panel which are connected to the DC grid using two-stage cascaded LFRs to step up the low voltage of the PV panel to the DC voltage of the grid (380 V). The stability analysis shows that the overall system is stable whenever the two-stage subsystems in each branch are in turn stable. The regulation of the DC bus and the direction of the power flow can be dictated by comparing the grid voltage and the reference voltage using a PI controller. Numerical simulations have been carried out for a system consisting of four branches corroborate the theoretical derivations.

Future work

As concluded before, the two cascaded LFRs have efficiency slightly lower than other converters of high gain conversion ratio. Thus, increasing the efficiency of the two cascaded LFRs by regulating the intermediate voltage to the optimal value should be considered as a future work. Moreover, the whole control system could be implemented digitally including the MPPT. In addition, research are in progress to validate the analysis and numerical simulations of Chapter 7 with experimental results.

Moreover, including a battery management system (BMS) and the effect of the cables in the nanogrid if more loads are connected can be also considered for as a future work. Nonlinear loads can be also considered for further research study. Implementing a DC nanogird, including two PV panels connected to a DC bus using two cascaded LFRs and a bidirectional converter connected to a back-up battery, experimentally is considered as a future work.

Appendix A

Experimental prototypes

This appendix explains the prototypes which have been implemented in the laboratory for verifying the analysis and simulation results. The used components and the schematic diagram of the experimental prototypes will be shown here.

A.1 Two Cascaded DC-Transformers

First, two prototypes of boost converter working as DC-transformers, have been implemented and are connected in cascade with the same set of parameters of the simulation. The used input voltage $V_g = 6$ V, related power $P_{in} = 18 \sim 36$ W, identical intermediate voltage $V_{c1} = 12$ V, identical output voltage $V_{c2} = 24$ V. The implementation of the prototypes has been carried out using Orcad program and the schematic diagram of the first BOF based a DC-transformer is depicted in Fig. A.1, which has the references of the used components. Fig. A.2 shows a picture for the experimental prototype for the first BOF converter based SMC while the picture of the two cascaded DC transformers has been depicted in Fig. A.3.

A very small resistance has been used for sensing the inductor currents. The part number of the gate drives which have been used for driving the MOSFETs are TC4420, while, the part number of the analog multipliers is AD835 and have been used for multiplying the factors k_{11} and k_{12} with the inductor currents. The comparator ,with number LM311, has been used for synthesizing the sliding surface. The used output capacitors are electrolytic and SMD types.

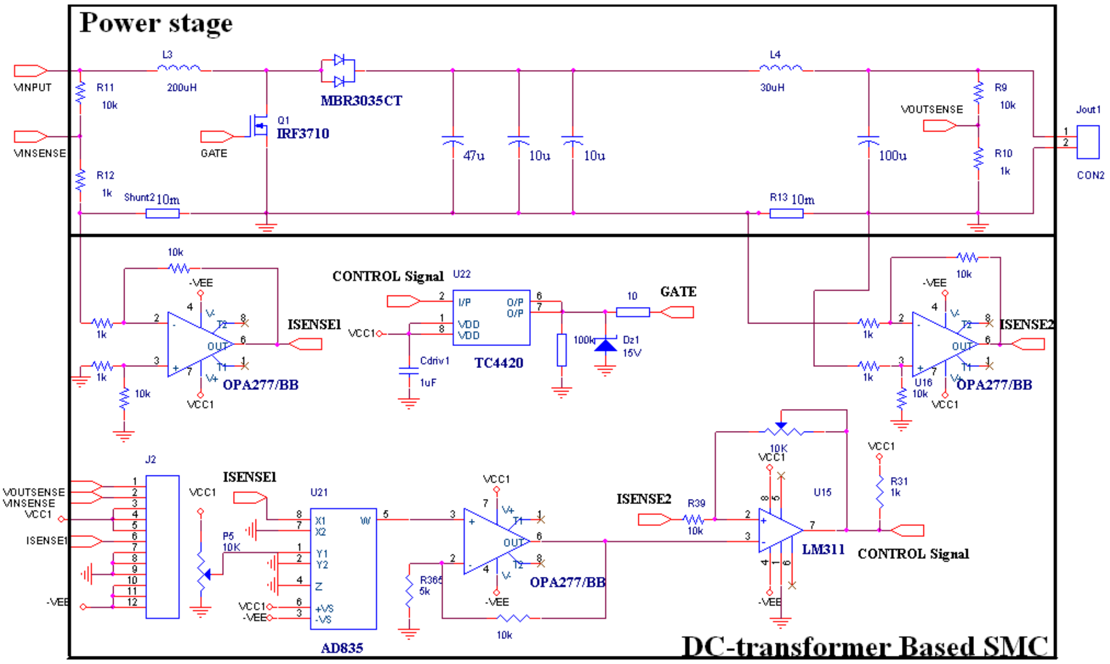

Figure A.1: The schematic diagram of the orcad program of the first BOF converter based DC-transformer using SMC.

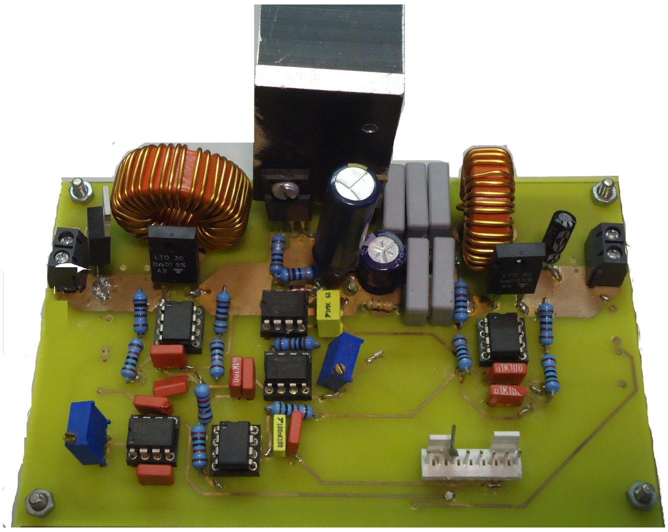

Figure A.2: Experimental prototype of the power stage and the control of the first DC-transformer using SMC.

A.2 Cascaded Connections of LFR and Gyrator

Second, two prototypes of boost converter working as LFRs or gyrators have been implemented and connected in cascade for obtaining a high conversion ratio. The

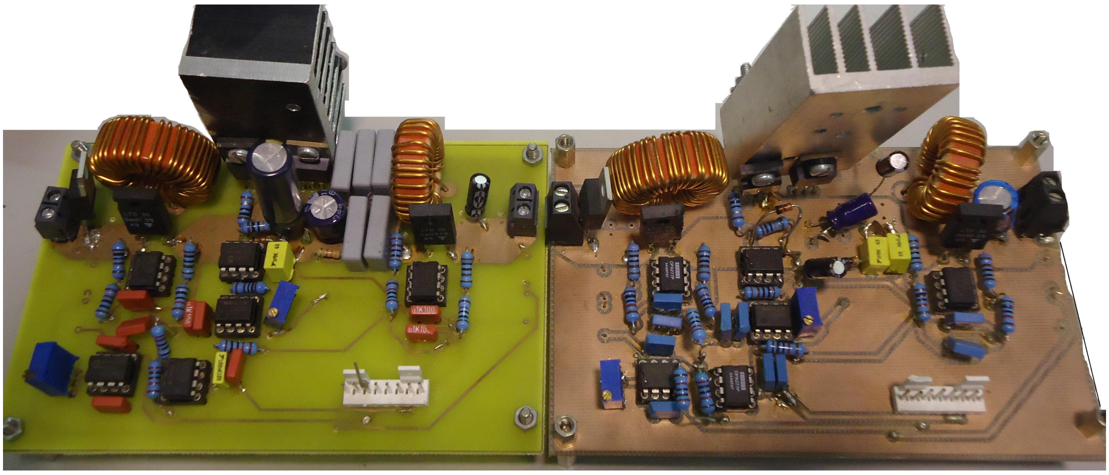

Figure A.3: Experimental prototypes of the two cascaded DC-transformers using SMC.

used input voltage $V_g = 15$ V from a DC voltage source, related power $P_{in} = 40 \sim 60$ W using a resistive load $1500 - 2500$ Ω, identical intermediate voltage $V_{c1} = 80$ V, identical output voltage $V_{c2} = 380$ V. The implementation of the prototypes has been carried out using Orcad program and the schematic diagram is depicted in Fig. A.4, which has the references of the used components. Current sensing is realized by means of a LA25-NP current transducer in both stages of the cascaded boost converters. A schottky diode is used for the first stage and a SiC diode is used for the second stage. The prototypes work as LFRs if the input voltage of the power stage board is sensed to the control board. However, if the output voltage of the power stage board is sensed to the control, it works as a gyrator. The power stage and the control of the first stage are shown in Fig. A.5 and A.6 respectively.

The previous two cascaded boost converters based LFRs prototypes are connected to a BP585 PV module in the laboratory. This PV module has a nominal power of 85 W. A picture of the used PV module is shown in Fig. A.7, while the system of the two cascaded LFRs are shown in Fig. A.8. The MPPT algorithm has been implemented using the microcontroller PIC18F1320 and an external integrator circuit. The output of the two cascaded boost converters is connected to an active load SPS800X13, which has been configured to work as constant DC voltage of 380 V and is depicted in Fig. A.9. In order to control such changing conditions, a PV emulator E4360A has been used as a source for the irradiance and temperature change measurements which is depicted in Fig. A.10.

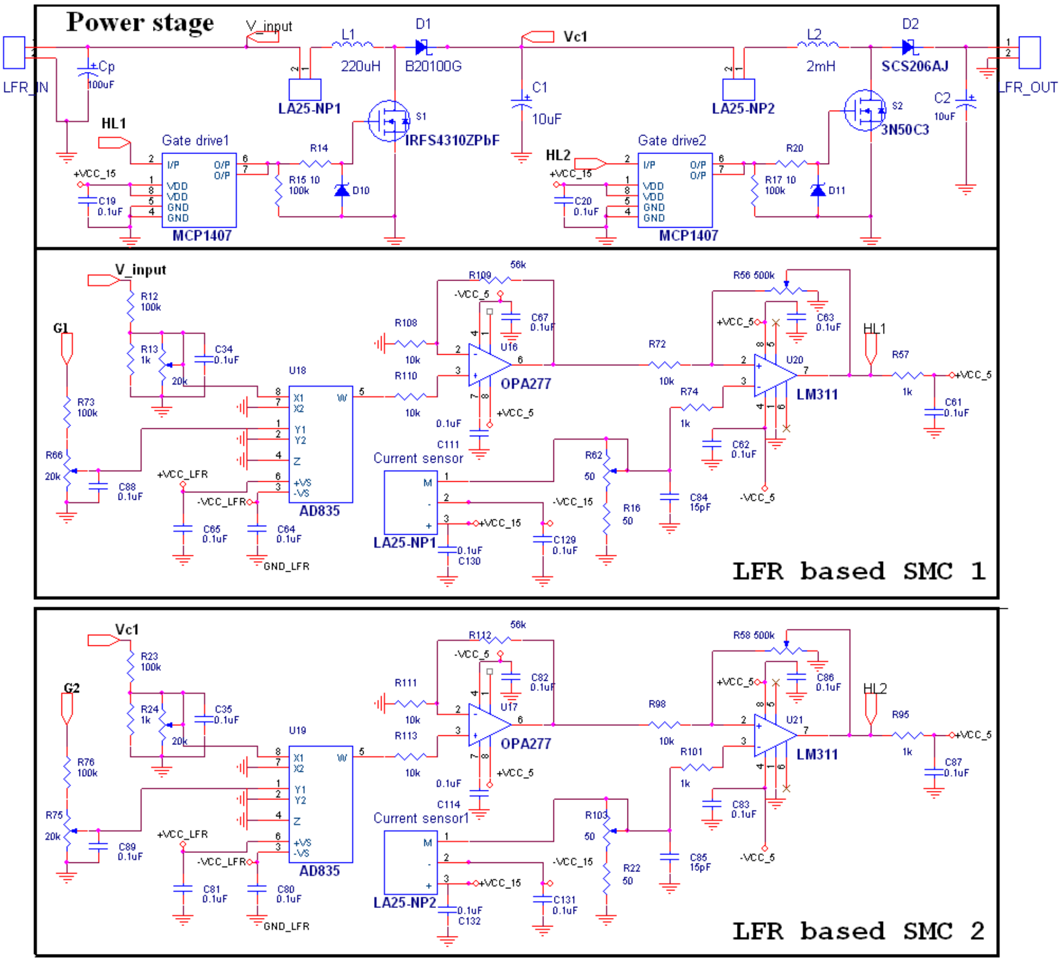

Figure A.4: The schematic diagram of the orcad program of the two cascaded LFRs or Gyrators based SMC.

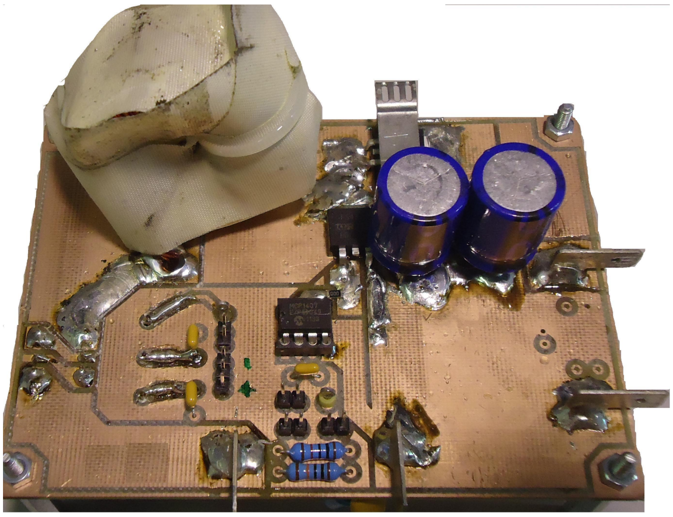

Figure A.5: Experimental prototype of the a boost converter which has been used for a high gain conversion ratio.

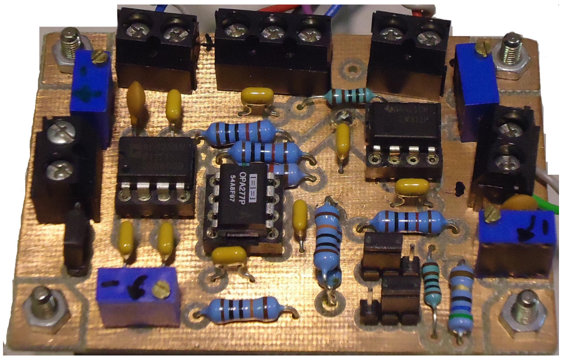

Figure A.6: Experimental prototype of the control board for applying LFR or gyrator based SMC.

Figure A.7: PV modules in the roof of the laboratory.

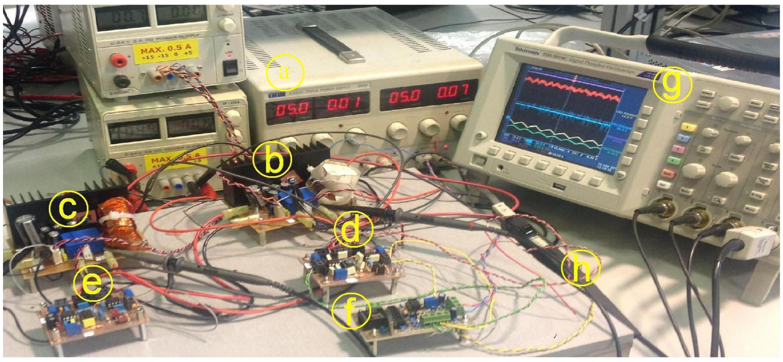

Figure A.8: Experimental prototypes of the two cascaded boost-based LFRs. (a) DC voltage source for supplying the control (b) First stage LFR. (c) Second stage LFR. (d) SMC for the first stage. (e) SMC for the second stage. (f) MPPT controller. (g) Tektronix oscilloscope TDS3014C. (h) Tektronix probe (TCP202).

Figure A.9: Active load working as a constant voltage source SPS800X13.

Figure A.10: PV emulator is used for making step change of irradiance or temperature E4360A.

Appendix B

Publications

This Appendix gives a list with the published conferences and journal papers during the dissertation research.

List of conference papers

1. El Aroudi A., Haroun R., Cid-Pastor A., and Martinez-Salamero, L.: Notch Filtering-Based Stabilization of PFC AC-DC Pre-regulators, 2010 14th International Power Electronics and Motion Control Conference and Exposition (EPE-PEMC 2010).

2. Haroun R., El Aroudi A., Cid-Pastor A., and Martinez-Salamero, L.: Cascade Connection of DC-DC Boost Converters Using the Loss-Free Resistor Concept and Sliding Mode Control, 2011 Seminario Anual de Automtica, Electrnica Industrial i Instrumentacin Conference (SAAEI 2011).

3. Haroun R., Cid-Pastor A., El Aroudi A., and Martinez-Salamero, L.: Cascade Connection of DC-DC Boost Converters Using the Loss-Free Resistor Concept and Sliding Mode Control, 2012 Seminario Anual de Automtica, Electrnica Industrial i Instrumentacin Conference (SAAEI 2012).

4. Haroun R., Cid-Pastor A., El Aroudi A., and Martinez-Salamero, L.: Cascade Connection of DC-DC Switching Converters by Means of Self-Oscillating DC-Transformers, 2012 15th International Power Electronics and Motion Control Conference and Exposition (EPE-PEMC 2012).

5. Haroun R., El Aroudi A., Cid-Pastor A., and Martinez-Salamero, L.: Synthesis of a Power Gyrator Based on Sliding Mode Control of two Cascaded

Boost Converters Using a Single Sliding Surface, 2013 10th International Multiconference on Signals, Systems and Devices (SSD 2013).

6. Haroun R., El Aroudi A., Cid-Pastor A., and Martinez-Salamero, L.: Stability Issues in Cascade Connected Switching Converters for DC Microgrid Applications, 2013 International Symposium on Circuits and Systems (ISCAS 2013).
7. Haroun R., Olalla C., El Aroudi A., Cid-Pastor A., and Martinez-Salamero, L.: Efficiency Optimization of Cascaded Boost Converters Under Sliding Mode Control, 2013 Seminario Anual de Automtica, Electrnica Industrial i Instrumentacin Conference (SAAEI 2013).
8. Haroun R., El Aroudi A., Cid-Pastor A., and Martinez-Salamero, L.: Sliding-Mode Control of a Three-Stage DC-AC Inverter for PV Applications, 2013 International Conference on Power Electronics and their Applications (ICPEA 2013).
9. Haroun R., El Aroudi A., Cid-Pastor A., and Martinez-Salamero, L.: Large-Signal Modeling and Stability Analysis of Two-cascaded Boost Converters Connected to a PV Panel Under SMC with MPPT, 2013 39th Annual Conference of the IEEE Industrial Electronics Society (IECON 2013).
10. Haroun R., El Aroudi A., Cid-Pastor A., and Martinez-Salamero, L.: Sliding Mode Control of Output-Parallel-Connected Two-Stage Boost Converters for PV Systems, 2014 11th International Multiconference on Signals, Systems and Devices (SSD 2014).

List of journal papers

1. El Aroudi A., Orabi, M., Haroun R., and Martinez-Salamero, L.: Slow Scale Stability Boundary of PFC AC-DC Power Converters: Theoretical Prediction and Experimental Validation, IEEE, Transactions on Industrial Electronics, vol. 58 ,pp. 3448 - 3460, no. 8, August 2011.
2. El Aroudi A., Haroun R., Cid-Pastor A., and Martinez-Salamero, L.: Suppression of Line Frequency Instabilities in PFC AC-DC Power Supplies by Feedback Notch Filtering the Pre-regulator Output Voltage, IEEE, Transactions on Circuits and Systems, vol. 60, pp. 796-809, no. 03, March 2013.
3. El Aroudi A., Haroun R., Cid-Pastor A., Kouzou A., and Martinez-Salamero, L.: A comparison between static and dynamic performances of a Z-source

and a dual-stage boost converter under SMC for PV energy applications, Energy Procedia, vol. 42, pp. 587 - 596, Nov., 2013.

4. Haroun R., Cid-Pastor A., El Aroudi A., and Martinez-Salamero, L.: Synthesis of Canonical Elements for Power Processing in DC Distribution Systems Using Cascaded Converters and Sliding Mode Control, IEEE, Transactions on Power Electronics, vol. 29, pp. 1366-1381, no. 03, March, 2014.

5. Haroun R., El Aroudi A., Cid-Pastor A., and Martinez-Salamero, L.: Synthesis of a Power Gyrator Based on Sliding Mode Control of two Cascaded Boost Converters Using a Single Sliding Surface, International Journal Transactions on Systems, Signals and Devices, vol. 9, pp. 01-18, 2014.

6. Haroun R., El Aroudi A., Cid-Pastor A., and Martinez-Salamero, L.: Impedance Matching in Photovoltaic Systems Using Cascaded Boost Converters and Sliding-Mode Control, IEEE, Transactions on Power Electronics, in press.

Bibliography

Abrishamifar, A., Ahmad, A., and Mohamadian, M. (2012). Fixed switching frequency sliding mode control for single-phase unipolar inverters. *IEEE Transactions on Power Electronics*, 27(5):2507–2514.

A.G. de Brito, M., Galotto, L., P. Sampaio, L., de Azevedo e Melo, G., and A. Canesin, C. (2013). Evaluation of the main MPPT techniques for photovoltaic applications. *IEEE Transactions on Industrial Electronics*, 60(3):1156– 1167.

Akagi, H. (2011). Classification, terminology, and application of the modular multilevel cascade converter (MMCC). *IEEE Transactions on Power Electronics*, 26(11):3119–3130.

Anderson, J. and Peng, F. (2008). Four quasi-Z-Source inverters. In *IEEE Power Electronics Specialists Conference (PESC)*, pages 2743–2749.

Axler, S. (1997). *Linear Algebra Done Right*. Undergraduate Texts in Mathematics. Springer-Verlag, Springer-Verlag 175 Fifth Avenue, New York, New York 10010, U.S.A., 2nd edition.

Ayyanar, R., Giri, R., and Mohan, N. (2004). Active input-voltage and load-current sharing in input-series and output-parallel connected modular DC-DC converters using dynamic input-voltage reference scheme. *IEEE Transactions on Power Electronics*, 19(6):1462–1473.

Barazarte, R., Gonza Andlez, G., and Ehsani, M. (2010a). Generalized gyrator theory. *IEEE Transactions on Power Electronics*, 25(7):1832 –1837.

Barazarte, R., Gonzalez, G., and Ehsani, M. (2010b). Generalized gyrator theory. *IEEE Transactions on Power Electronics*, 25(7):1832–1837.

Barrado, J., El Aroudi, A., Valderrama-Blavi, H., Calvente, J., and Martinez-Salamero, L. (2012). Analysis of a self-oscillating bidirectional DC-DC converter in battery energy storage applications. *IEEE Transactions on Power Delivery*, 27(3):1292–1300.

Boroyevich, D., Cvetkovic, I., Burgos, R., and Dong, D. (2013). Intergrid: A Future Electronic Energy Network? *IEEE Journal of Emerging and Selected Topics in Power Electronics*, 1(3):127–138.

Boroyevich, D., Cvetkovic, I., Dong, D., Burgos, R., Wang, F., and Lee, F. (2010). Future electronic power distribution systems a contemplative view. In *IEEE 12th International Conference on Optimization of Electrical and Electronic Equipment (OPTIM)*, pages 1369– 1380.

Bratcu, A. I., Munteanu, I., Bacha, S., Picault, D., and Raison, B. (2011). Cascaded DC-DC converter photovoltaic systems: power optimization issues. *IEEE Transactions on Industrial Electronics*, 58(2):403–411.

Brenna, M., Lazaroiu, G., and Tironi, E. (2006). High power quality and DG integrated low voltage DC distribution system. In *IEEE Power Engineering Society General Meeting.*

Bryan, J., Duke, R., and Round, S. (2004). Decentralized generator scheduling in a nanogrid using DC bus signaling. In *IEEE Power Engineering Society General Meeting,*, volume 1, pages 977–982.

Camur, S., Arifoglu, B., Beser, E., and Beser, E. (2006). A novel topology for single-phase five-level inverter compared with H-bridge inverter. In *International Symposium on Power Electronics, Electrical Drives, Automation and Motion*, pages 556–560.

Cao, D., Jiang, S., Yu, X., and Peng, F. (2011). Low cost single-phase semi-Z-source inverter. In *Twenty-Sixth Annual IEEE Applied Power Electronics Conference and Exposition (APEC)*, pages 429–436.

Castillo, S., Balog, R., and Enjeti, P. (2010). Predicting capacitor reliability in a module-integrated photovoltaic inverter using stress factors from an environmental usage model. In *North American Power Symposium (NAPS)*, pages 1–6.

Cecati, C., Citro, C., and Siano, P. (2011). Combined operations of renewable energy systems and responsive demand in a smart grid. *IEEE Transactions on Sustainable Energy*, 2(2):468–476.

Cellatoglu, A. and Balasubramanian, K. (2010). Renewable energy resources for residential applications in coastal areas: A modular approach. In *42nd Southeastern Symposium on System Theory (SSST).*

Chang, Y.-C., Kuo, C.-L., Sun, K.-H., and Li, T.-C. (2013). Development and operational control of two-string maximum power point trackers in DC distribution systems. *IEEE Transactions on Power Electronics*, 28(4):1852–1861.

Chen, S.-M., Liang, T.-J., and Hu, K.-R. (2013). Design, analysis, and implementation of solar power optimizer for DC distribution system. *IEEE Transactions on Power Electronics*, 28(4):1764–1772.

Cid Pastor, A. (2005). *Energy processing by means of power gyrators.* PhD thesis, Technical University of Catalonia (UPC), Barcelona.

Cid-Pastor, A., Martinez-Salamero, L., Alonso, C., El Aroudi, A., and Valderrama-Blavi, H. (2009). Power distribution based on gyrators. *IEEE Transactions on Power Electronics*, 24(12):2907– 2909.

Cid-Pastor, A., Martinez-Salamero, L., Alonso, C., Estibals, B., Alzieu, J., Schweitz, G., and Shmilovitz, D. (2005). Analysis and design of power gyrators in sliding-mode operation. *IEE Proceedings Electric Power Applications*, 152(4):821– 826.

Cid-Pastor, A., Martinez-Salamero, L., Alonso, C., Leyva, R., and Singer, S. (2007a). Paralleling dc-dc switching converters by means of power gyrators. *IEEE Transactions on Power Electronics*, 22(6):2444– 2453.

Cid-Pastor, A., Martinez-Salamero, L., Alonso, C., Schweitz, G., Calvente, J., and Singer, S. (2006a). Classification and synthesis of power gyrators. In *IEE Proceedings on Electric Power Applications*, volume 153, pages 802–808.

Cid-Pastor, A., Martinez-Salamero, L., Alonso, C., Schweitz, G., Calvente, J., and Singer, S. (2006b). Synthesis of power gyrators operating at constant switching frequency. *Electric Power Applications, IEE Proceedings*, 153(6):842–847.

Cid-Pastor, A., Martinez-Salamero, L., El Aroudi, A., Giral, R., Calvente, J., and Leyva, R. (2013). Synthesis of loss-free resistors based on sliding-mode control and its applications in power processing. *Control Engineering Practice*, 21(5):689–699.

Cid-Pastor, A., Martinez-Salamero, L., Leyva, R., Calvente, J., and Giral, R. (2011). Design of photovoltaic-based current sources for maximum power transfer by means of power gyrators. *Power Electronics IET*, 4(6):674– 682.

Cid-Pastor, A., Martinez-Salamero, L., Parody, N., and El Aroudi, A. (2010). Analysis and design of a loss-free resistor based on a boost converter in PWM operation. In *IEEE International Symposium on Circuits and Systems (ISCAS10)*, pages 2742–2745.

Cid-Pastor, A., Martinez-Salamero, L., Ribes, U., and El Aroudi, A. (2007b). Analysis and design of a loss-free resistor based on a boost converter in sliding-operation. In *14th International Symposium on Power Electronics.*

Dasgupta, S., Sahoo, S., and Panda, S. (2011a). Single-Phase inverter control techniques for interfacing renewable energy sources with microgrid -Part I: parallel-connected inverter topology with active and reactive power flow control along with Grid current shaping. *IEEE Transactions on Power Electronics,*, 26(3):717–731.

Dasgupta, S., Sahoo, S., Panda, S., and Amaratunga, G. (2011b). Single-Phase inverter-control techniques for interfacing renewable energy sources with microgrid - Part II: series-connected inverter topology to mitigate voltage-related problems along with active power flow control. *IEEE Transactions on Power Electronics,*, 26(3):732–746.

de Souza Ribeiro, L., Saavedra, O., de Lima, S., and Gomes de Matos, J. (2011). Isolated micro-grids with renewable hybrid generation: the case of lencois island. *IEEE Transactions on Sustainable Energy*, 2(1):1–11.

Dong, D., Cvetkovic, I., Boroyevich, D., Zhang, W., Wang, R., and Mattavelli, P. (2013a). Grid-interface bidirectional converter for residential DC distribution systems-part one: high-density two-stage topology. *IEEE Transactions on Power Electronics*, 28(4):1655–1666.

Dong, D., Luo, F., Zhang, X., Boroyevich, D., and Mattavelli, P. (2013b). Grid-interface bidirectional converter for residential DC distribution systems-Part 2: AC and DC interface design with passive components minimization. *IEEE Transactions on Power Electronics*, 28(4):1667–1679.

Du, W., Zhang, J., Zhang, Y., Qian, Z., and Peng, F. (2011). Large signal stability analysis based on gyrator model with constant power load. In *IEEE Power and Energy Society General Meeting*, pages 1–8.

Ehsani, M., Husain, I., and Bilgic, M. (1993a). Inverse dual converter (IDC) for high-power DC-DC applications. *IEEE Transactions on Power Electronics*, 8(2):216–223.

Ehsani, M., Husain, I., and Bilgic, M. (1993b). Power converters as natural gyrators. *IEEE Transactions on Circuits and Systems*, 40(12):946–949.

Emadi, A., Khaligh, A., Rivetta, C., and Williamson, G. (2006). Constant power loads and negative impedance instability in automotive systems: definition, modeling, stability, and control of power electronic converters and motor drives. *IEEE Transactions on Vehicular Technology*, 55(4):1112– 1125.

Emelyanov, S. V. (1970). *Theory of variable structure systems.* Nauke, Moskov, Russia.

Erickson, R. and Maksimovic, D. (2001). *Fundamentals of power electronics.* Springer Science and Business Media Inc.

Esram, T. and Chapman, P. (2007). Comparison of photovoltaic array maximum power point tracking techniques. *IEEE Transactions on Energy Conversion*, 22(2):439–449.

Fahimi, B., Kwasinski, A., Davoudi, A., Balog, R. S., and Kiani, M. (2011). Powering a more electrified planet. *IEEE power and energy magazine*, (2):54–64.

Femia, N., Petrone, G., Spagnuolo, G., and Vitelli, M. (2005). Optimization of perturb and observe maximum power point tracking method. *IEEE Transactions on Power Electronics*, 20(4):963– 973.

Flores-Bahamonde, F., Valderrama-Blavi, H., Martinez-Salamero, L., Maixe-Altes, J., and Garcia, G. (2014). Control of a three-phase AC/DC VIENNA converter based on the sliding mode loss-free resistor approach. *IET Power Electronics*, 7(5):1073–1082.

Gajanayake, C., Lin, L. F., Beng, G. H., Lam, S. P., and Kian, S. L. (2009). Extended boost Z-source inverters. In *IEEE Energy Conversion Congress and Exposition (ECCE)*, pages 3845–3852.

Galigekere, V. and Kazimierczuk, M. (2012). Analysis of PWM Z-Source DC-DC sonverter in CCM for steady state. *IEEE Transactions on Circuits and Systems I: Regular Papers*, 59(4):854–863.

Gao, F., Loh, P., Blaabjerg, F., Teodorescu, R., and Vilathgamuwa, D. (2010). Five-level Z-source diode-clamped inverter. *IET Power Electronics*, 3(4):500–510.

Gao, F., Loh, P., Li, D., and Blaabjerg, F. (2011). Asymmetrical and symmetrical embedded Z-source inverters. *Power Electronics, IET*, 4(2):181–193.

Giral, R., Font, J., Martinez, L., Calvente, J., Leyva, R., and Fossas, E. (1996). Self-oscillating boost converter with output filter for ideal load regulation. *International Symposium on Circuits and Systems*, 1(13):529–532.

Giri, R., Ayyanar, R., and Ledezma, E. (2004). Input-Series and Output-Series Connected Modular DC-DC Converters with Active Input Voltage and Output Voltage Sharing. In *Nineteenth Annual IEEE Applied Power Electronics Conference and Exposition, APEC '04.*, volume 3, pages 1751–1756 Vol.3.

Gu, B., Dominic, J., Lai, J.-S., Zhao, Z., and Liu, C. (2013). High boost ratio hybrid transformer DC-DC converter for photovoltaic module applications. *IEEE Transactions on Power Electronics*, 28(4):2048–2058.

Hamill, D. (1993). Lumped equivalent circuits of magnetic components: the gyrator-capacitor approach. *IEEE Transactions on Power Electronics*, 8(2):97– 103.

Hamoudi, F., Aziz Chaghi, A., Amimeur, H., and Merabet, E. K. (2011). Sliding mode control with fixed switching frequency for four-wire shunt active filter . *Journal of Electrical Engineering & Technology*, 6(5):647–657.

Hanif, M., Basu, M., and Gaughan, K. (2011). Understanding the operation of a Z-source inverter for photovoltaic application with a design example. *IET Power Electronics*, 4(3):278–287.

He, Y. and Luo, F. (2006). Sliding-mode control for dc-dc converters with constant switching frequency. *IEE Proceedings -Control Theory and Applications*, 153(1):37–45.

Heydt, G., Sathyanarayana, B., and Vittal, V. (2009.). Distribution system design enabling renewable energy resource deployment. In *IEEE Power and Energy Society General Meeting*, pages 1–5.

Hung, J., Gao, W., and Hung, J. (1993). Variable structure control: a survey. *IEEE Transactions on Industrial Electronics*, 40(1):2–22.

Itkis, U. (1976). *Control systems of variable structure.* John Wiley & Sons, New York.

Jong-Lick, L., Chien-Yang, C., and Sung-Pei, Y. (2004). Dynamics analysis of LFR model for a single-stage high power factor correction diagonal half-bridge flyback ac/dc converter. *Chinese Institute of Engineers*, 32:555–567.

Karlsson, P. and Svensson, J. (2003). DC bus voltage control for a distributed power system. *IEEE Transactions on Power Electronics*, 18(6):1405– 1412.

Kim, J.-W., Yon, J.-S., and Cho, B. H. (2001). Modeling, control, and design of input-series-output-parallel-connected converter for high-speed-train power system. *IEEE Transactions on Industrial Electronics*, 48(3):536–544.

Kjaer, S., Pedersen, J., and Blaabjerg, F. (2005). A review of single-phase grid-connected inverters for photovoltaic modules. *IEEE Transactions on Industry Applications*, 41(5):1292–1306.

Kjaer, S. B. (2012). Evaluation of the "Hill Climbing" and the "incremental conductance" maximum power point trackers for photovoltaic power systems. *IEEE Transactions on Energy Conversion*, 27(4):922–929.

Koutroulis, E. and Blaabjerg, F. (2013). Design optimization of transformerless grid-connected PV inverters including reliability. *IEEE Transactions on Power Electronics*, 28(1):325–335.

Kramer, W., Chakraborty, S., Kroposki, B., and Thomas, H. (2008). Advanced power electronic interfaces for distributed energy systems part 1: systems and topologies. *Technical Report.*

Latham, A., Pilawa-Podgurski, R., Odame, K., and Sullivan, C. (2013). Analysis and optimization of maximum power point tracking algorithms in the presence of noise. *IEEE Transactions on Power Electronics*, 28(7):3479–3494.

Lenz Cesar, E. and Pagano, D. D. (2013). Nonlinear control for bidirectional power converter in a Dc microgrid. *Nonlinear Control Systems*, 9:359–364.

Leyva, R., Alonso, C., Queinnec, I., Cid-Pastor, A., Lagrange, D., and Martinez-Salamero, L. (2006). MPPT of photovoltaic systems using extremum-seeking control. *IEEE Transactions on Aerospace and Electronic Systems*, 42(1):249–258.

Lim, Y. H. and Hamill, D. (2000). Simple maximum power point tracker for photovoltaic arrays. *Electronics Letters*, 36(11).

Liu, J., Hu, J., and Xu, L. (2007). Dynamic modeling and analysis of Z source converter-derivation of AC small signal model and design-oriented analysis. *IEEE Transactions onPower Electronics*, 22(5):1786– 1796.

Luo, S. and Batarseh, I. (2005). A Review of distributed power systems part I: DC distributed power system. *IEEE Aerospace and Electronic Systems Magazine*, 20(8):5–16.

Madan, T., Das, D., and Singh2, S. (2013). Role of power converters in photovoltaic cells . *International Journal of Engineering & Science Research*, 3(3):2597–2603.

Martinez-Salamero, L. (2009). Synthesis of canonical elements for power processing. In *6th International Multi-Conference on Systems, Signals and Devices*, pages 1–6.

Martinez-Salamero, L. and Cid-Pastor, A. (2012). Synthesis of canonical elements for power processing based on sliding-mode control. In Fridman, L., Moreno, J., and Iriarte, R., editors, *Sliding Modes after the First Decade of the 21st Century*, volume 412 of *Lecture Notes in Control and Information Sciences*, pages 517–540. Springer Berlin / Heidelberg.

Martinez-Salamero, L., Valderrama-Blavi, H., Giral, R., Alonso, C., Estibals, B., and Cid-Pastor, A. (2005). Self-oscillating DC-to-DC switching converters with transformer characteristics. *IEEE Transactions on Aerospace and Electronic Systems*, 41(2):710–716.

Marwali, M., Jung, J.-W., and Keyhani, A. (2004). Control of distributed generation systems - Part II: Load sharing control. *IEEE Transactions on Power Electronics*, 19(6):1551– 1561.

Mattavelli, P., Rossetto, L., Spiazzi, G., and Tenti, P. (1993). General-purpose sliding-mode controller for DC-DC converter applications. In *24th Annual IEEE Power Electronics Specialists Conference, (PESC)*, pages 609 – 615.

Middlebrook, R. D. (1976). Input filter consideration in design and application of switching regulators. In *IEEE Industry Applications Society annual Meeting*, pages 366–382.

Middlebrook, R. D. and Ćuk, S. (1976). A general unified approach to modelling switching-converter power stages. In *Power Electronics Specialists Conference*, pages 18–34.

Mozina, C. (2012). Impact of smart grid and green power generation on distribution systems. In *IEEE Innovative Smart Grid Technologies conference (ISGT)*, pages 1–13.

Naumanen, V., Luukko, J., Silventoinen, P., Pyrhonen, J., Saren, H., and Rauma, K. (2010). Compensation of DC link voltage variation of a multilevel series-connected H-bridge inverter. *IET Power Electronics*, 3(5):793–803.

Nguyen, M.-K., Jung, Y.-G., Yang, H.-Y., and Lim, Y.-C. (2010). Single-phase Z-source cycloconverter with safe-commutation strategy. *IET Power Electronics*, 3(2):232–242.

Nguyen, M.-K., Lim, Y.-C., and Choi, J.-H. (2012). Two switched-inductor quasi-Z-source inverters. *IET Power Electronics*, 5(7):1017–1025.

Nilsson, D. (2005). *DC distribution systems*. PhD thesis, Chalmers University of Technology, Sweden.

Noguchi, T., Togashi, S., and Nakamoto, R. (2002). Short-current pulse-based maximum-power-point tracking method for multiple photovoltaic-and-converter module system. *IEEE Transactions on Industrial Electronics*, 49(1):217– 223.

Onwuchekwa, C. and Kwasinski, A. (2010). Analysis of Boundary Control for Buck Converters With Instantaneous Constant-Power Loads. *IEEE Transactions on Power Electronics*, 25(8):2018–2032.

Onwuchekwa, C. and Kwasinski, A. (2011). Analysis of boundary control for boost and buck-boost converters in distributed power architectures with constant-power loads. In *IEEE Twenty-Sixth Annual Applied Power Electronics Conference and Exposition (APEC),*, pages 1816–1823.

Peng, F., Yuan, X., Fang, X., and Qian, Z. (2003). Z-source inverter for adjustable speed drives. *IEEE Power Electronics Letters*, 1(2):33–35.

Peng, F. Z. (2002). Z-source inverter. In *37th Annual Meeting. Conference Record of the Industry Applications Conference (IAS).*

Petrone, G., Spagnuolo, G., Teodorescu, R., Veerachary, M., and Vitelli, M. (2008). Reliability issues in photovoltaic power processing systems. *IEEE Transactions on Industrial Electronics*, 55(7):2569–2580.

Petrone, G., Spagnuolo, G., and Vitelli, M. (2007). Analytical model of mismatched photovoltaic fields by means of Lambert W-function. *Solar Energy Materials and Solar Cells*, 91(18):1652–1657.

Petrone, G., Spagnuolo, G., and Vitelli, M. (2012). An analog technique for distributed MPPT PV applications. *IEEE Transactions on Industrial Electronics*, 59(12):4713–4722.

Planas, E., Gil-de Muro, A., Andreu, J., Kortabarria, I., and Martinez de Alegria, I. (2013). Design and implementation of a droop control in d-q frame for islanded microgrids. *IET Renewable Power Generation*, 7(5):458–474.

Poshtkouhi, S., Palaniappan, V., Fard, M., and Trescases, O. (2012). A general approach for quantifying the benefit of distributed power electronics for fine grained MPPT in photovoltaic applications using 3-D modeling. *IEEE Transactions on Power Electronics*, 27(11):4656–4666.

Rahimi, A., Khaligh, A., and Emadi, A. (2006). Design and Implementation of an Analog Constant Power Load for Studying Cascaded Converters. In *IEEE 32nd Annual Conference on Industrial Electronics*, pages 1709–1714.

Ramos-Paja, C., Romero, A., Giral, R., Vidal-Idiarte, E., and Martinez-Salamero, L. (2009). Fuzzy-based modelling technique for PEMFC electrical power generation systems emulation. *Power Electronics IET*, 2(3):241– 255.

Ropp, M. and Gonzalez, S. (2009). Development of a MATLAB/Simulink model of a single-phase grid-connected photovoltaic system. *IEEE Transactions on Energy Conversion*, 24(1):195–202.

Rtten, E. and Harting, D. (2010). The german roadmap E-energy / smart grid.

Saglam, C., Baran, E., Nergiz, A., and Sabanovic, A. (2011). Model following control with discrete time SMC for time-delayed bilateral control systems. In *IEEE International Conference on Mechatronics (ICM)*, pages 997–1002.

Salomonsson, D. and Sannino, A. (2007). Low-voltage DC distribution system for commercial power systems with sensitive electronic loads. *IEEE Transactions on Power Delivery*, 22(3):1620– 1627.

Sannino, A., Postiglione, G., and Bollen, M. H. J. (2003). Feasibility of a DC network for commercial facilities. *IEEE Transactions on Industry Applications*, 39(5):1499–1507.

Schonberger, J., Duke, R., and Round, S. (2006). DC-bus signaling: A distributed control strategy for a hybrid renewable nanogrid. *IEEE Transactions on Industrial Electronics*, 53(5):1453– 1460.

Serna, R. J., Pierquet, B. J., Santiago, J., and Pilawa-Podgurski, R. C. (2013). Field measurements of transient effects in photovoltaic panels and its importance in the design of maximum power point trackers. In *Twenty-Eighth Annual IEEE Applied Power Electronics Conference and Exposition (APEC)*, pages 3005–3010.

Shen, M., Wang, J., Joseph, A., Peng, F., Tolbert, L., and Adams, D. (2004). Maximum constant boost control of the Z-source inverter. In *39th IAS Annual Meeting Industry Applications Conference*, volume 1, pages 142–147.

Shen, M., Wang, J., Joseph, A., Peng, F.-Z., Tolbert, L., and Adams, D. (2006). Constant boost control of the Z-source inverter to minimize current ripple and voltage stress. *IEEE Transactions on Industry Applications*, 42(3):770–778.

Shi, J., Zhou, L., and He, X. (2012). Common-duty-ratio control of input-parallel output-parallel (IPOP) connected DC-DC converter modules with automatic sharing of currents. *IEEE Transactions on Power Electronics*, 27(7):3277–3291.

Shmilovitz, D., Yaron, I., and Singer, S. (1998). Transmission-line-based gyrator. *IEEE Transactions on Circuits and Systems*, 45(4):428–433.

Shtessel, Y., Edwards, C., Fridman, L., and Levant, A. (2014). *Sliding mode control and observation.* Springer New York.

Singer, S. (1987). Gyrators Application in Power Processing Circuits. *IEEE Transactions on Industrial Electronics*, IE-34(3):313– 318.

Singer, S. (1988). Loss-free gyrator realization. *IEEE Transactions on Circuits and Systems*, 35(1):26– 34.

Singer, S. (1990). Realization of loss-free resistive elements. *IEEE Transactions on Circuits and Systems*, 37(1):54–60.

Singer, S. (1991). The application of loss-free resistors in power processing circuits. *IEEE Transactions on Power Electronics*, 6(4):595–600.

Singer, S. and Erickson, R. (1992). Canonical modeling of power processing circuits based on the POPI concept. *IEEE Transactions on Power Electronics*, 7(1):37–34.

Singer, S. and Erickson, R. (1994). Power-source element and its properties. *IEE Proceedings Circuits, Devices and Systems*, 141(3):220–226.

Sintupatsuk, P., Khomfoi, S., and Paisuwanna, P. (2012). A DC to DC multilevel modular capacitor clamped converter with electrical grounding isolation and bidirectional power flow for a dc microgrid application. In *9th International Conference on Electrical Engineering/Electronics, Computer, Telecommunications and Information Technology (ECTI-CON)*, pages 1–4.

Sira-Ramirez, H. (1987). Sliding motions in bilinear switched networks. *IEEE Transactions on Circuits and Systems*, 34(8):919–933.

Spiazzi, G. and Mattavelli, P. (2001). *The power electronics handbook.* CRC Press.

Spiazzi, G., Mattavelli, P., Rossetto, L., and Malesani, L. (1995). Application of sliding mode control to switch-mode power supplies. *Journal of Circuits, Systems and Computers*, 05(03):337–354.

Stramosk, V. and Pagano, D. (2013). Nonlinear control of a bidirectional dc-dc converter operating with boost-type Constant-Power Loads. In *Brazilian Power Electronics Conference (COBEP),*, pages 305–310.

Sullivan, C., Awerbuch, J., and Latham, A. (2013). Decrease in photovoltaic power output from ripple: simple general calculation and the effect of partial shading. *IEEE Transactions on Power Electronics*, 28(2):740–747.

Sun, K., Zhang, L., Xing, Y., and Guerrero, J. (2011). A distributed control strategy based on DC bus signaling for modular photovoltaic generation systems with battery energy storage. *IEEE Transactions on Power Electronics*, 26(10):3032–3045.

Suntio, T. and Gadoura, D. (2002). Use of unterminated two-port modeling technique in analysis of input filter interactions in telecom DPS systems. In *24th Telecommunications Energy Conference, 2002. (INTELEC)*, pages 560– 565.

Utkin, V. I. (1978). *Sliding modes and their application in variable structure systems.* MIR Publishers.

Utkin, V. I., Guldner, J., and Shi, J. X. (1999). *Sliding mode control in electromechanical systems.* Taylor and Francis.

Veerachary, M., Senjyu, T., and Uezato, K. (2002). Feedforward maximum power point tracking of PV systems using fuzzy controller. *IEEE Transactions on Aerospace and Electronic Systems*, 38(3):969– 981.

Veerachary, M. and Sudhakar, S. B. (2009). Stability analysis of cascaded DC-DC power electronic system. *IEEJ Transactions on Electrical and Electronic Engineering*, 4(6):763–770.

Vighetti, S., Ferrieux, J. P., and Lembeye, Y. (2012). Optimization and design of a cascaded DC-DC converter devoted to grid-connected photovoltaic systems. *IEEE Transactions on Power Electronics*, 27(4):2018 – 2027.

Villalva, M., Gazoli, J., and Filho, E. (2009). Comprehensive approach to modeling and simulation of photovoltaic arrays. *IEEE Transactions on Power Electronics*, 24(5):1198– 1208.

Wai, R.-J. and Duan, R.-Y. (2005). High step-up converter with coupled-inductor. *IEEE Transactions on Power Electronics*, 20(5):1025–1035.

Wai, R.-J., Wang, W.-H., and Lin, C.-Y. (2008). High-performance stand-alone photovoltaic generation system. *IEEE Transactions on Industrial Electronics*, 55(1):240–250.

Walker, G. R. (2001). Evaluating MPPT converter topologies using a MATLAB PV model. *Journal of Electrical & Electronics Engineering, Australia*, 21(1):49–56.

Walker, G. R. and Sernia, P. C. (2004). Cascaded DC-DC converter connection of photovoltaic modules. *IEEE Transactions on Power Electronics*, 19(7):1130–1139.

Wang, X., Yao, R., Member, S., and Rao, F. (2003). Three-step impedance criterion for small-signal stability analysis in two-stage DC distributed power systems. *IEEE Power Electronics Letters*, 1(3):83–87.

Wolfs, P. and Li, Q. (2002). An analysis of a resonant half bridge dual converter operating in continuous and discontinuous modes. In *33rd Annual IEEE Power Electronics Specialists Conference*, volume 3, pages 1313–1318.

Xu, C. and Cheng, K. (2011). A survey of distributed power system - AC versus DC distributed power system. In *4th International Conference on Power Electronics Systems and Applications (PESA)*, pages 1–12.

Yan, W., Chung, H., Au, K., and Ho, C. (2008). Fixed-frequency boundary control of buck converters with second-order switching surface. In *Power Electronics Specialists Conference (PESC)*, pages 629 –635.

Yang, X., Zhang, H., and Ma, X. (2009). Modeling and stability analysis of cascade buck converters with N power stages. *Mathematics and Computers in Simulation*, 80(3):533–546.

Yinger, R. and Kamiab, A. (2011). Good vibrations. *IEEE Power and Energy Magazine*, 9(5):22– 32.

Zhang, X., Ruan, X., Kim, H., and Tse, C. K. (2013). Adaptive active capacitor converter for improving stability of cascaded DC power supply system. *IEEE Transactions on Power Electronics*, 28(4):1807– 1816.

Zhao, Q. and Lee, F. (2003). High-efficiency, high step-up DC-DC converters. *IEEE Transactions on Power Electronics*, 18(1):65–73.